Title

Surface constraints on the global ocean overturning circulation: Southern Ocean vs North Atlantic

Permalink

https://escholarship.org/uc/item/3zt7z9s0

Author

Sun, Shantong

Publication Date

2019

Peer reviewed|Thesis/dissertation

UNIVERSITY OF CALIFORNIA SAN DIEGO

Surface constraints on the global ocean overturning circulation: Southern Ocean vs North Atlantic

A dissertation submitted in partial satisfaction of the
requirements for the degree
Doctor of Philosophy

in

Oceanography

by

Shantong Sun

Committee in charge:

Professor Ian Eisenman, Chair
Professor Paola Cessi
Professor Sutanu Sarkar
Professor Andrew Stewart
Professor Lynne Talley
Professor Shang-Ping Xie

2019

The dissertation of Shantong Sun is approved, and it is acceptable in quality and form for publication on microfilm and electronically:

Chair

University of California San Diego

2019

TABLE OF CONTENTS

LIST OF FIGURES

LIST OF TABLES

ACKNOWLEDGEMENTS

I would like to start by thanking my PhD advisor, Ian. He has been an awesome advisor and a great friend to me during the past 5 years. He has been my mentor in doing research, communicating with others, being a parent, and even fixing car problems. Without his continuous support and encouragement, this dissertation would not have been possible.

I am also deeply grateful for my committee members, Andrew, Shang-Ping, Lynne, Paola, and Sutanu. Andrew has been like a co-advisor to me and his physical intuition has always impressed me. Shang-Ping has played a big role in many of the big steps I have taken since 2012, including my admission to SIO in 2013. Lynne taught me to have more appreciation for ocean observations. Paola has been a great source of motivation for me to think deeper and do more creative work. Sutanu taught me numerical method and turbulence.

Thanks and appreciations for my amazing groupmates: Till Wagnar, Erica Rosenblum, Emma Beer, and Skipper. Their companions have made the challenging PhD life less stressful and more fun. Also thanks for many friends I met in SIO, Arjun Jagnathan, Cesar Rocha, Waen Anutaliya, Janin Guzman-Morales, Weijie Wang, Jun Liu, Wei Wang, Ru Chen, He Wang, and Bofu Zheng, etc. The experience with them has made the past 6 years more memorable.

Thanks to my wife Tingting and my daughter Iris. Without them, I would not have passed through the days when I was skeptical of myself. Iris keeps surprising me in the past two and half years. Her presence has been the best gift I have ever imagined in my life. I am also grateful for my other family members, including my parents, my parents-in-law, and my sisters. Without their support and understanding, I would not have done so much in my PhD.

Chapter 2, in full, is a reprint of the material as it appears in Geophysical Research Letters, “The influence of southern ocean surface buoyancy forcing on glacial-interglacial changes in the global deep ocean stratification”, by S. Sun, I. Eisenman, and A. L. Stewart (2016). The dissertation author was the primary investigator and author of this paper.

Chapter 3, in full, is a reprint of the material as it appears in Geophysical Research Letters,

"Does Southern Ocean surface forcing shape the global ocean overturning circulation?", by S. Sun, I. Eisenman, and A. L. Stewart (2018). The dissertation author was the primary investigator and author of this paper.

Chapter 4 is a reprint, with very minor revisions, of the material as it appears in Ocean Moddelling, "Sensitivity of the Antarctic Circumpolar Current transport to surface buoyancy conditions in the North Atlantic", by S. Sun and J. Liu (2017). The dissertation author was the primary investigator and author of this paper.

Chapter 5, in full, is draft in preparation for submission to the Journal of Climate as, "What sets the depth of the Atlantic Meridional Overturning Circulation?", by S. Sun, I. Eisenman, L. Zanna, and A. L. Stewart. The dissertation author was the primary investigator and author of this paper.

Chapter 6 is a summary of work in progress. The dissertation author is currently the only investigator and author of this chapter.

Chapter 7 is a draft of manuscript in preparation for submission as "The influence of ice velocity biases on the Antarctic sea ice extent trends", by S. Sun and I. Eisenman. The dissertation author was the primary investigator and author of this work.

VITA

2011	B.S. in Marine Science, Ocean University of China
2013	M.S. in Physical Oceanography, Ocean University of China
2019	Ph.D. in Oceanography, University of California San Diego

PUBLICATIONS

S. Sun, I. Eisenman, and A. L. Stewart, 2018: "Does Southern Ocean surface forcing shape the global ocean overturning circulation?" *Geophys. Res. Lett.*, 45(5), 2413-2423

S. Sun and J. Liu, 2017: "Sensitivity of the Antarctic Circumpolar Current transport to surface buoyancy conditions in the North Atlantic". *Ocean Modell.*, 118, 118-129

S. Sun, I. Eisenman, and A. L. Stewart, 2016: "The influence of southern ocean surface buoyancy forcing on glacial-interglacial changes in the global deep ocean stratification". *Geophys. Res. Lett.*, 43(15), 8124-8132

S. Sun, L. Wu, and B. Qiu, 2013: "Response of the inertial recirculation to intensified stratification in a two-layer quasigeostrophic ocean circulation model". *J. Phys. Oceanogr.*, 43(7), 1254-1269

ABSTRACT OF THE DISSERTATION

Surface constraints on the global ocean overturning circulation: Southern Ocean vs North Atlantic

by

Shantong Sun

Doctor of Philosophy in Oceanography

University of California San Diego, 2019

Professor Ian Eisenman, Chair

This thesis explores the physical connections between surface processes and the global ocean overturning circulation, which is a critical component of the climate system.

Chapter 2 discusses the influence of Southern Ocean surface buoyancy forcing on the global deep ocean stratification. It shows that Southern Ocean surface buoyancy forcing exerts a strong control on the global deep ocean stratification below 2000 m depth.

Chapter 3 investigates the impact of Southern Ocean surface buoyancy forcing on the depth of the Atlantic Meridional Overturning Circulation (AMOC). It concludes that diapycnal mixing diminishes the influence of Southern Ocean surface buoyancy forcing on the AMOC depth

and that the North Atlantic surface conditions can have a substantial influence on the AMOC depth.

Chapter 4 explores the influence of North Atlantic surface conditions on the Southern Ocean circulation. It highlights the importance of North Atlantic surface conditions in shaping the AMOC vertical structure.

Chapter 5 develops a framework that connects the AMOC depth to the surface density distributions in both the Southern Ocean and the North Atlantic.

Chapter 6 examines the role of the Southern Ocean in the AMOC variability. It highlights the importance of the Indo-Pacific ocean when the overturning circulation is not in steady state. Using a variety of models, it shows that changes in the Indo-Pacific component of the overturning circulation can compensate changes in the AMOC. This compensation decreases as the variability timescale becomes longer.

Chapter 7 is on a somewhat different subject. It investigates the influence of sea ice velocity biases on the simulated Antarctic sea ice extent trend during recent decades. It uses a state-of-the-art coupled climate model with the simulated ice velocity field replaced with a satellite-derived observational estimate to show that correcting the ice velocity bias could substantially improve the simulated Antarctic sea ice extent changes.

Chapter 1

Introduction

By redistributing heat and carbon around the globe, the global ocean overturning circulation is a critical component of the climate system (e.g., Buckley and Marshall, 2016). Changes in the global ocean overturning circulation have been frequently cited to contribute to climate variability on timescales from decades (e.g., Zhang and Zhang, 2015) to thousands of years (e.g., Sigman et al., 2010).

Historically, the global ocean overturning circulation is depicted as two separate cells stacked vertically in a two-dimensional depth-latitude space (Figure 1.1): an upper cell that is associated with northward transport of warm surface water and subsequent southward transport of the North Atlantic Deep Water (NADW) that forms near Greenland; and a lower cell that spreads the Antarctic Bottom Water (AABW) formed near Antarctica through the abyssal ocean.

This two-dimensional schematic in Figure 1.1 highlights the importance of Southern Ocean processes in ventilating the deep ocean (e.g., Marshall and Speer, 2012). Indeed, both observations and theories have recognized the Southern Ocean as a key player in constraining the global ocean overturning circulation (see schematic in Talley, 2013). Building on the residual-mean theory for the Southern Ocean overturning circulation, the overturning circulation has been connected to the surface buoyancy forcing as well as wind stress forcing in the Southern Ocean

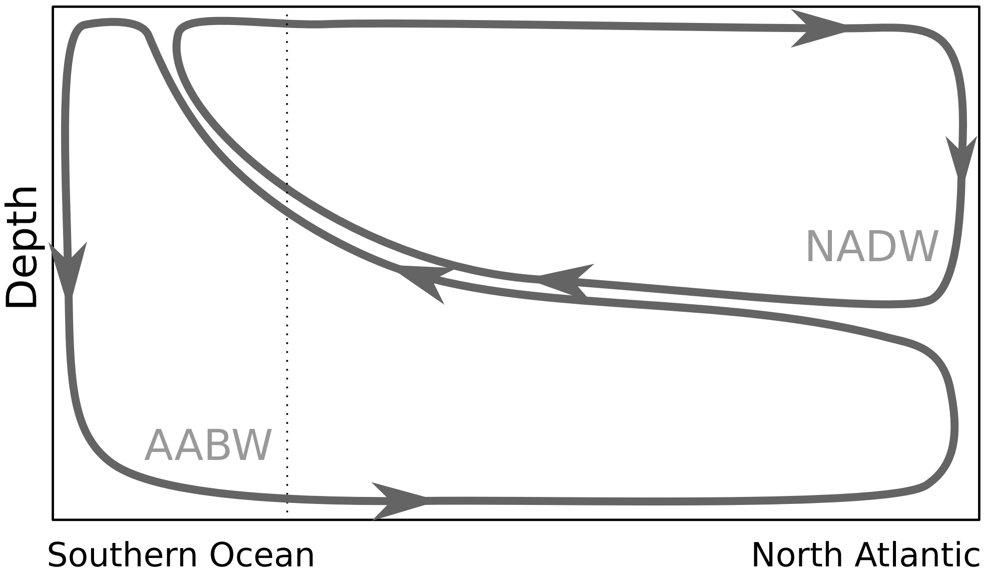

Figure 1.1: A two-dimensional schematic of the global ocean overturning circulation. This two dimensional perspective represents the globally zonal-integrated overturning circulation (e.g. Lumpkin and Speer, 2007).

(Marshall and Radko, 2003). Surface processes in the Southern Ocean have been suggested to play a significant role in controlling the global ocean overturning circulation (e.g., Ferrari et al., 2014)

On the other hand, the North Atlantic surface conditions have also been suggested to have substantial influence on the global ocean overturning circulation. For example, Muglia and Schmittner (2015) suggested that a stronger Northern Hemisphere westerly wind would lead to an increase in northward salt transport in the North Atlantic, more active NADW formation, and thus a deeper Atlantic Meridional Overturning Circulation (AMOC) at the Last Glacial Maximum (LGM).

In Chapter 2 to 5, I will explore the surface constraints on the steady-state global ocean overturning circulation, with a focus on the deep ocean stratification and the AMOC depth, using a combination of numerical simulations and idealized theories. I will develop a number of conceptual models to connect the global ocean overturning circulation to surface processes in the Southern Ocean as well as in the North Atlantic.

However, the ocean is never in steady state due to the long response timescales of the deep ocean (e.g., Zhang et al., 2013). In Chapter 6, I will discuss the trasient responses of the global ocean overturning circulation. I will highlight the importance of the Indo-Pacific basin in the transient response of the global ocean overturning circulation.

The last science chapter (Chapter 7) of this dissertation is on a different subject: sea ice. I will use a comprehensive coupled global climate model to investigate the influence of sea ice velocity biases on the Antarctic sea ice extent trends in the past three decades. Finally, I will end with concluding remarks on the extent to which the Southern Ocean and the North Atlantic each constrain the AMOC in Chapter 8.

Chapter 2

The influence of Southern Ocean surface buoyancy forcing on glacial-interglacial changes in the global deep ocean stratification

2.1 Introduction

During the Last Glacial Maximum (LGM), the climate was characterized by a colder global-mean temperature and lower atmospheric CO_2 concentration compared with today (e.g., Clark et al., 2009). An enhanced stratification of the deep ocean (below $\sim$1000m depth) has been proposed as a key contributor to the lower atmospheric CO_2 concentration at the LGM by acting as a more effective carbon trap (Bouttes et al., 2009; Adkins, 2013). The deep ocean stratification also influences the strength of the abyssal overturning circulation, which has been invoked to explain reduced CO_2 outgassing and hence a lower CO_2 concentration at the LGM (Sarmiento and Toggweiler, 1984; Anderson et al., 2009; Sigman et al., 2010).

As a large-scale feature that is closely tied to the global ocean overturning circulation, the processes that maintain the stratification of the deep ocean (including both abyssal and mid-depth regions) have attracted substantial attention for many years. Studies by Munk (1966) and Munk and Wunsch (1998) proposed that the deep stratification and overturning circulation are controlled to first order by a balance between the vertical advection and diffusion of buoyancy. More recent studies have suggested that Southern Ocean processes play a key role in closing the global overturning circulation and setting the deep ocean stratification (Marshall and Speer, 2012; Wolfe and Cessi, 2010).

Nikurashin and Vallis (2011, 2012) combined these ideas in a conceptual model, in which the surface density was specified in the Southern Ocean. In this model, the abyssal stratification associated with the abyssal overturning circulation, i.e., the lower cell that spreads Antarctic Bottom Water (AABW) throughout the global ocean below $\sim$3000m, is essentially set by the Southern Ocean surface density profile with some modulation by the competing wind-driven and eddy-driven overturning circulations in the Southern Ocean.

Above the abyssal overturning circulation and below the main thermocline (typically from 3000m to 1000m depth in the Atlantic Ocean), diapycnal mixing is relatively weak (Kunze et al., 2006). The stratification in this mid-depth region is associated with the nearly adiabatic pole-to-pole overturning circulation (i.e., the upper cell) (Wolfe and Cessi, 2011) that spreads NADW southward from the North Atlantic and spreads Antarctic Intermediate Water (AAIW) northward from the Southern Ocean (Talley, 2013; Lozier, 2012). The stratification at this depth is modulated by surface buoyancy and momentum forcing conditions in both the Southern Ocean and the North Atlantic (Wolfe and Cessi, 2011).

Though these idealized modeling studies are conceptually illuminating, the applicability of their predictions to the real ocean is limited. Most of these studies employ idealized topography, a single ocean basin, and a single thermodynamic variable (rather than including both temperature and salinity), which leads to an overturning circulation that is split into two isolated cells (e.g.

Wolfe and Cessi, 2010, 2011; Munday et al., 2013). However, a property-based reconstruction of the overturning circulation suggests that the upper and lower cells are in fact actively coupled and follow a three-dimensional pathway through all of the major ocean basins (Talley, 2013). Additionally, idealized modeling studies tend to employ restoring to a fixed buoyancy profile over a prescribed time scale at the ocean surface, which may not accurately reflect the surface buoyancy fluxes in regions where they are dominated by freshwater fluxes, such as the Southern Ocean (Cerovecki et al., 2011; Stewart et al., 2014).

The present study is the first (as far as the authors are aware) to investigate the influence of the Southern Ocean surface forcing on the global deep ocean stratification in the relatively realistic setting of a comprehensive climate model. In Section 2.2, we describe the experimental setup, which consists of three ocean-only climate model simulations that are designed to isolate the influence of the Southern Ocean surface forcing on the changes in the global deep ocean stratification between the LGM and the Pre-industrial (PI) climate. In Section 2.3, we present the model simulation results and discuss the relative roles of the Southern Ocean and the Northern Hemisphere surface forcing in setting the global deep ocean stratification. In Section 2.4, we use a conceptual model to interpret the results from the climate model simulations. Concluding remarks are provided in Section 2.5.

2.2 Experimental Design

We use a state-of-the-art climate model, the National Center for Atmospheric Research (NCAR) Community Earth System Model version 1.1.2 (CESM1.1.2), which we run in a configuration with only the ocean component active and the atmosphere, sea ice, and land runoff specified from two previous coupled simulations. One coupled simulation represents the PI climate (Gent et al., 2011), and the other coupled simulation represents the LGM climate (Brady et al., 2013). Further information about the model setup and forcing is included in Appendix A.1.

We perform three experiments that share the same model configuration (including the same PI ocean bathymetry) but have different ocean surface forcing: one control run (PI) is forced by PI surface conditions, a second control run (LGM) is forced by LGM surface conditions, and a test run (Test) is forced by LGM surface conditions in the Southern Ocean and PI surface conditions elsewhere. More precisely,

$$F_{\text{Test}} = \gamma F_{\text{PI}} + (1-\gamma) F_{\text{LGM}},$$

where γ is 0 to the south of 40°S, 1 to the north of 30°S, and increases linearly from 0 to 1 between 40°S and 30°S. Here F_{PI} and F_{LGM} denote the surface forcing fields derived from the PI and LGM coupled runs, respectively, and F_{Test} denotes the surface forcing fields used for Test run (see Appendix A for further details). In each case, the coupled model output is used to construct surface forcing fields that repeat every 30 years.

All three runs are initialized from the same initial conditions obtained from the PI coupled run. The length of each integration is listed in the Appendix table A1 along with the trend during the last 120 years of the global volume-average temperature, ideal age, and Atlantic Meridional Overturning Circulation (AMOC) maximum (defined as the maximum total overturning circulation streamfunction below 500m in the Atlantic Ocean including contribution from both the mean flow and the parameterized eddies). Although the trends are nonzero, Table A1 indicates that all three runs are close to equilibration (see also Figures A3 and A6, as well as discussions in Section A.2 in Appendix A). Note that all simulations are initiated from the PI coupled run, so the PI ocean-only run equilibrates more rapidly than the Test and LGM runs. Unless otherwise noted, the results presented in this study are averaged over the last 20 years of each model run.

Figure 2.1 shows the zonal-mean surface buoyancy flux (B) in each simulation, along with

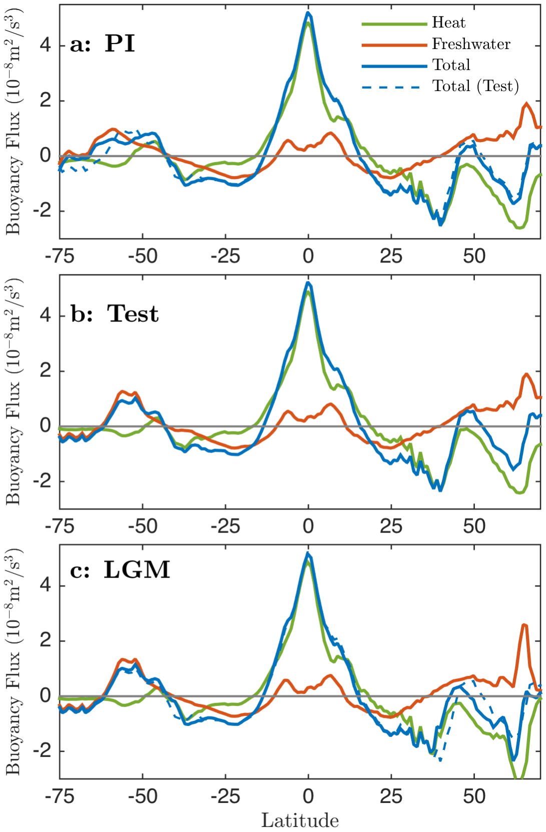

Figure 2.1: Zonal mean surface buoyancy flux for the three model runs along with its heat and freshwater components.The total buoyancy flux from the Test run is plotted for comparison in panels a and c as a blue dashed line.

its heat (B_{HF}) and freshwater (B_{FW}) components defined as

$$B = B_{\mathrm{HF}} + B_{\mathrm{FW}} \equiv -\alpha g \frac{Q_{\mathrm{HF}}}{c_p \rho_0} + \beta S g Q_{\mathrm{FW}}, \tag{2.1}$$

where g is the gravitational acceleration, ρ_0 is a reference density, c_p is the specific heat of seawater, S is the ocean surface salinity, α is the thermal expansion coefficient, β is the saline contraction coefficient, Q_{HF} is the net air-sea heat flux (positive for ocean heat gain), and Q_{FW} is the net freshwater flux (positive for ocean freshwater gain). The freshwater flux is approximately fixed by the prescribed forcing in each run. It is mainly associated with sea ice melting and freezing, river runoff, precipitation, and evaporation, and all but the last of these fields are fully specified in the simulations. The surface heat flux in these simulations, on the other hand, more closely resembles a restoring boundary condition (cf. Haney, 1971a). The freshwater flux does include a "weak restoring" component to avoid unbounded local salinity trends under mixed boundary conditions (Griffies et al., 2009), but this component does not appear to substantially influence the results presented here, as discussed in Appendix A.1. Figure 2.1 shows that south of 45°S, the buoyancy flux is mostly dominated by the freshwater flux [1], implying that the Southern Ocean is subject to a surface buoyancy flux that is approximately fixed, i.e., independent of ocean state.

Note that the form of the surface buoyancy flux (restoring boundary condition or fixed buoyancy flux) has been shown to strongly influence the response of the deep ocean to surface forcing perturbations. In an eddy-resolving channel model, Abernathey et al. (2011) found different sensitivities of the overturning circulation to surface wind stress between simulations with fixed buoyancy flux and those with restoring boundary conditions, as was similarly found in a conceptual model by Stewart et al. (2014).

2.3 CESM simulation results

2.3.1 Stratification and overturning circulation

We first discuss the mean stratification and overturning circulation in the Test simulation, introducing a conceptual decomposition of the domain into three dynamically distinct regions in order to facilitate interpretation of the results. We focus our analysis on the Atlantic basin because, due to the formation of the NADW, the Northern Hemisphere surface forcing is expected to have more influence on the deep ocean stratification in the Atlantic basin than in the Pacific

---

[1] The freshwater flux due to frazil ice formation in the ocean only model is not accounted here. If the frazil ice contribution is considered, the freshwater flux in the Test run would slightly differ from the LGM run. See Chapter 3 for more information.

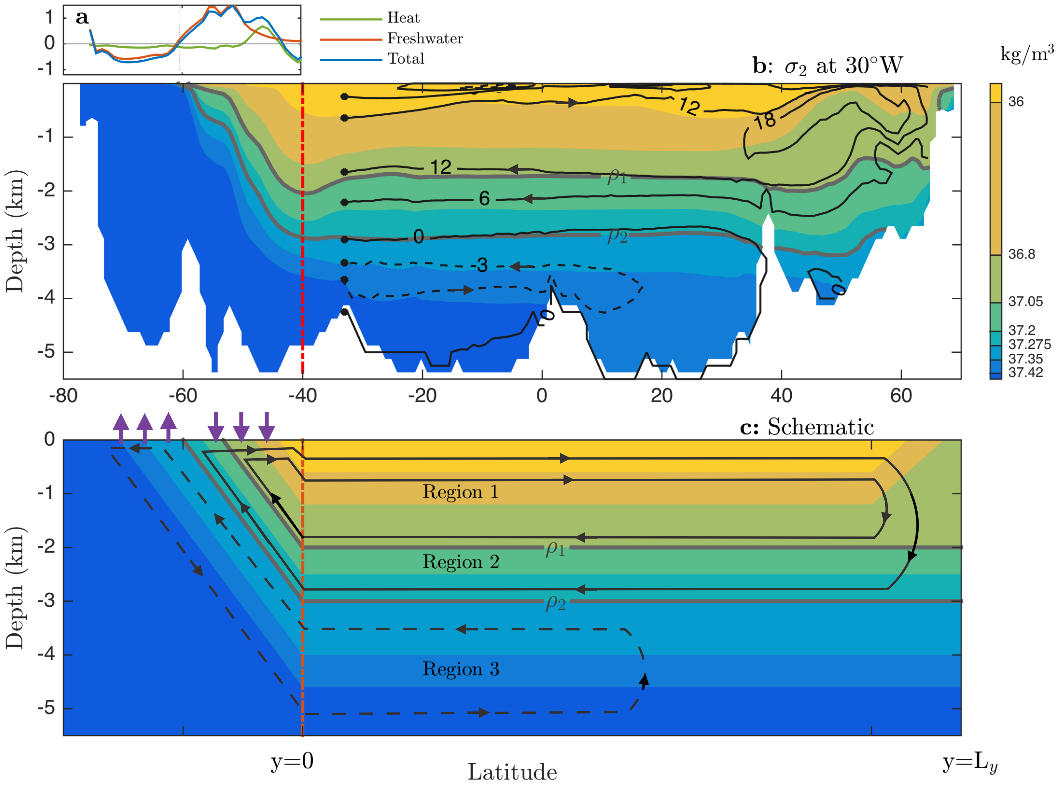

Figure 2.2: (a) Buoyancy forcing averaged between 25°W and 35°W in the Southern Ocean in the Test run, plotted in units of $10^{-8}\mathrm{m}^2/\mathrm{s}^3$. (b) Meridional section of σ_2 (shading) from the Test run, averaged zonally between 25°W and 35°W. The residual overturning circulation streamfunction in the Atlantic Ocean, calculated on σ_2 surfaces and then mapped back to depth coordinates, is included as black contours with arrows indicating the direction of flow. (c) Schematic of the isopycnals (shading) and overturning circulation (black lines with arrows). Purple arrows in the Southern Ocean indicate the direction of buoyancy flux, with ocean buoyancy loss indicated by upward arrows. The northern boundary of the ACC is indicated in panels b and c by a red dash-dotted line. The thick gray lines represent the isopycnals that separate these 3 regions (ρ_1 and ρ_2). Here ρ_2 is defined as the density of the isopycnal surface that separates the upper and lower overturning circulation cells, and ρ_1 is defined more approximately as the density of the isopycnal below which the isopycnal surfaces are approximately flat and hence are not substantially affected by the near-surface wind-driven circulation.

and Indian basins. A meridional section of σ_2 (i.e., potential density referenced to 2000 dbar) that is zonally averaged between 25°W and 35°W in the Test run is presented in Figure 2.2b, with the residual overturning circulation streamfunction in the Atlantic Ocean included as black contours.

By comparing the overturning circulation streamfunction to the potential density, we identify three distinct isopycnal regions in the Atlantic Basin which are separated by isopycnal surfaces ρ_1 and ρ_2. This is shown schematically in Figure 2.2c. Here ρ_2 is defined as the density of the isopycnal that separates the upper and lower overturning circulation cells. As shown in Figure 2.2a, it also coincides with the border between the regions of buoyancy loss and gain in the Southern Ocean in the long-term mean, which is approximately 10° south of the westerly wind maximum in the Atlantic Sector of the Southern Ocean. We define ρ_1 as the uppermost isopycnal surface that outcrops in the Southern Ocean but not in the Northern Hemisphere in the long-term mean. Below ρ_1, the isopycnal surfaces are nearly flat in Figure 2.2b, implying that they are not substantially affected by the surface wind-driven circulation.

In Region 3, isopycnals outcrop only in regions in the Southern Ocean where the ocean loses buoyancy at the surface (Figure 2.2b). Region 3 coincides with the depths spanned by the counterclockwise lower overturning circulation cell ($\psi < 0$). In Region 2, which represents the mid-depth ocean, isopycnals outcrop only in regions in the Southern Ocean where the ocean gains buoyancy in the long-term mean (Figure 2.2b), although they occasionally outcrop in the high-latitude North Atlantic during the winter season. In both Region 2 and Region 3, isopycnals are approximately flat except in the Southern Ocean, and hence they do not appear to be affected by the wind-driven circulation except in the Southern Ocean.

Region 1 spans from the top of Region 2 to the surface. Here isopycnals outcrop in both the Southern Ocean and the high-latitude North Atlantic in the long-term mean, and the influence of the wind-driven circulation becomes apparent particularly in the subpolar gyre of the North Atlantic (40 –60°N). In the PI and LGM model runs, we identify analogous regions and adjust the potential densities ρ_1 and ρ_2 to match the isopycnals that separate them (see Figure A8 for the PI and LGM).

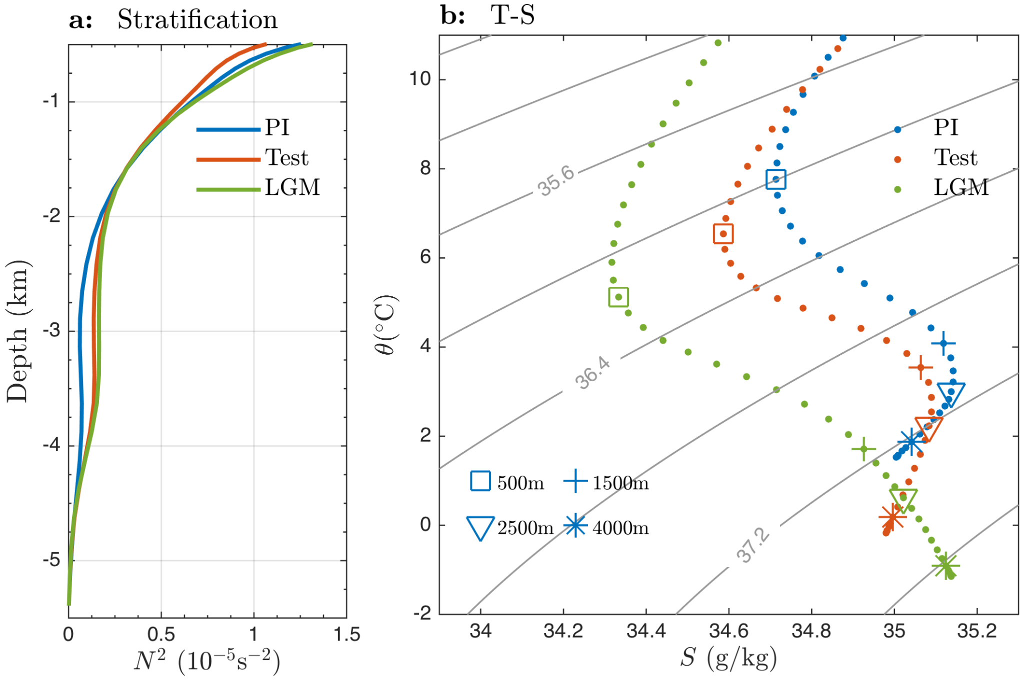

Figure 2.3: Left: Stratification (represented by the squared Brunt-Väisälä frequency N^2) averaged laterally between 20°S and 20°N in the Atlantic Ocean. Right: Temperature-Salinity diagram for the three runs averaged between 20°S and 20°N in the Atlantic Ocean. Contours of σ_2 are indicated. The differences in σ_2 between 500m and 1500m are 0.99, 0.89, and 1.01 kg/m^3 in the PI, Test, and LGM runs, respectively; the differences between 2500 and 4000m are 0.09, 0.20, and 0.27 kg/m^3, respectively.

2.3.2 Role of Southern Ocean surface forcing

We now compare the basin-average stratification in the Atlantic basin between 20°S and 20°N. The result is presented in Figure 2.3 as the squared Brunt-Väisälä frequency N^2, which is reported in CESM and calculated as $N^2 = -\frac{g}{\rho_0}\frac{\partial \sigma_{p_r}}{\partial z}$, where σ_{p_r} is the potential density referenced to the local pressure. The Test run closely reproduces the deep ocean stratification of the LGM run below approximately 2000m, but not between 500m and 1500m. This indicates that the influence of the Southern Ocean on the deep stratification extends much higher in depth level than previously thought (e.g., Nikurashin and Vallis, 2012), approximately 1000m above the boundary between the upper and lower overturning cells in the Atlantic. The stratification in the other major ocean basins largely supports this conclusion, suggesting that the surface forcing in the Southern Ocean is responsible for the enhanced global deep ocean stratification during the LGM in CESM (see Appendix A.2 for more details).

Next, we examine the thermal and haline components of the deep ocean density stratification. Figure 2.3b shows a temperature-salinity (T-S) diagram, averaged laterally over the Atlantic basin between 20°S and 20°N. This figure indicates that the density difference between 2500m (triangles) and 4000m (stars) is much smaller in the PI run than in the Test and LGM runs, consistent with Figure 2.3a. However, the deep ocean temperature and salinity stratification in the Test run is strikingly different from the LGM run, having a negative rather than positive deep salinity stratification that more closely resembles the PI run. Though the density stratification is more dynamically relevant, the temperature and salinity stratifications are also important because they influence the stored heat and solubility of the abyssal waters, thereby affecting the capacity for carbon storage in the ocean.

Hence Figure 2.3 implies that although North Atlantic surface forcing does not substantially affect the deep ocean density stratification, it does strongly influence the global deep ocean temperature and salinity profiles. This occurs in such a way that the deep ocean temperature and salinity differences between the simulations have cancelling contributions to the deep ocean density stratification. This may be because both isopycnal advection and diffusion can influence the temperature and salinity along isopycnals between the Southern Ocean surface and the abyssal ocean, whereas the deep ocean density stratification is constrained by the Southern Ocean surface forcing. Consequently, there is a degree of freedom in how temperature and salinity vary with depth in the deep ocean.

2.4 Conceptual model

Previous idealized studies (e.g., Nikurashin and Vallis, 2012) suggested that the density stratification in what we identify as Region 3 is constrained by the surface buoyancy forcing in the Southern Ocean. This is because surface buoyancy restoring essentially fixes the density gradient at the surface, and the approximately constant isopycnal slope in the Southern Ocean maps this surface density gradient to the abyssal ocean density stratification. In Region 2, however, they suggested that the stratification is substantially influenced by North Atlantic surface forcing as well, in contrast with the result presented in Section 3.

In this section we adapt the zonally-integrated conceptual model of Nikurashin and Vallis (2011) to investigate why the stratification in Region 2 in the CESM simulations appears to be largely controlled by the Southern Ocean alone. As discussed below, we find that the approximately fixed surface buoyancy flux in the Southern Ocean exerts a strong control over the density stratification in both Region 3 and Region 2, even though Region 2 contains the southward flow of the NADW.

As derived in the Appendix A.3.1, the deep ocean stratification (N^2) can be related to the Southern Ocean surface buoyancy forcing in the conceptual model via a buoyancy budget equation:

$$\frac{\kappa L_x L_y}{N^2(z)} \frac{\partial}{\partial z} N^2(z) = \psi^*(z) + L_x \frac{B(-z/s)}{s N^2(z)}. \tag{2.2}$$

This states that the net diffusively-driven upwelling across a given depth (or isopycnal surface) in the interior basin [left-hand side of Equation (2.2)] is equal to the net export of NADW below that depth at the northern end of the basin (ψ^*) plus the net transformation from lighter to denser water at the Southern Ocean surface due to the zonal-mean surface buoyancy flux (B). Here κ is the diapycnal diffusivity, L_y and L_x are the meridional and zonal length scales of the basin (as in Figure 2.2b), ψ^* is the residual overturning circulation streamfunction at the northern boundary of the basin (i.e., at $y = L_y$), and s is the isopycnal slope in the Southern Ocean. Note that positive values of B here correspond to positive buoyancy input to the ocean and that the isopycnal slope (s) is negative.

Motivated by Figure 2.1, we model the surface buoyancy forcing as a fixed flux that varies with latitude, $B = B(y)$. In Equation (2.2), B is evaluated at the location at which an isopycnal lying at depth z north of the Southern Ocean outcrops at the Southern Ocean surface, $y = -z/s$ (cf. Figure 2.2c). In order to simplify the conceptual model, we assume that both κ and s are constant. We find that s is approximately identical among the three simulations discussed above (cf. Gent and Danabasoglu, 2011), which is consistent with the assumption of constant isopycnal slope in the conceptual model. In Appendix A.3.2, we present a more general analysis that allows the isopycnal slope to change in response to the strength of of overturning circulation. Note that the depth dependence of κ has been shown to be important for aspects of the deep ocean stratification, especially close to the depth of bottom topography (Mashayek et al., 2015).

Region 3 is defined to lie below the southward flow of NADW, so ψ^* vanishes in this region (see Figure A8). Equation (2.2) in Region 3 thus can be written as

$$\frac{\partial}{\partial z} N^2(z) = \frac{B(-z/s)}{\kappa s L_y}. \tag{2.3}$$

Figure 2.3a shows that the stratification at the ocean bottom (N^2_{bot}) is close to zero in all three simulations, i.e., $N^2_{\text{bot}} \approx 0$. Therefore, the stratification N^2 at any depth z within Region 3 is equal to the vertical integral of the right-hand side of Equation (2.3) from the ocean bottom up to that depth, and hence it is solely determined by the Southern Ocean surface buoyancy forcing. Because $B_{\text{LGM}} \approx B_{\text{Test}}$ in Figure 2.1c, it follows that $N^2_{\text{LGM}} \approx N^2_{\text{Test}}$ throughout Region 3 in Figure 2.3, where the subscripts indicate the model run. It should be emphasized that this is true only because the buoyancy forcing takes the form of a fixed flux in Equation (2.2): if a relaxation boundary condition were applied as in previous idealized modeling studies (e.g., Wolfe and Cessi, 2011; Nikurashin and Vallis, 2012), then the deep ocean stratification may be impacted by inter-hemispheric effects, as shown by Fučkar and Vallis (2007) and in Equation (A7) in the appendix.

This argument does not extend to Region 2, because the southward flow of NADW is nonzero there, so the ψ^* term in Equation (2.2) does not vanish. Instead, it can be shown that in order to produce a substantial difference between the Test and LGM stratification in Region 2, a very large change in ψ^* would be required, which is much larger than the difference in ψ^* between the LGM and PI simulations. Rearranging Equation (2.2) and taking the difference between the LGM and Test simulations, we obtain

$$\kappa L_y L_x \frac{\partial}{\partial z}(N^2_{\text{LGM}}(z) - N^2_{\text{Test}}(z)) = N^2_{\text{LGM}}(z)\psi^*_{\text{LGM}}(z) - N^2_{\text{Test}}(z)\psi^*_{\text{Test}}(z) \tag{2.4}$$

in Region 2. Here we have neglected the difference between the Test and LGM fixed surface buoyancy fluxes in the Southern Ocean, $B_{\text{LGM}} - B_{\text{Test}}$, because Figure 2.1c shows this term to be small.

At the boundary between Region 2 and Region 3 ($\sim$3000m depth), Figure 2.3a indicates that the stratification at this depth is approximately equivalent between the LGM and Test simulations, i.e., $\Delta N^2 \equiv N^2_{\text{LGM}} - N^2_{\text{Test}} \approx 0$. Qualitatively, in order for the terms on the right-hand side of Equation (2.4) to produce a vertical change in ΔN^2 of order N^2, the difference between the NADW transports ($\Delta\psi^* \equiv \psi^*_{\text{LGM}} - \psi^*_{\text{Test}}$) in Region 2 must be large. Scaling arguments suggest that this requires $\Delta\psi^* \sim \kappa L_y L_x / H_2$, where $H_2 \approx 1000\,\text{m}$ is the vertical thickness of Region 2 (see Appendix A for details). For typical oceanic parameter values, this requires a change in the NADW transport streamfunction $\Delta\psi^*$ of $O(10\,\text{Sv})$. However, the strength of the streamfunction in this region is less than 10 Sv in the LGM and Test simulations, with the difference between the two being only $\Delta\psi^* \sim 2$ Sv. Thus in the absence of extreme perturbations to the high-latitude northern hemisphere surface forcing, the Southern Ocean essentially controls the stratification throughout Region 2, consistent with the CESM result (Figure 2.3). This is also true when we relax the assumption of constant isopycnal slope (see Appendix A.3.2).

In Region 1, where the isopycnals outcrop in both the Southern Ocean and the North Atlantic, the ocean stratification is expected to be affected by a variety of processes, including the wind-driven gyre circulation and surface forcing in the high northern and southern latitudes (Wolfe and Cessi, 2011).

Conceptually, the analysis above suggests that the stratification in Region 3 is constrained by the requirement that all buoyancy loss by density classes at the surface in the Southern Ocean south of the outcrop position of ρ_2 must be balanced outside of the Southern Ocean by the net interior diffusive buoyancy flux across ρ_2. This argument can almost be extended to Region 2, except that the injection of NADW also contributes to the buoyancy budget in this region. However, as the southward NADW transport in Region 2 needs to change by much more than it does between the LGM and PI runs to substantially impact the stratification, this contribution from NADW can thus be thought of as essentially constant. Consequently, the surface buoyancy flux in the Southern Ocean provides a strong control of the stratification up to $\sim$2000m depth, as the CESM simulations indicate. This stands in contrast with previous idealized modeling studies (e.g., Nikurashin and Vallis, 2012; Wolfe and Cessi, 2011), where the stratification in the depth range that we identify as Region 2 is affected by the Northern Hemisphere surface forcing as well.

We emphasize that this conceptual model provides only an approximate qualitative picture of the effect of Southern Ocean surface buoyancy forcing on the global deep ocean stratification. The simplifications involved in the conceptual model make it difficult to find direct quantitative points of contact with the CESM simulations. For example, as shown in Figure A4 and A5 of the Appendix, the stratification profiles in the Pacific and Indian Oceans look different from the Atlantic. Understanding of this difference would require knowledge of the 3-dimensional global overturning circulation, which is not included in the zonal-mean representation of the conceptual model.

2.5 Summary

The CESM ocean-only simulations presented here suggest that surface buoyancy forcing in the Southern Ocean largely controls the response of the abyssal stratification to LGM conditions. This is superficially consistent with previous understanding (Nikurashin and Vallis, 2011, 2012). However, we furthermore find that this control extends up to approximately 2000m depth, which is close to the core of the upper overturning circulation cell in the Atlantic. This is much shallower than expectations based on previous idealized modeling studies, which found the stratification above the abyssal ocean (i.e., the mid-depth) to be substantially affected by North Atlantic surface forcing (e.g., Nikurashin and Vallis, 2012; Wolfe and Cessi, 2011). We interpret the simulation results using a zonally-integrated conceptual model. The analysis suggests that the control of the Southern Ocean surface buoyancy forcing over the global deep ocean stratification relies crucially on the Southern Ocean surface buoyancy flux being dominated by approximately fixed freshwater fluxes. This is in contrast with previous idealized modeling studies (e.g., Nikurashin and Vallis, 2012; Wolfe and Cessi, 2011), in which the control of the Southern Ocean surface buoyancy forcing over the global deep ocean stratification relies on restoring thermal fluxes. This change in the form of the surface buoyancy forcing extends the control of the Southern Ocean surface forcing up to the core of the NADW overturning circulation cell.

In contrast to deep ocean density stratification, however, we find that although North Atlantic surface forcing does not substantially affect the deep ocean stratification, it does strongly influence the global deep ocean temperature and salinity profiles. In other words, the North Atlantic forcing causes temperature and salinity changes which have cancelling contributions to the density. The temperature and salinity stratifications are important because they influence the stored heat and solubility of the abyssal waters, thereby affecting the capacity for carbon storage in the ocean.

In this study we used the ocean component of a single comprehensive climate model, and it is possible that other models may exhibit different responses to similar changes in the surface forcing. For example, the response may depend on the choice of parameterization scheme for unresolved mesoscale eddies (e.g., Munday et al., 2013) and gravity currents (e.g., Legg et al., 2009). Running CCSM3.5 at an eddy-permitting resolution, Bryan et al. (2014) found that simulated Southern Ocean processes are substantially different than a standard-resolution simulation. The parametrization of diapycnal mixing induced by tidally-generated internal waves may also need to be modified to accurately simulate the LGM ocean (Green et al., 2009). Furthermore, it should also be noted that we are unable to isolate the influence of the Southern Ocean surface wind forcing in the model as it is varied together with the surface buoyancy forcing.

In conclusion, these results suggest that Southern Ocean surface freshwater forcing is largely responsible for the global deep ocean stratification differences between the LGM and PI climates. Considering the influence of deep ocean stratification on CO_2 outgassing (e.g., Bouttes et al., 2009; Adkins, 2013), this implies that Southern Ocean surface freshwater forcing plays a central role in glacial-interglacial changes in atmospheric CO_2 concentration. It also implies that Southern Ocean surface freshwater forcing may have a strong influence on the deep ocean stratification and CO_2 storage in future climate change scenarios.

Acknowledgments

This work was supported by National Science Foundation grant OCE 1357078. Without implying their endorsement, we thank Till Wagner, Shang-Ping Xie, Paola Cessi, Maxim Nikurashin, and Tim Merlis for helpful comments and discussions. We are also grateful to Frank Bryan and David Bailey for technical help with the CESM model setup. Files related to the setup of the CESM simulations, as well as processed model output, are available at http://eisenman.ucsd.edu/code.html. Unprocessed model output is available by request from the corresponding author.

This chapter, in full, is a reprint of the material as it appears in Geophysical Research Letters, “The influence of southern ocean surface buoyancy forcing on glacial-interglacial changes in the global deep ocean stratification”, by S. Sun, I. Eisenman, and A. L. Stewart (2016). The dissertation author was the primary investigator and author of this paper.

Chapter 3

Does Southern Ocean surface forcing shape the global ocean overturning circulation?

3.1 Introduction

In the modern climate, the deep Atlantic Ocean below 2000m is filled with Antarctic Bottom Water (AABW) as well as North Atlantic Deep Water (NADW) (Talley, 2013). At the Last Glacial Maximum (LGM) ∼21,000 years ago, however, paleoclimate proxy data suggests that NADW was absent below 2000m depth with an expanded volume occupied by AABW (e.g., Lund et al., 2011; Burke et al., 2015). This suggests that the Atlantic Meridional Overturning Circulation (AMOC), which is the Atlantic branch of the global ocean overturning circulation that spreads NADW southward from the North Atlantic, was shallower at the LGM compared with modern conditions. Attempts to simulate this difference with climate models have yielded mixed results (e.g., Otto-Bliesner et al., 2007; Muglia and Schmittner, 2015). For example, in the Paleoclimate Model Intercomparison Project Phase 3 (PMIP3), all models except for the Community Climate System Model version 4 (CCSM4) simulated a deeper AMOC in simulations of the LGM compared to simulations of the preindustrial (PI) climate (Muglia and Schmittner, 2015).

Because the deep ocean is the largest carbon reservoir in the land-atmosphere-ocean system (Sarmiento and Gruber, 2002), rearrangement of deep water masses could lead to substantial variations in the atmospheric CO_2 concentration (Sigman et al., 2010), which was approximately 80 ppm lower at the LGM than during the PI period (Monnin et al., 2001). Using an Earth System Model of Intermediate Complexity, Brovkin et al. (2007) suggested that expansion of the carbon-rich AABW at the LGM can draw down the atmospheric CO_2 level by 10-20 ppm. Furthermore, because mixing is most vigorous below 2000 m, the shoaling of the water mass boundary between AABW and NADW at the LGM has been suggested to have substantially reduced the mixing between the two water masses (Ferrari et al., 2014), which is a major source of leakage for abyssal carbon in the modern ocean (Lund et al., 2011). This reduced vertical mixing between AABW and NADW may have further enhanced the ability of the abyssal ocean to trap carbon and contribute to the lower atmospheric CO_2 levels at the LGM (Lund et al., 2011).

Based on analyses of model simulations and paleoclimate proxy data from the LGM, Ferrari et al. (2014) suggested that the shallower AMOC at the LGM is dynamically linked to changes in the surface buoyancy forcing in the Southern Ocean. This idea is further supported by a pair of idealized modeling studies which suggested that a broader region of surface buoyancy loss in the Southern Ocean, associated with the expansion of Antarctic sea ice, leads to a shallower AMOC at the LGM (Burke et al., 2015; Watson et al., 2015). Both studies are based on an idealized, two-dimensional, residual-mean model of the global ocean overturning circulation (Nikurashin and Vallis, 2011, 2012). In this two-dimensional view, the overturning circulation is composed of two overturning circulation cells: an upper cell (i.e., the AMOC) that is associated with the southward transport of NADW and occupies roughly the upper 3000 m in the modern Atlantic ocean, and a lower cell that spreads AABW northward from the Southern Ocean. The two overturning circulation cells diverge at the Southern Ocean surface where the surface buoyancy forcing changes sign.

Ferrari et al. (2014) suggested that the depth of the AMOC can thereby be inferred from the surface buoyancy flux in the Southern Ocean under two approximations: (1) fixed isopycnal slope in the Southern Ocean and (2) adiabatic circulation in the upper Southern Ocean so that the residual-mean overturning circulation follows isopycnal contours. They predicted that a 500 km equatorward expansion of sea ice, which is consistent with paleoclimate proxy reconstructions of the LGM (e.g., Gersonde et al., 2003, 2005), would expand the buoyancy loss region equatorward in the Southern Ocean and imply shoaling of the AMOC by 500 m.

Though conceptually illuminating, the applicability of the geometric argument of Ferrari et al. (2014) to the real ocean remains uncertain. Their approximation that the isopycnal slope in the Southern Ocean is insensitive to surface forcing perturbations is only qualitatively supported in observations (Böning et al., 2008) and models (Viebahn and Eden, 2010; Gent and Danabasoglu, 2011). More importantly, observations suggest that there is substantial diapycnal mixing over rough topography in the Southern Ocean (e.g., Naveira Garabato et al., 2004; Wu et al., 2011; Whalen et al., 2012; Mashayek et al., 2017), which is at odds with the adiabatic approximation for the Southern Ocean circulation. In the present study, three simulations that were carried out with the ocean component of a state-of-the-art climate model are analyzed to investigate the extent to which changes in Southern Ocean surface buoyancy forcing alone can explain the shoaling of the AMOC at the LGM.

3.2 Description of simulations

Three simulations were carried out with a configuration of the National Center for Atmospheric Research Community Earth System Model version 1.1.2 (NCAR CESM1.1.2) in which only the ocean is active, with the atmosphere, sea ice, and land runoff specified using output from previous coupled CCSM4 simulations of the PI (Gent et al., 2011) and LGM climates (Brady et al., 2013). The ocean component of CESM1.1.2 (Danabasoglu et al., 2012), which is identical to CCSM4, is run with a horizontal resolution of nominally 1°, with unresolved eddies parameterized using the Gent-McWilliams scheme (Gent and Mcwilliams, 1990). There are 60 vertical levels with thicknesses ranging from 10 m at the surface to 250 m at the ocean bottom. Vertical convection is represented by the non-local K-profile parameterization (Large et al., 1994), in which diapycnal diffusivity is parameterized to account for processes including convective instability, internal wave breaking, double diffusion, and tidally-driven mixing. Except in regions of deep convection or in the boundary layer, the dominant term in the diapycnal diffusivity is due to the parameterized tidally-driven mixing, which scales inversely with the density stratification (Jayne, 2009).

The three ocean-only simulations share the same model configuration, including the same PI ocean bathymetry, except that they have different surface forcing: one control run (called PI) is forced by PI surface conditions, a second control run (called LGM) is forced by LGM surface conditions, and a test run (called Test) is forced by LGM surface conditions south of 40°S and PI surface conditions north of 30°S, with a linear transition from LGM to PI conditions in the region between 40°S and 30°S. These simulations were originally carried out as part of Chapter 2, where more details can be found.

All three simulations are identically initialized from the end of the coupled PI run. As a result, the PI ocean-only simulation equilibrates most rapidly, and it is run for 510 years. The Test and LGM simulations are run for 1020 and 1440 years, respectively. At the end of the simulations, all three runs have approximately equilibrated (see Appendix B.1). Unless otherwise noted, the analyses in this study use 5-day mean model output during the last 20 years of each model run.

The zonal-mean wind stress forcing and wind stress curl are plotted in Figure B1. The westerly wind stress forcing in the Southern Ocean is shifted equatorward without much change in intensity at the LGM compared with PI (cf. Brady et al., 2013). Note that this is in contrast to an LGM simulation with an earlier version of the coupled model (Otto-Bliesner et al., 2006). Figure B2 shows the zonal-mean surface buoyancy flux in the Southern Ocean in the three ocean-only simulations. Close to Antarctica, the buoyancy flux is negative mainly due to brine rejection from sea ice formation. The LGM simulation has colder global ocean temperature than the Test simulation, which appears to lead to more frazil ice formation in the Southern Ocean and hence stronger buoyancy loss close to Antarctica. Consequently, the latitude where surface buoyancy flux changes sign differs slightly between the LGM and Test simulations: the region of negative buoyancy flux extends approximately 3.4° and 2.5° latitude farther equatorward in the LGM and Test simulations, respectively, compared to the PI simulation.

3.3 Simulation results

3.3.1 Meridional Overturning Circulation streamfunction

Here we calculate the Meridional Overturning Circulation (MOC) streamfunction ψ in σ_2 coordinates as:

$$\psi(y,\sigma_2) = -\frac{1}{T}\int_0^T \int_{x_w}^{x_e} \int_{z_{\text{bot}}}^{0} v_r(x,y,z,t)\mathcal{H}\left(\sigma_2'(x,y,z,t)-\sigma_2\right)\, dz\, dx\, dt, \tag{3.1}$$

where σ_2 is the potential density referenced to 2000 dbar, σ_2' is the σ_2 field reported by the model, x is the longitudinal displacement, y is the latitudinal displacement, z is depth with z_{bot} the depth of the ocean bottom, $T = 20$ years is the averaging period, $\mathcal{H}$ is the Heaviside step function, and v_r is the total meridional velocity that includes both the Eulerian-mean flow and the eddy-bolus contribution due to the parameterized mesoscale and submesoscale eddies. In the Atlantic basin, ψ is integrated from the western boundary (x_w) to the eastern boundary (x_e). In the Southern Ocean, we integrate zonally around the globe along each latitude circle. We calculate the MOC streamfunction ψ in Equation (3.1) using 5-day mean model output, which may be short enough to resolve much of the temporal variability that contributes to the overturning circulation (cf. Ballarotta et al., 2013).

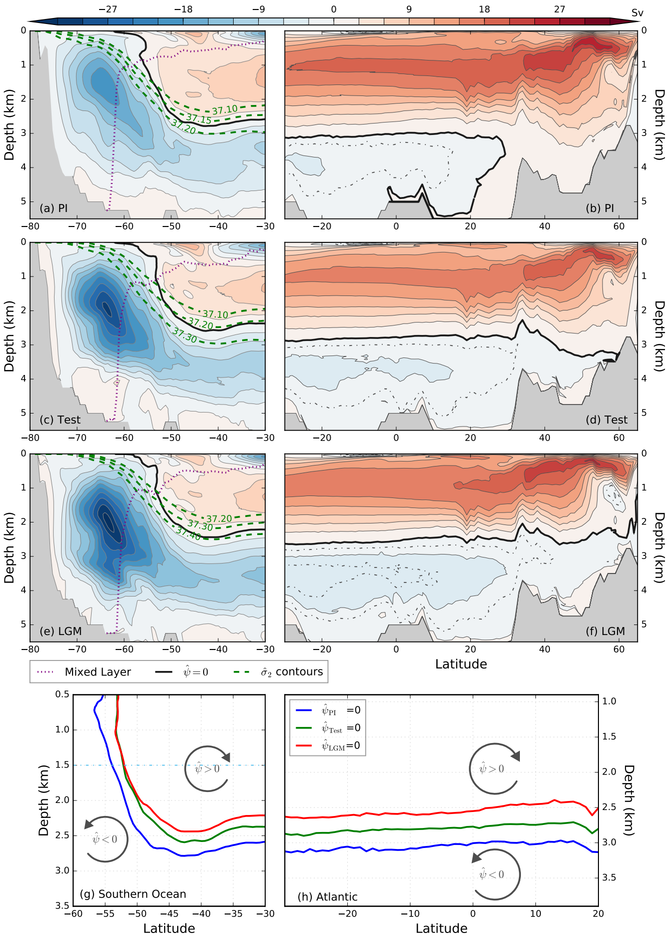

Figure 3.1: Overturning circulation streamfunction mapped to depth coordinates in (a,c,e) the Southern Ocean and (b,d,f) the Atlantic ocean. In each panel, the streamline that separates the upper and lower overturning circulation cells ($\hat{\psi}$=0) is plotted as a thick black contour. Three isopycnals near this streamline in the Southern Ocean are plotted as green dashed lines. The maximum depth of the surface mixed layer (MML) is plotted as a purple dotted line. The contour interval is 3 Sv; additional contours at -4.5 Sv and -1.5 Sv are also included in the Atlantic as dash-dotted lines. To remove noise at the grid scale, the overturning circulation streamfunction is smoothed using a five-point ($\sim 2.5^\circ$ latitude) running mean along isopycnal contours; the unsmoothed version is included in the Appendix as Figure B5. (g,h) The MOC depth, defined as the depth of the streamline $\hat{\psi}$=0, is plotted for comparison among the three simulations. The cyan dash-dotted line at 1.5km depth in the Southern Ocean indicates the approximate MML in the plotted latitude range. Note that the axis ranges in these panels differ from the panels above: the vertical ranges are adjusted to focus on the differences between the simulations, and the horizontal range in the Atlantic ends at 20°N due to the zero streamline not extending north of this latitude in the PI simulation.

The MOC streamfunction on σ_2 coordinates can be mapped to depth coordinates using the mean depth of each isopycnal. Here, we define the mean depth of an isopycnal $\hat{z}(y,\sigma_2)$ implicitly via

$$\int_{x_w}^{x^e}\int_{z_{\text{bot}}}^{\hat{z}(y,\sigma_2)} dx\,dz = \frac{1}{T}\int_0^T\int_{x_w}^{x_e}\int_{z_{\text{bot}}}^{0} \mathcal{H}\left(\sigma_2(x,y,z,t)-\sigma_2'\right) dx\,dz\,dt, \tag{3.2}$$

following Nurser and Lee (2004), i.e., the total cross-sectional area below $\hat{z}$ at latitude y is equal to the cross-sectional area of fluid denser than σ_2. We use this definition instead of the time- and zonal-mean isopycal depth because of the unstable density stratification in regions where convection occurs (Nurser and Lee, 2004). Therefore, the MOC streamfunction in depth coordinates, $\hat{\psi}$, can be written as $\hat{\psi}(y,z) = \hat{\psi}(y,\hat{z}(y,\sigma_2)) = \psi(y,\sigma_2)$, using $z = \hat{z}(y,\sigma_2)$. We use the mean isopycnal depth $\hat{z}$ to similarly define the mean potential density in depth coordinates, $\hat{\sigma}_2(y,z)$, such that $\hat{\sigma}_2 = \sigma_2$ at $z = \hat{z}(y,\sigma_2)$.

The MOC streamfunction in the three simulations is plotted on depth coordinates in Figure 3.1 (and on σ_2 coordinates in Figure B4). For purely adiabatic flow in steady state, $\hat{\psi}$ is constant along $\hat{\sigma}_2$ contours. Hence the deviation of $\hat{\psi}$ from $\hat{\sigma}_2$ contours in Figure 3.1 (and equivalently deviations from horizontal contours in Figure B4) in the Southern Ocean implies the presence of diapycnal mixing. Qualitatively similar features of flow crossing isopycnals in the Southern Ocean also occur in the 1/6° Southern Ocean State Estimate (Mazloff et al., 2013, their Fig. 1), a 1/10° CESM simulation (Bishop et al., 2016, their Fig. 8), and a 1/10° CCSM3.5 simulation (Newsom et al., 2016, their Fig. 7).

We quantify the diapycnal mixing in the Southern Ocean that occurs in the three simulations analyzed here in Appendix B.3. Specifically, we compare the MOC streamfunction at 30°S with the water mass transformation due to surface buoyancy forcing, following the framework of Walin (1982). We find that diapycnal mixing plays a dominant role in Southern Ocean water mass transformation. This finding is similar to the results of Newsom et al. (2016).

However, because the isopycnals vary both longitudinally and temporarily due to both standing eddies (cf. Tréguier et al., 2007) and the time-varying buoyancy forcing in the Southern Ocean, diapycnal mixing that occurs in some regions of Figure 3.1 could be caused by mixed layer eddies (Marshall et al., 1999; Karsten et al., 2002) or water mass transformation due to surface buoyancy forcing (see Figure B2). We construct an upper bound on the density classes impacted directly by mixed layer processes and surface forcing by defining the maximum depth of the mixed layer (MML) (cf. Marshall et al., 1999; Iudicone et al., 2008). Specifically, we define the MML as the densest isopycnal at each latitude that ever occurs within the mixed layer at any longitude and any time during the 20-year averaging period (purple line in Figure B4), which is then mapped to depth coordinates (purple dotted line in Figure 3.1). Hence isopycnals below the MML are not affected by mixed layer dynamics or surface transformation. Note that the MML is generally deeper than the mixed layer depth as reported directly in the CESM model output, where it is defined as the shallowest depth where the local, interpolated vertical buoyancy gradient matches the maximum buoyancy gradient within the full column (Large et al., 1997). Due to the occurrence of deep convection close to Antarctica in the model, the MML reaches the seafloor south of 60°S (Figure 3.1).

3.3.2 MOC depth and shoaling of the AMOC

In this study, we define the MOC depth as the depth of the streamline $\hat{\psi} = 0$ (thick solid line in Figure 3.1), which separates the upper and lower overturning circulation cells. In the PI run, the AMOC extends approximately over the upper 3000 m. This is roughly consistent with modern observations (Lozier, 2012). The AMOC is approximately 500 m shallower in the LGM run, which is forced by the LGM surface conditions globally (Figure 3.1h). This shoaling in the LGM run compared with the PI run approximately matches the depth change predicted by Ferrari et al. (2014). Note that it is smaller than the 1000 m shoaling suggested by some paleo-proxy reconstructions (e.g., Lund et al., 2011), and it is approximately 200 m larger than in the coupled CCSM4 simulations (cf. Muglia and Schmittner, 2015), although the deep ocean circulation in the coupled CCSM4 LGM simulation does not appear to be fully equilibrated (Marzocchi and Jansen, 2017).

In the Test run, which has LGM surface conditions only in the Southern Ocean and PI surface conditions elsewhere, the geometric argument of Ferrari et al. (2014) predicts that the AMOC depth should be similar to the LGM run. However, in contrast with this expectation, the AMOC in the Test run is only approximately 250 m shallower than in the PI run, which is half as much shoaling as in the LGM run. The AMOC depth changes in these simulations appear to be largely explained by the MOC depth differences in the Southern Ocean (Figure B6), consistent with the approximately uniform changes in the AMOC depth throughout the Atlantic basin between the three simulations (Figure 3.1h). In contrast with Jansen and Nadeau (2016), who attributed differences in the AMOC depth to changes in the abyssal stratification that occur due to surface buoyancy loss in the Southern Ocean, here the abyssal stratification in the Test run is similar to the LGM run (Sun et al., 2016).

Note that we use σ_2 in this analysis rather than neutral density, even though adiabatic motion occurs on local neutral surfaces and hence neutral density is better conserved (McDougall, 1987). This choice is made because the calculation of neutral density involves a pre-labeled global reference dataset that is derived from observations (Jackett and McDougall, 1997), which is not available for the LGM and Test simulations. For this and other reasons, the σ_2 coordinate is often used in studies of the overturning circulation in climate model simulations (e.g., Gent and Danabasoglu, 2011; Bishop et al., 2016; Newsom et al., 2016). To test the sensitivity of our results to this choice, we also perform the above calculations using a different potential density coordinate (σ_1), and the results appear not to be substantially different. For example, the difference in the AMOC depth at 30°S between the Test and LGM runs calculated on σ_1 coordinates is 262 m, which is very close to the value of 250 m calculated on σ_2 coordinates (cf. Figure 3.1h). We also examine the influence of model equilibrium on our results in Appendix B.1. The results suggest that the model is approximately equilibrated, and that the difference in AMOC depth between the Test and LGM simulations is substantially larger than any adjustments that would likely occur if the simulations were run longer.

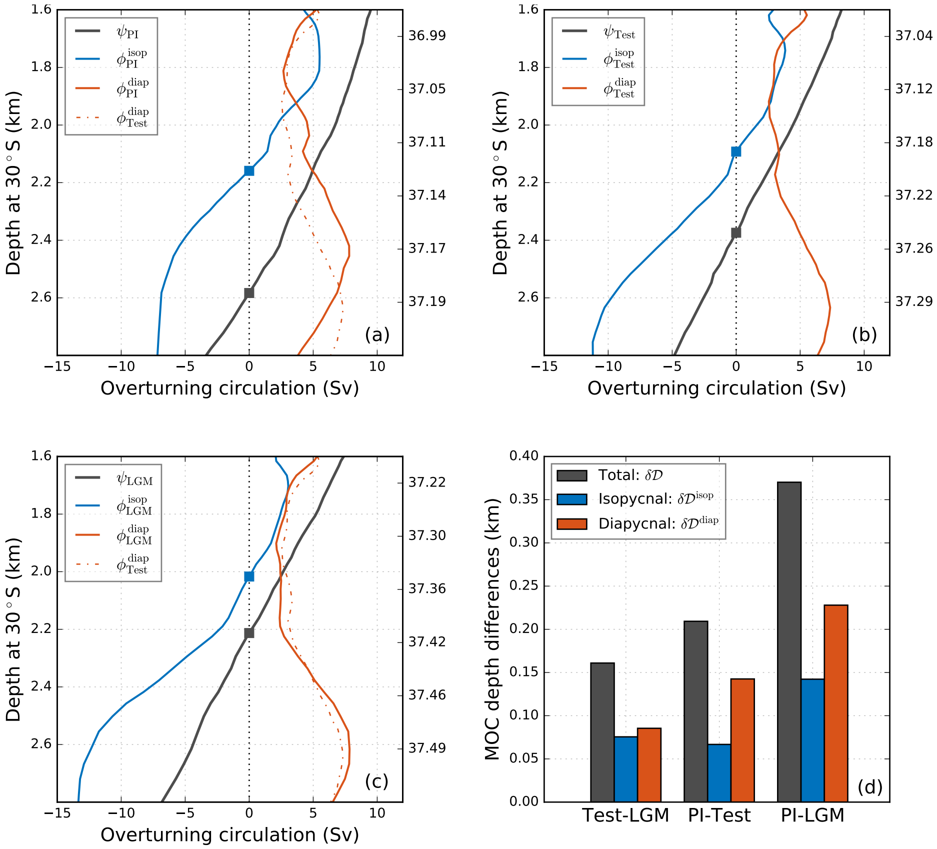

Figure 3.2: (a-c) MOC streamfunction components $\psi(30°\mathrm{S}, \sigma_2)$, $\phi^{\rm isop}(\sigma_2)$, and $\phi^{\rm diap}(\sigma_2)$, mapped to depth coordinates using the mean isopycnal depth at 30°S (see details in Section 3.4), with corresponding potential densities σ_2 labelled on the right axis, for each simulation. The three solid curves in each panel can be interpreted as follows: the black line shows the simulated overturning circulation streamfunction at 30°S, the blue line ($\phi^{\rm isop}$) shows the MOC streamfunction that would occur at 30°S if the circulation were purely adiabatic below $z_{\rm ref}$ in the Southern Ocean, and the red line ($\phi^{\rm diap}$) shows the difference between ϕ and $\phi^{\rm isop}$. Hence $\phi^{\rm diap}$ quantifies the along-isopycnal change in the MOC streamfunction due to diapycnal mixing below $z_{\rm ref}$=-1.5 km in the Southern Ocean. The $\phi^{\rm diap}$ curve in the Test run is repeated for comparison in panels (a) and (c) as a dash-dotted red line. The MOC depths corresponding to $\psi(30°\mathrm{S}, \sigma_2)$ and $\phi^{\rm isop}$ are indicated in each panel by the blue and black squares, respectively. (d) Contribution to the inter-simulation differences in the MOC depths (black) due to changes in shapes of isopycnals and surface forcing (blue) and due to changes in deviations of the MOC depth from isopycnals (red). See Section 3.4 for definitions of $\delta\mathcal{D}$, $\delta\mathcal{D}^{\rm isop}$, and $\delta\mathcal{D}^{\rm diap}$. In order to avoid the influence of grid-level noise, the smoothed MOC streamfunction shown in Figure 3.1 is used here. An equivalent figure that instead uses the raw unsmoothed MOC streamfunction is included in the Appendix (Figure B10).

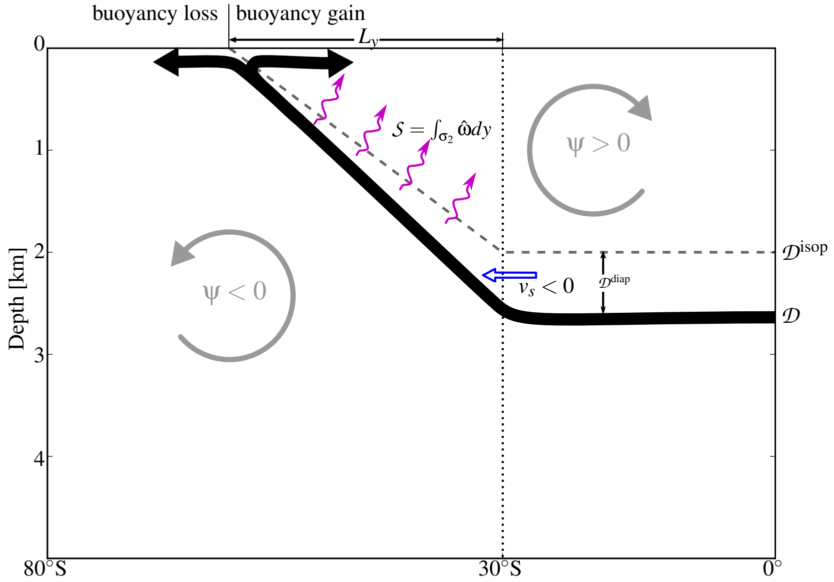

Figure 3.3: Schematic of the conceptual model used to derive the scaling relationships for the Southern Ocean MOC. The streamline that separates the upper and lower overturning circulation cells ($\hat{\psi}$=0) is indicated by a thick black line, with arrows indicating the flow direction near the surface. The gray dashed line indicates the isopycnal that connects $z = 0$ at the latitude where buoyancy forcing changes sign. The diapycnal velocity ($\hat{\omega}$) is indicated by purple arrows, and the isopycnal flow (v_s) at the northern edge of the Southern Ocean is represented by a blue arrow. The directions of the overturning circulation in each overturning circulation cell are indicated by gray circle arrows. Volume conservation implies that $-v_s\mathcal{D}^{\text{diap}}=\mathcal{S}$, where $\mathcal{S}$ is the latitudinal integration across the Southern Ocean of $\hat{\omega}$ along the isopycnal contour associated with $\mathcal{D}^{\text{isop}}$ (gray dashed line). Depth in this schematic is referenced such that the top of the figure (z=0 km) is at the base of the maximum range of the surface mixed layer, rather than the sea surface. This is to exclude the effects of temporal and zonal variations in the isopycnal depth and diapycnal mixing due to mixed layer eddies (see Section 3.3.1).

3.4 Interpretation of the MOC depth changes

The Southern Ocean MOC depth in the Test run is approximately the same as in the LGM run throughout the upper 1500 m (Figure 3.1g), consistent with the two runs having similar surface buoyancy forcing (Figure B2). Below 1500m, however, the Test run diverges from the LGM run in Figure 3.1g. This can be caused by the small changes in the isopycnal slope (see Figures B7 and B8, as well as Section B.2), by the presence of diapycnal mixing (see Figure B9 and Section B.3), or by both. In this section, we derive a scaling relationship which we use to attribute the contributions to the differences in AMOC depth between the simulations that arise due to differences in surface forcing, isopycnal slope, diapycnal mixing, and isopycnal upwelling.

The MOC streamfunction at the northern edge of the Southern Ocean (30°S; black lines in Figure 3.2a-c) can be expressed as

$$\psi(30^\circ\mathrm{S},\sigma_2) = \phi^{\mathrm{isop}}(\sigma_2) + \phi^{\mathrm{diap}}(\sigma_2), \tag{3.3}$$

where $\phi^{\mathrm{isop}}(\sigma_2) = \psi(y,\sigma_2)\mid_{\hat{z}(y,\sigma_2)=z_{\mathrm{ref}}}$ denotes the value of the MOC streamfunction at a reference depth z_{ref}. By default we take $z_{\mathrm{ref}} = -1.5$ km to be just below the MML (purple dotted lines in Figure 3.1). Hence $\phi^{\mathrm{isop}}(\sigma_2)$ represents the MOC streamfunction that would occur at 30°S if the circulation were purely adiabatic below z_{ref} (blue lines in Figure 3.2a-c). We define $\phi^{\mathrm{diap}}(\sigma_2)$ as the difference between $\psi(30^\circ\mathrm{S},\sigma_2)$ and $\phi^{\mathrm{isop}}(\sigma_2)$ (red lines in Figure 3.2a-c), and hence it represents the MOC streamfunction component associated with diapycnal mixing below z_{ref} in the Southern Ocean. The MOC depth at 30°S (black squares in Figure 3.2a-c) is

$$\mathcal{D} \equiv \hat{z}(30^\circ\mathrm{S},\sigma_2^*), \tag{3.4}$$

where σ_2^* is defined to satisfy $\psi(30^\circ\mathrm{S},\sigma_2^*) = 0$.

If the circulation is purely adiabatic, as in Ferrari et al. (2014), the MOC depth can be predicted using the depth of the isopycnal that intersects the streamline $\hat{\psi} = 0$ at the base of the surface mixed layer (blue squares in Figure 3.2a-c), i.e., $\mathcal{D} = \mathcal{D}^{\mathrm{isop}}$, where

$$\mathcal{D}^{\mathrm{isop}} \equiv \hat{z}(30^\circ\mathrm{S},\sigma_2^{**}), \tag{3.5}$$

and σ_2^{**} is defined to satisfy $\phi^{\mathrm{isop}}(\sigma_2^{**}) = 0$. This is indicated by the gray dashed line in Figure 3.3, and it is constrained by the slope of this isopycnal contour, as well as surface buoyancy forcing and mixed layer processes in the Southern Ocean.

However, due to diapycnal mixing, the simulated MOC depth is deeper than $\mathcal{D}^{\mathrm{isop}}$ (see

Figure 3.3). In analogy with Equation (3.3), this can be written as

$$\mathcal{D} = \mathcal{D}^{\text{isop}} + \mathcal{D}^{\text{diap}}, \tag{3.6}$$

where $\mathcal{D}^{\text{diap}}$ is defined here as the contribution to the MOC depth due to the presence of dipayncal mixing. As can be seen from Figure 3.3, volume conservation requires that

$$\mathcal{D}^{\text{diap}} = -\mathcal{S}/v_s, \tag{3.7}$$

where $\mathcal{S}$ is the diapycnal velocity $\hat{\omega}$ integrated latitudinally along the isopycnal contour in the Southern Ocean (the gray dashed line south of 30°S in Figure 3.3), and v_s denotes the residual-mean meridional velocity at the northern edge of the Southern Ocean. Note that $v_s < 0$ near the streamline $\hat{\psi} = 0$, so Equation (3.7) implies a positive value of $\mathcal{D}^{\text{diap}}$. This relationship (3.7) arises because there can be no residual flow across the $\hat{\psi} = 0$ streamline.

Equations (3.6)-(3.7) show that the MOC depth can be modified below the surface mixed layer by changes in the isopycnal slope ($\mathcal{D}^{\text{isop}}$), the intensity of diapycnal mixing ($\mathcal{S}$), and the strength of meridional flow in the Southern Ocean (v_s). This implies that surface forcing in the Northern Hemisphere (such as in the North Atlantic) can affect the MOC depth through its influence on the interhemispheric AMOC strength (v_s) (e.g., Nikurashin and Vallis, 2012), but only if diapycnal mixing in the Southern Ocean is non-negligible ($\mathcal{S} \neq 0$).

Thus, differences in the MOC depth between any two simulations ($\delta\mathcal{D}$) can be attributed to changes in $\mathcal{D}^{\text{isop}}$ and $\mathcal{D}^{\text{diap}}$:

$$\delta\mathcal{D} = \delta\mathcal{D}^{\text{isop}} + \delta\mathcal{D}^{\text{diap}}, \tag{3.8}$$

where δ denotes the difference in the value of a variable between the two simulations, and

$$\delta\mathcal{D}^{\text{diap}} \approx \overline{\mathcal{D}^{\text{diap}}} \left(\frac{\delta\mathcal{S}}{\overline{\mathcal{S}}} - \frac{\delta v_s}{\overline{v_s}} \right), \tag{3.9}$$

where the overline denotes the average between the two simulations being compared and the approximate equality becomes exact in the limit of small differences δv_s and $\delta \mathcal{S}$.

We consider the contributions of $\delta \mathcal{D}^{\mathrm{isop}}$ and $\delta \mathcal{D}^{\mathrm{diap}}$ to changes in the MOC depth in Figure 3.2d following Equation (3.8). We find that changes in $\mathcal{D}^{\mathrm{diap}}$ between the three simulations are larger than $\mathcal{D}^{\mathrm{isop}}$, implying that diapycnal mixing plays a dominant role in setting the MOC depth. This result is largely insensitive to the choice of z_{ref} (Figure B11). A decomposition of $\delta \mathcal{D}^{\mathrm{diap}}$ into $\delta \mathcal{S}$ and δv, following Equation (3.9), reveals that changes in $\mathcal{D}^{\mathrm{diap}}$ are mostly due to changes in the diapycnal flow $\delta \mathcal{S}$ (Figure B14). Therefore, we conclude that the MOC depth changes in these simulations arise primarily due to differences in diapycnal flow ($\delta \mathcal{S}$), with somewhat smaller but still substantial contributions from changes in the buoyancy forcing integrated through the surface mixed layer and isopycnal slope ($\mathcal{D}^{\mathrm{isop}}$). A minor contribution (less than 10% of the total MOC depth changes) comes from changes in isopycnal upwelling (δv_s). The diapycnal transport may be approximated in terms of the simulated diapycnal diffusivity and stratification (cf. Munk, 1966). We find that differences in the diapycnal diffusivity profiles between the three simulations (Figure B12), which occur due to differences in the density stratification between the three simulations, are consistent with the diapycnal transport differences (Appendix B.3).

The diapycnal diffusivity profiles in the Southern Ocean that are computed by the model (Figure B12) are within the range of observational estimates from Waterhouse et al. (2014, their Fig. 7) and Watson et al. (2013). This suggests that effects of diapycnal mixing on the MOC depth similar to what we find in these simulations may plausibly be expected in nature. Previous studies have suggested that numerical discretization of the nonlinear advection terms in tracer equations can cause substantial numerical diapycnal mixing (e.g., Griffies et al., 2000; Hill et al., 2012), but we find that numerical mixing does not appear to contribute substantially to the diapycnal mixing in these simulations (see Appendix B.3 and Figure B13).

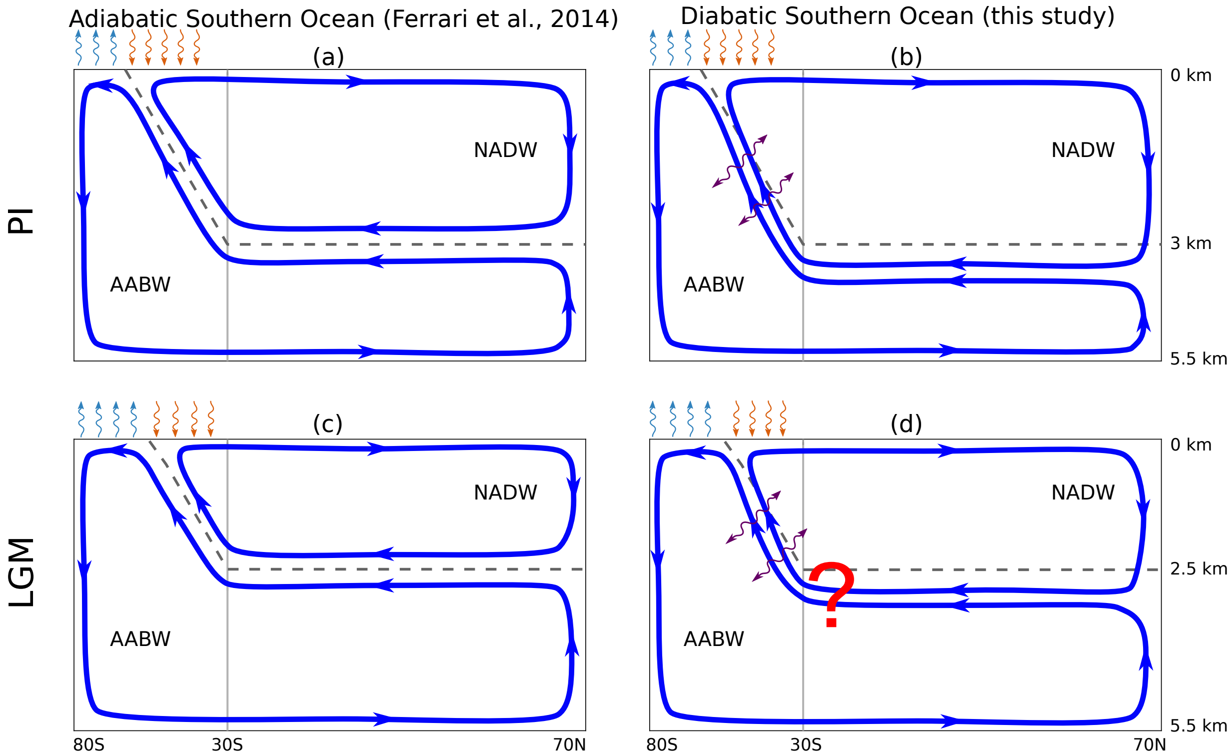

Figure 3.4: Schematic diagrams illustrating theories for how Southern Ocean buoyancy forcing influences the global ocean circulation. (a-b) PI ocean. (c-d) LGM ocean. Panels on the left side (a,c) represent the theory that the circulation is adiabatic in the Southern Ocean (Ferrari et al., 2014). In this case, the AMOC depth can be predicted from the Southern Ocean surface buoyancy forcing (arrows above the Southern Ocean surface; upward for buoyancy loss and downward for buoyancy gain). Panels on the right side (b,d) correspond to the case of a circulation that is more diabatic in the Southern Ocean, as suggested by our findings as well as in situ measurements (e.g., Whalen et al., 2012). In this case, the AMOC depth is sensitive to the amount of diapycnal mixing in the Southern Ocean (purple double arrows), which is influenced by the surface forcing outside the Southern Ocean through its effect on the Southern Ocean density stratification. Hence the AMOC depth cannot be predicted from the Southern Ocean surface buoyancy forcing alone; this is indicated as a red question mark in panel d. The gray dashed line in each panel represents the isopycnal that outcrops in the Southern Ocean at the latitude where surface buoyancy flux changes sign. This schematic represents an idealized two-dimensional view of the overturning circulation; the rearrangement of the three-dimensional overturning circulation associated with the AMOC shoaling may also play an important role (cf. Ferrari et al., 2014). As in Figure 3.3, the depth is referenced here to the base of the surface mixed layer.

3.5 Summary and discussion

Paleoclimate proxy data suggests that the AMOC was shallower by approximately 1000 m at the LGM than during the PI period (e.g., Lund et al., 2011; Burke et al., 2015). Previous studies have suggested that this shoaling is dynamically linked to the expansion of the region of negative surface buoyancy forcing in the Southern Ocean (Ferrari et al., 2014; Watson et al., 2015; Burke et al., 2015). In this study, we analyze three ocean-only CESM simulations to investigate the influence of Southern Ocean surface forcing on the depth of the AMOC. In contrast to expectations based on these previous studies (Ferrari et al., 2014; Watson et al., 2015; Burke et al., 2015), we find that applying LGM surface forcing in the Southern Ocean and PI forcing elsewhere causes the AMOC to shoal only about half as much as when LGM surface forcing is applied globally.

We explain the AMOC depth changes through variations in the MOC depth at the northern edge of the Southern Ocean. We develop a scaling relation that determines this depth as a function of Southern Ocean buoyancy forcing, diapycnal mixing, and isopycnal upwelling. We use this scaling relation to show that the AMOC depth changes in the CESM simulations arise primarily due to changes in diapycnal transport and isopycnal slope in the Southern Ocean, with a minor contribution from changes in isopycnal upwelling. Therefore, the AMOC depth can be influenced by any processes that affect the buoyancy budget in the surface mixed layer, the isopycnal slope, diapycnal mixing rates, and isopycnal upwelling in the Southern Ocean. These processes, in addition to buoyancy forcing in the Southern Ocean, include the wind stress forcing in the Southern Ocean and surface forcing in the North Atlantic (e.g., Muglia and Schmittner, 2015). The buoyancy loss rate in the Southern Ocean could also affect the AMOC depth by changing the stratification and hence modifying the diapycnal mixing rate in the Southern Ocean (cf. Jansen and Nadeau, 2016; Marzocchi and Jansen, 2017).

The influence of diapycnal mixing on the AMOC depth is shown schematically in Figure

3.4. The isopcynal contour that outcrops in the Southern Ocean where the surface buoyancy forcing changes sign (gray dashed line in each panel) also outcrops in the North Atlantic, which occurs due to issues associated with multiple ocean basins that have different density structures (not shown in this single-basin view). Hence North Atlantic surface forcing can influence the stratification around this isopycnal contour in the Southern Ocean (cf. Nikurashin and Vallis, 2012; Sun et al., 2016). Note that changes in the isopycnal upweling in the Southern Ocean, which we find to cause less than 10% of the MOC depth difference between the LGM and Test simulations (see Section 3.4), can also be affected by North Atlantic surface forcing changes (e.g., Wolfe and Cessi, 2011; Sun and Liu, 2017). In the case with no diapycnal mixing in the Southern Ocean (left column of Figure 3.4), the $\hat{\psi} = 0$ streamline (blue cells) follows exactly along the isopycnal contour in the Southern Ocean, so the MOC depth at 30°S is influenced only by the location where the surface buoyancy forcing changes sign as well as the slope of the isopycnal contour, and the stratification does not play a role. In the diabatic case (right column in Figure 3.4), by contrast, the stratification can influence the level of diapcynal mixing close to the $\hat{\psi} = 0$ streamline, and hence changes in North Atlantic surface forcing can modify the MOC depth at 30°S. Using an idealized setup that has only one basin, Jansen (2017) shows that the Northern Hemisphere surface forcing has a modest effect on the AMOC depth and contributes only $\sim$15% of the AMOC depth shoaling in his simulations of the LGM (compare "LGM dTSH" and "LGM" with "PI" in his Table 1). This suggests that the influence of North Atlantic surface forcing on the AMOC depth changes may depend on the complexity of the model.

There are some caveats associated with the model used in this study. The nominal 1° ocean resolution in CESM does not resolve eddies, which have been shown to be important in the response of the Southern Ocean circulation to perturbations in the surface forcing (e.g., Abernathey et al., 2011; Munday et al., 2013), nor does it resolve the near coastal processes in the Antarctic regions, which have been suggested to be important for the simulation of AABW production (e.g., Snow et al., 2016; Newsom et al., 2016). Nonetheless, the present study highlights the importance of diapycnal mixing in the Southern Ocean, which has typically been neglected in previous conceptual model studies of the deep ocean stratification (e.g., Nikurashin and Vallis, 2011; Stewart et al., 2014; Sun et al., 2016). Diapycnal mixing in the Southern Ocean can be neglected in these studies as long as the diapycnal transport below the surface mixed layer in the Southern Ocean is small compared to the ocean basins to the north, such that the buoyancy budget is predominantly balanced between the Southern Ocean surface buoyancy forcing and diapycnal mixing in the basins north of the Southern Ocean. This appears to apply for the world oceans mainly because the Southern Ocean is much smaller than the total area of the basins north of it. However, the results of the present study suggest that diapycnal mixing in the Southern Ocean must be considered in order to describe the influence of Southern Ocean surface forcing on the depth of the AMOC.

A number of factors further complicate the adiabatic picture presented in Ferrari et al. (2014). First, Schmittner et al. (2015) suggest that the global-mean diapycnal diffusivity was larger at the LGM by a factor of three compared to the present ocean as a result of the lower sea level, which shifts tidal mixing from shallow coastal regions into the deep ocean. This implies a possibly even larger influence of diapycnal mixing on the AMOC depth at the LGM than was found here. Second, Muglia and Schmittner (2015) find that a number of other current climate models simulate a deeper AMOC under LGM forcing, in contrast to CCSM4. These models have expanded Southern Ocean sea ice cover in their LGM simulations (Marzocchi and Jansen, 2017, their Figure 3) but nonetheless do not simulate a shoaling of the AMOC, implying that the connection between Southern Ocean surface forcing and AMOC depth may not be a robust result among current climate models. Third, the buoyancy forcing tends to be weak in the vicinity of the latitude of zero buoyancy forcing (Figure B2). Therefore, the overturning circulation close to the zero-buoyancy flux region could be overwhelmed by processes in the surface mixed layer (cf. Marshall et al., 1999; Karsten et al., 2002) or by standing eddies associated with the complex three-dimensional structure of the Southern Ocean circulation (Tréguier et al., 2007), further weakening the link between Southern Ocean surface buoyancy forcing and the AMOC depth and highlighting the role of other processes within and outside the Southern Ocean.

In summary, this study used CESM ocean-only simulations to investigate the influence of Southern Ocean surface forcing on the AMOC depth, which is believed to play an important role in glacial-interglacial changes in atmospheric CO_2. The results suggest that the AMOC depth is sensitive to both Southern Ocean and North Atlantic surface buoyancy forcing due to diapcynal mixing in the Southern Ocean.

Acknowledgments

Without implying their endorsement, we thank Paola Cessi, Shang-Ping Xie, Lynne Talley, Raffaele Ferrari, Malte Jansen, Jess Adkins, and Paul Kushner for helpful comments and discussions. This work was supported by National Science Foundation grants OCE-1357078, OCE-1538702, and OPP-1643445. Files related to the setup of the CESM simulations, as well as processed model output, are available at http://eisenman.ucsd.edu/code.html. Unprocessed model output is available by request from the corresponding author.

This chapter, in full, is a reprint of the material as it appears in Geophysical Research Letters, “Does Southern Ocean surface forcing shape the global ocean overturning circulation?”, by S. Sun, I. Eisenman, and A. L. Stewart (2018). The dissertation author was the primary investigator and author of this paper.

Chapter 4

Sensitivity of the Antarctic Circumpolar Current transport to surface buoyancy conditions in the North Atlantic

4.1 Introduction

The Antarctic Circumpolar Current (ACC) is the world's largest current system. Driven at least partly by the Southern hemisphere westerly wind, the ACC is associated with strongly titled surfaces of constant density, i.e., isopycnals. Through the tilting isopycnals, deep water upwells and ventilates at the Southern Ocean surface (e.g., Marshall and Speer, 2012; Talley, 2013), providing an effective connection between the surface and deep ocean. Consequently, the ACC is uniquely important for global water mass formation (e.g., Talley, 2013; Lamy et al., 2015), air-sea exchanges and redistribution of heat, fresh water, and anthropogenic carbon (e.g., Toggweiler and Russell, 2008; Ito et al., 2010; Tamsitt et al., 2016), and thus for the global climate system.

The ACC is an important part of the global ocean overturning circulation (e.g., Marshall and Speer, 2012; Talley, 2013). In a two-dimensional zonally-integrated view, the global ocean overturning circulation is composed of an upper overturning circulation cell, which is due to the Atlantic Meridional Overturning Circulation (AMOC) and is associated with sinking of the North Atlantic Deep Water (NADW) in the high-latitude North Atlantic, and a lower overturning circulation cell, which is associated with the Antarctic Bottom Water (AABW) formation (Lumpkin and Speer, 2007). Through the ACC, the two overturning circulation cells are coupled to each other, forming a complex three-dimensional structure of the global ocean overturning circulation (Talley, 2013; Ferrari et al., 2014).

In the pycnocline model by Gnanadesikan (1999), the global pycnocline depth and T_{ACC} are linked to processes in the Southern Ocean including surface wind forcing and meso-scale eddies and also to processes outside of the Southern Ocean including deep water formation in the high-latitude North Atlantic and global diapycnal diffusivity. Recent studies using eddy-rich models find that the ACC is largely in an eddy saturated state (e.g., Munday et al., 2013; Bishop et al., 2016), in which additional power input from a stronger wind forcing can be balanced by an intensification of eddies without changing the mean circumpolar flow (Hogg, 2010). Consistent with those eddy-rich simulations, no significant relationship between the ACC transport with changes in the magnitude or position of the wind stress is identified in the Coupled Model Intercomparison Project (CMIP) Phase 5 (e.g., Meijers et al., 2012; Downes and Hogg, 2013). In contrast to the relative insensitivity of T_{ACC} to local processes in the Southern Ocean, the remote effects have been suggested to have noticeable influence on the ACC (Munday et al., 2011; Fučkar and Vallis, 2007). Using an ocean general circulation model (OGCM) with an idealized setup, Fučkar and Vallis (2007) found that T_{ACC} varies substantially in response to changes in the surface buoyancy conditions in the North Atlantic, implying a great sensitivity of the T_{ACC} to the NADW formation.

The strong sensitivity of the ACC transport to the NADW formation in Fučkar and Vallis (2007) appears to contradict some studies using coupled comprehensive climate models (e.g., Wang et al., 2011). By analyzing multiple model simulations from the CMIP 3, which predict consistent weakening of the AMOC in response to anthropogenic activities in the 21st century, Wang et al. (2011) concluded that changes in the AMOC have very minor influence on the ACC transport. The conclusion of Wang et al. (2011) is consistent with some recent studies that emphasize the critical role played by the Southern Ocean processes in determining the global deep ocean stratification (Nikurashin and Vallis, 2011; Wolfe and Cessi, 2010; Sun et al., 2016) and global ocean overturning circulation (Ferrari et al., 2014). However, the complexity of the comprehensive climate models makes it hard to compare directly with Fučkar and Vallis (2007). In particular, the intensification and poleward shift of the westerly wind over the Southern Ocean in Wang et al. (2011) might have counteracted the influence of the AMOC on the ACC transport.

In this study, we revisit the influence of the North Atlantic surface buoyancy conditions on the ACC transport using an OGCM in an idealized configuration. A series of numerical simulations are performed. Two conceptual models are used to interpret the simulation results. We find that the sensitivity of the ACC transport to North Atlantic surface buoyancy conditions strongly depends on the simulated vertical structure of the AMOC.

4.2 Model and results

4.2.1 Model setup

We employ the Massachusetts Institute of Technology General Circulation Model (MITgcm; Marshall et al., 1997) to integrate the hydrostatic primitive equations. The model has a flat-bottom rectangular geometry with a reentrant channel to the south (Figure 4.1a). The semi-enclosed basin represents an idealized Atlantic Ocean, and the reentrant channel represents the Southern Ocean. The model has 25 vertical levels, of which the thickness ranges from 10 m at the surface to 250 m at the ocean bottom. The domain is 2800 m deep, 3200 km wide in the zonal direction, and 8000 km long in the meridional direction. This is half as deep, half as

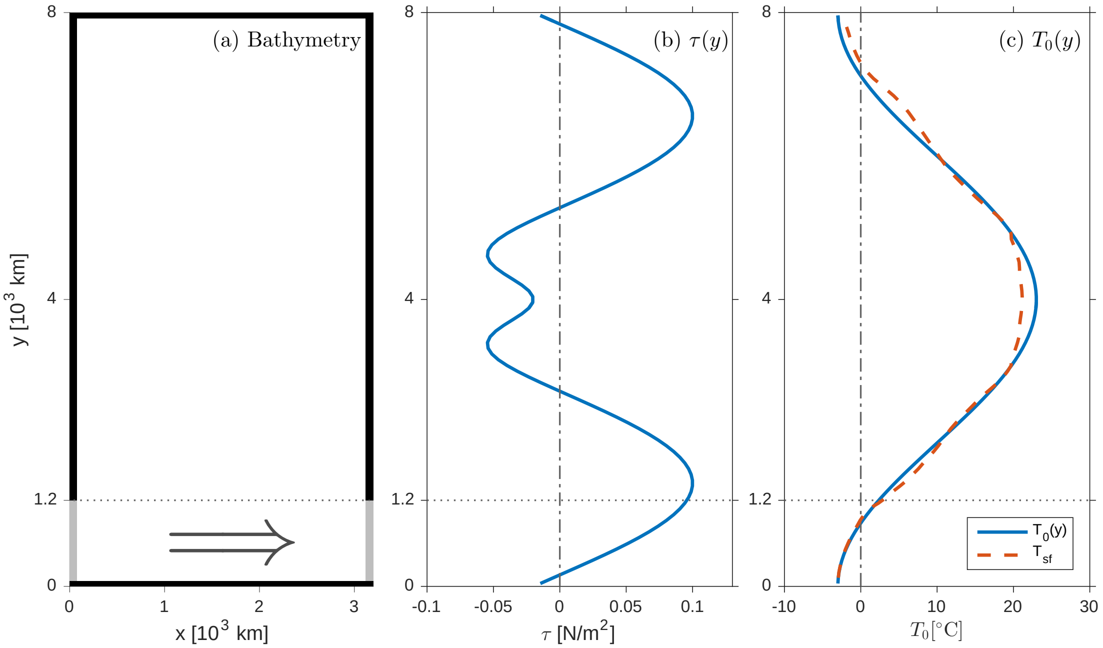

Figure 4.1: (a) Bathymetry of the basin. The black thick line indicates the idealized continents. The gray thick line indicates the submarine sill that represents the Drake passage. The gray arrow indicates the direction of the ACC. (b) Surface wind stress forcing ($\tau(y)$) which is symmetric about the equator ($y = 4000$ km) in the meridional and uniform in the zonal direction. (c) Profile of the symmetric reference temperature ($T_0(y)$; blue solid line) in Equation (4.1). The zonal-mean surface temperature at $\delta_T = 0.5$°C (T_{sf}) is plotted as red dashed line for comparison. The northern boundary of the reentrant channel is plotted in each panel as gray dotted lines. The zero position of τ and T are plotted in panels (b) and (c) as gray dash-dotted lines.

wide, and half as long as the Atlantic in the real ocean in order to perform sufficient amount of simulations on limited computing resources. A submarine sill of 2060 m depth is placed in the reentrant channel to represent the Drake passage. This submarine sill also provides the bottom form stress that balances the momentum input into the ACC from surface wind forcing (Munk and Palmén, 1951). Consistent with the Cartesian grid, a beta plane is adopted and the Coriolis parameter varies linearly in the meridional direction, i.e., $f(y) = f_0 + \beta y$, with $f_0 = -8 \times 10^{-5}\text{s}^{-1}$, $\beta = 2.0 \times 10^{-11}\text{m}^{-1}\text{s}^{-1}$, and y is a Cartesian coordinate that corresponds to latitude.

The horizontal resolution of the model is 80 km. The unresolved mesoscale eddies are represented by the advective form of the Gent and McWilliams (GM) parameterization (Gent and Mcwilliams, 1990) with a mixing coefficient $K_{\text{GM}} = 488\text{m}^2/\text{s}$ following Wolfe and Cessi

(2011). The GM parameterization is implemented using the boundary-value problem scheme of Ferrari et al. (2010) that parameterizes the diabatic component of eddy flux at the surface layer of ocean where eddy motions become horizontal. The diabatic eddy flux in the surface mixed layer is ignored in Fučkar and Vallis (2007), and this has been suggested by Wolfe and Cessi (2010) to lead to a large residual-mean flow in the Southern Ocean.

The density of seawater is linearly dependent on temperature with a constant thermal expansion coefficient $2.0 \times 10^{-4}\mathrm{K}^{-1}$. The seawater salinity is kept at 35g/kg. We adopt a constant background vertical diffusivity of $2 \times 10^{-5}\mathrm{m}^2/\mathrm{s}$ to diffuse the temperature vertically. This small vertical diffusivity is used because we are focusing on the upper overturning circulation cell, which is located above the bottom topography and can be considered to be approximately adiabatic (e.g., Wolfe and Cessi, 2011). The lower overturning circulation, which is associated with the export of AABW, is not well-resolved in this model. The momentum is dissipated via Laplacian viscosity, biharmonic viscosity, vertical viscosity, and bottom drag with coefficients $A_h = 1.0 \times 10^4\mathrm{m}^2/\mathrm{s}$, $A_4 = 5.0 \times 10^{12}\mathrm{m}^2/\mathrm{s}$, $A_v = 3.0 \times 10^{-3}\mathrm{m}^2/\mathrm{s}$, and $r = 4.1 \times 10^{-6}\mathrm{s}^{-1}$, respectively. Convection is handled by the K-Profile Parameterization (KPP) scheme (Large et al., 1994). Therefore, the actual vertical diffusivity and viscosity can be different from the background value depending on the state of hydrostatic stability.

The wind stress forcing is symmetric with respect to the equator ($y = 4000$ km) and is uniform in the zonal direction (Figure 4.1b). The surface temperature is relaxed to a profile ($T_s(y)$) that is expressed as

$$T_s(y) = T_0(y) + \delta_T \mathrm{e}^{-20(y/L_y - 1)^2}, \tag{4.1}$$

where $T_0(y)$ is the symmetric reference temperature profile and is given in Figure 4.1c, L_y is the meridional width of the basin, and δ_T controls how much warmer the surface ocean in the North Atlantic is than the Southern Ocean. The relaxation time scale is 10 days and is close to that concluded by Haney (1971b) from observations. Because of this fast-restoring boundary condition, the surface density is essentially specified in the Southern Ocean (see Figure 4.1c and Figure 4.2) and the ACC transport is determined by the isopycnal slope, which is coupled to the overturning circulation based on the residual-mean theory in Marshall and Radko (2003). Previous studies have shown that the AMOC strength scales linearly with the shared surface density range between the Southern Ocean and the North Atlantic (Nikurashin and Vallis, 2012; Wolfe and Cessi, 2011). Therefore, by changing the surface density in the North Atlantic and keeping the surface density largely unchanged in the Southern Ocean, the strength of the AMOC is varied. Throughout this study except for Section 4.4, we have kept the other processes unchanged, including surface wind forcing, eddy diffusivity, and diapycnal diffusivity.

Accordingly, δ_T determines the shared density range between the Southern Ocean and the North Atlantic, and consequently it controls the intensity of the AMOC (Wolfe and Cessi, 2011; Nikurashin and Vallis, 2012). At $\delta_T = 0°$C, the temperature forcing is symmetric with respect to the equator. By increasing δ_T, the shared density between the Southern Ocean and the North Atlantic is reduced such that the AMOC is weakened (see Figure 4.2; Wolfe and Cessi, 2011; Nikurashin and Vallis, 2012), along with a slight increase in the lower overturning circulation cell due to the contraction of the upper cell (cf. Jansen and Nadeau, 2016). Beyond $\delta_T \approx 5°$C, there is no shared density between the North Atlantic and the Southern Ocean, and the pole-to-pole overturning circulation disappears.

4.2.2 Simulation results

A series of simulations are performed to test the sensitivity of T_{ACC} to the surface buoyancy condition in the North Atlantic, which is achieved by varying δ_T systematically. Each simulation is initiated from a motionless state and is run for over 3500 years until approximate equilibrium, at which the linear trend of T_{ACC} over the last 100 years is less than 1 Sv/century (1 Sv=10^6m^3/s). The last 50 years of each simulation is used for the following analysis.

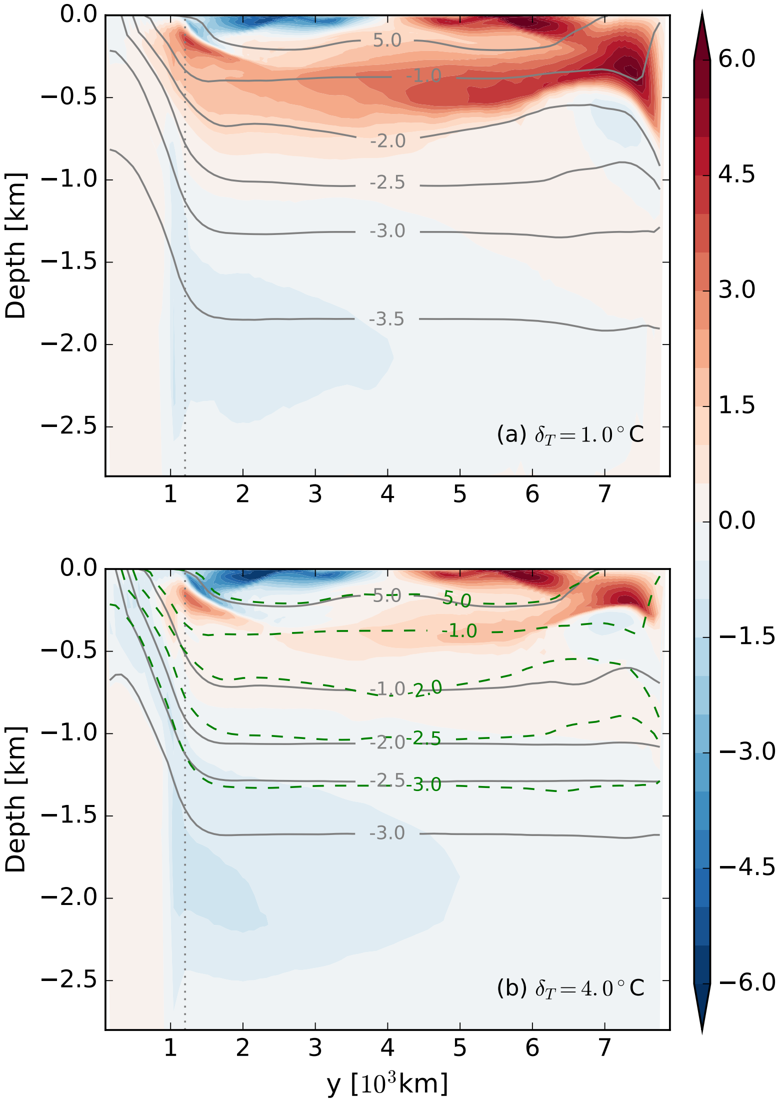

Figure 4.2: Residual-mean overturning circulation streamfunction (color shading) $\psi(y,\theta)$ remapped to height coordinate at $\delta_T = 1^\circ$C (a) and $\delta_T = 4^\circ$C (b), plotted in units of Sv. The gray solid lines represent the mean depth of isotherms that is defined by Equation (4.3) and labeled in unit of °C. Five isotherms from panel (a) are plotted in panel (b) as green dashed lines to show the change of isopycnal slope. The northern boundary of the reentrant Southern Ocean is plotted as gray dotted lines.

The residual-mean overturning circulation streamfunction is defined as:

$$\psi(y,\theta) = \frac{1}{t_0}\int_0^{t_0}\int_0^{L_x}\int_{-H}^{\zeta(x,y,\theta,t)} v_r\,dz\,dx\,dt, \tag{4.2}$$

where x and z are Cartesian coordinates that correspond to longitude and depth, t is time, H is the depth of the basin, L_x is the zonal width of the basin, $t_0 = 50$ years, θ is potential temperature, $\zeta(x,y,\theta,t)$ represents the height of isotherm θ, and v_r is the residual velocity that includes both Eulerian-mean velocity and eddy bolus velocity due to the GM parameterization. Figure 4.2 shows two examples of the residual-mean overturning circulation streamfunction that are remapped to height coordinate using the the zonal-mean time-mean depth of each isotherm

$$\overline{\zeta}(y,\theta) = \frac{1}{t_0}\int_0^{t_0}\frac{1}{L_x}\int_0^{L_x}\zeta(x,y,\theta,t)\,dz\,dx\,dt, \tag{4.3}$$

for $\delta_T = 1°\mathrm{C}$ and $\delta_T = 4°\mathrm{C}$, respectively. The clockwise pole-to-pole overturning circulation is an idealized representation of the AMOC. It is substantially reduced at $\delta_T = 4°\mathrm{C}$ compared to $\delta_T = 1°\mathrm{C}$ as expected. The lower overturning circulation cell is not well resolved because of the low diapycnal diffusivity used in our model.

The intensity of the pole-to-pole overturning circulation (ψ_i) is defined as the maximum streamfunction that connects the Southern Ocean and the North Atlantic, i.e., the minimum of the maximum streamfunction at each latitude below the surface wind-driven gyre:

$$\psi_i = \min\{\max\{\psi(y,\theta < 3°\mathrm{C}),\theta\},y\} \text{ for } 1200\mathrm{km} < y < 7000\mathrm{km}, \tag{4.4}$$

where the operator $\max\{f(\mu_1,\mu_2),\mu_2\}$ and $\min\{f(\mu_1,\mu_2),\mu_2\}$ represent the maximum and minimum of the function $f(\mu_1,\mu_2)$ with respect to the dimension μ_2 for a constant μ_1, respectively. This is defined for $\theta < 3°\mathrm{C}$ in order to exclude the wind-driven gyre circulation. Because the isopycnal slope is more relevant to local overturning circulation as discussed in Section 4.3, we also define the intensity of the Southern Ocean residual-mean overturning circulation (ψ_s) as

$$\psi_s = \max\{\psi(L_s, \theta)\}, \tag{4.5}$$

where $L_s = 1200$ km represents the northern boundary of the reentrant Southern Ocean. Variations of ψ_i and ψ_s with respect to δ_T are given in Figure 4.3a. At $\delta_T = 5°\mathrm{C}$, ψ_s is reduced to around 1.2 Sv although the pole-to-pole overturning circulation disappears as the shared density range between the North Atlantic and the Southern Ocean is reduced to zero. The difference between the locally defined ψ_s and the pole-to-pole overturning circulation is due to a local clockwise overturning circulation between $y = 1200$ km and $y = 2000$ km (Figure 4.2). This local overturning circulation is a remanent of the wind-driven overturning circulation (sometimes called "Deacon cell"). It is likely due to the constant eddy thickness diffusivity adopted in our model, which might underestimate the effect of eddies in compensating the wind-driven overturning circulation (cf. Gent and Danabasoglu, 2011; Gent, 2016).

The circumpolar transport of the ACC with respect to changes in ψ_s is plotted in Figure 4.3b. From $\delta_T = 0.5°\mathrm{C}$ to $\delta_T = 5.0°\mathrm{C}$, ψ_s decreases from 2.6 Sv to 1.2 Sv and T_{ACC} increases from 62 Sv to 76 Sv. In comparison, T_{ACC} increases from 25 Sv to 125 Sv in Fučkar and Vallis (2007, their Figure 3) for a similar change of the temperature forcing. To exclude the possibly geometrical influence due to the different size of model domain, we will normalize the ACC transport in the following discussions with a reference ACC transport (see details below).

Wolfe and Cessi (2010) attributed the large sensitivity of T_{ACC} observed in Fučkar and Vallis (2007) to their strong residual-mean overturning circulation in the Southern Ocean. However, the magnitude of the residual-mean overturning circulation in our simulation (see Figure 4.3a) is actually close to or even larger than Fučkar and Vallis (2007, their Figure 2). Therefore, the strong sensitivity of T_{ACC} to the North Atlantic surface forcing in Fučkar and Vallis (2007) can not be explained by the magnitude of the residual-mean overturning circulation in the Southern

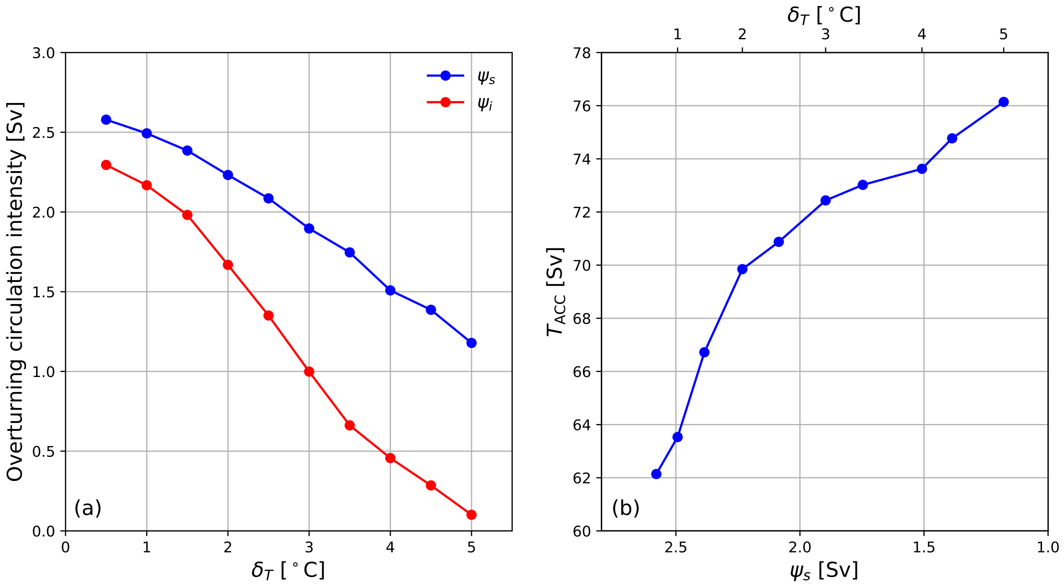

Figure 4.3: (a) Variation of the magnitude of the AMOC (ψ_i) and Southern Ocean overturning circulation (ψ_s) with changes in δ_T. (b) Variation of the ACC transport T_{ACC} with respect to the decrease of ψ_s. The x-axis is reversed because ψ_s decreases with δ_T.

Ocean. As seen in Figure 4.2, the clockwise pole-to-pole overturning circulation is limited to the upper 1 km in both cases of Figure 4.2. In comparison, the AMOC in Fučkar and Vallis (2007) reaches around 2500 m in their symmetric forcing case (corresponding to $\delta_T = 0$°C in our study) and then shoals upward substantially to a shallower depth as the surface temperature increases in the North Atlantic (their Figure 2). Therefore, the different sensitivity of the ACC transport is likely related to the different vertical structure of the overturning circulation as explained in the next section using conceptual models.

4.3 Conceptual models

In this section, we develop a 2.5-layer conceptual model and a continuously stratified conceptual model of the Southern Ocean circulation based on the residual-mean theory of Marshall and Radko (2003) in order to understand the influence of the overturning circulation structure on the ACC transport. The 2.5-layer conceptual model can be considered to be a generalization of the pycnocline model of Gnanadesikan (1999). A similar multi-layer generalization of Gnanadesikan (1999) is developed for the Atlantic basin by Marshall and Zanna (2014). Different from Marshall and Radko (2003), in which the overturning circulation is part of the solution, we specify the overturning circulation streamfunction as an input for our conceptual model in order to discuss the response of the ACC transport to variations in the overturning circulation. In the conceptual models of this section, we use a shifted coordinate ($y_s = y - L_s$) for analytical convenience. The subscript for y_s is dropped in the discussion hereafter for notation conciseness, i.e., the origin of the y axis is at the northern boundary of the Southern Ocean in this section.

4.3.1 2.5-layer conceptual model

In this subsection, a 2.5-layer conceptual model is developed that includes two active layers (ρ_1 and ρ_2) and an abyssal layer (ρ_3), where the zonal flow is blocked by bottom topgraphy, as shown in the schematic Figure 4.4. The three layers, which are separated by two pycnoclines, respectively represent intermediate water, deep water, and bottom water from top to bottom. The stratification across the two pycnoclines is respectively noted as g'_1 and g'_2, where $g'_1 = g(\rho_2 - \rho_1)/\rho_0$, $g'_2 = g(\rho_3 - \rho_2)/\rho_0$, and ρ_0 is the reference density. The two active layers outcrop through the surface mixed layer in the Southern Ocean. For simplicity, we keep the outcropping position of the two pycnoclines $y = -L_1$ and $y = -L_2$ unchanged, i.e., we assume L_1 and L_2 to be constant. In the continuously stratified model, we will relax the assumption of constant L_1 and L_2.

The AMOC is carried by the top two layers. Following Marshall and Radko (2003), we define the residual-mean overturning circulation streamfunction for our layer model as

$$\psi_1 = \int_0^{L_x} \int_{-h_1}^{0} v\,dz dx = \psi_1^+ + \psi_1^*, \tag{4.6}$$

$$\text{and} \quad \psi_2 = \int_0^{L_x} \int_{-h_2}^{0} v\,dz dx = \psi_2^+ + \psi_2^*.$$

where [1]

$$\psi_1^+ \equiv L_x \int_{-h_1}^{0} \overline{v} dz, \quad \psi_1^* \equiv L_x \overline{v_1' h_1'}, \tag{4.7}$$

$$\psi_2^+ \equiv L_x \int_{-h_2}^{0} \overline{v} dz, \quad \text{and} \quad \psi_2^* \equiv L_x \overline{v_2' h_2'}.$$

Here, the overbar means zonal average, primes represent deviations from zonal average, ψ^+ represent the Eulerian-mean overturning circulation, ψ^* represents the eddy-driven overturning circulation, v is meridional velocity, h denotes pycnocline depth, $\psi = \psi^+ + \psi^*$ represents the residual-mean overturning circulation streamfunction associated with the two pycnoclines, and L_x is the longitudinal width of the Southern Ocean. The subscript 1 and 2 indicate the layer each variable refers to (see Figure 4.4). Physically, ψ_1 and ψ_2 represent the net meridional volume transport above the upper and lower pycnoclines, respectively. Because we assume that the overturning circulation is carried by the top two layers and that the circulation to be adiabatic below the surface mixed layer, we should obtain

$$\psi_1 = \Psi, \tag{4.8}$$

$$\text{and} \quad \psi_2 = 0,$$

---

[1] $\psi_2^* = L_x\left(\overline{v_1'h_1'} + \overline{v_2'(h_2'-h_1')}\right) = L_x\left(\overline{v_2'h_2'} + \overline{(v_1'-v_2')h_1'}\right) = L_x\left(\overline{v_2'h_2'} + \frac{g_1'}{f_0}\overline{\frac{\partial h_1'^2}{\partial x}}\right) = L_x\overline{v_2'h_2'}$, and note $v_3' \neq 0$ in order to balance the southward mean flow below the submarine sill such that the residual-mean meridional transport in the bottom layer is zero.

where Ψ is a constant that defines the intensity of the AMOC and represents the effects of North Atlantic surface buoyancy conditions in our conceptual model.

In the Southern Ocean, the Eulerian zonal-mean momentum balance in steady state within the reentrant Southern Ocean is

$$-f_0\overline{v} = \frac{\partial F}{\partial z}, \text{ with } F = \frac{\tau_0}{\rho_0} \text{ at } z = 0, \tag{4.9}$$

where the nonlinear Reynolds terms and horizontal frictional forces have been neglected (Marshall and Radko, 2003), F represents vertical momentum flux, and τ_0 represents surface wind stress. For analytical simplicity, τ_0 and f_0 are assumed to be constant. The pressure gradient force is not present due to the absence of meridional boundaries in the Southern Ocean. The balance in Equation (4.9) is valid as long as it is above the submarine sill. Vertical integration of Equation (4.9) gives the expression of the Eulerian-mean overturning circulation streamfunction (ψ^+)

$$\psi^+|_z = L_x \int_z^0 \overline{v} dz = -\frac{\tau_0 L_x}{\rho_0 f_0}, \text{ for } -h_m > z > -h_s, \tag{4.10}$$

if the vertical momentum flux below the surface mixed layer is also neglected. Here, h_s is the depth of the submarine sill at the Drake passage, and h_m is the depth of surface mixed layer. Therefore, we can express ψ_1^+ and ψ_2^+ as

$$\psi_1^+ = \psi_2^+ = -\frac{\tau_0 L_x}{\rho_0 f_0}, \tag{4.11}$$

i.e., the Eulerian-mean overturning circulation streamfunction is given by the surface Ekman transport that is driven by the westerly wind over the Southern Ocean.

Following Gnanadesikan (1999), we can parameterize the eddy-driven overturning circulation (ψ_1^* and ψ_2^*) in Equation (4.7) as

$$\psi_1^* = L_x K_{\mathrm{GM}} s_1, \qquad (4.12)$$

$$\text{and} \quad \psi_2^* = L_x K_{\mathrm{GM}} s_2,$$

where s_1 and s_2 are respectively the slope of the upper and lower pycnocline, and K_{GM} is the GM thickness diffusivity, which is assumed to be constant in this section. This assumption (constant K_{GM}) is relaxed in Section 4.4.2, where we discuss the potential influence of a more realistic representation of K_{GM} on the results.

Combining Equation (4.6), (4.8), (4.11), and (4.12), we have the expression for the residual-mean overturning circulation associated with the two pycnoclines

$$\psi_1 = -\frac{\tau_0 L_x}{\rho_0 f_0} + L_x K_{\mathrm{GM}} s_1 = \Psi, \qquad (4.13)$$

$$\text{and} \quad \psi_2 = -\frac{\tau_0 L_x}{\rho_0 f_0} + L_x K_{\mathrm{GM}} s_2 = 0.$$

From Equation (4.13), we obtain the expression for the slope of the two pycnoclines as

$$s_1(\Psi) = s_2 + \frac{\Psi}{L_x K_{\mathrm{GM}}}, \qquad (4.14)$$

$$\text{and} \quad s_2 = \frac{\tau_0}{\rho_0 f_0 K_{\mathrm{GM}}}.$$

The parentheses in $s_1(\Psi)$ means that s_1 is subject to changes with respect to variations in Ψ. Because we keep the wind stress forcing (τ_0) and eddy effect (K_{GM}) constant, s_2 is also constant here. This implies an invariant depth of the lower pycnocline (h_2), i.e., h_2 is constant with respect to Ψ (Figure 4.4), which is relaxed in the continuously stratified model in the next subsection.

From thermal wind balance, the zonal velocity at each layer can be expressed as

$$u_1 = u_2 - \frac{g_1'}{f_0}\frac{\partial h_1'(\Psi, y)}{\partial y}, \tag{4.15}$$

$$\text{and} \quad u_2 = -\frac{g_2'}{f_0}\frac{\partial h_2'(y)}{\partial y},$$

where

$$h_1'(\Psi, 0) = h_1(\Psi) = -L_1\, s_1(\Psi) \quad \text{and} \quad h_2'(0) = h_2 = -L_2\, s_2. \tag{4.16}$$

Integrating Equation (4.15) with respect to latitude and depth, we have the circumpolar transport of the ACC as

$$T_{\text{ACC}}(\Psi) = \int_{-L_s}^{0}\left[\int_{-h_2}^{-h_1} u_2 dz + \int_{-h_1}^{0} u_1 dz\right] dy = -\frac{1}{2f_0}\left[g_1'\, h_1^2(\Psi) + g_2'\, h_2^2\right]. \tag{4.17}$$

To obtain Equation (4.16) and (4.17), the assumption of $h_m \ll h_1$ is used. This assumption is true in both simulations and the real ocean. For example in the real ocean, h_m is normally of order 100m, but h_1 is at around 1000m. Because h_2 is constant here, changes in T_{ACC} can only be caused by variations in h_1, i.e.,

$$\Delta T_{\text{ACC}}(\Psi) \equiv T_{\text{ACC}}(\Psi) - T_{\text{ACC}}(0) \approx -\frac{1}{f_0} g_1'\, h_1(0) \Delta h_1(\Psi), \tag{4.18}$$

where the changes are evaluated with respect to $\Psi = 0$,

$$h_1(0) = -L_1\, s_1(0) = -L_1 s_2, \tag{4.19}$$

and

$$\Delta h_1(\Psi) = h_1(\Psi) - h_1(0) = -L_1\left[s_1(\Psi) - s_1(0)\right] = -\frac{L_1\,\Psi}{L_x K_{\text{GM}}}, \tag{4.20}$$

which is obtained by combining Equation (4.14) and Equation (4.16).

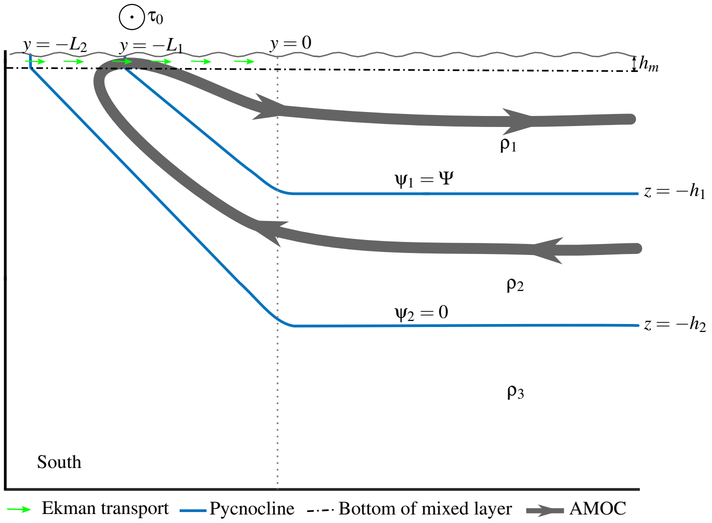

Figure 4.4: Schematic of the 2.5-layer model. A mixed layer (dash-dotted line) of depth h_m is included that carries the Ekman transport (green arrow) in the Southern Ocean. The density of the three layers are ρ_1, ρ_2, and ρ_3 from top to bottom. The three layers are separated by two pycnoclines that are indicated as blue lines. The two pycnoclines outcrop at surface in the Southern Ocean at $y=-L_1$ and $y=-L_2$, respectively. The depth of the two pycnoclines are $z=-h_1$ and $z=-h_2$, respectively. The northern boundary of the Southern Ocean is represented by the gray dotted line ($y=0$). The thin gray sinusoidal line indicates the sea surface. The solid black line represents the bottom topography and the idealized Antarctica continent. The AMOC is carried by the top two layers and are represented by the thick gray lines with arrows indicating the directions of the overturning circulation. The streamfunction for the top pycnocline is noted as ψ_1, and the streamfunction for the bottom pycocline is noted as ψ_2. Only the southern hemisphere is plotted here.

Hereafter, the parentheses in $h(0)$ and $\Delta h(\Psi)$ will be dropped for conciseness. Dividing Equation (4.18) by $T_{\text{ACC}}(0)$, we have

$$\frac{\Delta T_{\text{ACC}}(\Psi)}{T_{\text{ACC}}(0)} \approx \frac{2g_1'\,h_1\,\Delta h_1}{g_1'\,h_1^2+g_2'\,h_2^2} = \frac{2h_1\,\Delta h_1}{h_1^2+h_2^2/r_g}, \tag{4.21}$$

where $r_g \equiv g_1'/g_2'$ is usually larger than 1 and defines the vertical structure of ocean density stratification in our 2.5-layer model.

Substituting Equation (4.20) into Equation (4.21), we have

$$\frac{\Delta T_{\mathrm{ACC}}(\Psi)}{T_{\mathrm{ACC}}(0)} \approx -\frac{2h_1 L_1 \Psi / L_x}{K_{\mathrm{GM}}\left[h_1^2 + h_2^2/r_g\right]}. \tag{4.22}$$

Substituting L_1 from Equation (4.19) into Equation (4.22), we have

$$\frac{\Delta T_{\mathrm{ACC}}(\Psi)}{T_{\mathrm{ACC}}(0)} \approx \frac{2h_1^2 \Psi \rho_0 f_0}{\tau_0 L_x \left[h_1^2 + \frac{h_2^2}{r_g}\right]} = -\Re\, \Gamma, \tag{4.23}$$

where h_1 is evaluated at $\Psi = 0$,

$$\Re \equiv \frac{2}{1 + \frac{1}{r_g r_h^2}} \tag{4.24}$$

represents the sensitivity of the ACC transport to the intensity of overturning circulation, $r_h = h_1/h_2$ represents the vertical structure of the overturning circulation, and

$$\Gamma \equiv \Psi / \psi^{+} \tag{4.25}$$

is the residual-mean overturning circulation streamfunction normalized by the wind-driven overturning circulation streamfunction that is defined in Equation (4.11). The negative sign in Equation (4.23) indicates that the ACC transport decreases for a stronger overturning circulation consistent with Figure 4.3b. The variable Γ is a simplified representation of the North Atlantic surface buoyancy forcing in our conceptual model. For a larger r_h, the upper pycnocline is deeper and the ACC transport is more sensitive to the changes in the overturning circulation intensity and thus is more sensitive to surface forcing in the North Atlantic.

For parameters relevant to our MITgcm simulations at $\delta_T = 0.5$°C in Section 4.2, $\Psi/L_x = 0.5\ \mathrm{m^2/s}$, $f_0 = 8 \times 10^{-5}\,\mathrm{s^{-1}}$, $\tau_0 = 0.1\,\mathrm{N/m^2}$, and $\rho_0 = 1000\,\mathrm{kg/m^3}$, the dependence of the relative change of circumpolar transport of the ACC ($\Delta T_{\mathrm{ACC}}/T_{\mathrm{ACC}}$) on these two non-dimensional parameters r_g and r_h is presented in Figure 4.5. With slight change of the structure of the

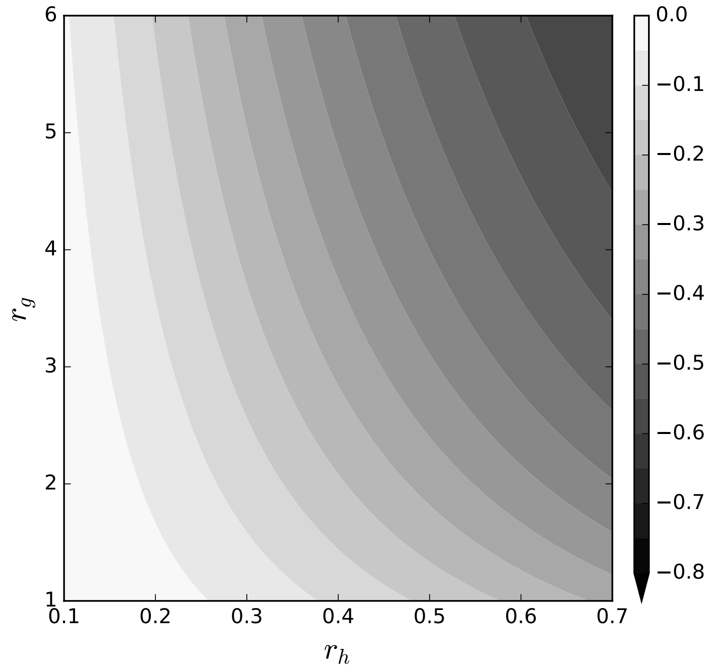

Figure 4.5: Plot of $\Delta T_{\text{ACC}}(\Psi)/T_{\text{ACC}}(0)$ with respect to two nondimensional parameters r_g and r_h at $\Gamma = 0.4$. The nondimensional parameter r_g represents the shape of stratification, and r_h defines the structure of the overturning circulation. A larger r_g represents a stronger stratification in the mid-depth compared to the abyss. A larger r_h indicates that the overturning circulation has a deeper structure.

overturning circulation, the response of T_{ACC} to changes in the overturning circulation intensity can be substantially different. As an example, if we take $T_{\text{ACC}}(0) = 100\,\text{Sv}$, $r_g = 2.0$, and $\Psi/L_x = 0.5\,\text{m}^2/\text{s}$ (corresponding to $\sim$10 Sv in the real ocean), $T_{\text{ACC}}(\Psi)$ can be 81 Sv at $r_h = 0.4$ but is only 60 Sv at $r_h = 0.7$.

4.3.2 Continuous stratification

In the 2.5-layer conceptual model above, we use two pycnoclines to represent the upper overturning circulation cell. By warming the surface North Atlantic in our simulations, the overturning circulation structure is shifted to warmer temperatures (see Figure 4.6). As a result, the depth associated with the zero-streamfunction (i.e., h_2 in our 2.5-layer model) becomes

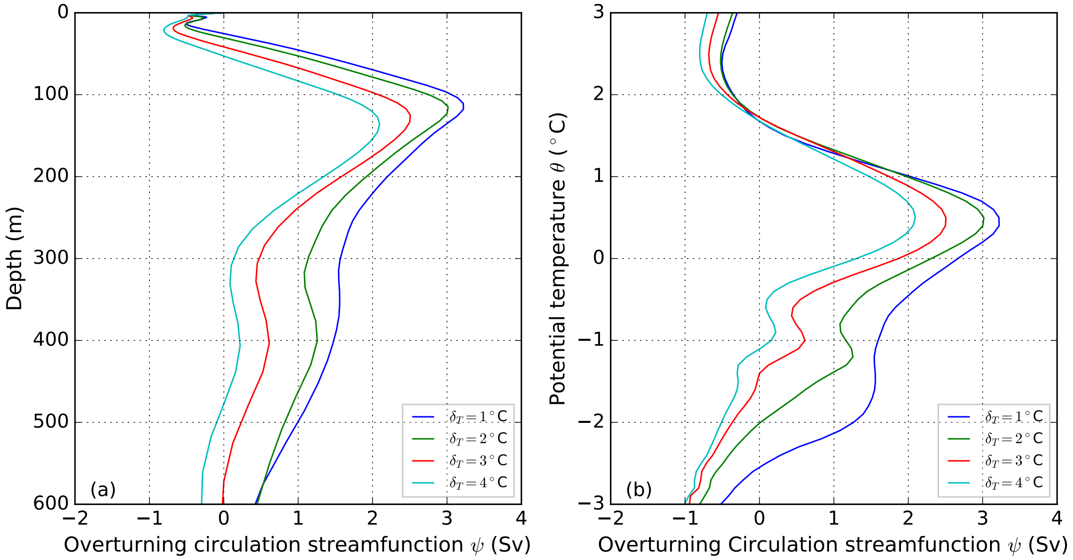

Figure 4.6: Residual-mean overturning circulation at the northern edge of the reentrant Southern Ocean on depth coordinate (a) and θ coordinate (b). For clarity, only 4 runs are plotted.

shallower as δ_T increases, although there is no significant change in the depth and potential temperature that is associated with the maximum overturning circulation streamfunction. This appears to account for the reduced sensitivity of the ACC transport to AMOC intensity for higher δ_T (Figure 4.3b), which cannot be resolved by our simplified 2.5-layer conceptual model. Therefore, in order to make better comparison with our MITgcm simulations, we extend the 2.5-layer model to continuous stratification. Although the conceptual model below is presented in terms of density, we present our figures on potential temperature coordinate (e.g., Figures 4.7 and 4.8) for better comparison with the MITgcm simulations.

In the Southern Ocean, we specify the surface density structure ($\rho_s(y)$) similar to the MITgcm simulations. The flow is assumed to be adiabatic again. With the surface wind stress forcing ($\tau(y)$) and the GM diffusivity (K_{GM}) specified, the residual-mean overturning circulation streamfunction ($\psi(\rho)$) in continuous stratification can be expressed as (Marshall and Radko, 2003; Nikurashin and Vallis, 2011)

$$\psi(\rho)/L_x = K_{\mathrm{GM}}\, s(\rho, y) - \frac{\tau(y)}{\rho_0 f(y)}, \tag{4.26}$$

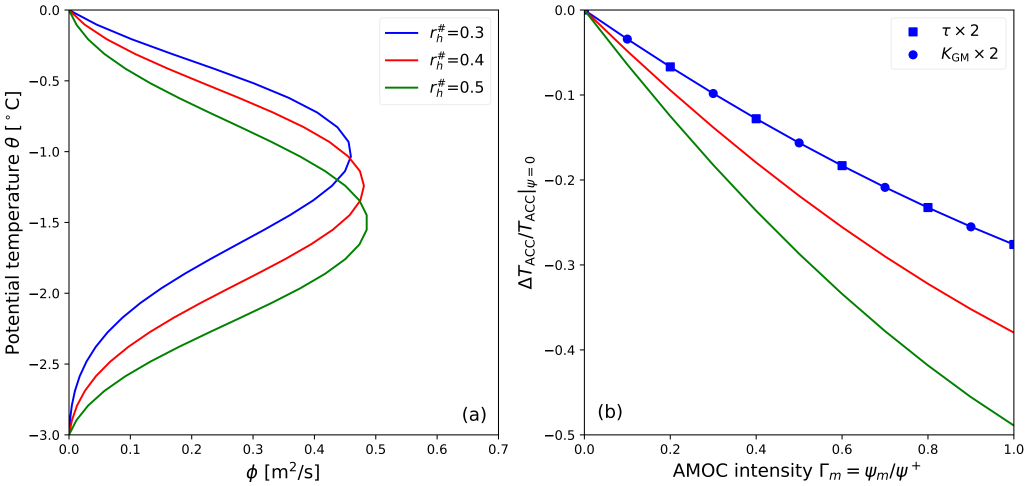

Figure 4.7: (a) Residual-mean overturning circulation streamfunction defined by Equation (4.34) for different $r_h^\#$ at $\phi_0 = 0.5$ and $\lambda = 10$. Larger $r_h^\#$ means that the overturning circulation is associated with higher density or lower potential temperature. The overturning circulation is only defined between -3°C and 0°C here. The result would not change if a different potential temperature range is used. (b) Normalized changes in the ACC transport (normalized by the ACC transport at $\psi = 0$) with respect to changes in the normalized AMOC intensity (Equation (4.42)) predicted by the continuously stratified conceptual model. Each line corresponds to a line in Panel (a) of the same color. The wind stress forcing and $K_{\rm GM}$ are doubled at $r_h^\# = 0.3$ and shown as blue squares and circles, respectively. This is discussed in Section 4.4.1.

where both the wind stress forcing (τ) and isopycnal slope (s) vary with latitude. This is the continuously stratified version of Equation (4.13). The isopycnal slope can be calculated from Equation (4.26) as

$$s(\rho, y) = \left[\phi(\rho) + \frac{\tau(y)}{\rho_0 f(y)}\right] / K_{\rm GM}, \tag{4.27}$$

where $\phi(\rho) = \Psi(\rho)/L_x$. Then the depth of each isopycnal can be found by integrating Equation (4.27) as

$$z(\rho, y) = \int_{y_s(\rho)}^{y} s(\rho, y')dy' = \int_{y_s(\rho)}^{y} \left[\phi(\rho) + \frac{\tau(y')}{\rho_0 f(y')}\right] / K_{\rm GM} dy', \tag{4.28}$$

which can be inverted to give the density structure $\rho(y, z)$ (see Figures 5 and 6 of Marshall and Radko (2003) for examples). Here, $y_s(\rho)$ represents the outcropping latitude of each isopycnal (ρ) at the Southern Ocean surface. Applying the thermal wind balance and assuming a no-slip

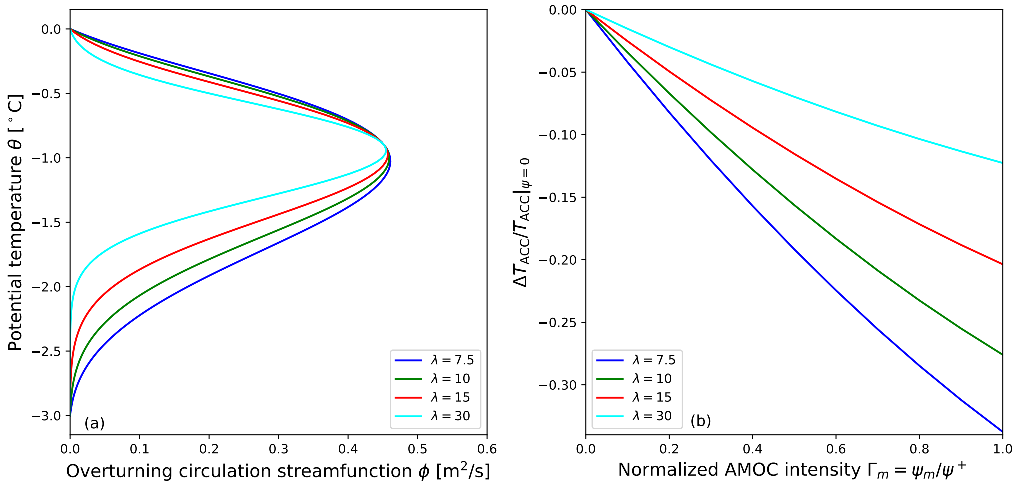

Figure 4.8: (a) Residual-mean overturning circulation streamfunction defined by Equation (4.34) for different λ at $\phi_0 = 0.5$ and $r_h^\# = 0.4$. This resembles the changes in the overturning circulation streamfunction in Figure 4.6b. Lower λ means that the overturning circulation is associated with more isotherms/isopycnals. (b) Normalized changes in the ACC transport with respect to the AMOC intensity normalized by the Eulerian-mean overturning circulation as predicted by the continuously stratified conceptual model. Each line corresponds to a line in Panel (a) of the same color.

boundary condition in the bottom, we can calculate the ACC transport as

$$T_{\mathrm{ACC}} = \int_{-L_s}^{0} \int_{-H}^{0} \int_{-H}^{z} \frac{g}{f(y)\rho_0} \frac{\partial \rho(y,z')}{\partial y} dz' \, dz \, dy, \tag{4.29}$$

where L_s is the meridional width of the reentrant channel, H is the depth of the ocean, and $-L_s \leq y \leq 0$ defines the range of the Southern Ocean as in Figure 4.4. From Equation (4.28) and (4.29), we can see that the ACC transport is a function of only the residual-mean overturning circulation if we keep the wind stress forcing ($\tau(y)$) and eddy thickness diffusivity (K_{GM}) constant. The potential influence of wind stress forcing and eddy thickness diffusivity on the result is discussed in Section 4.4.1.

For simplicity, we adopt a form of surface density that linearly depends on y in the

Southern Ocean, i.e.,

$$\rho_s(y) = -\Delta\rho \frac{y}{L_s} + \rho_r, \quad \text{for} \quad -L_s \leq y \leq 0, \tag{4.30}$$

where

$$\rho_s(0) = \rho_r, \tag{4.31}$$

and $\Delta\rho$ represents the density contrast across the Southern Ocean. The surface wind stress forcing is taken to be linear as well that resembles Figure 4.1b in the Southern Ocean,

$$\tau(y) = \tau_0(y/L_s + 1), \quad \text{for} \quad -L_s \leq y \leq 0, \tag{4.32}$$

where

$$\tau_0 = 0.1\,\mathrm{N/m^2}. \tag{4.33}$$

The residual-mean overturning circulation streamfunction is assumed to be

$$\psi(\rho) = L_x\phi(\rho) = L_x\phi_0 M\left(\chi(\rho)\right)\exp\left(-\lambda\xi(\rho)^2\right), \tag{4.34}$$

where

$$\xi(\rho) = \frac{\rho - \rho_d}{\rho_{l1} - \rho_{l2}}, \tag{4.35}$$

$$\chi(\rho) = \frac{\rho - \rho_{l2}}{\rho_{l1} - \rho_{l2}}, \tag{4.36}$$

and

$$M(\chi) = -\tanh(5(\chi - 1)) \times \tanh(5\chi) \tag{4.37}$$

for

$$\rho_{l1} \leq \rho \leq \rho_{l2}. \tag{4.38}$$

The function $M(\chi)$ is to ensure that ψ disappears for density outside of the density range defined by Equation (4.38), and its form would not affect the result qualitatively. Here, $\rho_{l1} = \rho_s(0)$ is the lightest isopycnal associated with the overturning circulation, $\rho_{l2} = \rho_s(-L)$ is the densest isopycnal associated with the overturning circulation, ϕ_0 sets the magnitude of overturning circulation streamfunction, λ sets the spread of the streamfunction in density space (see Figure 4.8a for examples),

$$\rho_d = \rho_{l1} + r_h^{\#}[\rho_{l2} - \rho_{l1}], \tag{4.39}$$

where $r_h^{\#}$ is a nondimensional number (similar to r_h in Section 4.3a) that controls the position of maximum streamfunction in the density space (see Figure 4.7a for examples). A larger λ means smaller spread of the overturning circulation in the density space (Figure 4.8a), and a larger $r_h^{\#}$ means that the overturning circulation is associated with denser isopycnals (Figure 4.7a). The two nondimensional parameters λ and $r_h^{\#}$ together control the vertical structure of the overturning circulation streamfunction in density space. We note that the forms of $\rho_s(y)$, τ_y, and $\psi(\rho)$ are chosen for illustrative purpose and will not affect our results qualitatively.

Consistent with the 2.5-layer conceptual model, we define the intensity of the overturning circulation (ϕ_m) as

$$\phi_m = \psi_m / L_x = \max\{\psi(\rho)\}/L_x, \text{ for } \quad \rho_{l1} \leq \rho \leq \rho_{l2}, \tag{4.40}$$

which represents the AMOC intensity and parameterizes the influence of the North Atlantic surface buoyancy condition on the overturning circulation intensity. Associated with the maximum streamfunction ψ_m, we also define a normalized AMOC intensity as

$$\Gamma_m = \psi_m / \psi^+, \tag{4.41}$$

where

$$\psi^+ = -\frac{\tau_0 L_x}{\rho_0 f_0}. \tag{4.42}$$

Now we explore the dependence of the ACC transport on the overturning circulation intensity (ϕ_m) and structure ($r_h^\#$) with constant wind stress forcing and eddy thickness diffusivity. In Figure 4.7b, we plot the relative changes in the ACC transport with respect to changes in both ϕ_m and $r_h^\#$. The relative change in T_{ACC} is defined as

$$R = \frac{T_{\mathrm{ACC}}|_{\phi_m} - T_{\mathrm{ACC}}|_{\phi_m=0}}{T_{\mathrm{ACC}}|_{\phi_m=0}}, \tag{4.43}$$

where $T_{\mathrm{ACC}}|_{\phi_m=0}$ represents the ACC transport at $\phi_m = 0$ and is a constant. This is similar to the definition in Equation (4.21). Figure 4.7b shows that variations of the ACC transport in response to changes in the overturning circulation intensity are strongly sensitive to the vertical structure of the overturning circulation, which is controlled by $r_h^\#$. For a larger $r_h^\#$, variations in ϕ_m are associated with changes in the overturning circulation on denser isopycnals, which means that changes in ϕ_m can affect the zonal-velocity distribution over a larger depth range and result in a bigger change in the ACC transport.

The sensitivity of the ACC transport can also be affected by λ, which sets the spread of streamfunction on density space. In Figure 4.8a, we plot the overturning circulation streamfunction for different λ to resemble the changes in the overturning circulation in Figure 4.6. The response of the ACC transport to AMOC intensity changes is plotted in Figure 4.8b, in which the sensitivity of the ACC transport to AMOC intensity is higher for smaller λ, which corresponds to a larger spread of the streamfunction in the density space. This explains the reduced sensitivity of the ACC transport in our MITgcm simulations for higher δ_T (compare Figure 4.3b & Figure 4.6 with Figure 4.8).

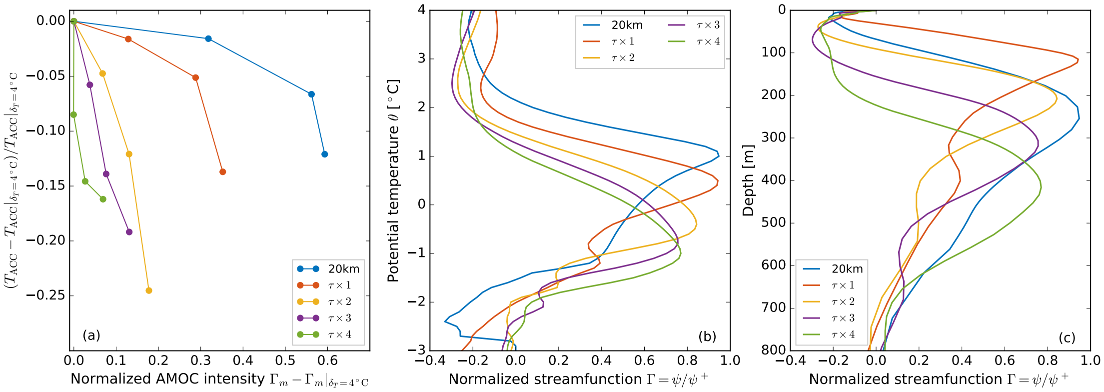

Figure 4.9: (a) Variation of the ACC transport with the AMOC intensity at the northern edge of the Southern Ocean in the MITgcm simulations. The ACC transport is referenced to and then normalized by the ACC transport at $\delta_T = 4^\circ$C. The AMOC intensity is normalized by $\psi^+ = -\frac{\tau_0 L_x}{\rho_0 f_0}$, i.e., $\Gamma = \psi_s/\psi^+$, where ψ_s is defined in Equation (4.5). From left to right, the four points in each set of simulation corresponds to $\delta_T = 4^\circ$C, 3°C, 2°C, and 1°C. Here, "$\tau \times n$" means that the wind stress forcing is multiplied by n in the Southern Ocean ("$\tau \times 1$" represents the simulations discussed in Section 4.2), and "20km" refers to the simulation at 20km resolution that is discussed in Section 4.4.3. (b) Normalized overturning circulation streamfunction at the northern edge of the reentrant Southern Ocean on θ coordinate at $\delta_T = 1^\circ$C. (c) Normalized overturning circulation streamfunction at the northern edge of the reentrant Southern Ocean on depth coordinate at $\delta_T = 1^\circ$C. The result is not significantly different for other choices of δ_T.

4.4 Discussion

4.4.1 Magnitude of wind stress forcing and K_{GM}

The 2.5-layer model in Section 4.3.1 (Equation (4.23)) suggests that the response of the ACC transport to changes in the North Atlantic surface forcing is independent of the wind stress forcing (τ) and eddy thickness diffusivity (K_{GM}). We now test whether this is true in the continuously stratified conceptual model and the MITgcm simulations.

In the continuously stratified model, we double the wind stress forcing ($\tau \times 2$) and eddy thickness diffusivity ($K_{\mathrm{GM}} \times 2$) but keep the overturning circulation structure (controlled by λ and $r_h^\#$) unchanged ($r_h^\# = 0.3$ in Figure 4.7a). Although the intensity of the ACC and AMOC varies substantially in response to changes in the τ and K_{GM} (not shown), we find that the response of the normalized ACC transport to changes in the AMOC intensity is shown to be independent of the wind stress forcing and eddies (Figure 4.7b), consistent with the 2.5-layer conceptual model.

However, this is not true in the MITgcm simulations because variations in the wind stress forcing and eddies could change the structure of the overturning circulation (e.g., Marshall et al., 2017). Using the same model setup as Section 4.2, another 3 sets of simulations are performed with increased wind stress forcing in the Southern Ocean. Each set of simulations contains 4 runs with $\delta_T = 1°\text{C}$, 2°C, 3°C, and 4°C respectively. We show that the sensitivity of the ACC transport to the AMOC intensity increases with wind stress forcing (Figure 4.9a) while the AMOC is shifted to colder potential temperature (Figure 4.9b) and deeper depth (Figure 4.9c) in the Southern Ocean, i.e., the overturning circulation structure changes with wind stress forcing. This increased sensitivity with wind can be reproduced by our continuously stratified conceptual model if the changes in the overturning circulation structure is considered such as by increasing $r_h^\#$ (Figure 4.7).

We note that the conceptual models are developed just to interpret the influence of the AMOC structure on the ACC transport variations and thus should not be considered as complete models for the ACC or the overturning circulation in the Southern Ocean. To make a complete conceptual model, the influence of surface forcing on the intensity and structure of the overturning circulation needs to be parameterized. Therefore, in order to use our conceptual models to interpret model results, such as the different sensitivity at different wind stress forcing, the overturning circulation structure should be adjusted along with the model simulations such that they are dynamically in concert with each other.

4.4.2 State-dependent K_{GM}

In the conceptual model above, a constant GM thickness diffusivity is used. In this subsection, we relax this assumption and make it proportional to the isopycnal slope as suggested by Visbeck et al. (1997), i.e.,

$$K_{\text{GM}} = k|s|, \tag{4.44}$$

where k is a positive scaling constant. As a result, the isopycnal slope in Equation (4.14) becomes

$$s_2 = -\sqrt{\frac{\tau_0}{\rho_0 |f_0| k}}, \tag{4.45}$$
$$\text{and } s_1 = -\sqrt{s_2^2 - \frac{\Psi}{L_x k}}.$$

The change in h_1 with Ψ in Equation (4.20) can be expressed as

$$\begin{aligned} \Delta h_1(\Psi) &= -L_1 \left[s_1(\Psi) - s_2(0) \right] \\ &= \frac{h_1(0)}{s_2} \left[\sqrt{s_2^2} - \sqrt{\left(s_2^2 - \frac{\Psi}{L_x k} \right)} \right] \\ &= -h_1(0) \left[1 - \sqrt{(1-\Gamma)} \right], \end{aligned} \tag{4.46}$$

where Γ is the nondimensional residual-mean overturning circulation intensity that is defined in Equation (4.25). Substitute Equation (4.46) in to Equation (4.21) and we have

$$\frac{\Delta T_{\mathrm{ACC}}(\Psi)}{T_{\mathrm{ACC}}} \approx -\frac{-2h_1^2}{h_1^2 + h_2^2/r_g} \left[1 - \sqrt{(1-\Gamma)} \right], \tag{4.47}$$

where the parenthesis in $h_1(0)$ is dropped again for conciseness. For the upper overturning circulation cell discussed in this paper, $0 < \Gamma < 1$. Thus, we would obtain by Taylor expansion

$$\frac{\Delta T_{\mathrm{ACC}}(\Psi)}{T_{\mathrm{ACC}}} \approx -\frac{1}{2} \Re \Gamma, \tag{4.48}$$

where $\Re$ is defined in Equation (4.24) and the terms of order $O(\Gamma^2)$ and higher are dropped. Therefore, for a more realistic representation of K_{GM} that evolves with the model states, the sensitivity of the ACC transport to the overturning circulation is reduced by 50%. Similar results can be obtained for our continuously stratified conceptual model (not shown). This implies that the ACC sensitivity to the overturning circulation could also be reduced in OGCM simulations if the eddy is resolved or parameterized with a more realistic scheme (cf. Gent and Danabasoglu, 2011), as is also evidenced by the next subsection.

It is suggested by previous model studies that the eddy thickness diffusivity has a vertical structure that peaks at the top and bottom of the water column (e.g., Fig. 7 of Abernathey et al., 2013). This depth dependence of the eddy diffusivity is not resolved in our parameterization of the eddy thickness diffusivity, and it has been shown to have noticeable influences on the structure and magnitude of the overturning circulation (Chapman and Sallée, 2017). Future studies should employ more realistic representations of the eddy diffusivity. However, the discussion in this section suggests that a different parameterization of the eddy diffusivity would not change our results qualitatively.

4.4.3 Model resolution

Previous studies suggested that the ACC and the Southern Ocean overturning circulation can behave differently in response to surface forcing perturbations in models from coarse resolution to eddy-resolving resolution (e.g., Munday et al., 2013; Morrison and Hogg, 2013; Abernathey et al., 2011). Using an ocean basin similar to this study, Munday et al. (2013) showed that the ACC reaches eddy saturation when the model resolution is 1/2° and finer, consistent with Morrison and Hogg (2013). Here, the influence of model resolution on our results is tested with a set of experiments at 20km resolution. The resolution of 20km is chosen to represent the scenario with eddy saturation while it would not require too much computing resources.

In the 20km resolution experiments, the GM thickness diffusivity is $20\text{m}^2/\text{s}$ that represents an adiabatic sub-grid scale closure for the turbulent dissipation of potential temperature (cf. Munday et al., 2013; Roberts and Marshall, 1998). We also have a smaller biharmonic viscosity (A_4) of $1.0 \times 10^{12}\text{m}^2/\text{s}$ compared to the coarse-resolution simulations in Section 4.2 to damp the sub-grid noise close to the boundary and a small harmonic viscosity (A_h) of $2.0 \times 10^2\text{m}^2/\text{s}$

(cf. Griffies and Hallberg, 2000). The other parameters and model geometry follow the coarse-resolution model setup.

The model is spun up from rest and run for 500 years at $\delta_T = 1°\mathrm{C}$. At the end of the 500 years, another three experiments are branched out with δ_T as 2°C, 3°C, and 4°C. These four experiments are continued for another 500 years. Because eddies are permitted at this resolution that could enhance the Southern Ocean ventilation (e.g. Kamenkovich et al., 2017), it takes shorter time for the deep ocean to reach equilibrium (cf. Wolfe and Cessi, 2011). At the end of each simulation, the trend of ACC transport is less than 1Sv/Century.

Different from the coarse-resolution runs, in which the changes in potential temperature space are consistent with changes in the depth space when the wind stress forcing increases, the overturning circulation in the 20km-resolution simulations is shifted to warmer isotherms but deeper depth (Figure 4.9). This discrepancy is due to the much smaller meridional temperature gradient in the Southern Ocean in the 20km-resolution simulations (the temperature contrast across the Southern Ocean is reduced by 1°C; not shown), which results from the higher eddy activity that enhances meridional heat flux across the ACC.

In the continuously stratified conceptual model, a fixed surface density structure is assumed at the Southern Ocean surface, which is not true when comparing the 20km-resolution simulations to the coarse resolution runs. Therefore, the overturning circulation in depth space is a better indicator than that in the potential temperature space for comparing sensitivity of the ACC to the AMOC intensity here. Figure 4.9c implies that the sensitivity of the ACC transport is at least larger than the simulation in Section 4.2 ("$\tau \times 1$" in Figure 4.9) because the overturning circulation is located at a deeper depth. However, the sensitivity in the 20km-resolution simulations is significantly smaller than expected (Figure 4.9a). This is due to the higher eddy activity in the 20km-resolution simulations that is more efficient in compensating the changes in the overturning circulation. Thus, a smaller change in the isopycnal slope is expected for increasing δ_T at this resolution compared to the coarse ones, consistent with what is concluded from the conceptual models that use a state-dependent eddy thickness diffusivity (Section 4.4.2). This implies that the sensitivity of the ACC to the surface conditions in the North Atlantic could be even smaller if the eddy is fully resolved.

4.5 Summary

The sensitivity of the circumpolar transport of the ACC to the North Atlantic surface buoyancy conditions is explored in a sector configuration of an ocean general circulation model. Because a fast restoring buoyancy boundary condition, which strongly constrains the surface buoyancy structure at the Southern Ocean surface, is used in this study, the ACC transport is determined by the isopycnal slope that is coupled to the overturning circulation. By changing the surface buoyancy in the North Atlantic, the shared buoyancy contour between the North Atlantic and the Southern Ocean is varied, and consequently the strength of the overturning circulation is modified. We find that the sensitivity in our simulations is substantially weaker than previous study by Fučkar and Vallis (2007). We propose that the different sensitivity relies on the different vertical structure of the simulated AMOC. For different depth of the simulated overturning circulation, the response of the ACC transport to changes in the strength of the overturning circulation varies substantially.

The results are interpreted using a 2.5-layer conceptual model and a continuously stratified conceptual model based on the residual-mean theory of the overturning circulation (Marshall and Radko, 2003). We show that the sensitivity depends on the vertical structure of the overturning circulation. Conceptually, this is true because a deeper change in the overturning circulation can affect more isopycnals by changing their slope, which leads to larger changes in the circumpolar transport of the ACC. The wind stress forcing and eddies can affect this sensitivity by modifying the structure of the overturning circulation.

Considering that the structure of the overturning circulation varies substantially among different climate models especially in simulations of the LGM (e.g., Otto-Bliesner et al., 2007; Muglia and Schmittner, 2015), the sensitivity of the ACC transport is expected to vary significantly among different climate models. This has implication for discussions regarding the response of the ACC in simulations of the future climate change or paleo-climate variations.

The above analyses are based on coarse resolution model simulations, in which the mesoscale eddies are parameterized. We test the influence of model resolutions on the result by performing a set of eddy-permitting simulations and find that the sensitivity is smaller due to the higher eddy activity at this resolution. This implies that the sensitivity of the ACC transport to North Atlantic surface forcing is likely to be low in the real world, considering that the influence of the North Atlantic surface forcing on the ACC transport relies on changes in the isopycnal slope, which has been shown to be rather insensitive to external forcing perturbations in both observations (Böning et al., 2008) and model simulations (Gent and Danabasoglu, 2011).

In this study, we have focused on the upper overturning circulation cell that is assumed to be separated from the lower AABW overturning circulation cell. However, in the real ocean, the two overturning circulation cells are coupled to each other, forming a complex three-dimensional structure of the global overturning circulation (Talley, 2013). It is possible that the North Atlantic surface condition could impose a larger influence on the ACC through changes in the AABW overturning circulation, which has been shown to be able to significantly impact the ACC transport (Gent et al., 2001), than what is concluded in this paper. Future studies should address this by running a more complex model that resolves the three-dimensional structure of the overturning circulation.

Acknowledgments

This work used the Extreme Science and Engineering Discovery Environment (XSEDE), which is supported by National Science Foundation grant number ACI-1548562. S. Sun is supported by National Science Foundation grant OCE-1357078. Without implying their endorsement, the authors thank Ian Eisenman, Andrew Stewart, Ru Chen, Arjun Jagannathan, and Cesar Rocha for their helpful comments and discussions. The authors are also grateful for the helpful comments from two anonymous reviewers.

This chapter is a reprint, with very minor revisions, of the material as it appears in Ocean Moddelling, “Sensitivity of the Antarctic Circumpolar Current transport to surface buoyancy conditions in the North Atlantic”, by S. Sun and J. Liu (2017). The dissertation author was the primary investigator and author of this paper.

Chapter 5

What sets the depth of the Atlantic Meridional Overturning Circulation?

5.1 Introduction

The meridional overturning circulation in the Atlantic ocean is composed of two overturning circulation cells: an upper cell, normally referred to as the Atlantic Meridional Overturning Circulation (AMOC), which advects the North Atlantic Deep Water (NADW) southward from the North Atlantic, and a lower cell that transports the Antarctic Bottom Water (AABW) northward from the Southern Ocean (e.g., Lumpkin and Speer, 2007). In the modern climate, the upper cell extends to approximately 3,000 m below the surface (Lozier, 2012). At the Last Glacial Maximum (LGM) about 21,000 years ago, however, studies based on paleoclimate proxy data suggest that the AMOC depth was substantially shallower (e.g., Lund et al., 2011), although this is debated (Gebbie, 2014). This shoaling of the AMOC has been suggested to contribute to the lower atmospheric CO_2 at the LGM by increasing the carbon storage in the ocean (e.g., Watson et al., 2015; Ferrari et al., 2014).

There have been concerted efforts to simulate the glacial-interglacial changes in the

AMOC depth using comprehensive coupled climate models, which have led to widely varied results (e.g., Otto-Bliesner et al., 2007; Muglia and Schmittner, 2015). For example, in the Paleoclimate Model Intercomparison Project Phase 3 (PMIP3), only the NCAR Community Climate System Model (CCSM4) simulated a shallower AMOC at the LGM compared with the simulated preindustrial (PI) climate, and most of the other models simulated a deeper and stronger AMOC at the LGM (Muglia and Schmittner, 2015). Previous studies have attributed the deeper AMOC in simulations of the LGM in most of the PMIP3 models to a range of different processes, including a stronger Northern Hemispheric westerly wind due to the presence of the Laurentide Ice Sheet (Muglia and Schmittner, 2015), unrealistically low levels of simulated Antarctic sea ice formation (Marzocchi and Jansen, 2017), and a nonlinear response of the climate system to boundary conditions (Oka et al., 2012; Klockmann et al., 2018). The situation is further complicated by the possibility that these simulations are not in equilibrium with the surface forcing, which has been suggested in some previous studies (Zhang et al., 2013; Marzocchi and Jansen, 2017).

Much progress has been made toward understanding the deep ocean circulation based on numerical simulations and theoretical arguments (e.g., Gnanadesikan, 1999; Nikurashin and Vallis, 2012; Marshall and Speer, 2012). By assuming an adiabatic circulation in the Southern Ocean, Ferrari et al. (2014) proposed a geometric model in which the AMOC depth is dynamically linked to the extent of surface buoyancy loss near the coast of Antarctica, which approximately coincides with the region covered by sea ice in summer. This suggests that a shallower AMOC necessarily accompanies an expansion of Southern Ocean sea ice at the LGM. However, it was later shown in a climate model that diabatic processes in the Southern Ocean, which were neglected in Ferrari et al. (2014), diminish the influence of Southern Ocean surface buoyancy forcing and cause the AMOC depth to depend on other factors as well (Sun et al., 2018).

The surface buoyancy loss rate in the Southern Ocean has also been proposed to set the AMOC depth, based on a balance between the Southern Ocean surface buoyancy loss and the interior diapycnal buoyancy gain across the boundary between the two overturning circulation cells (Jansen and Nadeau, 2016). This idea neglects the contribution from diapycnal mixing in the Southern Ocean to the buoyancy budget (cf. Sun et al., 2018) and is based on a zonally-integrated perspective of the global ocean overturning circulation that neglects any potential contribution from the Indo-Pacific ocean (cf. Newsom and Thompson, 2018). Thus it remains unclear the extent to which the surface buoyancy loss rate in the Southern Ocean could be used to predict the AMOC depth in the real ocean.

In addition to Southern Ocean processes, North Atlantic processes have also been suggested to influence the AMOC depth (e.g., Muglia and Schmittner, 2015; Wolfe and Cessi, 2014; Sun and Liu, 2017; Cessi, 2018). For example, Muglia and Schmittner (2015) suggested that a stronger Northern Hemisphere westerly wind would lead to an increase in northward salt transport in the North Atlantic, more active NADW formation, and thus a deeper AMOC in climate model simulations. In an idealized modeling study, Wolfe and Cessi (2014) found a nonlinear dependence of the AMOC depth and strength on the range of surface density shared between the North Atlantic and the Southern Ocean. This highlights the connections between the simulated surface density and the overturning circulation, although the application of this idea to the real ocean may be limited by their simplified representation of the global ocean overturning circulation.

The goal of this study is to create a framework for understanding what sets the AMOC depth and use it to identify the key processes responsible for the wide spread among climate model simulations of the AMOC depth at the LGM compared with the PI climate. To address this, we use a global ocean-only model with surface forcing based on previous coupled climate model simulations, as described in Section 5.2. We find that by modifying the surface restoring timescale, we can evaluate the relative importance of surface buoyancy flux compared with surface density in constraining the AMOC depth, which we investigate in Section 5.3. The results suggest that the AMOC depth is directly connected to the surface density field in both the North Atlantic and

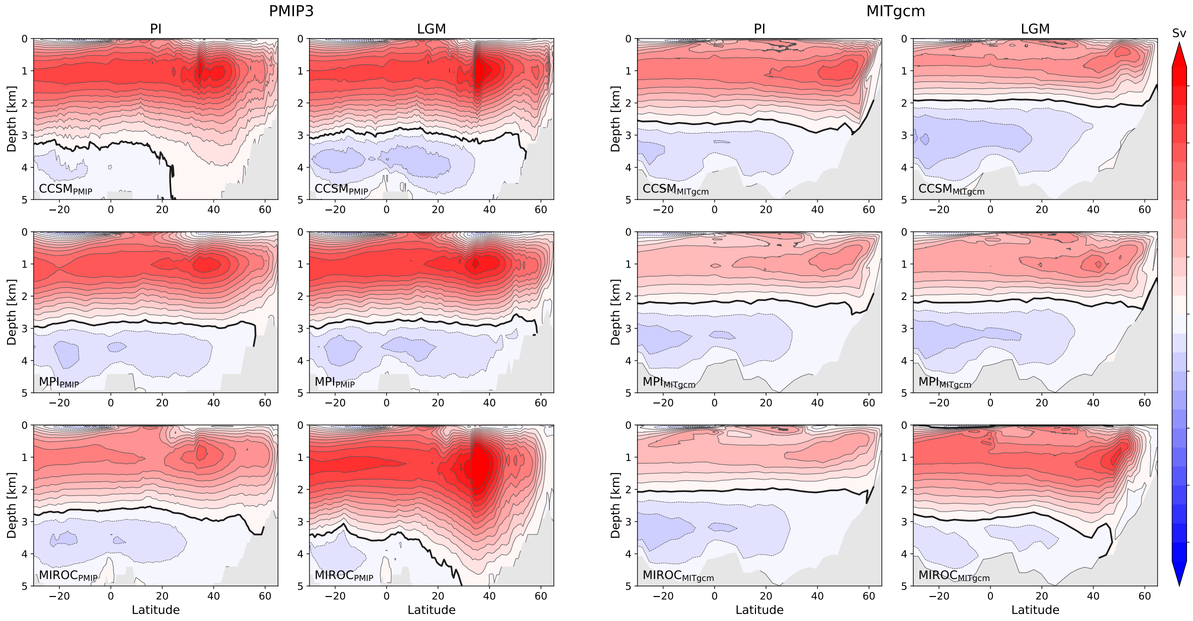

Figure 5.1: Eulerian-mean overturning circulation streamfunction in the Atlantic Ocean ($\overline{\Psi}$) simulated with the PMIP3 coupled models (left) and with the MITgcm ocean-only model forced with the surface fields from the PMIP3 runs (right). The thick black contour in each panel indicates the zero streamline that separates the upper and lower overturning circulation cells in the Atlantic Ocean.

the Southern Ocean. In Section 5.4, we demonstrate this connection using a set of simulations with idealized perturbations to the surface density field, as well as a geometric model that relates the AMOC depth to surface density in both regions. Further discussion and comparisons with previous theories for the AMOC depth are provided in Section 5.5. The findings are summarized in Section 5.6.

5.2 Reproducing AMOC changes in the PMIP3 simulations

In this section, we describe the ocean-only simulations and evaluate how well they reproduce the AMOC depths in the PMIP3 simulations.

5.2.1 Overturning circulation in PMIP3 simulations

PMIP3 is an effort to simulate the climate at several past time periods including the LGM in a number of different comprehensive climate models (Braconnot et al., 2012). For the LGM simulations, the models use prescribed glacial forcing conditions including orbital parameters, specified ice sheets, and atmospheric CO_2 levels. Details can be found in Braconnot et al. (2012).

Because most of the PMIP3 models, including MPI-ESM and MIROC-ESM, do not report the eddy bolus velocity in the simulation output, we use the Eulerian-mean overturning circulation streamfunction in this analysis to represent the AMOC in all of the PMIP3 models. We define the climatological Eulerian-mean overturning circulation streamfunction in the Atlantic Ocean ($\overline{\psi}$) as

$$\overline{\psi}(y,z) = -\int_{z_{\mathrm{bot}}}^{z} \int_{x_w}^{x_e} \overline{v}(x,y,z')\, dx\, dz'. \tag{5.1}$$

where x is longitudinal displacement, y is latitudinal displacement, z is depth with z_{bot} the depth of the ocean bottom, v is meridional velocity, the bar refers to a time-average over the final 100 years of each PMIP3 simulation, and w_x and x_e are the western and eastern boundaries of the basin.

We define the AMOC depth (D) as the depth of the zero-contour of $\overline{\psi}$ in the Atlantic (thick black contours in Fig. 5.1) averaged between 30°S and the equator, as in Sun et al. (2018), i.e.,

$$D = -\frac{1}{L_y}\int_{-L_y}^{0} \zeta(y) dy, \tag{5.2}$$

where L_y represents the meridional distance between 30°S and the equator and ζ is the depth of the streamline $\overline{\psi} = 0$ at meridional location y such that

$$\overline{\psi}(y, \zeta(y)) = 0. \tag{5.3}$$

We limit the definition to the South Atlantic because the lower overturning circulation cell is weak in the Northern Hemisphere and the cell boundary is not well defined in some simulations (see, e.g., the MIROC-ESM LGM simulation in Fig. 5.1).

In this study we focus on three of the PMIP3 models: CCSM4, MPI-ESM, and MIROC-ESM. These models were selected because they are the only ones that reported enough simulation output data for us to create the surface forcing fields for the ocean-only simulations that are described in the next subsection. All three of the models have a nominal ocean resolution of 1°. These models broadly cover each of the three possibilities for AMOC depth differences between the LGM and PI climates (Fig. 5.1): CCSM4 simulates a shallower AMOC at the LGM, MPI-ESM simulates a similar AMOC at the LGM as the PI climate, and MIROC-ESM simulates a deeper AMOC at the LGM.

5.2.2 Model setup

Investigations such as this into the processes that set the AMOC depth in different climate models can be complicated by differences in the representations of the physics in the models and what output each model reports. In order to explore the physical constraints on the AMOC depth, here we use a single ocean-only model with surface forcing based on the PMIP3 coupled climate model simulations. This approach follows Huber and Zanna (2017), who used a similar methodology to evaluate preindustrial climate states and future climate change projections.

We use the Massachusetts Institute of Technology General Circulation Model (MITgcm; Marshall et al., 1997), which integrates the hydrostatic primitive equations. The model is configured to run at a relatively coarse resolution ($2.8^\circ \times 2.8^\circ$), which allows for a relatively large number of simulations without too large computational costs. The model has an approximately realistic bathymetry that is equivalent to what was used by Huber and Zanna (2017). There are 15 layers in the vertical with thickness ranging from 50 m at the top to 690 m at the bottom. We use a vertical diffusivity that is a function of depth and varies from $3\times10^{-5}\mathrm{m}^2/\mathrm{s}$ at the surface to $1.3\times10^{-4}\mathrm{m}^2/\mathrm{s}$ at the transition depth of 2,000 m (Bryan and Lewis, 1979). Momentum is dissipated via Laplacian viscosity and vertical viscosity with coefficients $A_h = 2.0 \times 10^5 \mathrm{m}^2/\mathrm{s}$ and $A_z = 1.0 \times 10^{-3} \mathrm{m}^2/\mathrm{s}$, respectively. Unresolved eddies are represented using the skew-flux form of the Gent and McWilliams (GM) parameterization with an eddy thickness diffusivity of 1,000 m^2/s (Griffies, 1998). Convection is represented by an implicit vertical diffusion with diffusivity of 100 m^2/s whenever the stratification is unstable. We use a nonlinear equation of state for the ocean (Jackett and Mcdougall, 1995). All simulations performed in this study are integrated for at least 6,000 years in order to approximately achieve steady states, using the tracer acceleration method (Bryan, 1984). Note that the tracer acceleration method can distort the transient response, but it is not expected to substantially affect the equilibrium solution (Danabasoglu et al., 1996).

The model is forced with the mean climatological seasonal cycle during the last 100 years from each of the PMIP3 simulations. Specifically, we use the PMIP3 monthly-mean surface wind stress vector for the momentum forcing in the MITgcm simulations, and the buoyancy boundary conditions at the sea surface are given by

$$Q_{\mathrm{net}} = -\frac{\rho_0 c_p \delta_s}{t_\theta}(\theta - \theta^*) + Q^*_{\mathrm{net}}, \tag{5.4a}$$

$$\mathcal{S} = -\frac{\delta_s}{t_{\mathrm{salt}}}(S - S^*) + \mathcal{S}^*. \tag{5.4b}$$

Here, the superscript “*” indicates climatological monthly-mean fields from the PMIP3 simulations, θ is sea surface temperature, S is sea surface salinity, t_θ and t_{salt} are the restoring timescales for temperature and salinity, Q_{net} is the net surface heat flux with positive values indicating fluxes that warm the ocean, and $\mathcal{S}$ represents the surface salt flux. The surface salt flux in the PMIP3 simulations is diagnosed as the net freshwater flux from precipitation, evaporation, and sea ice melting and freezing scaled by the reference salinity of 35g/kg. The thickness of the top layer is δ_s=50 m, and the reference sea water density and specific heat capacity are ρ_0=1035 kg/m^3 and $c_p = 3994 \mathrm{J}\,^\circ\mathrm{C}^{-1}\,\mathrm{kg}^{-1}$.

We use the form of boundary conditions in Equation (5.4a) and (5.4b), rather than mixed boundary conditions which have a relaxation boundary condition for temperature and a flux boundary condition for salinity (Stommel, 1961) as have been used in some previous ocean model studies. By varying the restoring timescales (t_θ and t_{salt}), this form of buoyancy boundary conditions allows us to explore the relative importance of the surface density versus the surface buoyancy flux, as described in the next section. Unless otherwise specified, we use relaxation timescales for surface temperature and salinity of t_θ=2 months and t_{salt}=3 months, respectively, which are the same as Huber and Zanna (2017) and similar to the timescale implied by Haney (1971a).

We performed MITgcm simulations with surface forcing fields specified from each of the six PMIP3 simulations in Fig. 5.1. The Eulerian-mean AMOC streamfunction is plotted in Fig. 5.1 for the PMIP3 simulations (left) and for the MITgcm simulations (right). The results in Fig. 5.1 indicate that the MITgcm simulations capture the AMOC depth changes between the PI and LGM climates in the PMIP3 simulations. However, each of the MITgcm simulations can be seen to underestimate the AMOC depth and strength in the corresponding PMIP3 simulation, which is similar to the results of Huber and Zanna (2017, their Figure 2b). This underestimate may be due to differences in the physical representations and parameters in the MITgcm simulations compared with each PMIP3 model, as was discussed for preindustrial and future simulated climates by Huber and Zanna (2017, their Figure 4). For example, we use a GM thickness diffusivity of 1000 m^2/s in order to suppress grid noise at the relatively coarse resolution in MITgcm, and this is about three times larger than the default background value in each of the three PMIP3 models (Danabasoglu et al., 2012; Watanabe et al., 2010; Exarchou et al., 2015). This larger GM thickness diffusivity can weaken and shoal the AMOC due to its effect on the compensation of the wind-driven overturning circulation in the Southern Ocean (Marshall et al., 2017). Additionally, the Nordic Seas overflows, which have been suggested to deepen the AMOC depth in model simulations (Danabasoglu et al., 2010; Nakano and Suginohara, 2002; Marsland et al., 2003), are not represented in MITgcm but are parameterized in each of the three PMIP3

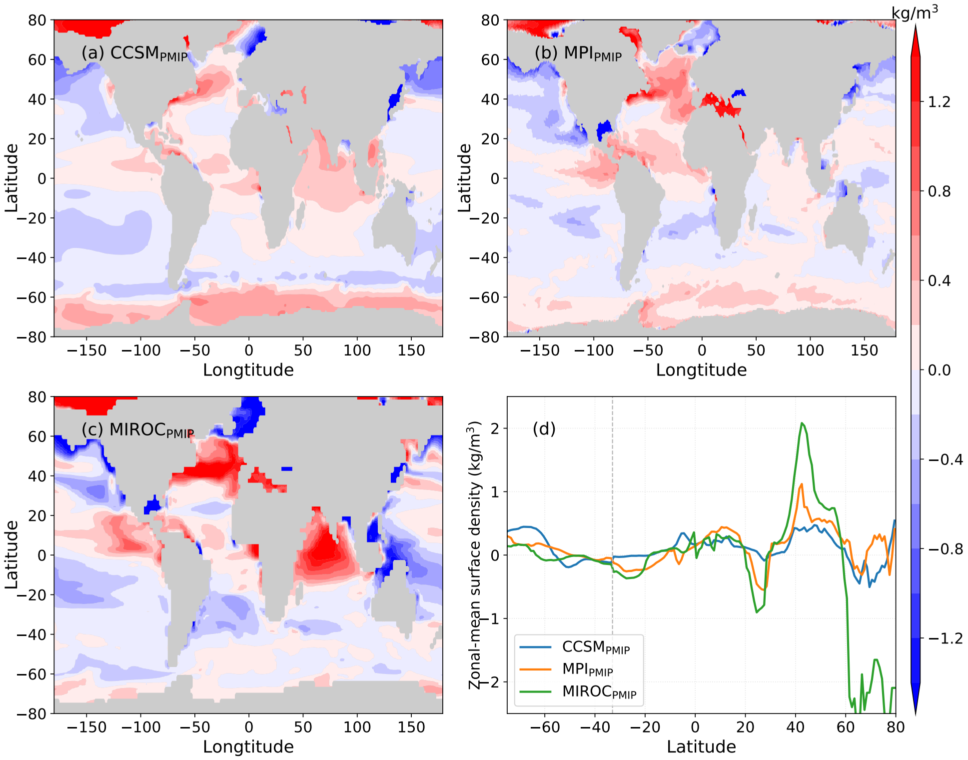

Figure 5.2: (a-c) Difference in the annual-mean surface density between the PMIP3 simulated LGM and the PI climates (LGM minus PI) in CCSM4, MPI-ESM, and MIROC-ESM. In each panel, the global average has been subtracted to highlight the regional distributions. (d) Annual-mean zonal-mean values of the surface density differences. The zonal averages are calculated over the full range of longitudes south of 33°S but only in the Atlantic Ocean north of 33°S, with a gray dashed line indicating 33°S. As in the other panels, the global-mean values have been subtracted from each curve. The negative surface density difference in the Nordic Seas (north of 60°) is associated with an extended sea ice coverage at the LGM that reduces heat loss to the atmosphere; the impacts of the Nordics Seas are discussed in Section 5.5d.

models. This could also contribute to the underestimated depth and strength of the AMOC in the MITgcm simulations. In the following analysis, we will focus on changes in the AMOC depth between the PI and LGM climates, which are better reproduced in the MITgcm simulations than the AMOC depth in each climate.

5.3 Relative importance of surface density compared with surface buoyancy flux

Previous work suggested that diapycnal processes in the upper ocean could diminish the influence of Southern Ocean surface buoyancy forcing on the AMOC depth (Sun et al., 2018). Therefore, in this section, we use the ocean-only MITgcm configuration described in Section 5.2.2 to investigate the possibility that the global surface density distribution is the dominant factor in determining the inter-model spread of the AMOC depth among the PMIP3 models (cf. Nikurashin and Vallis, 2012; Wolfe and Cessi, 2014; Sun and Liu, 2017). Figure 5.2 shows the difference in surface density between the simulated LGM and PI climates in the three PMIP3 models. The surface density difference field in each model tends to be more positive in the subpolar North Atlantic (40°N-60°N) than in the Southern Ocean. This applies most in MIROC-ESM, which simulates a deepening of the AMOC at the LGM, and least in CCSM4, which has a shoaling of the AMOC at the LGM. Indeed, the other PMIP3 models that simulate a deeper AMOC at the LGM also tend to have surface density changes at the LGM in the Atlantic compared to the Southern Ocean that resemble MIROC-ESM (not shown). This suggests the possible importance of this feature of the simulated surface density field for explaining the inter-model differences in AMOC depth among the PMIP3 models.

Here we evaluate the importance of the surface density distribution compared with the surface buoyancy flux for constraining the AMOC depth. We do this by varying the restoring timescales in Equation (5.4). As illustrated in Fig. 5.3 and further discussed in Appendix C, with strong relaxation (small t_θ and t_{salt}), the surface density simulated in MITgcm approximately reproduces the prescribed surface density, but the surface buoyancy flux simulated in MITgcm tends to differ substantially from the PMIP3 simulations (Appendix C.1). With weak relaxation (large t_θ and t_{salt}), on the other hand, the surface buoyancy fluxes approximately match but the surface densities tend to differ substantially between the MITgcm simulations and the PMIP3

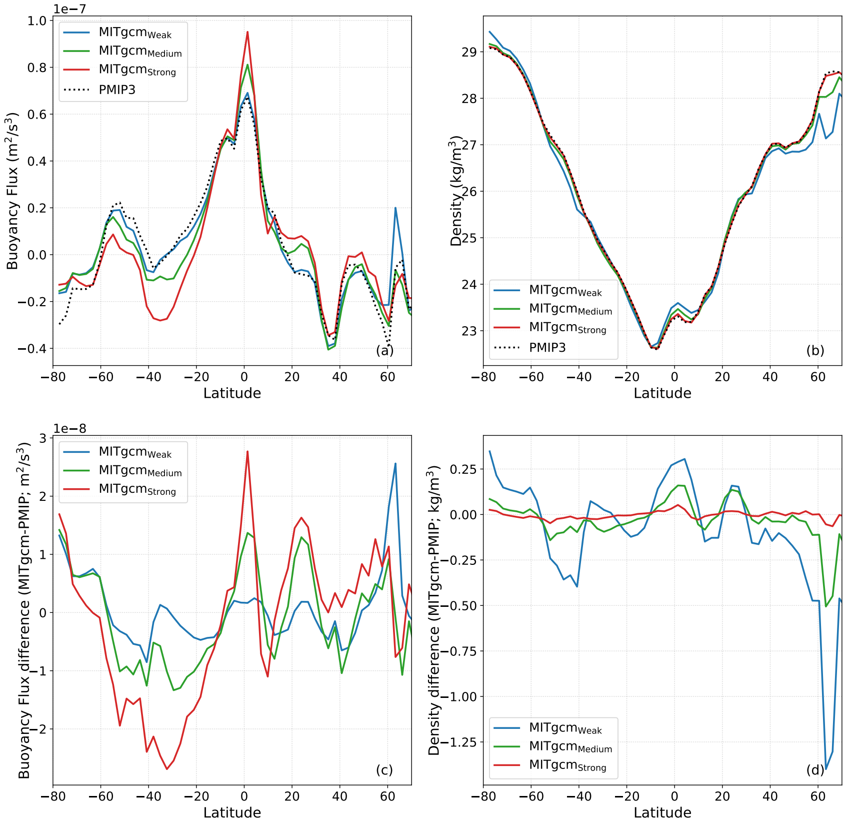

Figure 5.3: Zonal-mean (a) surface buoyancy flux and (b) surface density in the CCSM4 PMIP3 simulation of the LGM climate (dotted lines) and in the MITgcm run with surface forcing drawn from the CCSM4 PMIP3 simulation (solid lines). The differences in the zonal-mean (c) surface buoyancy flux and (d) surface density between the CCSM4 PMIP3 simulation MITgcm runs are also shown. The runs with stronger relaxation tend to more closely reproduce the surface density and less closely reproduce the surface buoyancy flux, as described in the text. Here the surface buoyancy flux is calculated as $F = g/\rho_0(\alpha Q_{\text{net}}/c_p - \rho_0 \beta \mathcal{S})$, where g is gravitational acceleration, α is the thermal expansion coefficient, and β is the haline contraction coefficient

simulations (Appendix C.2).

In addition to the six MITgcm simulations described in Section 5.2.2 above (t_θ=2 months and t_{salt}=3 months: “medium”), here we discuss the results of a set of six simulations with stronger relaxation (t_θ=12 days and t_{salt}=18 days: “strong”) and a set of six simulations with weaker relaxation (t_θ=10 months and t_{salt}=15 months: “weak”).

The MITgcm runs with strong relaxation and the MITgcm runs with medium relaxation largely reproduce the LGM–PI AMOC depth difference in the PMIP3 simulations (Fig. 5.4b),

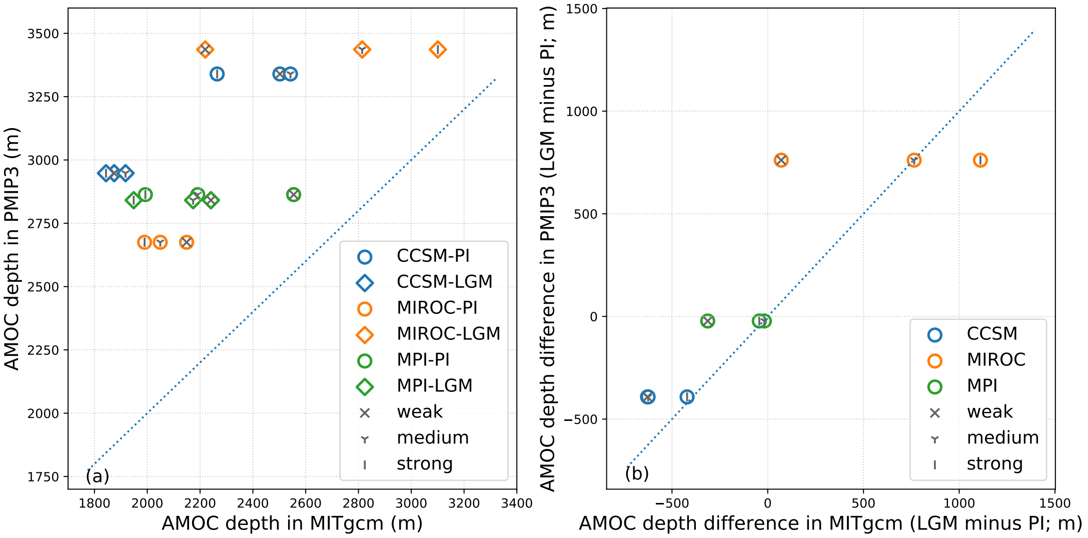

Figure 5.4: Comparison between the PMIP3 simulations and the three sets of MITgcm simulations with varied relaxation timescales in terms of (a) the LGM and PI AMOC depth and (b) the LGM–PI AMOC depth difference. The colors of the circles and diamonds in each panel indicate the PMIP3 simulation that was used for the surface forcing, and the gray symbols indicate the level of relaxation. The blue dotted line in each panel represents equality between the quantities on the vertical and horizontal axes.

although the MITgcm simulations underestimate the AMOC depth in all of the PMIP3 simulations (Fig. 5.4a). The MITgcm runs with weak relaxation underestimate the AMOC deepening at the LGM by 700 m for MIROC-ESM, simulate a shoaling of 300 m at the LGM for MPI-ESM, and overestimate the shoaling at the LGM by 240 m for CCSM. The MITgcm runs with medium relaxation closely reproduce the AMOC depth changes for both MPI-ESM and MIROC-ESM within 50 m, but they overestimate the shoaling for CCSM by 230 m at the LGM. The MITgcm runs with strong relaxation reproduce the AMOC depth changes for CCSM and MPI-ESM within 50 m, but they overestimate the AMOC deepening by 350 m for MIROC-ESM.

Hence the results in Fig. 5.4b show that the simulations with weak relaxation, which most closely reproduce the surface buoyancy flux in the PMIP3 simulations, do a substantially worse job of reproducing the LGM–PI changes in the AMOC depth than the simulations with stronger relaxation, which most closely reproduce the surface density distribution in the PMIP3 simulations. This suggests that the simulated LGM–PI changes in AMOC depth in the PMIP3

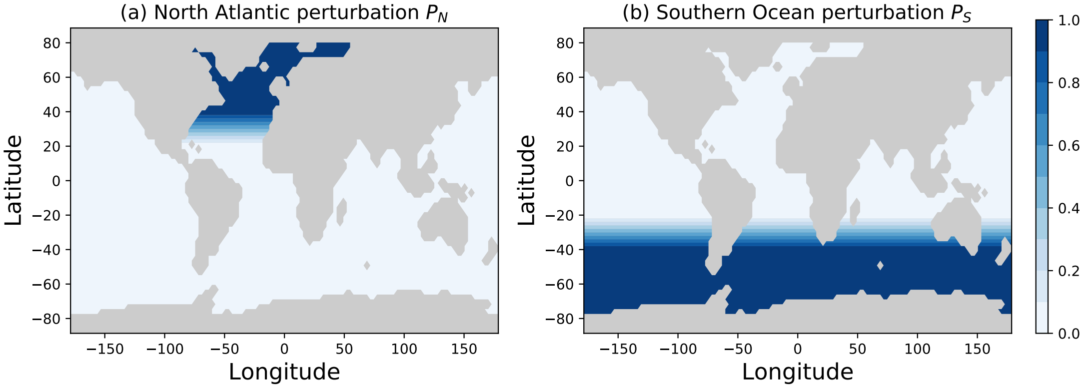

Figure 5.5: Salinity perturbation distributions in (a) the North Atlantic (P_N) and (b) the Southern Ocean (P_S).

simulations is closely connected to the simulated surface density field. This stands in contrast with previous emphases on surface buoyancy flux in controlling the AMOC depth (e.g., Ferrari et al., 2014; Jansen and Nadeau, 2016), which is further discussed in Section 5.5.

5.4 How the surface density constrains the AMOC depth

In this section, we investigate how the surface density field constrains the AMOC depth. We carry out a series of idealized perturbation simulations with MITgcm and then construct a geometric model that relates the AMOC depth to the surface density field in the North Atlantic as well as the Southern Ocean.

5.4.1 Idealized perturbation runs

We carry out a series of simulations with perturbed surface density fields in the North Atlantic and the Southern Ocean, since these are the two regions where the deep ocean primarily ventilates. The MITgcm simulation with the surface forcing derived from the CCSM4 PMIP3 PI run is adopted as the reference simulation, except that in this series of simulations we use a very strong relaxation ($t_\theta = 6$ days and t_{salt}=9 days) such that the simulated surface density closely follows the restoring surface density. We perturb the surface density by adding a salinity perturbation (ΔS^*) to the restoring surface salinity field S^*:

$$\Delta S^* = \Delta S_N^* P_N + \Delta S_S^* P_S, \tag{5.5}$$

where ΔS_N^* and ΔS_S^* are scalar parameters with units of g/kg that control the magnitude of the salinity perturbations, and P_N and P_S are dimensionless fields that represent the geographical distribution of the salinity perturbations. As indicated in Fig. 5.5, the North Atlantic perturbation field (P_N) is 1 to the north of 40°N in the Atlantic Ocean and decays southward to a value of 0 at 20°N, and the Southern Ocean perturbation field (P_S) is 1 to the south of 40°S and decays northward to a value of 0 at 20°S. We use salinity instead of temperature to perturb the surface density because the haline contraction coefficient (β) is relatively constant with respect to varying temperature and salinity. For example, if the temperature varies from -2°C to 10°S and the salinity remains at 35 g/kg at the sea surface, β varies from 7.93×10^{-4} to $7.65\times10^{-4}(\mathrm{g/kg})^{-1}$, whereas the thermal expansion coefficient α varies from 0.4×10^{-4} to 1.67×10^{-4} $^\circ\mathrm{C}^{-1}$. Consequently, a salinity perturbation represents roughly the same surface density perturbation in the North Atlantic as in the Southern Ocean. In the following discussions, we will assume $\beta = 7.8\times10^{-4}(\mathrm{g/kg})^{-1}$ to translate the salinity perturbations to density perturbations.

Four sets of perturbation runs are performed (Table 5.1): North Atlantic, Southern Ocean, Symmetric, and Antisymmetric. The perturbations are uniform in the high latitudes (Fig. 5.5), which ensures that the deep convection occurs at approximately the same locations in the North Atlantic and the Southern Ocean as the salinity perturbations are varied. As a result, changes in the density of NADW and AABW in their source locations follow the surface perturbations in the greater North Atlantic and the Southern Ocean regions, respectively. This is indicated in Fig. 5.6, which shows that changes in the density of the NADW core and AABW are approximately equal to the values of the surface perturbations (Fig. 5.6b).

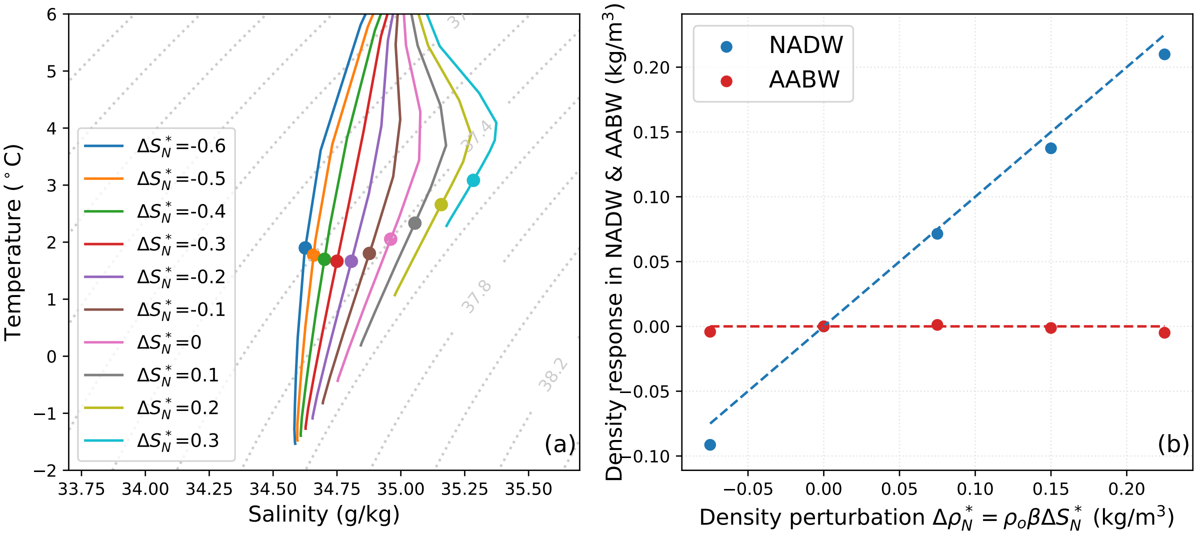

Figure 5.6: (a) Temperature-salinity diagram for the North Atlantic perturbation runs. This diagram is obtained by averaging the time-averaged temperature and salinity fields on constant depth levels between 20°S and 20°N in the Atlantic Ocean. Water masses with temperature higher than 6°C are not shown. The dots represent the isopycnal that separates the two overturning circulation cells in the Atlantic Ocean (defined in Equation (5.8)). Contours of σ_2 are indicated as gray dotted lines. (b) Potential density of the NADW core and AABW in the North Atlantic perturbation runs with $\Delta S_N^* \geq -0.1\,\mathrm{g/kg}$. The NADW core is characterized by a salinity maximum in the temperature-salinity diagram for the deep ocean, and it is defined here as the maximum salinity in the diagram plotted in panel a. The density of AABW is defined as the maximum of the potential density profile averaged between 20°S and 20°N in the Atlantic Ocean. For the runs with $\Delta S_N^* < -0.1\,\mathrm{g/kg}$ that are not included here, the NADW core is too fresh and too shallow, and there is no interior salinity maximum in the temperature-salinity diagram. The blue dashed line in panel b represents equality between the vertical and horizontal plotted quantities, and the red dashed line represents zero density response.

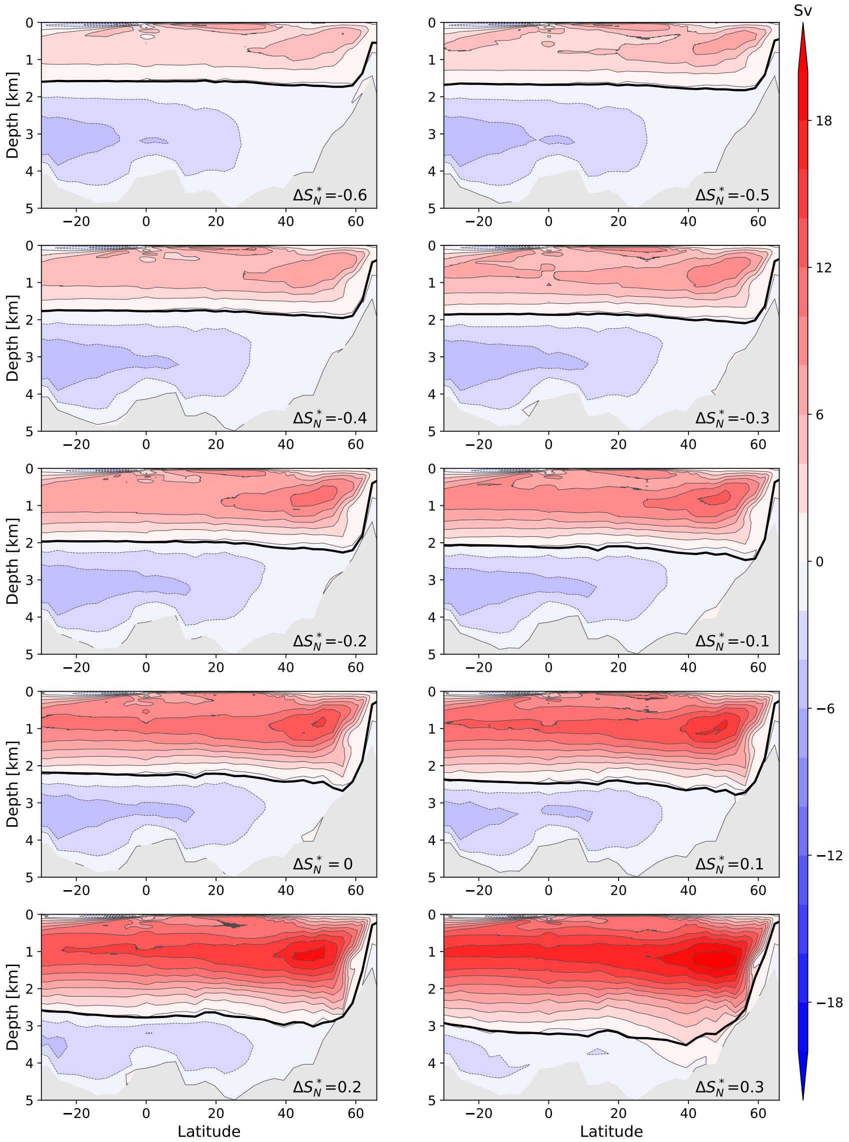

Figure 5.7: The isopycnal overturning circulation streamfunction mapped to depth coordinates in the Atlantic Ocean in each of the North Atlantic perturbation runs (ψ). The value of the salinity perturbation parameter in g/kg is indicated in each panel. The thick black line in each panel represents the isopycnal contour of potential density $\tilde{\rho}$ that separates the two overturning circulation cells in the Atlantic Ocean. Note that the overturning circulation streamfunction in each of the Southern Ocean perturbation runs (not shown) is approximately equivalent to the North Atlantic perturbation run with the opposite perturbation parameter value, e.g., the Southern Ocean perturbation run with $\Delta S_S^* = 0.6$ g/kg has an overturning circulation streamfunction approximately equivalent to the North Atlantic perturbation run with $\Delta S_N^* = -0.6$ g/kg.

Table 5.1: Summary of the four sets of perturbation runs discussed in Section 5.4. The first column indicates the name of the set, the second column indicates the range of values scaling the perturbation to the North Atlantic salinity, and the third column indicates the range of values scaling the perturbation to the Southern Ocean salinity. These represent the full ranges over which the AMOC reaches the Southern Ocean but does not reach the ocean bottom: for $\Delta S_N^* > 0.3\,\mathrm{g/kg}$ in the North Atlantic perturbation runs, $\Delta S_S^* < -0.3\,\mathrm{g/kg}$ in the Southern Ocean perturbation runs, and $\Delta S_N^* > 0.15$ g/kg in the Antisymetric perturbation runs, the AMOC reaches the ocean bottom; and for $\Delta S_N^* < -0.6\,\mathrm{g/kg}$ in the North Atlantic perturbation runs, $\Delta S_S^* > 0.6\,\mathrm{g/kg}$ in the Southern Ocean perturbation runs, and $\Delta S_N^* < -0.3\,\mathrm{g/kg}$ in the Antisymetric perturbation runs, the AMOC does not reach the Southern Ocean.

Perturbation runs	ΔS_N^* (g/kg)	ΔS_S^* (g/kg)
North Atlantic	-0.6to0.3	0
Southern Ocean	0	-0.3to0.6
Symmetric	-0.6to0.3	$\Delta S_S^* = \Delta S_N^*$
Antisymmetric	-0.3to0.1	$\Delta S_S^* = -\Delta S_N^*$

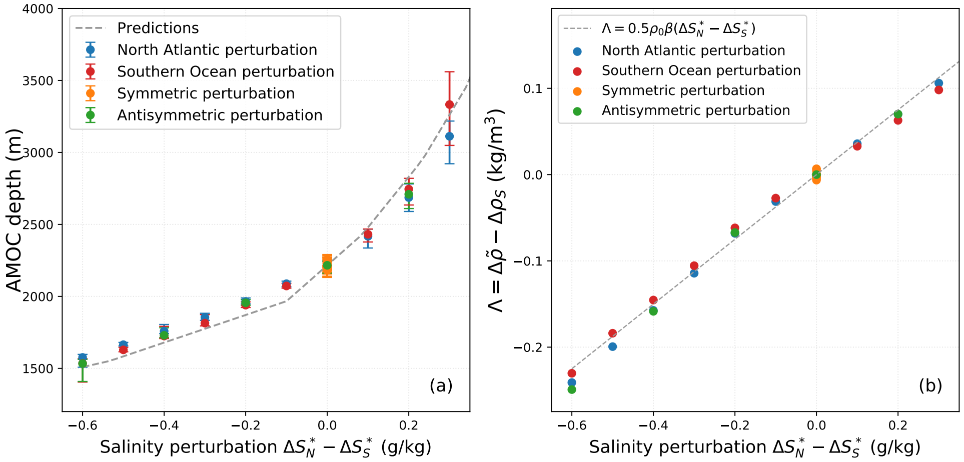

Figure 5.8: (a) The AMOC depth (as defined in Equation (5.9)) in the four sets of perturbation runs. The gray dashed line represents the AMOC depth predicted by Equation (5.18) with $\Lambda = (1/2)\rho_0\beta(\Delta S_N^* - \Delta S_S^*)$. Each error bar represents the depth range among all locations (y) between 30°S and the equator of the zero streamline $(\xi(y))$ in Equation (5.9). (b) The difference in density between the isopycnal, which separates the upper and lower cells, and the Southern Ocean perturbation, $\Delta\tilde{\rho} - \Delta\rho_S$, in the four sets of perturbation runs. The gray dashed line represents the equality $\Lambda \equiv \Delta\tilde{\rho} - \Delta\rho_S = (1/2)\rho_0\beta(\Delta S_N^* - \Delta S_S^*)$. In both panels, all of the Symmetric perturbations runs (orange dots) are clumped in a small part of the plot and overlap each other.

In the analysis of the PMIP3 simulations above, we used the Eulerian-mean overturning circulation streamfunction ($\overline{\psi}$) to represent the overturning circulation because most of the PMIP3 models did not report the eddy bolus velocity. Here, because MITgcm does report this, we instead analyze the isopycnal overturning circulation streamfunction (ψ), which includes contributions from both the mean flow and the parameterized eddies. The isopycnal overturning circulation streamfunction (ψ) provides a more accurate representation of the overturning circulation (e.g., Karsten and Marshall, 2002). It is not substantially different from the Eulerian-mean in the Atlantic basin (except in regions of deep convection) due to the relatively small role played there by eddies, but it differs more substantially in the Southern Ocean where eddies play a larger role (e.g., Marshall and Radko, 2003). We calculate the isopycnal overturning circulation streamfunction on σ_2 coordinates (where σ_2 is the potential density referenced to 2,000 dbar) as

$$\psi(y,\sigma_2) = -\frac{1}{T}\int_0^T \int_{x_w}^{x_e} \int_{z_{\text{bot}}}^0 v_r(x,y,z,t)\mathcal{H}(\sigma_2'(x,y,z,t)-\sigma_2)dz\,dx\,dt, \tag{5.6}$$

where T=100 years is the averaging period, $\mathcal{H}$ is the Heaviside step function, v_r is the total meridional velocity that includes both the eulerian-mean flow and the eddy-bolus contribution due to the parameterized eddies, and σ_2' is the σ_2 field calculated by the model at each location. The isopycnal overturning circulation streamfunction ψ is then mapped to depth coordinates using the mean depth of each isopycnal. Following Nurser and Lee (2004), we define the mean depth of a given isopycnal $\hat{z}(y,\sigma_2)$ implicitly via

$$\int_{x_w}^{x_e} \int_{z_{\text{bot}}}^{\hat{z}(y,\sigma_2)} dx\,dz = \frac{1}{T}\int_0^T \int_{x_w}^{x_e} \int_{z_{\text{bot}}}^0 \mathcal{H}(\sigma_2(x,y,z,t)-\sigma_2')dx\,dz\,dt, \tag{5.7}$$

such that the cross-sectional area below $\hat{z}$ at latitude y is equal to the cross sectional area of fluid denser than σ_2. The resulting streamfunction for each North Atlantic perturbation simulation is plotted in Fig. 5.7.

We define the potential density of the isopycnal that separates the two overturning circulation cells in the Atlantic Ocean ($\tilde{\rho}$) implicitly as

$$\int_{30^\circ\mathrm{S}}^{0} \psi_{\mathrm{atl}}(y,\tilde{\rho})dy = 0. \tag{5.8}$$

This isopycnal represents the water mass boundary between NADW and AABW (dots in Fig. 5.6a).

Next, we define the AMOC depth as the mean depth of the isopycnal contour $\tilde{\rho}$ between 30°S and the equator

$$H = -\frac{1}{L_y}\int_{-L_y}^{0} \hat{z}(y,\tilde{\rho})dy, \tag{5.9}$$

where L_y represents the meridional distance between 30°S and the equator as used above. The AMOC depth defined here (H) is somewhat different from that defined using the Eulerian-mean overturning circulation (D in Equation (5.2)). However, the response of the AMOC depth to surface perturbations is approximately equivalent between the two definitions (not shown).

In response to increasing salinity perturbation in the North Atlantic or decreasing salinity perturbation in the Southern Ocean, the AMOC becomes deeper (Fig. 5.8). These results suggest a symmetry between the North Atlantic and the Southern Ocean perturbation runs:

$$H(\Delta S_N^* = \Delta S, \Delta S_S^* = 0) \approx H(\Delta S_N^* = 0, \Delta S_S^* = -\Delta S), \tag{5.10}$$

where the left-hand side of the expression represents one of the the North Atlantic perturbation runs, the right-hand side of the expression represents one of the Southern Ocean perturbation runs, and ΔS is any value of the salinity perturbation. In the following section, we construct a geometric model to explore the reasons for this symmetry.

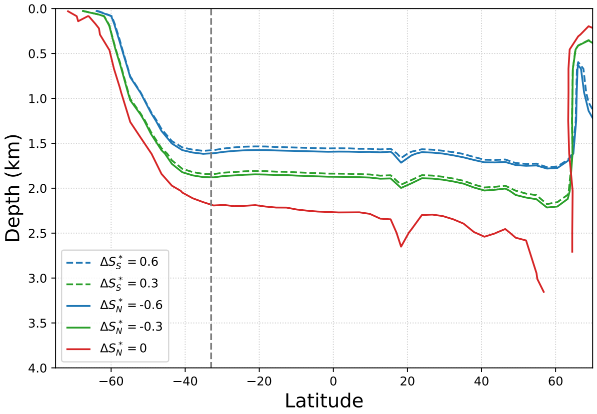

Figure 5.9: Contours of the isopycnal that separates the two overturning circulation cells ($\tilde{\rho}$), with potential density zonally averaged in the Atlantic Ocean (north of 33°S) and in the Atlantic sector of the Southern Ocean (south of 33°S) in the Southern Ocean perturbation runs (dashed) and the North Atlantic perturbation runs (solid). Only a subset of the runs are included for clarity. The red line represents the control run, which is equivalent to the North Atlantic perturbation run $\Delta S_N^* = 0$ and the Southern Ocean perturbation runs $\Delta S_S^* = 0$. The gray dashed line represents 33°S.

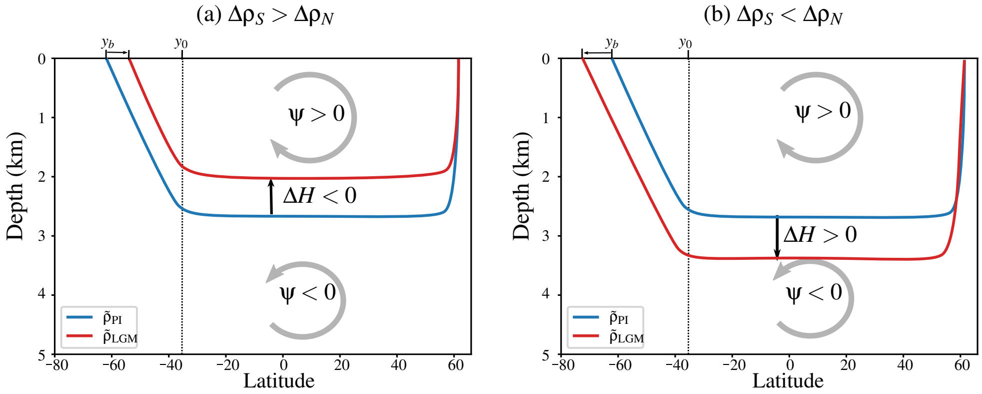

Figure 5.10: Schematic diagrams illustrating the proposed connections between the AMOC depth differences between the LGM and PI climates and the surface density changes in the North Atlantic and the Southern Ocean. (a) If the surface density change from the PI to the LGM in the Southern Ocean ($\Delta\rho_S$) is larger than in the North Atlantic ($\Delta\rho_N$), then the isopycnal boundary ($\tilde{\rho}$) that separates the two overturning circulation cells will outcrop in the Southern Ocean at a latitudinal location that is more equatorward by $\Delta H/s$ (Equation (5.14)). Assuming the isopycnal slope remains approximately constant in the Southern Ocean, this means that the AMOC will be shallower by ΔH (Equations (5.30) and (5.18)) at the LGM. (b) If $\Delta\rho_S$ is smaller than $\Delta\rho_N$, then $\tilde{\rho}$ will outcrop in the Southern Ocean at a location that is more poleward by $\Delta H/s$ and the AMOC will be deeper by ΔH at the LGM.

5.4.2 Geometric model

The depth of the isopycnal $\tilde{\rho}$ that separates the two overturning circulation cells at the northern boundary of the Southern Ocean is related to its outcropping latitudinal location (y_b) and mean slope (s) in the Southern Ocean as

$$H = (y_b - y_0)\, s, \tag{5.11}$$

where y_0 represents the latitudinal location of the northern boundary of Southern Ocean.

For the control run ($\Delta S_N^* = \Delta S_S^* = 0$), the isopycnal boundary satisfies

$$\rho_S^c(y_b^c) = \tilde{\rho}^c, \tag{5.12}$$

where ρ_S^c is the zonal-mean surface density in the Southern Ocean as a function of latitudinal location in the control run, and y_b^c is the outcropping location of the isopycnal boundary $\tilde{\rho}^c$ in the Southern Ocean.

For a given perturbation run, the zonal-mean Southern Ocean surface density changes by approximately $\Delta\rho_S \equiv = \rho_0 \beta \Delta S_S^*$ compared with the control run, and hence the isopycnal boundary outcrops at the location y_b^p that satisfies

$$\rho_S^c(y_b^p) + \Delta\rho_S = \tilde{\rho}^p. \tag{5.13}$$

We define the shift in the potential density of the isopycnal boundary in the perturbation run compared with the control run as $\Delta\tilde{\rho} \equiv \tilde{\rho}^p - \tilde{\rho}^c$.

Assuming that the isopycnal slope stays approximately constant under perturbations to the Southern Ocean surface density (e.g., Böning et al., 2008; Gent and Danabasoglu, 2011) and combining Equations (5.11), (5.12), and (5.13), the difference in the AMOC depth between a given perturbation run and the control run can be written as

$$\begin{aligned}\Delta H &= s\left(y_b^p - y_b^c\right)\\ &\approx \frac{s\Lambda}{\left(d\rho_S^c/dy\right)|_{y_b^c}},\end{aligned} \tag{5.14}$$

where a Taylor expansion of ρ_S^c at y^c is used to obtain the last approximation and

$$\Lambda \equiv \Delta\tilde{\rho} - \Delta\rho_S \tag{5.15}$$

represents the change in the density of the isopycnal boundary ($\Delta\tilde{\rho}$) minus the surface density perturbation in the Southern Ocean ($\Delta\rho_S$). Equation (5.14) states that the change in AMOC depth in the perturbation runs is determined by the specified changes in the Southern Ocean surface density ($\Delta\rho_S$), the surface meridional density gradient in the Southern Ocean in the control run ($d\rho_S^c/dy$), the approximately invariant slope of the isopycnal $\tilde{\rho}$ in the Southern Ocean (s), and the simulated changes in the density of the isopycnal boundary ($\Delta\tilde{\rho}$). This applies because Λ, along with the meridional surface density gradient, determines the shift in the outcropping latitude of $\tilde{\rho}$, which is associated with changes in the AMOC depth through Equation (5.11). The approximate invariance of the isopycnal slope is indicated in Fig. 5.9 and is discussed in Section 5.5c.

Under the approximation that the AMOC depth remains constant in the tropical Atlantic Ocean, if the Southern Ocean surface density does not change then the change in the AMOC depth will be

$$\Delta H = \mathcal{D}(\tilde{\rho}^c + \Delta\tilde{\rho}) - \mathcal{D}(\tilde{\rho}^c), \tag{5.16}$$

where $\mathcal{D}$ is the inverse function of the vertical density profile in the control run $\rho^c(z)$, $\mathcal{D}(\rho^c) = z$, which is obtained by averaging the vertical density profile in the Atlantic Ocean between 30°S and the equator. In runs with perturbed Southern Ocean surface density, if we approximate that the isopycnal slope in the Southern Ocean is constant such that the surface density in the Southern

Ocean ($\rho_S^c(y)$) maps to the deep ocean along isopycnals via

$$\rho^c(z) = \rho_S^c(y_0 - zs), \tag{5.17}$$

then we can generalize the expression for the change in AMOC depth to be

$$\Delta H = \mathcal{D}(\tilde{\rho}^c + \Lambda) - \mathcal{D}(\tilde{\rho}^c). \tag{5.18}$$

The changes in $\tilde{\rho}$ in the perturbation runs compared with the control runs are expected to be expressible in terms of the specified surface density perturbations in the Southern Ocean and the North Atlantic, i.e.,

$$\Delta\tilde{\rho} = \Pi(\Delta\rho_S, \Delta\rho_N), \tag{5.19}$$

where $\Delta\rho_N \equiv \rho_0 \beta \Delta S_N^*$ represents the surface density perturbation in the North Atlantic. Note that this expression also implies that the change in $\tilde{\rho}$ compared with the Southern Ocean surface density perturbation, Λ, is also a function of the surface density perturbations in the Southern Ocean and the North Atlantic. Next, we investigate the form of the function $\Pi(\Delta\rho_S, \Delta\rho_N)$ in the perturbation runs.

Symmetric perturbation runs

In the Symmetric perturbation runs, the surface densities in the North Atlantic and the Southern Ocean are perturbed by the same amount, $\Delta\rho_S = \Delta\rho_N$. Because the deep ocean ventilates only in the North Atlantic and the Southern Ocean, this is expected to shift the density uniformly by $\Delta\rho_N$ without any dynamical consequence, with the possible exception of regions close to the ocean surface in the low-latitude Atlantic and in the Indo-Pacific where mixing with the surface water may have some impacts. Therefore, we expect that the changes in $\tilde{\rho}$ will be approximately

$$\Delta\tilde{\rho} = \Pi(\Delta\rho_S, \Delta\rho_S) = \Delta\rho_S, \tag{5.20}$$

and therefore

$$\Lambda \equiv \Delta\tilde{\rho} - \Delta\rho_S = 0. \tag{5.21}$$

This suggests no changes in the AMOC depth based on Equation (5.14), i.e.,

$$\Delta H = 0. \tag{5.22}$$

Figure 5.8 (orange dots) indicates that this is indeed approximately the case in the Symmetric perturbation runs.

North Atlantic perturbation runs

In the North Atlantic perturbation runs, $\Delta\rho_S = 0$ and hence $\Delta\tilde{\rho}$ is a function only of $\Delta\rho_N$. This can be written as

$$\Delta\tilde{\rho} = \Pi(0, \Delta\rho_N) = \Pi_1(\Delta\rho_N), \tag{5.23}$$

and changes in $\tilde{\rho}$ compared with the specified Southern Ocean surface density changes similarly satisfy

$$\Lambda = \Pi_1(\Delta\rho_N), \tag{5.24}$$

where Π_1 is an unknown function that satisfies $\Pi_1(0) = 0$.

Southern Ocean perturbation runs

In the Southern Ocean perturbation runs, $\Delta\rho_N = 0$ and hence $\Delta\tilde{\rho}$ is a function only of $\Delta\rho_S$. The forcing of a given Southern Ocean perturbation run with $(\Delta\rho_N = 0, \Delta\rho_S = \Delta\rho)$ is equivalent to the sum of a North Atlantic perturbation run with $(\Delta\rho_N = -\Delta\rho, \Delta\rho_S = 0)$ and a Symmetrical perturbation run with $(\Delta\rho_N = \Delta\rho_S = \Delta\rho)$. Approximating that the Symmetric perturbation modifies the density field with no consequence for the AMOC depth, as above, implies that the change in the density of the isopycnal that separates the two cells in this Southern Ocean perturbation run will be

$$\Delta\tilde{\rho} = \Pi(\Delta\rho_S, 0) = \Pi_1(-\Delta\rho_S) + \Delta\rho_S. \tag{5.25}$$

This implies that the change in $\tilde{\rho}$ relative to the Southern Ocean surface density perturbation satisfies

$$\Lambda = \Pi_1(-\Delta\rho_S). \tag{5.26}$$

in the Southern Ocean perturbation runs. Figure 5.8 (compare red and blue dots) indicates that this is approximately the case.

Antisymmetric perturbation runs

Similar to the Southern Ocean perturbation runs, a given Antisymmetric perturbation run with $(\Delta\rho_N = \Delta\rho, \Delta\rho_S = -\Delta\rho)$ can be approximately decomposed into the sum of a North Atlantic perturbation run with $(\Delta\rho_N = 2\Delta\rho, \Delta\rho_S = 0)$ and a Symmetric perturbation run with $(\Delta\rho_N = -\Delta\rho, \Delta\rho_S = -\Delta\rho)$. Therefore, we expect the change in the density of the isopycnal $\Delta\tilde{\rho}$ in the Antisymmetric perturbation runs to be approximately

$$\Delta\tilde{\rho} = \Pi_1(2\Delta\rho_N) - \Delta\rho_N, \tag{5.27}$$

with the change in $\tilde{\rho}$ relative to the Southern Ocean surface density perturbation being

$$\Lambda = \Pi_1(2\Delta\rho_N). \tag{5.28}$$

This can be seen to be approximately the case in the Antisymmetric perturbation runs by comparing the green and blue dots in Fig. 5.8.

Synthesis

Taken together, this suggests that Λ can be expressed as

$$\Lambda = \Pi_1(\Delta\rho_N - \Delta\rho_S). \tag{5.29}$$

In other words, this implies that the change in the potential density $\tilde{\rho}$ of the isopycnal boundary relative to the Southern Ocean surface density perturbation is a function of the difference between the surface density perturbation in the North Atlantic and the surface density perturbation in the Southern Ocean. This is shown to be the case in the simulations in Fig. 5.8b.

Therefore, the difference in the AMOC depth between a given perturbation run and the control run can be written from Equation (5.14) as

$$\Delta H \approx \frac{s}{\left(d\rho_S^c/dy\right)|_{y^c}} \Pi_1(\Delta\rho_N - \Delta\rho_S). \tag{5.30}$$

This indicates that changes in the AMOC depth can be attributed to the differences between the perturbations to the North Atlantic surface density and the Southern Ocean surface density, which is shown to be the case in the simulations in Fig. 5.8a.

We use the results of the perturbation simulations to determine the actual form of Π_1. The scatter plot of Λ vs $\Delta\rho_N - \Delta\rho_S$ in Fig. 5.8b suggests that

$$\Lambda \approx \frac{1}{2}\left(\Delta\rho_N - \Delta\rho_S\right). \tag{5.31}$$

Combined with Equation (5.29), this implies

$$\Pi_1(\Delta\rho) = \frac{1}{2}\Delta\rho \tag{5.32}$$

for a given density perturbation $\Delta\rho$. Combined with the definition $\Lambda \equiv \Delta\tilde{\rho} - \Delta\rho_S$, this implies

$$\Delta\tilde{\rho} = \frac{1}{2}\left(\Delta\rho_N + \Delta\rho_S\right). \tag{5.33}$$

This indicates that the change in the isopycnal boundary density ($\tilde{\rho}$) is given by the average between the change in surface density in the North Atlantic and in the Southern Ocean. This result is in contrast with previous theoretical studies that have assumed $\tilde{\rho}$ to be the maximum surface density in the North Atlantic, and hence that $\Delta\tilde{\rho}$ depends solely on North Atlantic surface conditions (e.g., Nikurashin and Vallis, 2012).

Combining Equations (5.18) and (5.33), along with the density profile ($\rho^c(z)$) in the Atlantic Ocean for the control run, we can predict the variations in the AMOC depth in response to surface density perturbations. This prediction of the geometric model (gray dashed lin in Fig. 5.8a) is shown to be consistent with the perturbation runs.

This implies that the changes in the AMOC depth simulated in the PMIP3 models can be approximately understood in terms of how the variations in the surface density field compare between the North Atlantic and the Southern Ocean. As illustrated in the schematic Fig. 5.10, if the surface density change from the PI to the LGM climate in the Southern Ocean ($\Delta\rho_S$) is larger than the North Atlantic ($\Delta\rho_N$), the isopycnal boundary ($\tilde{\rho}$) that separates the two overturning circulation cells will outcrop in the Southern Ocean at a lower latitude and thus the AMOC will be shallower at the LGM by ΔH (Equations (5.14), (5.30), and (5.18)). On the other hand, if $\Delta\rho_S$ is smaller than $\Delta\rho_N$, then $\tilde{\rho}$ will outcrop in the Southern Ocean at a higher latitude and thus the AMOC will be deeper at the LGM.

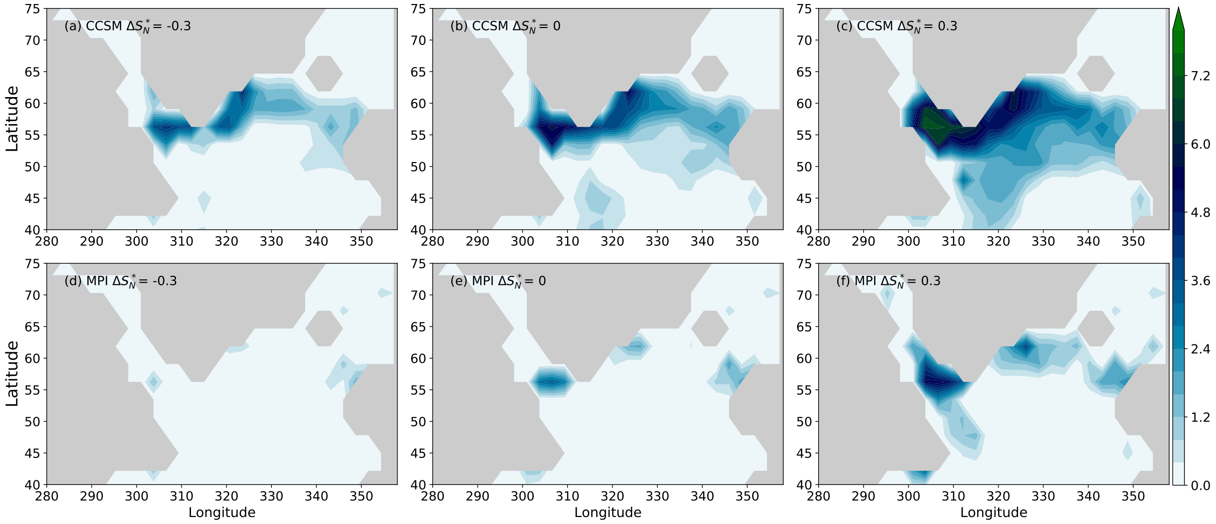

Figure 5.11: (a-c) Annual-mean frequency of convective adjustments in the North Atlantic perturbation runs described in Section 5.4a above, which use the CCSM4 PMIP3 PI run as the reference simulation. (d-f) As in the upper panel, except using the MPI-ESM PMIP3 PI run as the reference simulation. This frequency indicates the annual-mean column-integrated number of convective instability events in the MITgcm representation of mixing from static instability, and hence it indicates the horizontal locations of deepwater formation.

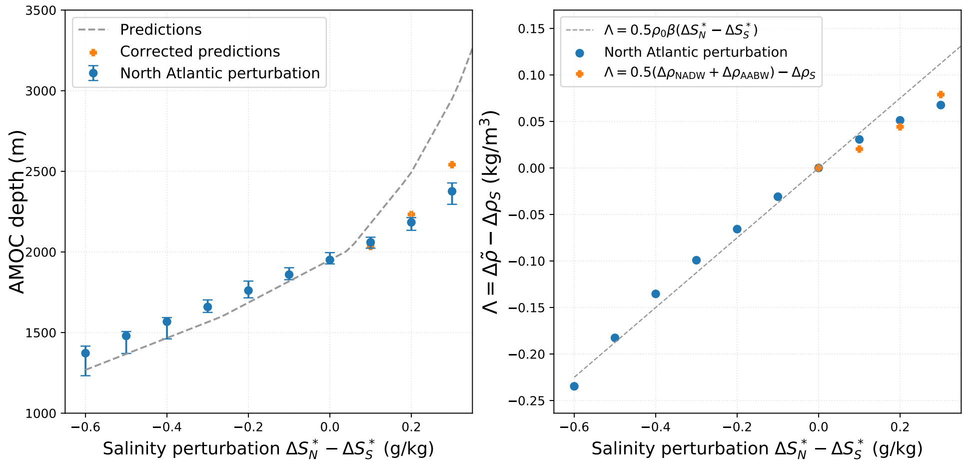

Figure 5.12: As in Fig. 5.8 but using the MPI-ESM PMIP3 PI run as the reference simulation rather than the CCSM4 PMIP3 PI run, and considering only North Atlantic perturbation runs. Here corrected predictions for $\Delta S_N^* - \Delta S_S^* \geq 0$ are made using Equation (5.34) (orange "+"), which draw on the density of NADW and AABW diagnosed from the simulations.

5.5 Discussion

5.5.1 What sets the density of the isopycnal boundary between the two overturning circulation cells ($\tilde{\rho}$)?

In the MITgcm runs described in Section 5.4a above that have surface forcing from the CCSM4 PMIP3 PI simulation plus a specified perturbation, the convection sites in the North Atlantic do not move substantially in response to the surface density perturbations. This is shown in Fig. 5.11a-c. Here we test the extent to which this depends on the reference simulation by carrying out another set of MITgcm runs that have surface forcing from the MPI-ESM PMIP3 PI simulation plus the same specified perturbation fields as in the North Atlantic perturbation runs described in Section 5.4a. We find that in these runs, the convection sites shift from the eastern North Atlantic to the south of Greenland in response to the perturbations as ΔS_N^* increases, especially when $\Delta S_N^* > 0$. This is shown in Fig. 5.11d-f. Whether the convection sites shift in response to a uniform high-latitude perturbation field is expected to depend on factors including the deep ocean stratification in the reference simulation and the strength of the surface perturbation. Due to the shifted North Atlantic convection sites in the perturbed MPI-ESM simulations, the change in the NADW density is expected to differ from $\Delta\rho_N$. Indeed, we find that when $\Delta S_N^* \geq 0$, the simulated value of $\Lambda \equiv \Delta\tilde{\rho} - \Delta\rho_S$ is lower than the value predicted by Equation (5.31), and the simulated change in AMOC depth is smaller than the change predicted by Equation (5.18), as shown in Fig. 5.12.

These results suggest that changes in the isopycnal boundary density $\Delta\tilde{\rho}$ follow

$$\Delta\tilde{\rho} = \frac{1}{2}(\Delta\rho_{\mathrm{NADW}} + \Delta\rho_{\mathrm{AABW}}), \tag{5.34}$$

rather than (5.33), with ρ_{NADW} and ρ_{AABW} the density of NADW and AABW diagnosed from the simulation. With $\Lambda \equiv \Delta\tilde{\rho} - \Delta\rho_S$ and Equation (5.18), this change in the expression for $\Delta\tilde{\rho}$

revises the prediction for the changes in the AMOC depth. This is indicated in Fig. 5.12a as the "corrected predictions". It should be emphasized, however, that unlike the predictions that draw on Equation (5.33), these corrected predictions that draw on Equation (5.34) require the density of NADW and AABW to be diagnosed from the GCM simulation results.

Note that if the the Southern Ocean surface density profile changes by the same amount as ρ_{AABW}, then Equation (5.31) is replaced by

$$\Lambda = \frac{1}{2}(\Delta\rho_{\mathrm{NADW}} - \Delta\rho_{\mathrm{AABW}}). \tag{5.35}$$

In this case, the geometric model presented here (Equation (5.14)) suggests that the AMOC depth will be correlated with the density difference between the NADW and AABW, as has been found in some climate model studies (e.g., Galbraith and de Lavergne, 2018).

The results shown in Fig. 5.12 imply that the isopycnal boundary that separates the two overturning circulation cells is determined by the densities of the NADW and AABW water masses, and that under a given perturbation, the change in the density of the isopycnal boundary between the two cells is approximately equal to the average of the changes in the densities of the two water masses (Equation (5.34)). This is expected to result from the vertical mixing between the two water masses in the Atlantic Ocean (see Fig. 5.6a). Given that the isopycnal boundary moves between 1,500m and 3,000m (Figs. 5.8a and 5.12a), the relationship in Equation (5.34) appears to be relatively insensitive to the value of the diapycnal diffusivity (see Figs. 5.8b and 5.12b), which varies in this configuration of MITgcm from $3\times10^{-5}\mathrm{m}^2/\mathrm{s}$ at the surface to $1.3\times10^{-4}\mathrm{m}^2/\mathrm{s}$ below 2,000m depth.

The finding here that the density of the isopycnal separating the two cells ($\tilde{\rho}$) is related to both North Atlantic and Southern Ocean conditions (Equation (5.34)) is in contrast with previous theoretical studies that explicitly or implicitly assume that $\tilde{\rho}$ is the maximum surface density in the North Atlantic (e.g., Nikurashin and Vallis, 2012; Ferrari et al., 2014; Thompson et al., 2016), which would imply $\Delta\tilde{\rho} = \Delta\rho_{\mathrm{NADW}}$. This previous assumption was based on a simplified viewpoint of the overturning circulation which ignored the temporal and longitudinal variations of the density fields, in which case only isopycnals above $\tilde{\rho}$ could outcrop in both the Southern Ocean and the North Atlantic (e.g., Nikurashin and Vallis, 2012). In a more realistic setup, water masses below $\tilde{\rho}$ can also outcrop in the North Atlantic even though their isopycnals do not outcrop in the time-mean zonally-integrated overturning circulation streamfunction.

5.5.2 Comparison with previous studies

Previous studies have differed on whether the surface of the North Atlantic or the Southern Ocean dictates the depth of the boundary between the upper and lower ocean circulation cell. The present study suggests that it is both.

The geometric model developed in Section 5.4 relies on the spatial uniformity of the high-latitude surface density differences in the idealized perturbation runs. This can be applied to other GCM simulations by approximating that the NADW potential density (ρ_{NADW}) is equal to the maximum zonal-mean wintertime surface density in the subpolar North Atlantic (ρ_{m1}) and the AABW potential density (ρ_{AABW}) is equal to the maximum zonal-mean surface density in the Southern Ocean (ρ_{m2}), $\rho_{\mathrm{NADW}} = \rho_{m1}$ and $\rho_{\mathrm{AABW}} = \rho_{m2}$. Under these approximations, the geometric model (5.34) predicts that

$$\tilde{\rho}' \equiv \frac{1}{2}\left(\rho_{m1} + \rho_{m2}\right) \tag{5.36}$$

will be the potential density of the isopycnal separating the two overturning circulation cells, $\tilde{\rho}' \approx \tilde{\rho}$. According to the geometric model, the shift in the outcropping latitude of the isopycnal $\tilde{\rho}'$ in the Southern Ocean will explain the change in the AMOC depth changes between simulations of the PI and LGM climates. Indeed, in Fig. 5.13e we show that the shift in the outcropping latitude of the predicted isopycnal boundary ($\tilde{\rho}'$) is approximately consistent with the shift in the outcropping latitude of the actual simulated isopycnal boundary ($\tilde{\rho}$) in the perturbation runs, and in Fig 5.13f we show that it explains over 90% of the variance in the simulated AMOC depth differences between the PI and LGM climates among the PMIP3 simulations and the MITgcm ocean-only runs described in Section 5.3.

Next, we compare the framework developed in the present study with the implications of two previous influential theoretical studies that each proposed a separate way in which the Southern Ocean surface buoyancy forcing alone controls the AMOC depth.

Ferrari et al. (2014)

Ferrari et al. (2014) approximate the circulation in the Southern Ocean to be adiabatic, and based on this and several other assumptions they propose that the AMOC depth is determined by the transition latitude (y_t) where the Southern Ocean surface buoyancy flux changes sign. Here we test this idea using the simulations described in the present study.

In response to surface perturbations in the North Atlantic perturbation runs, the overturning circulation varies in the Southern Ocean, and there are changes in the Southern Ocean surface buoyancy forcing associated with this due to the surface temperature and salinity being relaxed toward specified values. As a result, the transition latitude (y_t) of the Southern Ocean surface buoyancy flux shifts in response to surface perturbations (Fig. 5.13a).

Ferrari et al. (2014) posited that the isopycnal boundary $\tilde{\rho}$ outcrops at y_t. However, we find that the shift in the transitional latitude y_t differs substantially from the outcropping latitude of the isopycnal boundary $\tilde{\rho}$ (Fig. 5.13a). We find that the AMOC depth is not substantially related to y_t, with the shift in the transition latitude (y_t) explaining only 16% of the variance in simulated AMOC depth differences between the PI and LGM climates among the PMIP3 simulations and the MITgcm ocean-only runs described in Section 5.3. Previous work (Sun et al., 2018) used CESM ocean-only simulations to attribute the discrepancy between the Southern Ocean surface buoyancy flux and the AMOC depth to the diapycnal processes in the Southern Ocean, which were neglected in Ferrari et al. (2014).

Jansen and Nadeau (2016)

Jansen and Nadeau (2016) used idealized model simulations with a single basin that represents the Atlantic ocean to suggest that the rate of surface buoyancy loss across the surface of the Southern Ocean determines the AMOC depth. This was based on the approximation that the total surface buoyancy loss in the Southern Ocean is balanced by the interior buoyancy gain through diapycnal mixing associated with the lower overturning circulation cell outside the Southern Ocean, which can be written as

$$\mathcal{B} = \int\int \kappa \frac{\partial}{\partial z} b(x,y,H')dxdy. \tag{5.37}$$

Here $\mathcal{B}$ is buoyancy loss integrated over all ocean locations to the south of 60°S and hence is expected to include most of the negative buoyancy flux associated with deep water formation in the Southern Ocean, $b(x,y,z)$ represents three dimensional buoyancy field ($b = -g(\rho - \rho_0)/\rho_0$), and the integration on the right-hand-side is performed along the upper boundary of the lower circulation cell ($z = H'(x,y)$) across all locations to the north of 30°S. We examined the extent to which $\mathcal{B}$ can be used to predict the mean value of H' in the simulation results.

In the North Atlantic perturbation runs as well as the Southern Ocean perturbation runs, the deep ocean stratification remains approximately the same as in the control run because the perturbations in the Southern Ocean are spatially uniform. Thus, H' can be predicted from the vertical profile of the diagnosed integrated interior diapycnal buoyancy flux simulated in the Atlantic and Indo-Pacific basins. We find that the depth (H') where the buoyancy balance in Equation (5.37) applies is substantially shallower in the perturbation simulations than the actual simulated AMOC depth (Fig. 5.13c). This difference may be due to diabatic processes in the Southern Ocean that are neglected in Equation (5.37). In the MITgcm simulations, the integrated interior diapycnal fluxes, which support the interior diapycnal transformation of water masses, increase upward (cf. Munk, 1966). Therefore, neglecting diabatic processes in the Southern Ocean, especially in the surface mixed layer (cf. Marshall et al., 1999), may be expected to result in an overestimatation of the interior buoyancy gain and an underestimation of the AMOC depth based on Equation (5.37).

Hence the difference between H' and the actual AMOC depth is expected to depend on the amount of diapycnal mixing in the Southern Ocean, which is a function of the density stratification. In the perturbation runs, which all have approximately the same deep ocean stratification, this difference is fairly uniform (Fig. 5.13c) such that changes in the AMOC depth between simulations are approximately consistent with changes in H'. However, the deep ocean stratification varies among the PMIP3 simulations and the MITgcm ocean-only runs described in Section 5.3. Consequently, the difference between H' and the simulated AMOC depth is not uniform in these runs. Consistent with this, we find that changes in the surface buoyancy forcing in the Southern Ocean have only limited ability to explain the changes in the AMOC depth among the simulations plotted in Fig. 5.13d (correlation of $r^2 = 0.46$).

5.5.3 Isopycnal slope

Varations of the isopycnal slope in response to surface perturbations in simulations that use a single-basin model with a flat bottom (e.g., Wolfe and Cessi, 2014) tend to be larger than in the MITgcm simulations presented here. In these single-basin models, the contributions to the Southern Ocean overturning circulation due to standing eddies are minimal (e.g., Wolfe and Cessi, 2014, their Fig. 13), and the isopycnal slope can be connected to the Southern Ocean overturning circulation through residual-mean theory using (Marshall and Radko, 2003)

$$\psi = \frac{\tau_x L_x}{\rho_0 f} + K_{\mathrm{GM}} s L_x, \tag{5.38}$$

where τ_x represents the zonally-averaged zonal wind stress forcing, L_x is the length of a latitude circle in the Southern Ocean, K_{GM} is the GM thickness diffusivity, and f is the Coriolis parameter. Note that $K_{\mathrm{GM}} s L_x$ is a representation of the transient eddies. Based on this relationship, the isopycnal slope in the North Atlantic perturbation runs would be expected to become smaller in order to balance the more positive Southern Ocean overturning circulation streamfunction (Fig. 5.14).

However, the MITgcm simulations in this study have a more realistic setup with two basins and a non-flat bottom, and in these simulations standing eddies can contribute a substantial component to the Southern Ocean overturning circulation (e.g., Tréguier et al., 2007; Ballarotta et al., 2013). Therefore, changes in the Southern Ocean overturning circulation can be balanced by an enhancement of the standing eddy contributions, which are not represented in Equation (5.38), thereby allowing the isopycnal slope to stay approximately constant.

Additionally, the Southern Ocean overturning circulation streamfunction associated with the isopycnal $\tilde{\rho}$ is approximately constant in the North Atlantic perturbation runs, especially for $\Delta S_N^* < 0.3$ (Fig. 5.14b). This approximately constant streamfunction associated with $\tilde{\rho}$ reflects a similar contribution from the Indo-Pacific Ocean among the idealized perturbation runs, which in turn is due to the approximately constant deep ocean stratificaiton in the Indo-Pacific basin (Equation (5.17)). This, together with the standing eddies, contributes to the approximately constant slope of the isopycnal contour $\tilde{\rho}$ in the idealized perturbation runs (Fig. 5.9.

5.5.4 Nordic Seas

In the MITgcm simulations of the present study, NADW is formed exclusively in the subpolar North Atlantic. This is consistent with previous climate model studies that have emphasized the impact of the subpolar North Atlantic on the AMOC (e.g., Yeager and Danabasoglu, 2014). However, recent observations suggest that the southward branch of the AMOC originates mainly from the Nordic Sea overflows, rather than from deep convection in the subpolar North Atlantic

(Lozier et al., 2019).

At the LGM, sea ice in the Northern Hemisphere has been suggested to have covered the Nordic Seas, thereby reducing the heat loss from the ocean to the atmosphere in these regions (e.g., Brady et al., 2013, their Fig. 10). This may have caused a decrease in surface density at the LGM, which may plausibly have contributed to shoaling of the AMOC. The lack of representing of such processes is a caveat of the present study.

5.6 Summary

Paleoclimate proxy data suggest that the AMOC was approximately 1,000 m shallower at the LGM compared with the current climate (e.g., Lund et al., 2011). Some previous studies have connected this change to variations in surface buoyancy forcing in the Southern Ocean (Ferrari et al., 2014; Jansen and Nadeau, 2016), and others have alternatively connected it to surface conditions in the North Atlantic (e.g., Muglia and Schmittner, 2015; Oka et al., 2012). A concerted effort to simulate the LGM climate in comprehensive models (PMIP3) has yielded widely varied results for the LGM–PI difference in AMOC depth, with the majority of models simulating a deeper and stronger AMOC at the LGM (e.g., Muglia and Schmittner, 2015). The causes for this inter-model spread and relatedly for the discrepancy between the model simulations and proxy reconstructions have remained unresolved.

The present study examines the simulated surface density field and AMOC depth in the PMIP3 simulations of the PI and LGM climates. Based on the findings presented here, we suggest that the changes in the AMOC depth are directly connected to changes in the surface density fields in the North Atlantic and the Southern Ocean. We demonstrate this using simulations with an ocean-only model with varying restoring strengths in the surface forcing.

Next, using a series of ocean-only model simulations that have idealized perturbations to the surface salinity field, in concert with a geometric model of the overturning circulation, we propose a way to quantify the connection between the AMOC depth and the simulated surface density field in both the North Atlantic and the Southern Ocean(Equations (5.14) and (5.35)). The resulting theory predicts AMOC depth changes between different simulated climates based on the change in the densities of NADW and AABW waters as well as the surface density distribution and isopycnal slope in the Southern Ocean.

Hence the viewpoint proposed in this study allows a two-step process for identifying the AMOC depth. First, a potential density representing the average between NADW and AABW is selected. Next, assuming that the isopycnal of this density has a constant slope in the Southern Ocean and is horizontal elsewhere, the depth of this isopycnal outside the Southern Ocean is identified as the AMOC depth using the isopycnal slope and its outcropping latitude in the Southern Ocean. This method is shown to provide an accurate estimate of the change in AMOC depth between the LGM and PI simulations in a range of different models and surface forcing fields. The viewpoint presented here sheds light on how changes in surface forcing in both the North Atlantic and the Southern Ocean influence the AMOC depth changes between two climate states.

There are a number of caveats that should accompany these results. This study focuses on models, which offer an incomplete picture of the real world. Furthermore, the coarse resolution ocean-only simulations do not resolve eddies, which have been suggested to be important for the response of the Southern Ocean circulation to surface perturbations (e.g., Munday et al., 2013). The model also does not resolve coastal processes in the North Atlantic and the Southern Ocean, which have been suggested to be important for the formation of NADW and AABW (e.g., Snow et al., 2016).

In conclusion, the results in this study highlight the close connection of the simulated surface density in both the North Atlantic and the Southern Ocean to the depth of the AMOC. This implies that any process that affects the density of NADW, the density of the AABW, or the Southern Ocean surface density distribution should be expected to influence the AMOC depth.

Such processes may include surface buoyancy forcing, wind stress forcing, and mixed layer processes in both high-latitude and low-latitude regions.

Acknowledgments

Without implying their endorsement, we thank Paola Cessi, Lynne Talley, Shang-ping Xie, and Andrew Thompson for helpful discussions. This work was supported by National Science Foundation grant OPP-1643445.

This chapter, in full, is draft in preparation for submission to the Journal of Climate as, "What sets the depth of the Atlantic Meridional Overturning Circulation?", by S. Sun, I. Eisenman, L. Zanna, and A. L. Stewart. The dissertation author was the primary investigator and author of this paper.

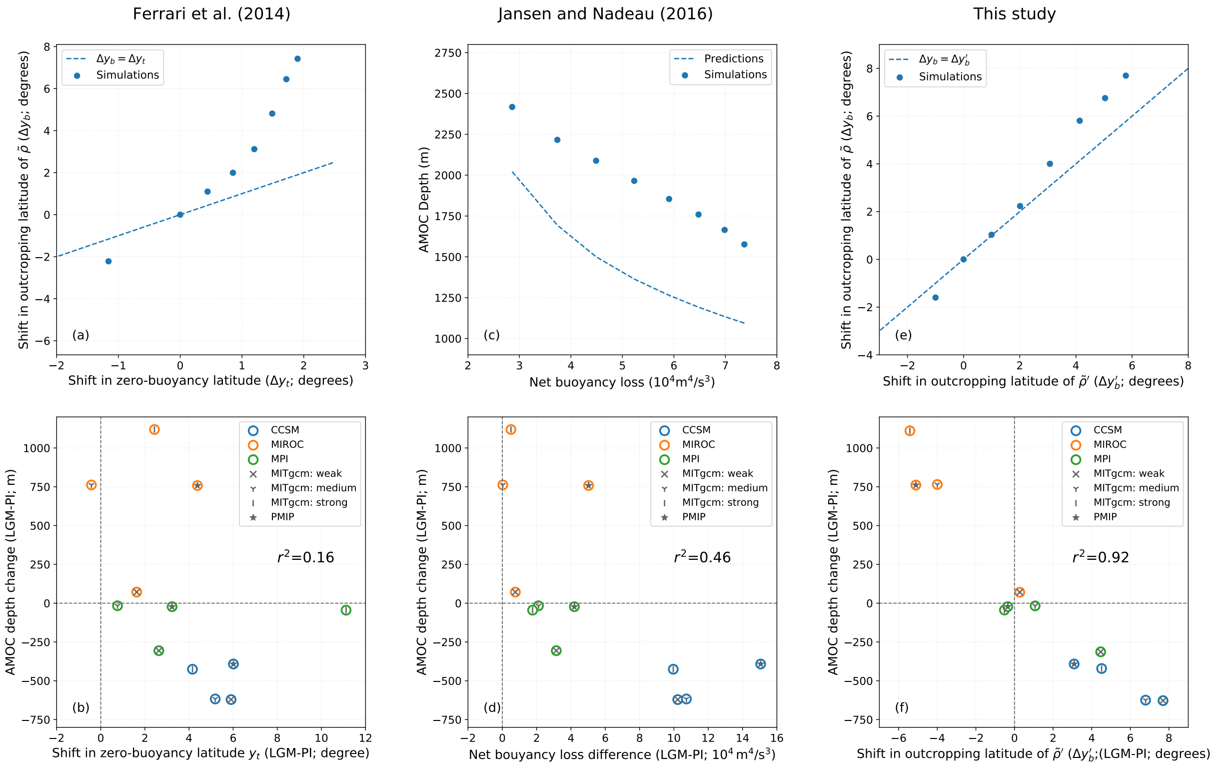

Figure 5.13: (a) Shift in the outcropping latitude of $\tilde{\rho}$ (y_b) versus the shift in transition latitude (y_t) of the zonal-mean surface buoyancy flux in the Southern Ocean. The circles represent the simulation results from the North Atlantic perturbation runs, and the dashed line represents the prediction of the conceptual model in Ferrari et al. (2014). (b) Change in the AMOC depth between the simulated PI and LGM climates versus the shift in the transition latitude (y_t) of the zonal-mean surface buoyancy flux in the Southern Ocean. Results from the PMIP3 simulations and the MITgcm ocean-only runs described in Section 5.3 are plotted. (c) AMOC depth versus the net surface buoyancy loss in southern high latitudes, which is computed by integrating across all ocean locations to the south of 60°S, similar to Marzocchi and Jansen (2017). The circles represent the simulation results from the North Atlantic perturbation runs, and the dashed line represents the AMOC depth predicted from the buoyancy balance as in Marzocchi and Jansen (2017), which is expressed in Equation (5.37) of the main text. (d) As in panel b, but with the change in net surface buoyancy loss to the south of 60°S between the simulated PI and LGM climates plotted on the horizontal axis. (e) The shift in the outcropping latitude of the isopycnal boundary $\tilde{\rho}$ versus the shift in the outcropping latitude of the isopycnal $\tilde{\rho}'$, which is defined in Equation (5.36). The circles represent the simulation results from the North Atlantic perturbation runs, and the dashed line represents the prediction based on this study, which implies equality between the two plotted quantities. Shifts in both quantities are calculated as differences compared with the reference simulation of the perturbation runs ($\Delta S_N^* = 0$). (f) As in panel b, but with the shift in the outcropping latitude of the isopycnal $\tilde{\rho}'$ between the simulated PI and LGM climates plotted on the horizontal axis. In the lower row (panels a, c, e), only the eight North Atlantic perturbation runs with $\Delta S_N^* \leq 0.1$ g/kg are plotted because the outcropping latitude y_b defined using the zonal-mean surface density reaches the Antarctic continent in the other runs. Correlation coefficients between the plotted quantities are included in the lower row.

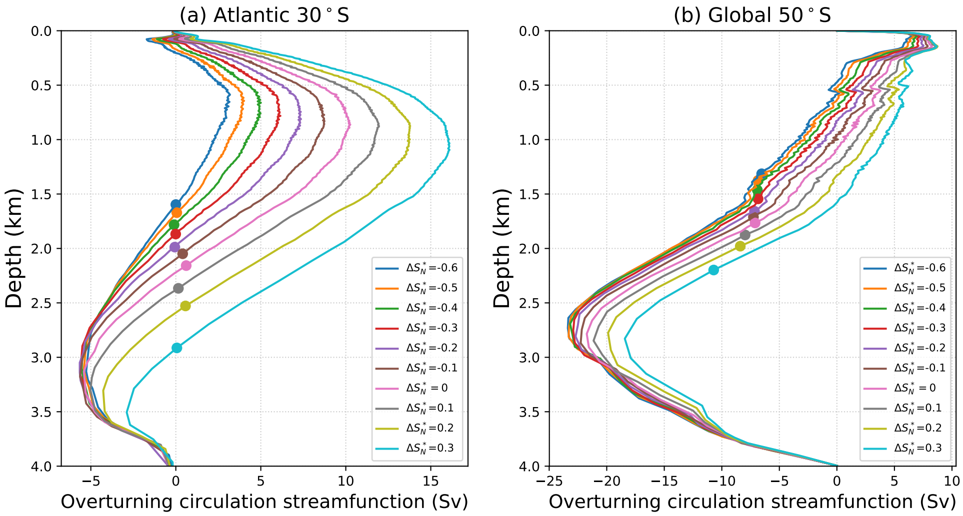

Figure 5.14: The isopycnal overturning circulation streamfunction in the North Atlantic perturbation runs at (a) 30°S in the Atlantic basin and (b) 50°S in the Southern Ocean. The overturning circulation streamfunction in the Southern Ocean is calculated according to Equation (5.6) with the zonal integral expanded to include all longitudes around the globe. The dots represent the depth of the $\tilde{\rho}$ isopycnal. Note that the dots in panel b do not closely correspond with the depth where the streamfunction is zero because the depth of the $\tilde{\rho}$ isopycnal is defined as the average between 30°S and the equator in the Atlantic Ocean.

Chapter 6

How important is the Southern Ocean for the Atlantic Meridional Overturning Circulation variability?

6.1 Introduction

In Chapter 2-5, we have focused our discussions on the equilibrium solution of the global ocean overturning circulation. However, the ocean is never in steady state due to the long response time scales of deep ocean (e.g., Zhang et al., 2013). Indeed, previous studies have suggested that the Atlantic Meridional Overturning Circulation (AMOC) could vary over broad time scales, ranging from months to thousands of years (e.g., Zhao and Johns, 2014; Sigman et al., 2010). These variability associated with the AMOC may have substantial consequences for the climate by modifying the meridional oceanic heat transport and sea surface temperature. For example, changes in the AMOC and the associated heat convergence have been suggested to play an essential role in driving the decadal variability of upper ocean heat content in the subpolar North Atlantic (e.g., Zhang and Zhang, 2015).

In an idealized one-basin setup for the ocean (e.g., Chapter 4), the North Atlantic Deep Water (NADW) exiting the Atlantic must upwell in the Southern Ocean, even if the global ocean overturning circulation is not in steady state. This implies that the strength of the AMOC at the southern boundary (30°S) of the Atlantic Ocean is equal to the Southern Ocean overturning circulation and can be expressed as

$$\psi = -\frac{\tau L_x}{\rho_0 f} + K_{\mathrm{GM}} s L_x, \tag{6.1}$$

based on the residual-mean theory of the overturning circulation (see Chapter 4). Here, ψ represents the AMOC streamfunction, τ refers to the zonal-mean wind stress, ρ_0 is the reference density of seawater, f is the Coriolis parameter, K_{GM} represents the eddy thickness diffusivity, s is the isopycnal slope, and L_x represents the width of the ocean. All these parameters are evaluated at 30°S.

This suggests a stronger AMOC if the Southern Ocean surface wind stress forcing is strengthened (e.g., Toggweiler and Samuels, 1995), although eddies in the Southern Ocean could act to partially compensate this effect (e.g., Abernathey et al., 2011; Bishop et al., 2016). However, this idea contradicts the current climate model simulations, which robustly predict the AMOC to decline in the 21st century mainly due to warming in the North Atlantic (Gregory et al., 2005), despite that a stronger westerly is consistently simulated in these models (Yin, 2005). This contradiction appears to suggest an overestimated link between the Southern Ocean and the AMOC changes.

On decadal and multidecadal time scales, the AMOC strength variability has been linked to processes in the subpolar North Atlantic (e.g., Buckley and Marshall, 2016). Using a coupled ice-ocean model, Yeager and Danabasoglu (2014) showed that the multidecadal variability of AMOC could be mostly attributed to variations in surface buoyancy forcing in the Labrador Sea. On mcuh longer time scales (e.g., $>$1000 years), on the other hand, the Southern Ocean has been

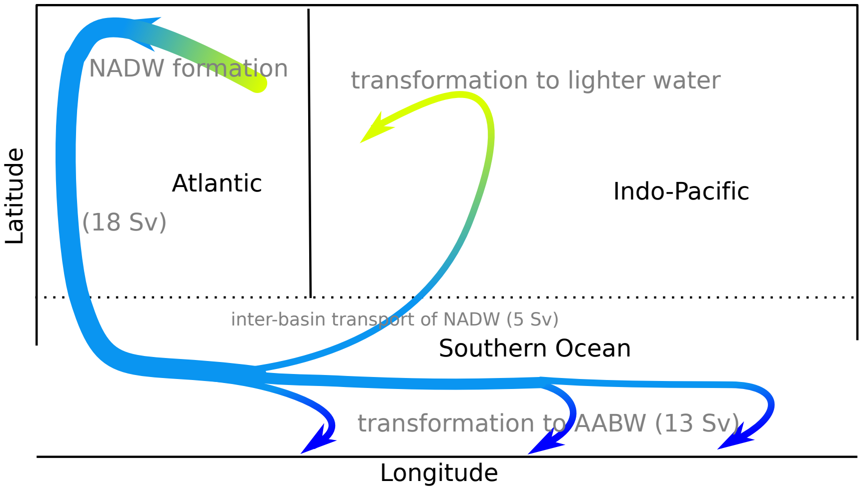

Figure 6.1: A schematic of the NADW pathways based on Talley (2013). In the Southern Ocean, a major part of NADW flows approximately along isopycnals and outcrop close to Antarctica (e.g., Tamsitt et al., 2017), where it is transformed to AABW. Changes in colors along the pathways indicate water mass transformation, and the density of water mass increases from warm to cold colors.

emphasized to play a significant role in the AMOC variability (e.g., Ferrari et al., 2014; Watson et al., 2015; Thompson et al., 2019). For example, using an idealized box model, Thompson et al. (2019) related the Southern Ocean surface forcing to the millenial variability of the AMOC and the North Atlantic surface temperature during the last glacial period. These studies together suggest an increasing importance of the Southern Ocean processes on the AMOC variability from short to long time scales.

In this study, we will explore the importance of the Southern Ocean to the AMOC variability and show that this importance depends on the time scales associated with the AMOC variability. We will highlight the importance of the inter-basin overturning circulation from the Atlantic to the Indo-Pacific basins (Figure 6.1) in balancing the AMOC variability.

6.2 Global ocean overturning circulation in the warming climate

Climate models consistently predict a weakening of the AMOC in the 21^{st} century in response to CO_2 forcing (Cheng et al., 2013). This weakening of the AMOC appears to contradict the strengthening of the Southern Hemisphere westerly wind in the warming climate (e.g., Yin, 2005), which shall drive a stronger upwelling in the Southern Ocean (e.g., Toggweiler and Samuels, 1995). In order to reoncile this contradiction, here we will analyze the transient response of the global ocean overturning circulation to increasing CO_2 forcing in a fully-coupled climate model. We will look at the existing simulations from both the CESM Large Ensemble ("LENS") (Kay et al., 2015) and the CCSM4 Abrupt CO_2 quadrupling ("4xCO2") experiments, which is part of phase 5 of the Coupled Model Intercomparison Project (CMIP5) (Taylor et al., 2012). Note that CCSM4 is a subset of CESM1, i.e., "LENS" and "4xCO2" largely share the same code.

The model reports the residual-mean overturning circulation streamfunction in both "LENS" and "4xCO2", which is defined as

$$\psi_r(y,z) = -\frac{1}{T}\int_0^T \int_{x_w}^{x_e} \int_{z_{\text{bot}}}^{z} \big(v(x,y,z,t) + v'(x,y,z,t)\big)\, dz\, dx\, dt. \tag{6.2}$$

Here, x is longitudinal displacement, y is latitudinal displacement, z is depth with z_{bot} the depth of ocean bottom, T is the average period, $\bar{v}$ is meridional velocity, v' is the parameterized eddy bolus velocity, and ψ_r is the residual-mean overturning circulation streamfunction. For the global ocean, the integration is along the latitude circle; for the Atlantic or Indo-Pacific ocean, the integration is from the western boundary (x_w) to the eastern boundary (x_e). The residual-mean overturning circulation streamfunction ψ_r is an approximation to the isopycnal overturning

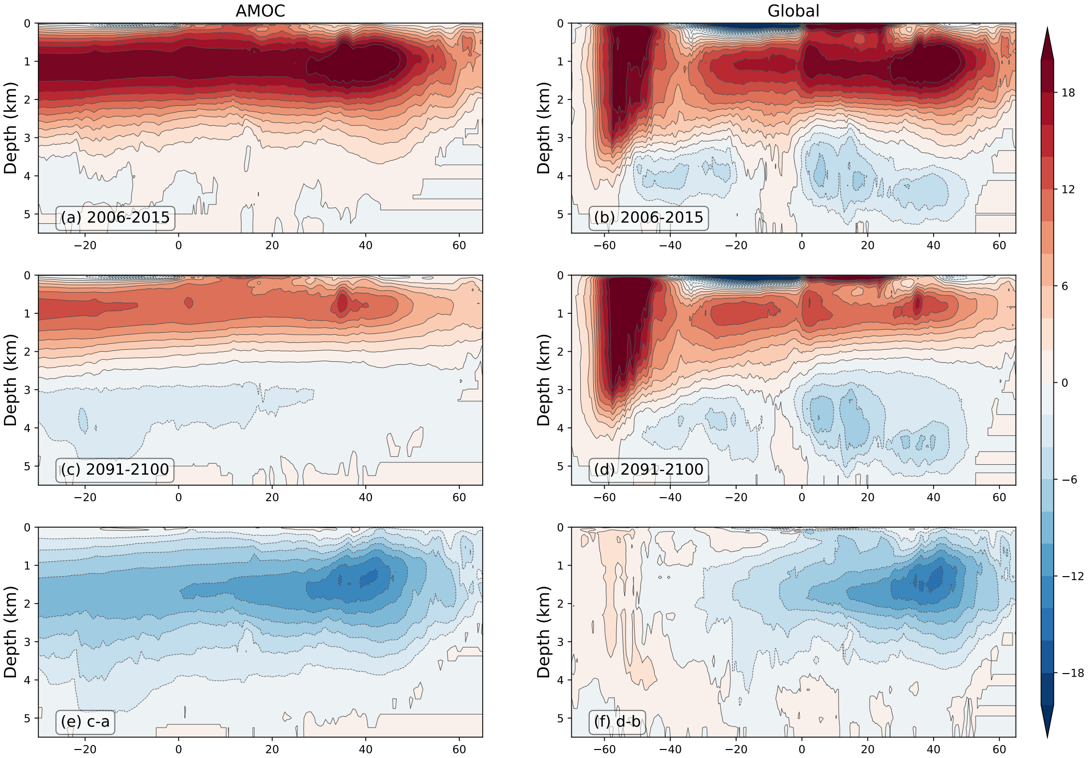

Figure 6.2: Ensemble-mean residual-mean overturning circulation streamfunction of the Atlantic (left) and Global (right) oceans in the CESM LENS. The top two panels are averaged between 2006-2015, the middle two panels are averaged between 2091-2100, and the bottom two panels are the changes from 2006-2015 to 2091-2100. Because the standing eddies are not accounted in Equation (6.2), the wind driven "Deacon cell" is still present in the Southern Ocean.

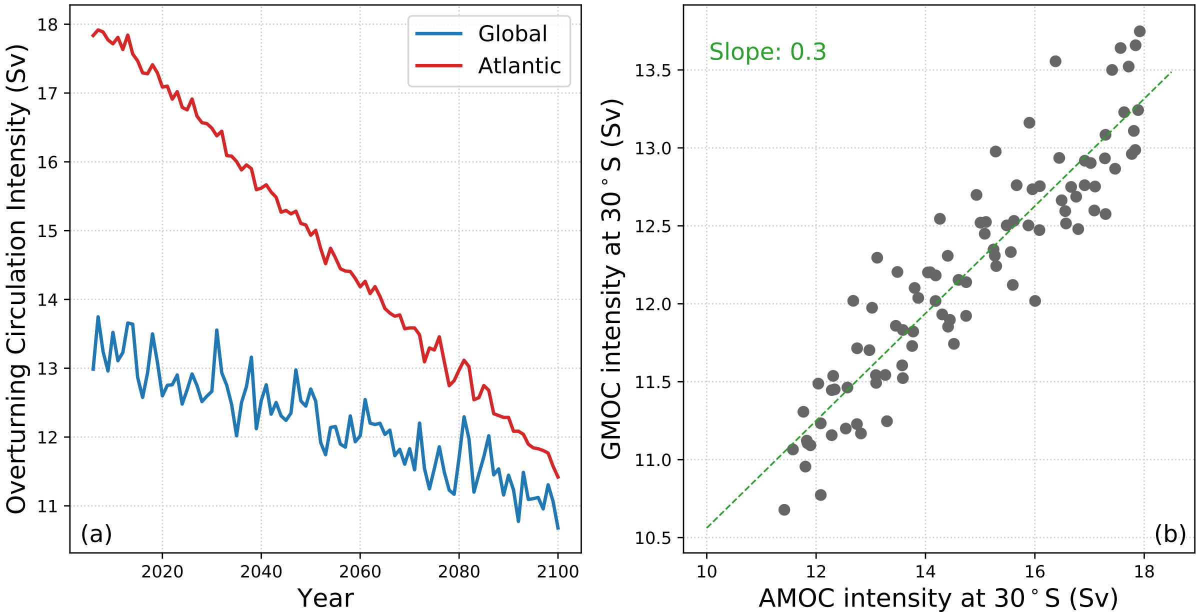

Figure 6.3: (a) Ensemble-mean variations of the AMOC and GMOC strength at 30°S in the 21^{st} century, simulated by the "LENS". (b) Scatter plot of the GMOC strength vs the AMOC strength. The green line represents a linearly fitted straight line

circulation streamfunction (ψ), which is usually calculated in isopycnal coordinate

$$\psi(y,b) = -\frac{1}{T}\int_0^T \int_{x_w}^{x_e} \int_{z_{\text{bot}}}^0 \left(v(x,y,z,t) + v'(x,y,z,t)\right) \mathcal{H}\left(b - b'(x,y,z,t)\right) dz dx dt, \tag{6.3}$$

and can be remapped back to depth coordinate using the mean isopycnal depth (Nurser and Lee, 2004). In the above equation, $\mathcal{H}$ represents the Heaviside equation, b is buoyancy that is linearly related to density as $b = -g(\rho - \rho_0)/\rho_0$, and b' is the buoyancy field. The isopycnal overturning circulation is a more accurate description of the overturning circulation that is responsible for buoyancy redistribution (cf. Marshall and Radko, 2003). Except for regions where strong currents exist (e.g., Southern Ocean), the residual-mean overturning circulation streamfunction ψ_r is a good approximate to the isopycnal overturning circulation streamfunction ψ (Ballarotta et al., 2013).

We present the CESM LENS ensemble-mean residual-mean overturning circulation

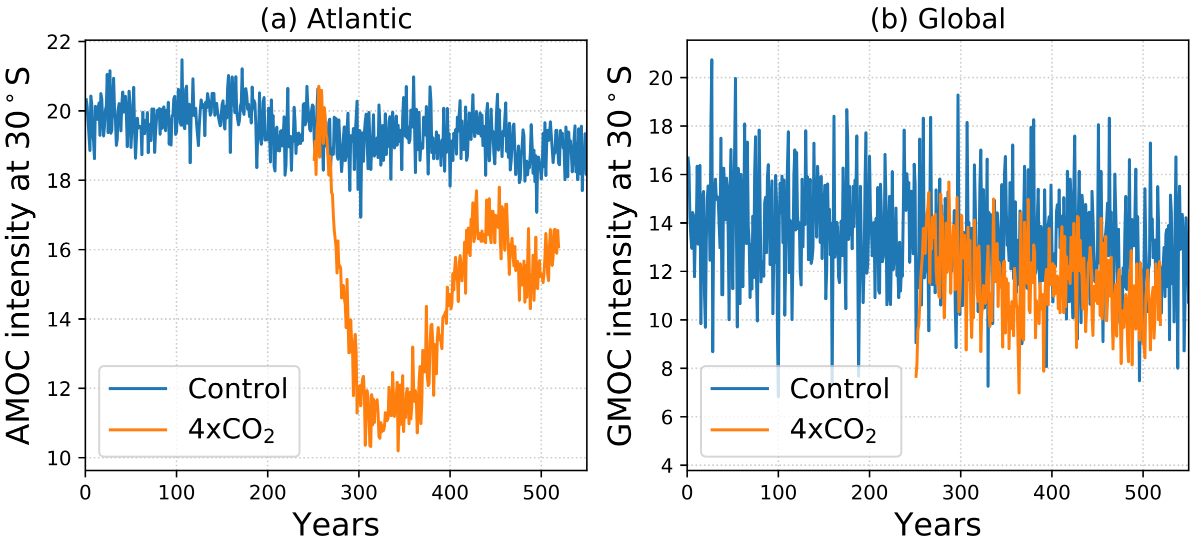

Figure 6.4: Variations of the AMOC (a) and GMOC (b) strength at 30°S in the "4xCO2" experiments. The "Control" run refers to the pre-industrial run by CCSM4 as part of the CMIP5. The "4xCO2" experiments start from year 251 of the "Control" run.

streamfunction averaged in 2006-2015 and 2091-2100 in Figure 6.2. In response to the continued warming, the AMOC is substantially weaker at the end of the 21st century (left panels in Figure 6.2). This weakening of the AMOC stands in contrast with what happens to the global-integrated overturning circulation (GMOC hereafter) in the Southern Hemisphere (right panels in Figure 6.2), where only minimal changes are observed. The changes in the Southern Hemisphere GMOC are largely consistent with the stronger westerly wind in the warming climate, which drives stronger upwelling in the Southern Ocean (Toggweiler and Samuels, 1995).

We quantify the strength of the AMOC and GMOC using their respective maximum residual-mean streamfunction at 30°S (Figure 6.3). The latitude 30°S is outside of the Southern Ocean and the GMOC streanfunction evaluated here is not substantially affected by the missing standing eddies in Equation (6.2). Therefore, the GMOC at 30°S shall largely reflect the strength of the isopycnal overturning circulation in the Southern Ocean.

Contrary to what we expect from a single-basin model, the AMOC variations differ substantially from the Southern Ocean. In the climate simulations for the 21st century, the GMOC weakens by only 30% of the AMOC changes at 30°S (Figure 6.3). Similar features are also observed in the “4xCO2” experiments (Figure 6.4): the AMOC changes substantially in response to the abrupt CO_2 forcing, but the GMOC is barely different from the run without the abrupt CO_2 forcing.

By definition, the GMOC is a combination of the overturning circulation in the Atlantic and Indo-Pacific basins. Therefore, the different response between the GMOC and AMOC suggests an important role of the Indo-Pacific overturning circulation (PMOC) in the AMOC variability: changes in the PMOC could compensate the AMOC variations such that the GMOC stays largely unchanged. In the next section, we will run an ocean-only model to see how this compensation happens and how this compensation depends on the time scales of the AMOC variability.

6.3 Dependence of the inter-basin compensation on variability timescales

In this section, we will carry out a number of experiments using an ocean-only model, which is configured in an idealized two-basin setup. We will discuss the response of the global ocean overturning circulation to perturbations that vary on a range of time scales.

6.3.1 Model setup

We use the Massachusetts Institution of Technology General Circulation Model (MITgcm; Marshall et al., 1997) to integrate the hydrostatic primitive equations. The domain is a spherical sector that spans 144° in latitude (72°S-72°N) and 180° in longitude (Figure 6.5). The geometrical configuration has two idealized basins that are joined by a reentrant channel. The reentrant chanel is an idealized representation of the Southern Ocean and spans from 72°S to 44°S. The wider

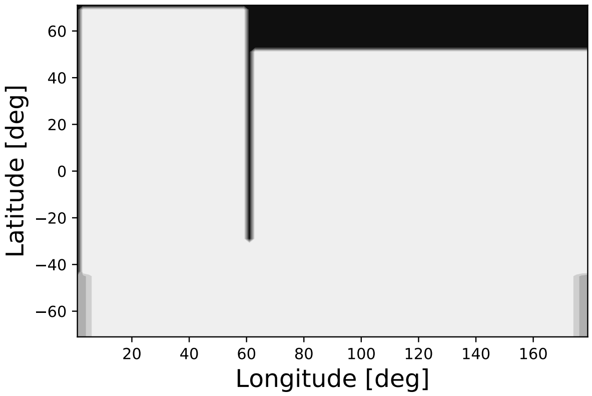

Figure 6.5: Geometry of the domain used in the ocean-only simulations. The black represents continent; the white denotes ocean at 4000 m deep; and the gray shading represents the submarine sill at the Drake passage.

basin (120° wide) is an idealized representation of the Indo-Pacific ocean, and the narrower one (60° wide) represents the Atlantic Ocean. A landmass is added between 52°N and 72°N in the northern Indo-Pacific ocean to create a buoyancy forcing asymmetry between the two basins, such that deep water only forms in the Atlantic ocean.

We use a 2° horizontal grid resolution. The unresolved eddies are represented using the skew-flux form of the Gent and McWilliams parameterization with an eddy thickness diffusivity of 1000 $\mathrm{m^2/s}$ (Griffies, 1998). The bottom is flat and 4000 m deep except for a sill (gray shading in Figure 6.5) in the periodic channel. The sill is 1500 m high above the bottom and decays longitudinally as a gausian function. There are 30 vertical levels of thickness increasing from 20 m at the surface to 250 m at the bottom. The equation of state is linear and depends only on temperature with a constant thermal expansion coefficient $2.0 \times 10^{-4}\mathrm{K}^{-1}$. The vertical diffusivity that we use is a function of depth and varies from $2.0 \times 10^{-5}\mathrm{m^2/s}$ at the surface to $1.0\times10^{-4}\mathrm{m^2/s}$ with a transition depth of 2000 m (Bryan and Lewis, 1979). Convection is represented by an implicit vertical diffusion with diffusivity of 100 $\mathrm{m^2/s}$ whenever the stratification is unstable.

The surface wind stress forcing is steady and zonally uniform (Figure 6.6a). The surface

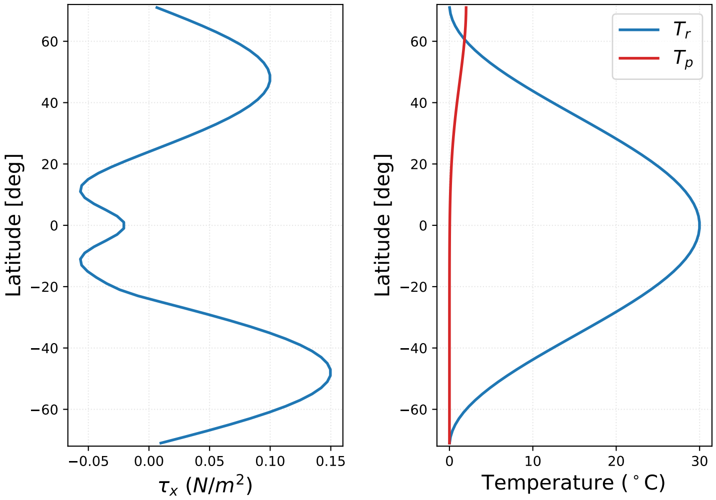

Figure 6.6: Surface wind stress forcing (a) and restoring temperature profile (b) in the MITgcm ocean-only simulations.

temperature is restored to a prescribed temperature fields $T_s(x,y,t)$:

$$T_s(x,y,t) = T_r(y) + \Delta T_s(x,y,t), \tag{6.4}$$

where T_r is symmetric latitudinally and uniform in the zonal (Figure 6.6b); ΔT_s refers to the the perturbation that is added to the restoring surface temperature and will be discussed in the next subsection. The restoring time scale is 20 days.

Similar to the above section, we quantify the meridional overturning circulation (MOC) strength at 30° but using the isopycnal overturning circulation streamfunction:

$$\Psi_{\text{AMOC}} = \max\left(\psi_A(30^\circ\text{S}, \text{b})\right), \tag{6.5a}$$

$$\Psi_{\text{GMOC}} = \max\left(\psi_G(30^\circ\text{S}, \text{b})\right), \tag{6.5b}$$

where ψ_A and ψ_G represent the isopycnal overturning circulation streamfunction calculated over the Atlantic and Global ocean. To reflect the contributions from the Indo-Pacific, we define the PMOC strength as the PMOC streamfunction (ψ_P) associated with the isopycnal that the AMOC

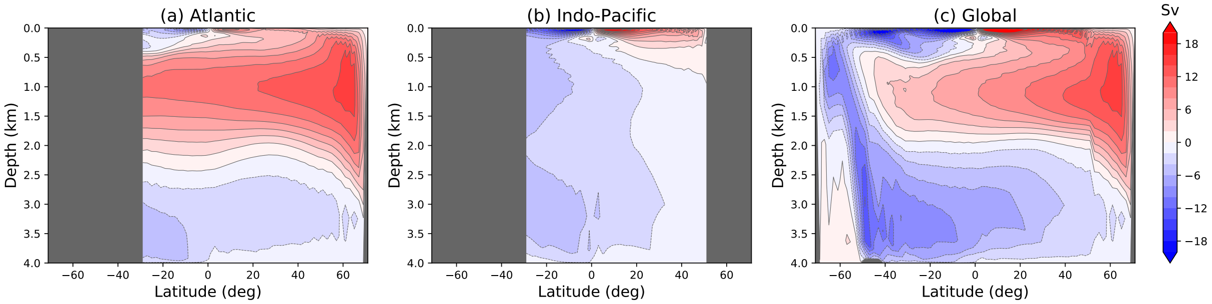

Figure 6.7: Isopycnal overturning circulation streamfunction in the (a) Atlantic, (b) Indo-Pacific, and (c) Global ocean at $\alpha = 0$ in the equilibrium runs. The isopycnal overturning circulation streamfunction is mapped back to depth coordinate using the mean isopycnal depth for presentation (see Chapter 3).

reaches maximum, i.e.,

$$\Psi_{\mathrm{PMOC}} = \psi_P(30^\circ\mathrm{S}, \mathrm{b_m}), \tag{6.6}$$

where b_m satisfies

$$\psi_A(30^\circ\mathrm{S}, \mathrm{b_m}) = \Psi_{\mathrm{AMOC}}. \tag{6.7}$$

6.3.2 Results and discussions

Two sets of simulations are performed: (1) Equilibrium runs and (2) Periodic perturbation runs. In the equilibrium runs, ΔT_s is steady in time and we will discuss the equilibrium solution of the overturning circulation to constant perturbations. In the periodic perturbation runs, ΔT_s is sinusoidal in time and we will discuss the dependence of the AMOC variability on the associated time scales.

Equilibrium runs

In the equilibrium runs, the perturbation $\Delta T_S(x,y,t)$ is expressed as

$$\Delta T_S(x,y,t) = \begin{cases} \alpha T_p(y), & x < 60^\circ(\text{Atlantic}) \\ 0, & x \geq 60^\circ(\text{Indo-Pacific}) \end{cases} \tag{6.8}$$

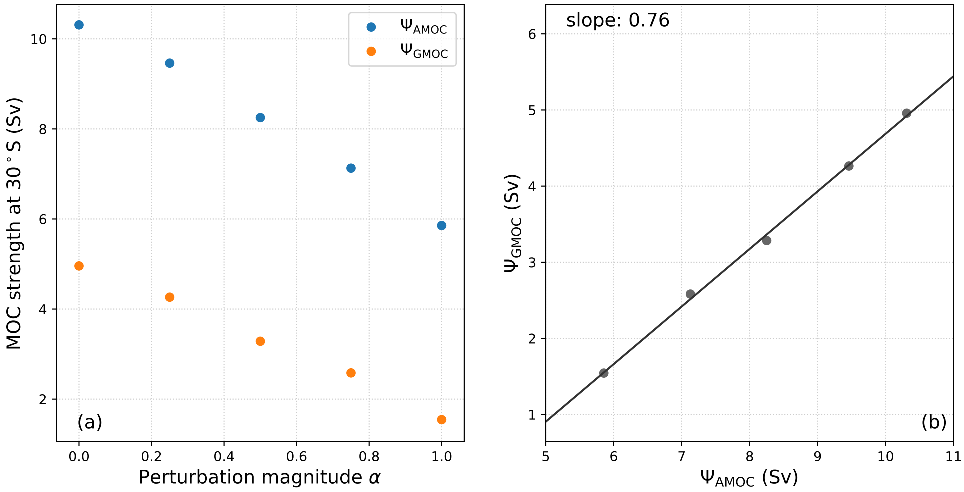

Figure 6.8: (a) Variations of the MOC strength in the equilibrium runs, evaluated at 30°S. (b) Scatter plot of the GMOC vs the AMOC strength. The straight black line is linearly fitted to the scatter plot with a slope 0.76.

where α varies from 0 to 1. At the maximum perturbation, $\alpha = 1$, the surface temperature at the northern boundary of the Atlantic is still colder than that of the Indo-Pacific. This ensures that no deepwater is formed in the Indo-Pacific basin. For each equilibrium run, we initialize the model from a motionless state and continue for over 5,000 years until the model approximately reaches a steady state. We present the isopycnal overturning circulation streamfunction (ψ) for $\alpha = 0$ in Figure 6.7. This largely represents the overturning circulation streamfunction in the current climate.

For increasing temperature (larger α) in the North Atlantic, the shared surface buoyancy between the North Atlantic and the Southern Ocean is decreasing. Thus, the AMOC weakens as α increases (Figure 6.8a) (e.g., Nikurashin and Vallis, 2012). However, different from the transient response in the climate model simulations in Section 6.2, the GMOC varies by around 76% of the AMOC changes, i.e., the PMOC changes only compensate 24% of the AMOC changes. This compensation is much smaller than the transient responses in the CESM "LENS" runs and implies a larger role of the Southern Ocean processes in determining the AMOC strength in steady state. In the following subsection, we wil discuss the dependence of the inter-basin compensation on

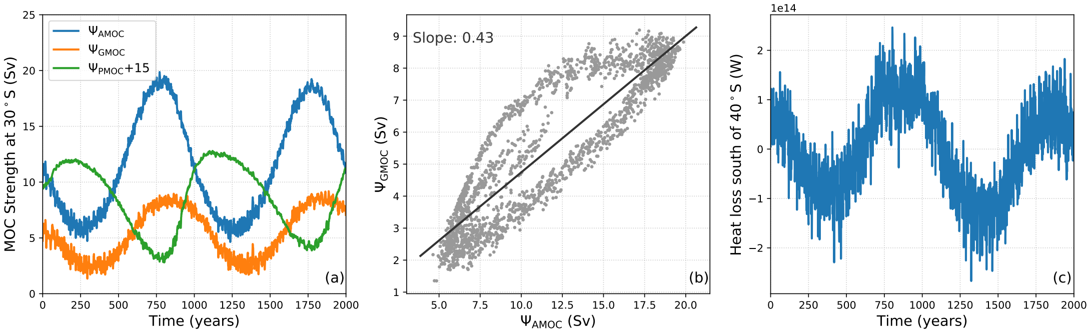

Figure 6.9: (a) Variations of the MOC strength at 30°S in the periodic perturbation run at $\mathcal{T} = 1000$ years. (b) Scatter plot of the GMOC strength vs the AMOC strength at 30°S. A straight black line is fitted to the gray dot with a slope 0.43. (c) Integrated surface heat loss to the south of 60°S in the periodic perturbation run at $\mathcal{T} = 1000$ years. The MOC strength and heat loss is calculated annually and then smoothed with a 5-year moving mean.

the time scales associated with the AMOC variability by applying periodic perturbations in the North Atlantic.

Periodic perturbation runs

In the periodic perturbation runs, the surface temperature perturbation

$$\Delta T_S(x,y,t) = \begin{cases} T_p(y)\sin\left(\frac{2\pi t}{\mathcal{T}}\right), & x < 60^\circ \ (\text{Atlantic}) \\ 0, & x \geq 60^\circ \ (\text{Indo-Pacific}) \end{cases} \tag{6.9}$$

where $\mathcal{T}$ varies from 50 years to 2000 years and sets the time scale of the AMOC variability. For each perturbation run, we initialize from the equilibrium run at $\alpha = 0$ and continue for either 1000 or $2\mathcal{T}$ years, whichever is longer.

Figure 6.9 presents an example of the MOC strength variations at 30°S in the periodic perturbation run at $\mathcal{T} = 1000$ years. In response to the sinusoidal surface temperature perturbations in the North Atlantic, both the AMOC and GMOC vary sinusoidally. In contrary to the equilibrium runs, the GMOC varies by only 43% of the AMOC changes, i.e., the PMOC conpensates 57% of the AMOC changes. This is similar to the transient responses in the CESM

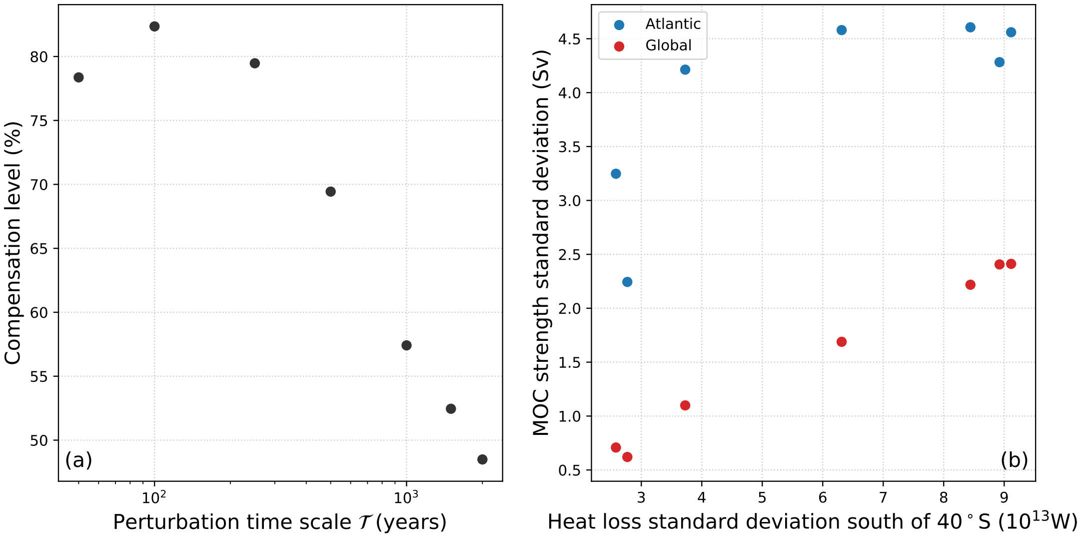

Figure 6.10: (a) Dependence of the interbasin compensation level, defined as 1 minus the slope of Ψ_{GMOC} vs Ψ_{AMOC} (Figure 6.9b), on the perturbation time scale $\mathcal{T}$. (b) Scatter plot of the standard deviation (STD) of Ψ_{AMOC} and Ψ_{GMOC} with respect to the STD of the integrated heat flux to the south of 60°S.

"LENS" runs. We integrate the surface heat flux in the Southern Ocean to the south of 60°S (Figure 6.9). This integrated heat flux varies due to changes in the upwelling rate of deepwater and reflects the water mass transformation rate in the Southern Ocean.

We carry out a number of perturbation runs with varying perturbation time scales ($\mathcal{T}$) and quantify the inter-basin compensation for varying $\mathcal{T}$ (Figure 6.10). For AMOC variability on time scales less than 500 years, the inter-basin compensation level could reach 80%. This suggests a minimal role of Southern Ocean processes in the AMOC variability on multidecadal or centennial time scales, consistent with previous studies that usually attributes the multidecadal AMOC variability to North Atlantic processes (e.g., Yeager and Danabasoglu, 2014). As the perturbation time scale $\mathcal{T}$ increases, the inter-basin compensation level gets smaller but is still as high as around 50% at $\mathcal{T}$=2000 years. This raises some alarms when we use the Southern Ocean processes to interpret the AMOC variability even on paleo-climate time scales (e.g., the Dansgaard-Oeschger events during the last glacial period).

We calculate the standard deviation of the MOC variability and the integrated heat flux to

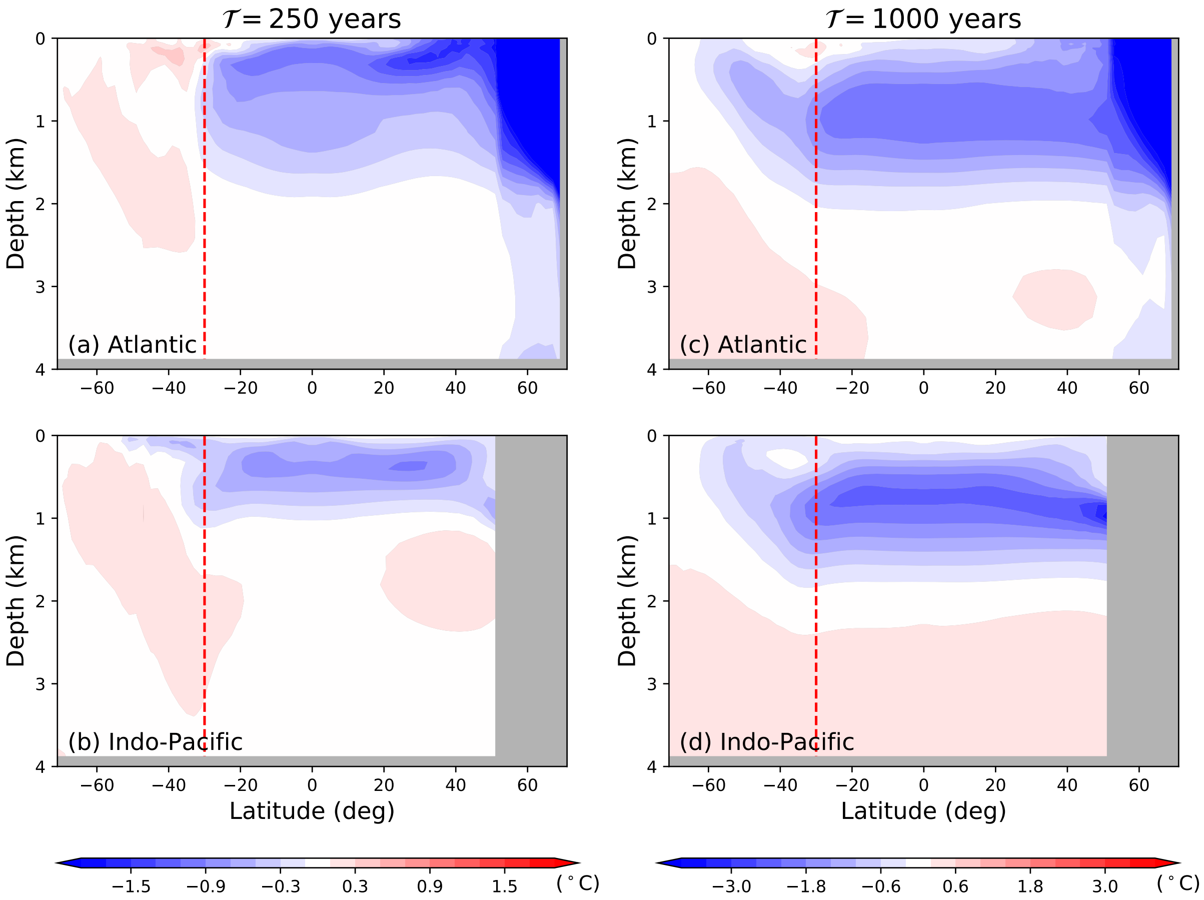

Figure 6.11: Zonal-mean temperature differences between years of maximum AMOC and minimum AMOC (max - min) for (a,b) $\mathcal{T} = 250$ years and (c,d) $\mathcal{T} = 1000$ years. The zonal-average is performed over the Atlantic longitude (0-60°; a & c) and the Indo-Pacific longitude (60°-180°; b & d) separately. The red dashed line in each panel represents 30°S, the southern boundary of the short continent.

the south of 60°S (Figure 6.10b). The results suggest a much stronger connection between the Southern Ocean surface buoyancy forcing and the GMOC, rather than the AMOC. This implies that the Southern Ocean surface forcing maybe not suitable to be used to predict the AMOC changes when the ocean is not in steady state (cf. Ferrari et al., 2014).

We compare the zonal-mean temperature between the maximum and minimum AMOC phases at $\mathcal{T} = 250$ years as well as $\mathcal{T} = 1000$ years (Figure 6.11). At $\mathcal{T} = 250$ years, almost all of the isopycnal adjustments take place to the north of 30°S. This stands in contrast with the case at $\mathcal{T} = 1000$ years, where significant adjustments of the isopycnals are observed in the

Southern Ocean. The difference between the two cases suggest a two-timescale problem: a fast response that is associated with the inter-basin transport of deepwater and a slow response that is associated with the adjustment of the isopycnal slopes in the Southern Ocean. Note that changes in the isopycnal slopes in the Southern Ocean are related to variations in the global upwelling rate of deepwater and thus the GMOC (Equation (6.2)). The inter-basin transport is accomplished through a geostrophic exchange transport between the Atlantic and Indo-Pacific basins to the south of Africa (Figure 6.1), which is determined by the isopycnal depth difference between these two basins (Jones and Cessi, 2016). And this fast adjustment is associated with advection and wave processes that could occur in less than a decade (compare the blue and green lines in Figure 6.9a). In comparison, the adjustment of the Southern Ocean isopycnal slope is controlled by diapycnal mixing and Southern Ocean eddies, and it occurs on millenial time scales (e.g., Allison et al., 2011).

Therefore, for high-frequency variability of the AMOC, the PMOC compensates the AMOC changes through an inter-basin transport between the Atlantic and Indo-Pacific basins. As the AMOC variability time scale increases, the Southern Ocean upwelling begins to respond and the inter-basin compensation decreases. In the next section, we will reproduce this using a 1.5-layer reduced gravity model and a two-box model to illustrate this process.

6.4 Conceptual models

The two-timescale problem, as described above, can be best illustrated using a 1.5-layer reduced gravity model, which could simulate both the inter-basin transport and the adjustment of the pycnoclines (cf. Jones and Cessi, 2016). We will also try simplifying the reduced gravitiy model further to a two-box model based on the residual-mean theory, with each of the two box representing the two ocean basins, respectively. We will use these two conceptual models to reproduce the dependence of inter-basin compensation on the AMOC variability time scales.

6.4.1 1.5-layer reduced gravity model

The 1.5-layer reduced gravity model share the same model geometry as the MITgcm simulations (Figure 6.5). The active layer represents the upper branch of the AMOC that flows northward in the Atlantic Ocean and sinks in the North Atlantic. The momentum equation of the 1.5-layer model is

$$\frac{\partial \vec{u}}{\partial t} + \vec{u} \cdot \nabla(\vec{u}) + f\vec{k} \times \vec{u} = -g'\nabla h + A_h \nabla^2 \vec{u} + \frac{\vec{\tau}}{\rho_0 h} - r\vec{u}, \tag{6.10}$$

where the layer thickness h is calculated from the continuity equation

$$\frac{\partial h}{\partial t} + \nabla \cdot (h\vec{u}) = \nabla \cdot (K_{\mathrm{GM}} \nabla h) + \frac{\kappa}{h} + w_e - w_{\mathrm{NADW}}. \tag{6.11}$$

Here, $\vec{u}$ is velocity, $g' = 0.02 \mathrm{m/s}^2$ is the reduced gravity, $K_{\mathrm{GM}} = 1000 \mathrm{m}^2/\mathrm{s}$ is the eddy thickness diffusivity, $\kappa = 2.0 \times 10^{-5} \mathrm{m}^2/\mathrm{s}$ is the diapycnal diffusivity. We use both laplacian dissipation ($A_h = 1.0 \times 10^4 \mathrm{m}^2/\mathrm{s}$) and bottom friction ($r = 1.0 \times 10^{-6} \mathrm{s}^{-1}$) to dissipate the momentum. The bottom friction is implemented to roughly represents the effect of baroclinic instability, in order to avoid an unrealistic strong zonal flow in the Southern Ocean. The NADW formation, 12 Sv in the equilibrium runs, is represented with a uniform vertical velocity (w_{NADW}) over a 5 degree latitude band in the North Atlantic close to the northern boundary. The water mass transformation in the Southern Ocean is parameterized by restoring the layer thickness toward $h_{\min}$ =10 m between 72°S and 62°S,

$$w_e = \frac{1}{\Lambda}(h_{\min} - h), \tag{6.12}$$

where the restoring time scale Λ linearly increases northward from 10 days at 72°S to 100 days at 62°S. A fast restoring is also used (3600 s) when the layer thickness is below $h_{\min}$ to ensure a postive h. For simplicity, the wind stress forcing deays to zero outside the Southern Ocean. The model is integrated forward using the 3$^{\text{rd}}$ order Adams-Bashforth method.

Consistent with Equation (6.5a), we define the MOC strength at 30°S in the 1.5-layer model as

$$\Psi_{\text{AMOC}} = \int_0^{x_1} \left(vh - K_{\text{GM}} \frac{\partial h}{\partial y} \right) dx, \tag{6.13a}$$

$$\Psi_{\text{PMOC}} = \int_{x_1}^{x_2} \left(vh - K_{\text{GM}} \frac{\partial h}{\partial y} \right) dx, \tag{6.13b}$$

$$\Psi_{\text{GMOC}} = \Psi_{\text{AMOC}} + \Psi_{\text{PMOC}}. \tag{6.13c}$$

where x_1 represents the longitudinal distance from 0 to 60° at 30°S, and x_2 is the longitudinal distance from 0 to 180° at 30°S. We run the model to equilibrium and then start a set of periodic perturbation runs, in which the NADW formation rate (S_{NADW}) is perturbed by a sinusoidal function as in Section 6.3:

$$S_{\text{NADW}} = S_0 + \delta S \sin(2\pi t/\mathcal{T}), \tag{6.14}$$

where S_0=12 Sv, and $\delta S = 6$ Sv. The inter-basin transport in the 1.5-layer reduced gravity model is related to the layer thickness in the Atlantic and Indo-Pacific basins as

$$\chi = -\frac{1}{2}\frac{g'}{f}(h_p^2 - h_a^2), \tag{6.15}$$

where h_p and h_a represents the mean layer thickness in the Indo-Pacific and Atlantic Oceans, respectively (Jones and Cessi, 2016).

In comparison with Figure 6.11, we calculate the zonal-mean layer thickness differences between the maximum and minimum AMOC phases in each basin for $\mathcal{T} = 250$ years as well as $\mathcal{T} = 1000$ years (Figure 6.12). Consistent with Figure 6.11, there are very minor changes in the Southern Ocean isopycnal slope at $\mathcal{T} = 250$ years, but at $\mathcal{T} = 1000$ years, the Southern Ocean isopycnal is substantially less steep, suggesting a much larger GMOC strength (Equation (6.2)), at the maximum AMOC phase compared to the minimum AMOC phase. We quantify

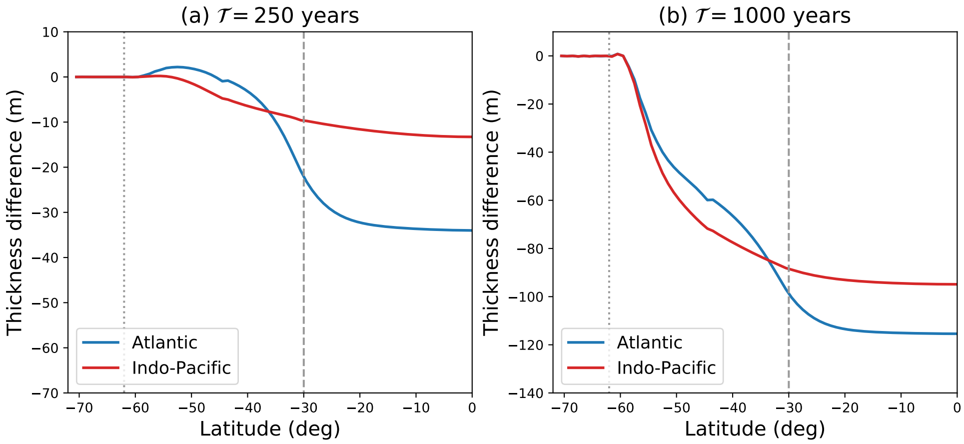

Figure 6.12: Basin-averaged layer thickness between the maximum and minimum AMOC phases (max - min) for (a) $\mathcal{T} = 250$ years and (b) $\mathcal{T} = 1000$ years. The thickness is smaller at maximum AMOC phase. The gray dashed line represents 30°S, the southern boundary of Africa. The gray dotted line marks the northern boundary of the restoring. Note that the two panels are plotted on different range.

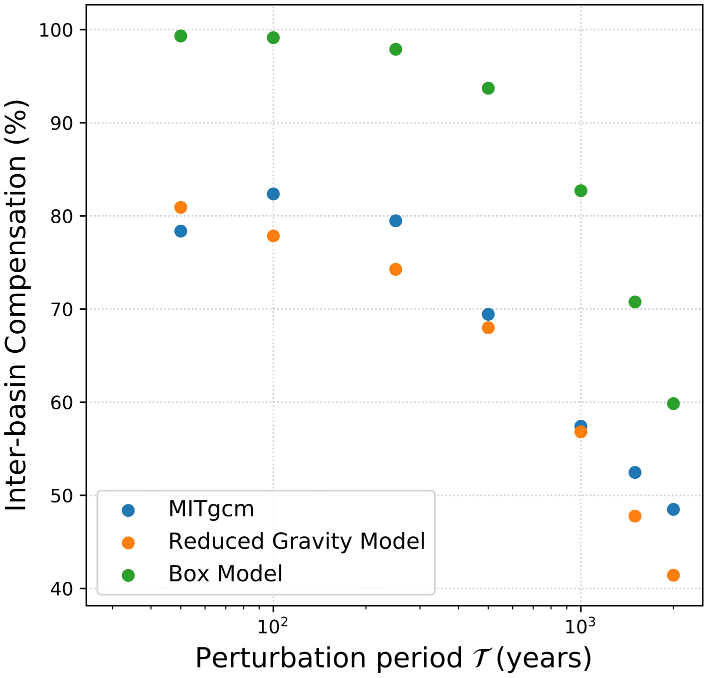

Figure 6.13: Inter-basin compensation level in the MITgcm, 1.5-layer reduced gravity model, and the box model.

the inter-basin compensation level the same way as in Section 6.3 and present the results in Figure 6.13. We show that the 1.5-layer model, despite its simplicity, approximately reproduces the MITgcm simulations regarding the dependence of inter-basin compensation on the AMOC variability time scales.

6.4.2 Box model

The dynamics for the inter-basin compensation can be further simplified to a two-box model, with each box representing one of the ocean basins between the Atlantic and Indo-Pacific. This box model solves for the mean upper layer thickness of the Atlantic (h_A) and Indo-Pacific basin (h_P), and it can be considered as a simplified version of the multi-basin model in Thompson et al. (2016):

$$\frac{dh_A}{dt} = \frac{\kappa}{h_A} - \frac{S_{\mathrm{NADW}}}{S_A} + \frac{\phi_A L_A + \chi}{S_A}, \tag{6.16a}$$

$$\frac{dh_P}{dt} = \frac{\kappa}{h_P} + \frac{\phi_P L_P - \chi}{S_P}, \tag{6.16b}$$

where

$$\phi_A = -\frac{\tau}{\rho f} - K_{\mathrm{GM}} \frac{h_A}{L_y}, \tag{6.17a}$$

$$\phi_P = -\frac{\tau}{\rho f} - K_{\mathrm{GM}} \frac{h_P}{L_y}. \tag{6.17b}$$

In the above, L_y is the Southern Ocean width in the meridional direction, $L_A = x_1$, $L_P = x_2 - x_1$, S_A is the area of the Atlantic Ocean, S_P is the area of the Indo-Pacific, and χ represents the inter-basin transport as defined in Equation (6.15). Similar to Equation (6.13a) for the reduced

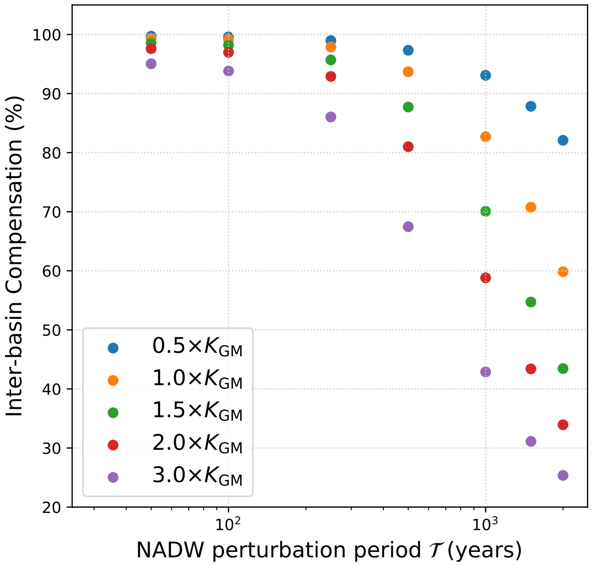

Figure 6.14: Sensitivity of the inter-basin compensation level to eddy thickness diffusivity. Here, for example, $2.0\times K_{\mathrm{GM}}$ means the eddy thickness diffusivity is doubled.

gravity model, we define the MOC strength as

$$\Psi_{\mathrm{AMOC}} = \phi_A L_A + \chi, \tag{6.18a}$$

$$\Psi_{\mathrm{PMOC}} = \phi_P L_P - \chi, \tag{6.18b}$$

$$\Psi_{\mathrm{GMOC}} = \Psi_{\mathrm{AMOC}} + \Psi_{\mathrm{GMOC}}. \tag{6.18c}$$

Solving the box model numerically using the same parameters as the 1.5-layer reduced gravity model, we obtain a similar dependence of the inter-basin compensation on the AMOC variability time scales (green dots in Figure 6.13). However, the box model predicts a much higher compensation level for the same perturbation period $\mathcal{T}$. For exmaple, for $\mathcal{T}$ less than 500 years, the inter-basin compensation level could be close to 100% in the box model, 20% higher than the reduced gravity model and the MITgcm. This overestimated compensation is likely due to the oversimplified representation of the inter-basin transport, which does not resolve the advection and wave processes.

We now discuss the parameter sensitivity of the box model. Previous studies have suggested two pertinent time scales in the adjustment of the Southern Ocean isopycnal slope (Marshall and Zanna, 2014):

- Southern Ocean eddies: $t_{\mathrm{eddy}} \sim \frac{AL_y}{K_{\mathrm{GM}}L_x}$
- Diapycnal mixing: $t_{\mathrm{diap}} \sim \frac{h^2}{\kappa}$,

where h is the global mean upper layer thickness. Using the equilibrium solution for the box model ($h \approx 1650$ m), we estimate that $t_{\mathrm{eddy}} \approx 600$ years and $t_{\mathrm{diap}} \approx 4000$ years. Therefore, the adjustment of the Southern Ocean isopycnal slope and GMOC is primarily determined by the Southern Ocean eddy processes. For larger eddy thickness diffusivity, the adjustment time scale of the Southern Ocean isopycnal slope is smaller and the Southern Ocean overturning shall play a bigger role in balancing the AMOC variability. Therefore, the inter-basin compensation shall decrease for larger K_{GM}, as confirmed in Figure 6.14.

We note that this sensitivity of the inter-basin compensation to K_{GM} is substantially overestimated in the box model, compared to both the MITgcm and the 1.5-layer reduced gravity model (not shown). We are still researching on this but suggest this might be due to the oversimplified representation of the eddy contribution to the overturning circulation in Equation (6.17a).

6.5 Summary

Climate models consistently predict a weakening of the AMOC in the 21$^{\mathrm{st}}$ century due to the warming climate (Cheng et al., 2013). However, this weakening in the AMOC appears to contradict the strengthening of the Southern Hemisphere westerly wind, which shall drive a stronger upwelling in the Southern Ocean (e.g., Toggweiler and Samuels, 1995). This contradiction is resolved by considering the Indo-Pacific component of the overturning circulation:

changes in the Indo-Pacific overturning circulation could compensate the AMOC variations, such that the globally integrated overturning circulation stays roughly constant in the Southern Ocean.

We explored this inter-basin compensation using an ocean-only model and find that this inter-basin compensation decreases as the AMOC variability time scale increases. As the inter-basin compensation decreases, the Southern Ocean becomes more important to the AMOC variability. We suggest that this dependence of the inter-basin compensation on time scales results from a two-timescale adjustment problem. The inter-basin compensation is accomplished through a geostrophic inter-basin exchange between the Atlantic and Indo-Pacific basins, which adjust through fast advection and wave processes, through the Southern Ocean. The adjustment of the Southern Ocean overturning circulation, on the other hand, is accomplished through Southern Ocean eddies and diapycnal mixing, which occur on a much longer time scales.

For relatively high-frequency variability of the AMOC, the Indo-Pacific overturning circulation largely compensates the AMOC changes through the inter-basin transport between the Atlantic and Indo-Pacific basins. As the AMOC variability time scales increases, the Southern ocean upwelling begins to respond and the inter-basin compensation decreases. The results are largely reproduced in a 1.5-layer reduced gravity model and a conceptual two-box model.

The Southern Ocean surface forcing appears to be only directly related to the global-integrated overturning circulation, rather than the AMOC, when the overturning circulation is not in steady state. Our results raise alarms when we use the Southern Ocean processes to interpret the AMOC variability even on glacial time scales.

There are some caveats in this study. The two-box conceptual model overestimate the inter-basin compensation level and its sensitivity to eddy thickness diffusivity, compared to the MITgcm simulations and the reduced gravity model. More efforts are required to clarify this. Additionally, we use restoring boundary conditions in our simulations. It may also be interesting to discuss the adjustment of the overturning circulation under prescribed surface buoyancy flux in the Southern Ocean (cf. Chapter 2).

Acknowledgement

This chapter benefits from discussions with Andrew Thompson, Ian Eisenman, Geoffrey Vallis, Shangping Xie, Kyle Armour, and Georgy Manucharyan. The authors are grateful for their supports and comments.

This chapter is a summary of work in progress. The dissertation author is currently the only investigator and author of this chapter, but some collaborators may be added as it progresses.

Chapter 7

Other works: The influence of sea ice velocity biases on the recent trend in Antarctic sea ice extent

7.1 Introduction

Despite continuous warming of the climate, the Antarctic has seen significant overall sea ice expansion in the satellite era (1979-2015) (e.g., Hobbs et al., 2016). This expansion in the Antarctic contrasts with the substantial sea ice loss in the Arctic during the same period (Simmonds, 2015), and it is at odds with most of the climate model simulations that are driven by realistic natural and anthropogenic forcing (Turner et al., 2013). The vast majority of climate model simulations have a retreating Antarctic sea ice coverage, and the other models that simulate a sea ice expansion in the Antarctic typically have too little global warming (Rosenblum and Eisenman, 2017).

A number of mechanisms have been proposed to account for the Antarctic sea ice expansion in the warming climate. These mechanisms typically involve changes in surface wind (e.g., Holland and Kwok, 2012), freshwater flux (e.g., Bintanja et al., 2013), ice-ocean interactions (Goosse and Zunz, 2014), deep ocean convection (e.g., Zhang et al., 2019), or a combination of them. Among these mechanisms, sea ice motion driven by surface wind changes has been suggested to play a leading role in the Antarctic sea ice expansion (e.g., Holland and Kwok, 2012).

Biases in the ice velocity field provides a compelling explanation to reconcile the observed and simulated sea ice changes. Sea ice motion is typically simulated with variants of the Hunke and Dukowicz (1997) elastic-viscous-plastic representation of sea ice rheology in most current climate models. This representation of sea ice motion has been found to have systematic bias in the simulated sea ice velocity fields when comparing with observations (Kwok, 2011). Even if the sea ice velocity were handled perfectly in the sea ice component of climate models, this motion is forced by winds and ocean currents, which in turn suffer from model inaccuracies (e.g., Purich et al., 2016).

In this study, we will investigate the influence of ice velocity biases on the Antarctic sea ice extent trend using a comprehensive climate model. By specifying the sea ice velocity with observations, we will see how much of the observed Antarctic sea ice expansion can be reproduced in model simulations.

7.2 Data and Method

We employ the NCAR Community Earth System Model version 1 (CESM1), the same model used to carry out the CESM Large Ensemble (LENS) (Kay et al., 2015). The model is fully coupled with active atmosphere, ocean, land, and sea ice components, with a horizontal resolution of approximately 1°. We employ the same boundary conditions (e.g., CO_2) as the CESM LENS (for more details, see Kay et al., 2015).

The CESM LENS contains 40 ensemble members that simulate the climate trajectories

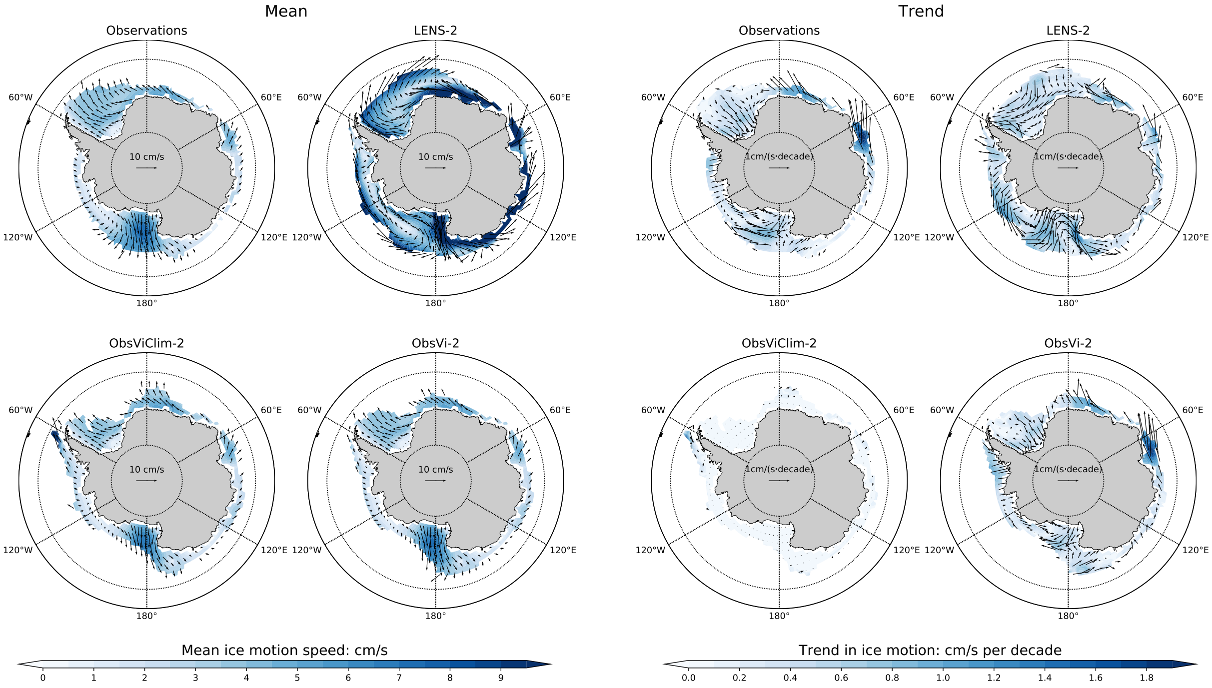

Figure 7.1: Climatological mean sea ice drift velocity (left) and linear trend in sea ice drift velocity (right) during 1992-2015, averaged over months from April to October, for "Observations", "LENS-2", "ObsViClim-2" and "ObsVi-2". The shading shows the magnitude of ice drift velocity and trend. The climatological mean and linear trend is calculated where sea ice is present over 60% of the time when the calculation is performed.

over 1920-2100 under historical (1920-2005) and Representative Concentration Pathway 8.5 emission scenario (2006-2100). These members share the same model physics and differ only by some round-off level differences in their atmospheric initial conditions. Therefore, the ensemble spread in the CESM LENS largely results from internally generated climate variability (Kay et al., 2015), which has been suggested to account for the discrepancies in the trend of Antarctic sea ice between observations and climate models (e.g., Polvani and Smith, 2013; Mahlstein et al., 2013; Jones et al., 2016).

We randomly choose 3 members from the CESM LENS: “LENS-2”, “LENS-4”, and “LENS-6”. Corresponding to each LENS run, we carrry out two simulations (“ObsViClim” and “ObsVi”) with ice velocity relaxed to observations, i.e.,

$$\frac{d\vec{v}}{dt} = \frac{1}{\tau}(\vec{v}_{\text{obs}} - \vec{v}). \tag{7.1}$$

Here, $\vec{v}$ represents the sea ice drift velocity in the model, $\vec{v}_{\text{obs}}$ denotes the observed sea ice drift velocity, and $\tau = 3,600$ s is a restoring time scale. We experimented with different restoring time scale and find that $\tau = 3,600$ s is small enough to constrain the sea ice drift velocity to resemble observations and also large enough to avoid numerical instabilities in the sea ice model. We use daily observed ice drift velocity in “ObsVi” and the climatology of observations in “ObsViClim” (Figure 7.1). When obervations are not available at some grid points, we use the default momentum equation to calculate the ice drift velocity but with the surface wind replaced with reanalysis data. Consistent with the observed ice velocity, we use the original wind product in “ObsVi” but with its climatology in “ObsViClim”.

We initialize “ObsViClim” from the CESM LENS on January 1$^{\text{st}}$, 1960, spin up for 32 years, and run for another 24 years until 2015. We initialize “ObsVi” from the “ObsViClim” on January 1$^{\text{st}}$, 1992 at the end of spin up. The model output between 1992-2015 will be used to compare with observations.

We use the sea ice drift velocities from the Polar Pathfinder Daily Sea Ice Motion Vectors, version 3 (Tschudi et al., 2016). This dataset combines data sources from buoy and satellite measurements, as well as free drift estimates calculated from NCEP-NCAR reanalysis geostrophic winds. It provides sea ice velocities that are interpolated onto a 25-km resolution Equal Area Scalable Earth (EASE) grid with daily temporal resolution from late 1978 to early 2016 at the time the data were downloaded. We interpolate the ice drift velocity from the 25-km resolution EASE grid to the nominal 1° resolution model grid by averaging the observations that are located within each grid cell. The surface wind reanalysis product is from ERA-interim (Dee et al., 2011). The wind product is reported on a 0.75° resolution and on 6-hour frequency. We interpolate it to the model grid using bilinear interpolation.

We focus this study on the period between 1992-2015, instead of 1979-2015, because we identified two spurious jumps with the ice motion data (see Figure D1 in Appendix D), which appear to be associated with the transition from the Scanning Multichannel Microwave Radiometer (SMMR) to the Special Sensor Microwave/Imager (SSM/I) on July 9, 1987 and the transition from the SSM/I flown on the Defense Meteorological Satellite Program F8 satellite to the SSM/I flown on the DMSP F11 satellite on December 3, 1991, respectively.

We use the monthly-mean sea ice concentration from Nimbus-7 SMMR and DMSP SSM/I-SSMIS Passive Microwave Data, Version 1 (Cavalieri et al., 1996) to compare with the model output. The sea ice concentration, provided on a 25-km resolution polar stereographic grid, is generated from brightness temperature data based on multiple sensors, including the Nimbus-7 SMMR, the Defense Meteorological Satellite Program (DMSP)-F8, -F11, and -F13 SSM/I, and the DMSP-F17 Special Sensor Microwave Imager/Sounder (SSMIS). We use sea ice extent, defined as the total area with sea ice concentration above 15%, to quantify the overall sea ice coverage in both observations and model simulations.

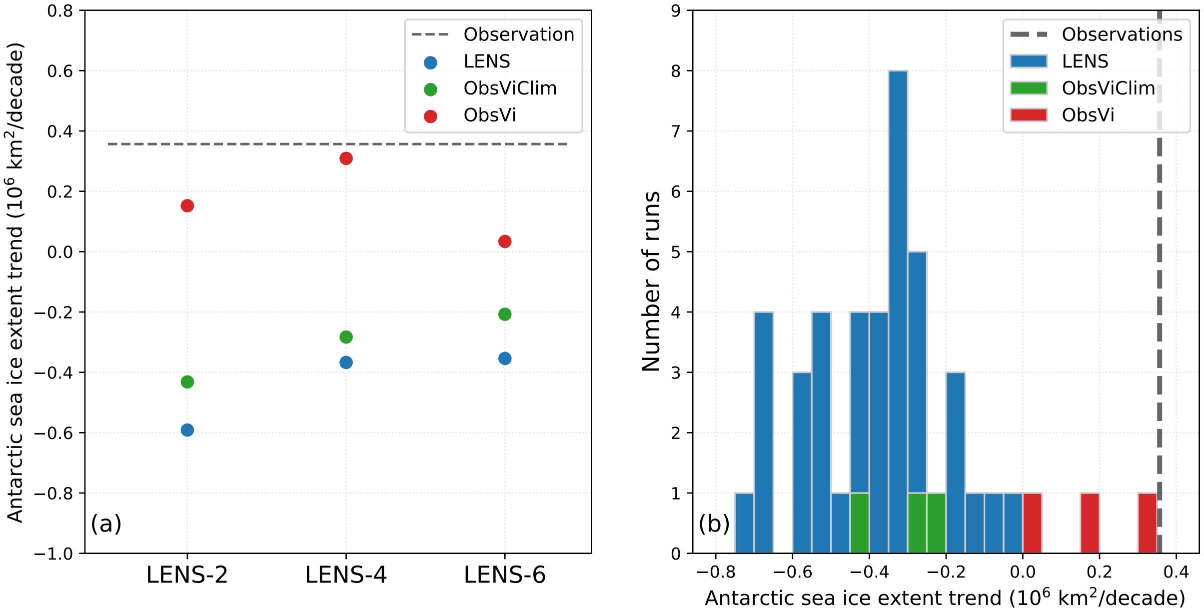

Figure 7.2: Linear trend (a) and its histogram (b) of the annual-mean sea ice extent in our simulations in comparison with observations and CESM LENS.

7.3 Results

7.3.1 Sea ice trend

The sea ice drift velocity in the CESM LENS differs from observations in both its mean and linear trend (Figures 7.1, D2, and D3). Although the CESM LENS largely capture the direction of the mean ice drift velocity in observations, they substantially overestimate its magnitude (Figures 7.1). In the Ross Sea, there is a strengthening of the northward ice drift in observations, likely in response to the deepening Amundsen Sea Low in recent decades (e.g., Raphael et al., 2016). This trend in the ice drift velocity has been suggested to be responsible for the expanding sea ice in the Ross sea (e.g., Holland and Kwok, 2012), but it is not simulated in “LENS-2” (Figure 7.1) or “LENS-6” (Figure D3), and it is overestimated in “LENS-4” (Figure D2). Similarly in the Weddell Sea, the simulated trend in the ice drift velocity is opposite to observations in all three LENS runs (Figures 7.1, D2, and D3). By relaxing ice velocity to observations in the model, we roughly correct the biases in the mean ice velocity field (“ObsViClim” and “ObsVi”) and its

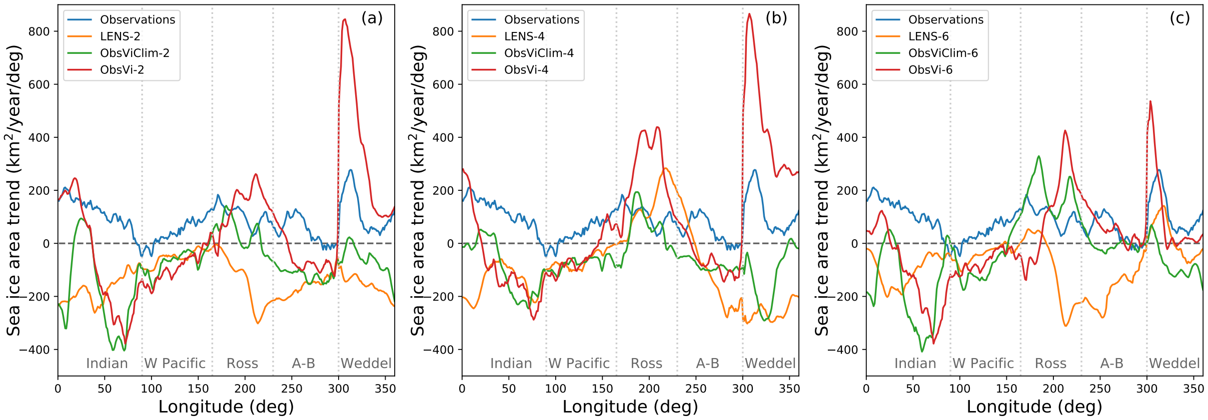

Figure 7.3: Latitudinal integration of the trend in annual-mean sea ice concentration during 1992-2015. The longitudinal integration of each line is equal to the overall linear trend of sea ice area, which is similar to Figure 7.2 (not shown). Here, "W Pacific" refers to "Western Pacific", and "A-B" refers to "Amundsen-Bellingshausen".

linear trend ("ObsVi").

In observations, there is an overall expansion of the Antarctic sea ice extent by 0.35×10^6 km^2/decade during 1992-2015. This expansion stands in contrast with the CESM LENS runs, which consistently simulated a decrease in the Antarctic sea ice extent during the same period (Figure 7.2). This contrast appears to suggest a trivial role of internal climate variability in explaning why climate models fail to simulate the observed Antarctic sea ice expansion (cf., Swart et al., 2018).

Removing the biases in the mean ice velocity fields ("ObsViClim") only marginally improves the overall Antarctic sea ice extent trend in the CESM simulations (Figure 7.2a). After the biases in the ice velocity trend is also removed ("ObsVi"), however, we see substantial improvements and simulate an overall Antarctic sea ice expansion in the "ObsVi" runs. This implies that the biases in the simulated ice velocity trend may play a significant role in explaining the discrepancies between the observed and simulated sea ice changes.

The observed overall increase in the Antarctic sea ice extent is an integration of the non-uniform sea ice changes in the Southern Ocean (see sea ice concentration trend in Figures D4, D5, and D6). Here, we discuss the regional sea ice changes by integrating the linear trend in annual-mean sea ice concentration latitudinally (Figure 7.3). This latitudinal integration shows contributions to the Antarctic sea ice extent changes from each sector in the Southern Ocean.

The annual-mean sea ice is expanding at almost every longitude during 1992-2015 in observations (blue line in Figure 7.3). Note that this is different from the trend calculated over a period that starts from 1979, which has subatantial ice loss in the Amundsen-Bellingshausen sea (e.g., Turner et al., 2015, their Figure 1a). Except for “LENS-4” in the Ross sea, the sea ice area trend simulated in the three CESM LENS is lower than observations at every longitude. The marjor contribution to the underestimated sea ice extent trend in the LENS runs comes from the Indian sector (“LENS-2”, “LENS-4”, and “LENS-6”), the Ross Sea (“LENS-2” and “LENS-6”), and the Weddell Sea (“LENS-2” and “LENS-4”). The exceptional sea ice expansion in the Ross Sea simulated by “LENS-4” is likely due to its overestimated strengthening of the northward ice velocity in this region (Figure D2).

Removing the biases in the mean ice velocity fields (“ObsViClim”) generally improves the simulated sea ice changes in the Ross Sea but not in the other Southern Ocean sectors. By further removing the ice velocity trend biases, we see substantial sea ice expansion in the Ross and Weddell seas (red lines in Figure 7.3), but no substantial changes in the other regions. This suggests that the ice motion plays a significant roles in the ice expansion in the Ross Sea and the Weddell Sea, but not necessarily in the other regions, where thermodynamics may dominate.

7.3.2 Sea ice budget

In this section, we quantify the sea ice changes due to dynamic processes (ice transport and ridging) and thermodynamic processes (melting and freezing) in the CESM simulations, i.e.,

$$\frac{\partial C}{\partial t} = \mathcal{T}_{\text{dyn}} + \mathcal{T}_{\text{therm}}. \tag{7.2}$$

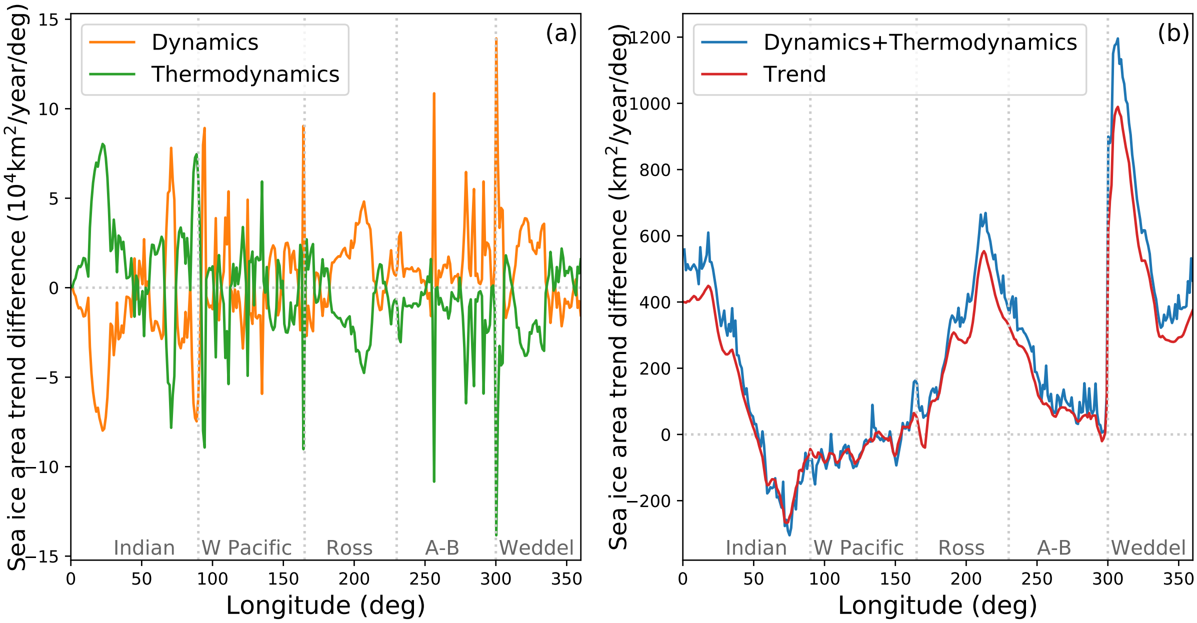

Figure 7.4: (a) Contributions to the sea ice area trend between “LENS-2” and “ObsVi-2” in Figure 7.3 due to dynamic processes (orange) and thermodynamic processes (green). (b) The sea ice area trend difference between “LENS-2” and “ObsVi-2” due to the combination of dynamic and thermodynamic processes (blue) and the diagniosed value from Figure 7.3a (red). The difference between the blue and red lines is due to the residual term in Equation (7.5).

Here C is sea ice concentration, $\mathcal{T}_{\text{dyn}}$ denotes the ice concentration tendency due to dynamic processes, and $\mathcal{T}_{\text{therm}}$ represents the ice concentration tendency due to thermodynamic processes. These two tendency terms are diagnosed and reported as monthly mean data in the model.

Integrating Equation (7.2) in time, we could separate the sea ice concentration at time t into two parts, i.e.,

$$C = \int_0^t \frac{\partial C}{\partial t'} dt' = \int_0^t \mathcal{T}_{\text{dyn}} dt' + \int_0^t \mathcal{T}_{\text{therm}} dt'. \tag{7.3}$$

Consequently, the trend in sea ice concentration could be decomposed into two parts that relate to the dynamic and thermodynamic processes, respectively, that is

$$s = s_{\text{dyn}} + s_{\text{therm}} + \mathcal{R}, \tag{7.4}$$

where s represents the long-term trend in sea ice concentration, s_{dyn} denotes the long-term trend in $\int_0^t \mathcal{T}_{\text{dyn}} dt'$, s_{dyn} represents the long-term trend in $\int_0^t \mathcal{T}_{\text{therm}} dt'$, and $\mathcal{R}$ is the residual. In a linear system, the long-term trend would be equal to the mean of tendency term in Equation (7.2) and the residual $\mathcal{R} = 0$.

Therefore, differences in the sea ice concentration trend between two CESM simulation can be attributed to a combination of dynamic and thermodynamic processes, i.e.,

$$\delta s = \delta s_{\text{dyn}} + \delta s_{\text{them}} + \mathcal{R}'. \tag{7.5}$$

Here R' represents the residual due to nonlinearity and time-averaging in the data. Integrating Equation (7.5) latitudinally, we could diagnose whether it is the ice dynamics or thermodynamics that are responsible for the different sea ice extent trend between "LENS" and "ObsVi" in Figure 7.3. We present the results in Figures 7.4, D7, and D8.

The contributions to sea ice area trend due to dynamic processes and thermodynamics processes largely concel each other (Figure 7.4a). The residual between the two roughly reproduces the linear trend in the latitudinally integrated sea ice area (Figure 7.4b). Imposing the observed ice velocity in “ObsVi” runs cause more ice expansion due to dynamic processes in the Ross Sea and Weddell Sea, comparing to the “LENS” runs (Figures 7.4a, D7, and D8). However, this is not true for the other Southern Ocean sectors, implying either thermodynamics dominate or there are no substantial biases in the ice velocity in these regions.

7.4 Summary and discussion

Sea ice coverage in the Antarctic has expanded significantly since the late 1970s until recently. However, most of the state-of-the-art climate models simulated a retreating Antarctic sea ice. Here, we test whether the ice velocity biases in climate models could explain the discrepancies between observations and climte models.

By restoring ice velocity to observations in a comprehensive climate model, we simulate an overall expansion of the Antarctic sea ice that is closer to observations. This increased ice expansion mainly takes place in the Ross and Weddell Seas, implying the importance of ice dynamics to simulating sea ice changes in these two regions, which is confirmed in our budget analysis.

However, our simulations with ice velocity relaxed to observations does not reproduce the observed distribution of sea ice trend. This infers the potential importance of thermodynamics to the observed sea ice changes (e.g., Bintanja et al., 2013; Su, 2017; Zhang et al., 2019).

Although we highlighted the importance of ice dynamics to sea ice changes in this study, it is still not clear what is causing the ice velocity biases in climate models. These biases could arise from uncertainties in the simulated wind and ocean current or from an inaccurate representation of the ice rheology in the models. Our preliminary results suggest that correcting the surface wind biases alone does not substantially improve the simulations of sea ice trend (not shown), implying the importance of improving the representation of ocean circulation and ice rheology to achieve a proper simulation of sea ice changes.

Acknowledgments

This chapter is a draft of manuscript in preparation for submission as “The influence of ice velocity biases on the Antarctic sea ice extent trends”, by S. Sun and I. Eisenman. The dissertation author was the primary investigator and author of this work.

Chapter 8

Concluding remarks

Variations in the global ocean overturning circulation have been suggested to be a key player in climate variability on time scales from decades (e.g., Zhang and Zhang, 2015) to thousands of years (e.g., Sigman et al., 2010). For example, both an enhanced deep ocean stratification and a shallower AMOC have been proposed as key contributors to the lower atmospheric CO_2 at the Last Glacial Maximum (LGM) (e.g., Sigman et al., 2010; Watson et al., 2015). A number of studies during recent decades have highlighted the importance of Southern Ocean processes in constraining the global ocean overturning circulation (e.g., Ferrari et al., 2014).

In the bulk of this dissertation (Chapter 2 to 6), I use a combination of numerical model simulations and conceptual theories to explore the surface constraints on the global ocean overturning circulation. Wheareas Chapter 2 demonstrates the importance of Southern Ocean surface buoyancy forcing in setting the deep ocean stratification, the later chapters (Chapter 3 to 5) illustrate that the North Atlantic can be equally important as the Southern Ocean in setting the AMOC depth. The importance of the Southern Ocean to the AMOC is further weakened when the overturning circulation is not in steady state (Chapter 6). The results in Chapter 6 also suggest that the Indo-Pacific Ocean needs to be considered in order to understand the transient response of the global ocean overturning circulation.

Deep ocean stratification

Previous studies have suggested that the global ocean density stratification below ~3000m is approximately set by its direct connection to the Southern Ocean surface density, which in turn is constrained by the atmosphere. In Chapter 2, the role of Southern Ocean surface forcing in the glacial-interglacial stratification changes is investigated using the ocean component of a comprehensive climate model and an idealized conceptual model. Southern Ocean surface forcing is found to control the global deep ocean stratification all the way up to ~2000m, which is a much wider depth range than previously thought and contrary to the expectation that the North Atlantic surface forcing should strongly influence the ocean at intermediate depths. We show that this is due to the approximately fixed surface freshwater fluxes, rather than a fixed surface density distribution in the Southern Ocean as was previously considered. These results suggest that Southern Ocean surface freshwater forcing controls glacial-interglacial stratification changes in much of the deep ocean.

AMOC depth

Paleoclimate proxy data suggests that the AMOC was shallower at the LGM than its preindustrial (PI) depth. In Chapter 3, we investigate the connections of the AMOC depth to the Southern Ocean surface buoyancy forcing, using a set of ocean-only simulations with surface forcing specified from the output of previous coupled PI and LGM simulations. In contrast to previous expectations, we find that applying LGM surface forcing in the Southern Ocean and PI surface forcing elsewhere causes the AMOC to shoal only about half as much as when LGM surface forcing is applied globally. We show that this occurs because diapycnal mixing renders the Southern Ocean overturning circulation more diabatic than previously assumed. The diabatic processes in the Southern Ocean diminish the influence of Southern Ocean surface buoyancy forcing on the AMOC depth such that the AMOC depth could also be affected by processes in the North Atlantic.

The impact of North Atlantic surface buoyancy conditions on the Southern Ocean circulation and the AMOC is investigated in Chapter 4 using a sector configuration of an ocean general circulation model. We find that the response of the Antarctic Circumpolar Currents (ACC) transport to North Atlantic surface buoyancy conditions is dependent on the simulated AMOC depth. As the surface density decreases in the North Atlantic, the AMOC gets shallower and the ACC transport becomes less sensitive to North Atlantic surface buoyancy forcing.

Building on these results, we explore how both hemispheres set the AMOC depth in Chapter 5. In order to identify the key processes that set the AMOC depth, we carry out a number of MITgcm ocean-only simulations with surface forcing fields specified from the simulation results of three coupled climate models that span the range of glacial AMOC depth changes in the Paleoclimate Model Intercomparison Project Phase 3 (PMIP3). We find that the MITgcm simulations successfully reproduce the changes in AMOC depth between glacial and modern conditions simulated in these three PMIP3 models. By varying the restoring timescale in the surface forcing, we show that the success of the MITgcm simulations in reproducing these changes hinges on the surface density field rather than the surface buoyancy flux field. Based on these results, we propose a mechanism by which the surface density fields in the high latitudes of both hemispheres are connected to the AMOC depth. We illustrate the mechanism using MITgcm simulations with idealized surface forcing perturbations as well as an idealized conceptual geometric model. These results suggest that the AMOC depth is largely determined by the surface density fields in both the North Atlantic and the Southern Ocean.

AMOC in transient states

In Chapter 6, we explore the importance of Southern Ocean processes in the transient response of the global ocean overturning circulation. The projected weakening of the AMOC in climate models appears to contradict the stronger Southern Hemisphere westerly wind in a warming climate. A resolution to this contradiction is proposed that involves the Indo-Pacific component of the global ocean overturning circulation: changes in the Indo-Pacific overturning circulation can compensate AMOC variations such that the globally integrated overturning circulation stays roughly constant in the Southern Ocean. We investigate this inter-basin compensation using an ocean-only model. We find that this compensation depends on the AMOC variability timescales. For relatively high-frequency variability of the AMOC (less than 1000 years), the Indo-Pacific overturning circulation can compensate most of the AMOC changes through the inter-basin transport between the Atlantic and Indo-Pacific basins. As the AMOC variability timescale increases, the Southern ocean upwelling begins to respond and the inter-basin compensation decreases. The results are largely reproduced in a 1.5-layer reduced gravity model and a conceptual two-box model. The results raises concerns on studies that use the Southern Ocean processes to interpret AMOC variability when the ocean is not in steady states.

Sea ice

In the last science chapter, Chapter 7, I switch to a somewhat different topic and investigate the influence of ice velocity baises on the Antarctic sea ice extent trend. In contrast to the Arctic, sea ice cover in the Antarctic has expanded significantly since the late 1970s until recently. However, this expansion is not captured in most state-of-the-art climate models. Among the many mechanisms that have been proposed to explain the Antarctic sea ice expansion, sea ice motion provides a compelling explanation to reconcile the observed and simulated sea ice changes. We find that the simulated sea ice extent trend in a comprehensive climate model becomes substantially closer to observations when the sea ice motion is specified based on observations rather than simulated. This suggests that biases in the simulated ice velocity fields can largely account for the discrepancies between the observed and simulated sea ice extent trend in the Southern Ocean and hence that better representation of sea ice motion is crucial for climate models to more accurately represent sea ice changes.

Appendix A

Appendix for Chapter 2

A.1 CESM setup

We run CESM version 1.1.2 using a configuration in which only the ocean is active. The ocean component of CESM is the Parallel Ocean Program version 2 (POP2) (Danabasoglu et al., 2012), which has 60 vertical levels ranging from 10m at the surface to 250m at the ocean bottom. We use the CESM "f09_g16" grid, which has a horizontal resolution of nominally 1° with the north pole of the ocean grid displaced to Greenland. This is the same grid configuration that was used in the coupled PI simulation (Gent et al., 2011) and the coupled LGM simulations (Brady et al., 2013), from which the forcing in this study is derived. The coupled simulations have a resolution for the land and atmosphere components of $1.9^\circ \times 2.5^\circ$ and the same resolution for the sea ice component as for the ocean.

The Gent-McWilliams (GM) parameterization (Gent and Mcwilliams, 1990) is used to represent the unresolved mesoscale eddies. A GM coefficient is adopted that varies proportional to the local density stratification. This coefficient varies in the horizontal directions and decays with depth, mimicking the decay of eddy activity with depth (Gent and Danabasoglu, 2011; Gent, 2016). This allows the model simulations to compare more favorably with observations than models that use a constant diffusivity (Danabasoglu and Marshall, 2007), and it enables the model to simulate a response to perturbations in the surface forcing that is comparable to simulations run at much higher resolutions (Gent and Danabasoglu, 2011; Gent, 2016).

The forcing for each ocean-only simulation is constructed from the coupled model output as a series of repeating 30-year cycles using simulations years 1050-1079 of the coupled PI simulation and 1870-1899 of the coupled LGM simulation. Atmospheric forcings including precipitation, solar radiation, surface winds speed, atmospheric pressure, and atmospheric humidity are taken from output reported by the CCSM4 coupler and have 3-hr temporal resolution. Fluxes across the atmosphere-ocean interface, including evaporation, wind stress, upward longwave radiation, latent heat flux, and sensible heat flux, are calculated in the ocean-only runs based on the simulated ocean state and the specified atmospheric state. For ice-related forcing including sea ice concentration (i.e., fraction of grid box covered by ice) and heat flux between the ice and the ocean, we use daily-mean data reported by the CCSM4 sea ice component (CICE). For other ice-related forcing including freshwater flux, ice/ocean stress, and salt flux, daily output is not available so we use monthly-mean data reported by CICE. For river runoff and glacial runoff we used monthly-mean data reported by the CCSM4 land component (CLM4).

In order to obtain better agreement between the coupled runs and the ocean-only runs, a process called “diddling” is performed on all monthly-mean data. This allows the monthly-mean values to be preserved when the model linearly interpolates between values at the midpoint of each month. Details are given in Killworth (1996).

The sea level was about 100m lower at the LGM than today due to the presence of larger high-latitude ice sheets. This gives rise to slightly different coastlines at the LGM, which is accounted for in the coupled CCSM4 LGM simulation. In order to isolate the influence of surface forcing alone, in the present study we use modern ocean bathymetry in the LGM and Test simulations, as in the PI simulation. As a result, some ocean regions in the ocean-only simulations are land in the coupled LGM simulation that is used to generate the forcing fields.

If these areas are not treated appropriately, they can lead to the generation of extremely cold surface water due to the direct contact with the cold terrestrial atmosphere in locations where sea ice would have formed if the sea ice model were active (this is exacerbated by the fact that the surface air in some of these locations is hundreds of meters above the sea level at the surface of the ice sheet in the coupled LGM simulation). To address this issue, both the sea ice concentration and atmospheric forcing need to be adjusted when we apply LGM forcing in locations that are ocean in the PI bathymetry but land in the coupled LGM simulation. We adjust the surface air temperature and potential temperature in these locations by assuming a constant lapse rate of $-6.5°\mathrm{C/km}$ to account for the change of surface geopotential height between the coupled LGM and coupled PI runs. The surface atmospheric pressure is adjusted by assuming exponential decay with height, $p = p_0 \exp(-z/H)$, where $H = 7.6\mathrm{km}$ is the scale height. The sea ice concentration (c) in these grid cells is prescribed based on the surface air temperature (T) as $c = 1/2\tanh[(T - T_0)/T_0] + 1/2$, where $T_0 = -2°\mathrm{C}$. This is motivated by the observation that in the coupled simulations, most ocean locations with surface air temperature below $-5°\mathrm{C}$ have ice concentrations close to 100%, and most ocean locations with surface air temperature above 0°C have ice concentrations close to 0%. All fluxes between the ice and ocean in these grid cells are set to zero, including the freshwater flux, salt flux, and momentum flux.

All forcing fields in the ocean-only simulations are from the coupled simulations as specified in Section 2.2, with two exceptions. First, all three ocean-only simulations use the same run-off forcing, which is derived from the coupled PI run. Second, for the weak restoring of surface salinity, which is included in the ocean-only model as described in Griffies et al. (2009), the Test run uses salinity restoring field derived from the coupled PI run at all locations, including the Southern Ocean. This simplification appears to have only a small influence on the Test run: the difference between the LGM and Test freshwater fluxes associated with the weak restoring of surface salinity in most Southern Ocean locations is less than 10% of the difference between the LGM and PI runs (not shown), and the surface buoyancy forcing profiles in the Southern Ocean are nearly indistinguishable between the LGM and Test runs (see Figure 2.1 in Chapter 2).

The surface temperature and salinity for the three ocean-only runs are shown in Figs. A1 and A2. In general, the surface salinity is less constrained by the forcing than the surface temperature. This is expected because the freshwater flux more closely resembles a fixed flux, while the heat flux more closely resembles a relaxation boundary condition (Haney, 1971b) that tends to fix the surface temperature. Under fixed flux boundary conditions, the actual value of surface salinity is strongly influenced by salt fluxes within the ocean.

Table A1: Durations of model simulations and trends of global volume-average temperature, ideal age, and AMOC max calculated over the last 120 years of each run.

Run Name	PI	Test	LGM
Surface forcing	PI	PI&LGM	LGM
Duration (years)	510	1020	1440
Temperature trend (°C/century)	-0.046	-0.048	-0.053
Ideal Age trend (year/century)	16.8	8.8	9.6
AMOC max trend (Sv/Century)	-0.28	-0.16	-0.64

A.2 Details of the deep ocean stratification and model equilibration

The zonal mean stratification in the Atlantic Ocean is shown in Figure A3, with the basin-average stratification profile given in Figure A4 for the South Atlantic, South Pacific, and Indian Oceans, and in Figure A5 for the North Atlantic, North Pacific, and Southern Oceans. In every ocean basin the Test run approximately reproduces the LGM deep ocean stratification below 2000m. The deep stratification in the Atlantic Ocean is stronger than in the other ocean basins, which is likely due to the presence of the North Atlantic Deep Water (NADW).

Figure A6 shows the change in the stratification between the last two 30-year periods in the Atlantic Ocean as an indication of the level of equilibration in the simulations. The PI run has a similar trend to the Test run, while the LGM run has a trend that is approximately 3 times

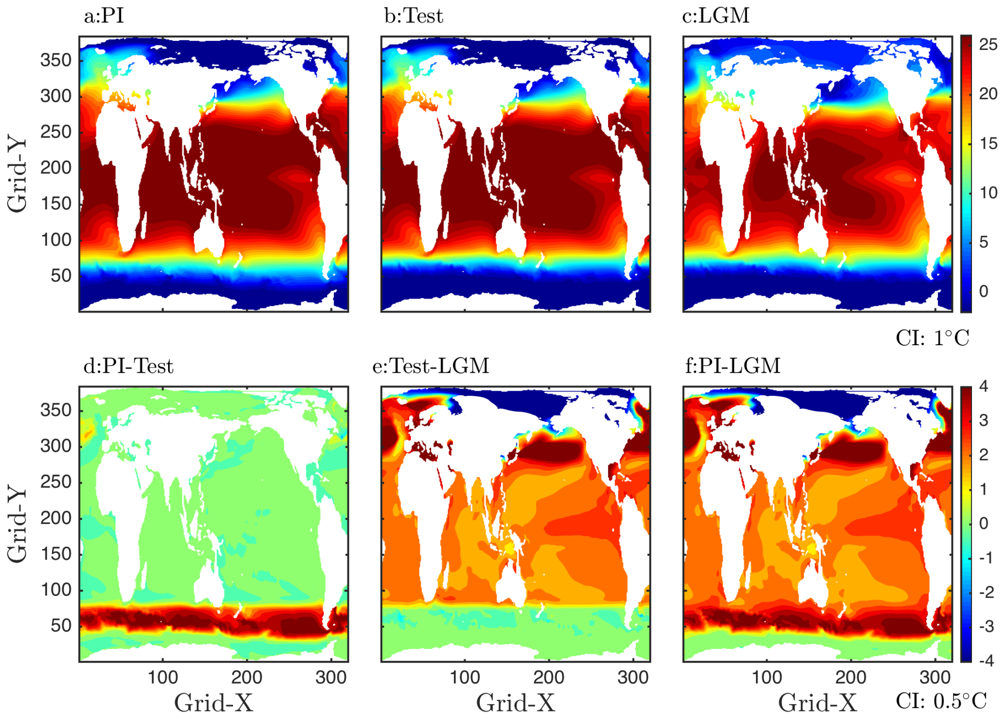

Figure A1: Long-term mean surface potential temperature (°C) in the three model runs and the differences between them. The fields are plotted here on the coordinates of the ocean model grid, which has the North Pole displaced to Greenland (Danabasoglu et al., 2006).

larger. The magnitude of the deep ocean stratification changes from one 30-year period to the next (Figure A6) are approximately 100 times smaller than the differences between the three simulations (Figure A3).

A.3 Conceptual model

A.3.1 Derivation of the conceptual model

The derivation of the conceptual model follows Nikurashin and Vallis (2011) and Nikurashin and Vallis (2012); see these studies for further details. The model takes a zonally-averaged view of the global stratification and overturning circulation, which are described by the zonal-mean buoyancy $b^* \equiv -g(\rho - \rho_0)/\rho_0$ and overturning circulation streamfunction $\psi(y,z)$. Here we use

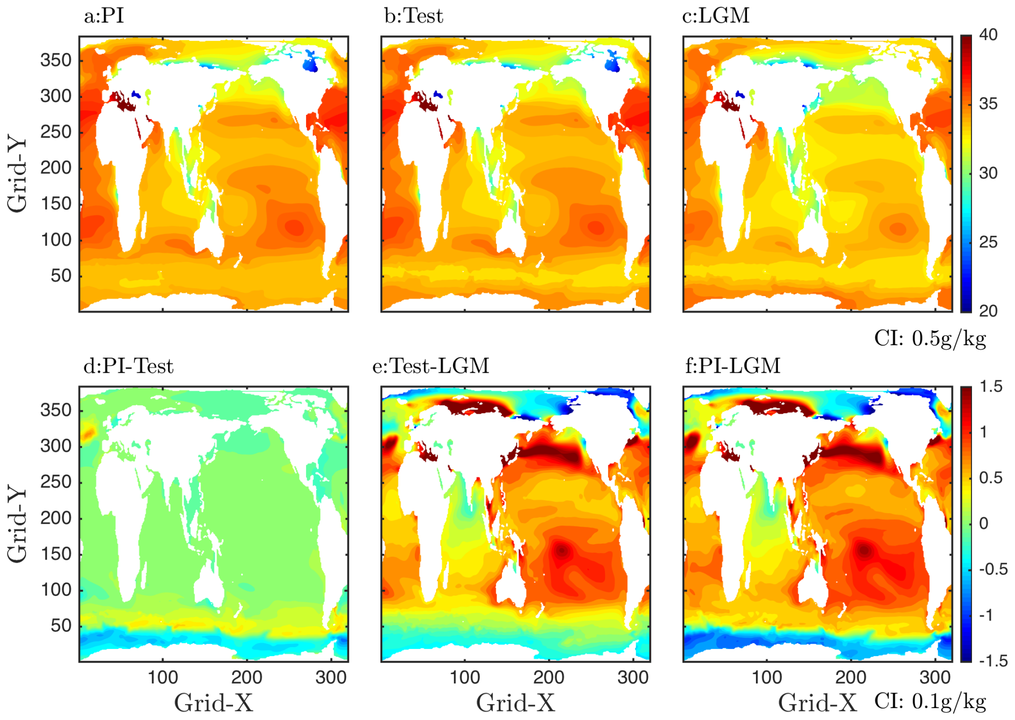

Figure A2: Long-term mean surface salinity (g/kg) in the three model runs and the differences between them. Coordinates are as in Figure A1.

ψ to describe the zonally integrated circulation rather than the zonal-mean circulation, i.e., ψ has units of m^3/s rather than m^2/s as in Nikurashin and Vallis (2012). The ocean is approximated to consist of a single basin (e.g., the Atlantic) of meridional length L_y and zonal length L_x, which is connected to a re-entrant zonal channel at the southern boundary (resembling the Southern Ocean). This configuration is sketched in Figure 2.2 in Chapter 2. In the basin the isopycnals are assumed to be flat, so we define $b(z) \equiv b^*(y,z)$ for all $y > 0$, while in the channel ($y < 0$) the isopycnals are assumed to have a constant isopycnal slope s. The surface of the channel is subject to a fixed downward buoyancy flux $B(y)$, and the formation of NADW at the northern end of the basin is represented by $\psi^*(z) \equiv \psi(L_y, z)$. The flow in the channel is assumed to be adiabatic, while the basin is subject to a constant diapycnal diffusivity κ.

Following Nikurashin and Vallis (2012), volume conservation implies that at a given depth, the change in the overturning streamfunction across the basin is equal to the net upwelling

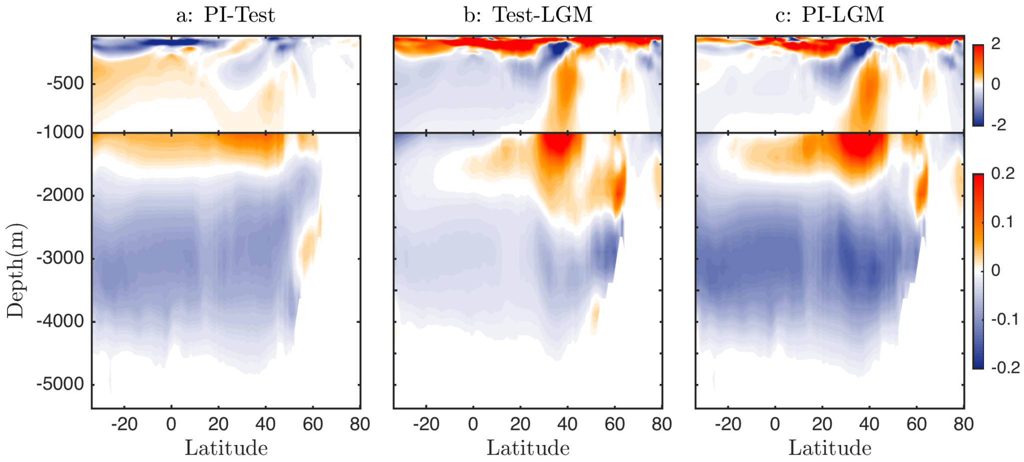

Figure A3: Comparison of the zonal-mean stratification in the Atlantic Ocean between the three model runs (N^2, in units of 10^{-5} s^{-2}). Note that the magnitude of the stratification difference in panel b below about 2000m is 10 times smaller than that in panels a and c.

driven by diapycnal diffusion within the basin,

$$\psi^*(z) - \psi(0,z) = \frac{\kappa L_y L_x}{N^2} \frac{\partial}{\partial z} N^2(z), \tag{A1}$$

where $y = 0$ represents the northern boundary of the Southern Ocean (Figure 2c). Here $N^2 \equiv \partial b/\partial z$ is the Brunt-Väisälä frequency, which is a measure of the ocean density stratification. For isopycnals that outcrop in the Southern Ocean, the overturning streamfunction at the base of the mixed layer ($z = 0$) can be related to the surface buoyancy forcing by

$$\psi(y,0) = \frac{L_x B(y)}{\partial b/\partial y} \tag{A2}$$

for $y < 0$ (cf. Marshall and Radko, 2003). Since the overturning circulation is assumed to be adiabatic in the Southern Ocean, the value of the streamfunction at the base of the mixed layer ($z = 0$) must match the value at the northern edge of the channel ($y = 0$) along the same isopycnal.

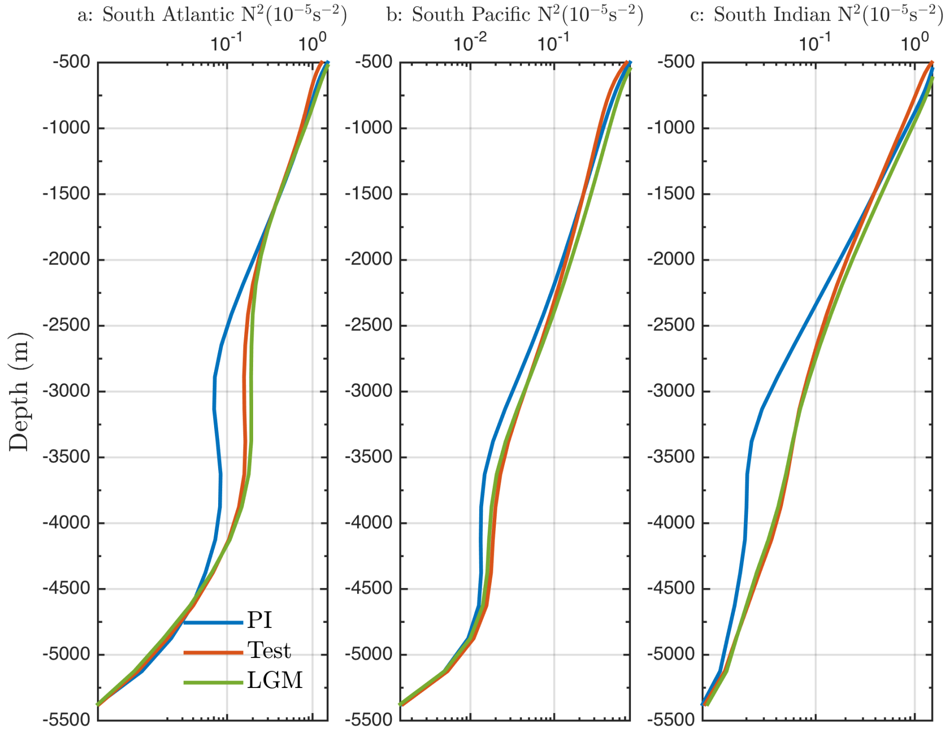

Figure A4: Basin-averaged stratification in the South Atlantic, South Pacific, and South Indian Oceans (N^2, in units of 10^{-5} s^{-2}).

For constant isopycnal slope s in the Southern Ocean, this implies

$$\psi(-z/s,0) = \psi(0,z). \tag{A3}$$

Combining equation (A1), (A2), and (A3), we obtain

$$\frac{\kappa L_y L_x}{N^2(z)} \frac{\partial}{\partial z} N^2(z) = \psi^*(z) + L_x \frac{B(-z/s)}{s N^2(z)}, \tag{A4}$$

which is equivalent to Equation (2.2) in Chapter 2.

Isopycnals in Region 3 outcrop only in the Southern Ocean, and ψ^* is zero at the northern boundary. Therefore Equation (A4) reduces to

$$\kappa s L_y \frac{\partial}{\partial z} N^2(z) = B(-z/s), \tag{A5}$$

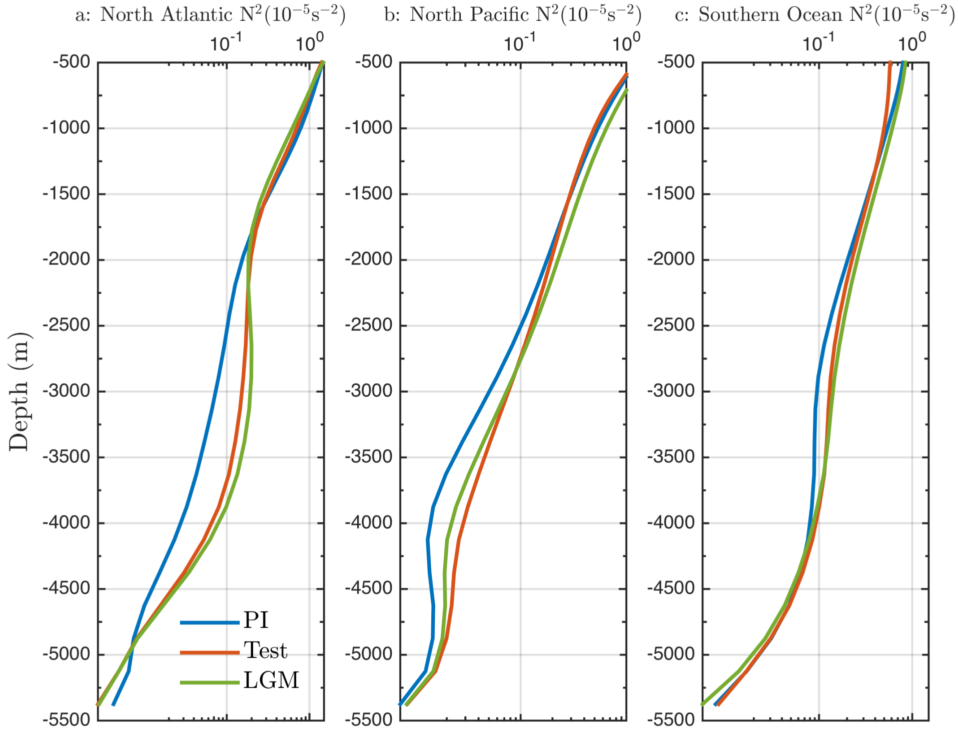

Figure A5: Basin-averaged stratification in the North Atlantic, North Pacific, and Southern Oceans (N^2, in units of 10^{-5} s^{-2}).

which is equivalent to Equation (2.3) in Chapter 2. Assuming that N^2 is negligibly small at the bottom boundary $z = z_{bot}$ (see Figure 2.3 in Chapter 2), integration of Equation (A5) shows that the stratification in Region 3 is determined by the surface buoyancy forcing in the Southern Ocean only as long as B is specified:

$$N^2(z) = \int_{z_{bot}}^{z} \frac{B(-z'/s)}{\kappa s L_y} dz'. \tag{A6}$$

However, if the surface buoyancy forcing takes the form of a relaxation boundary condition, $B(y) = r\,[b_s(y) - b^*(y,0)]$ with r the relaxation coefficient, b_s the specified surface buoyancy, and $b^*(y,0)$ the buoyancy at the surface of the Southern Ocean, then the buoyancy $b(z)$ appears on both sides of Equation (A6), so this equation no longer directly indicates what determines the

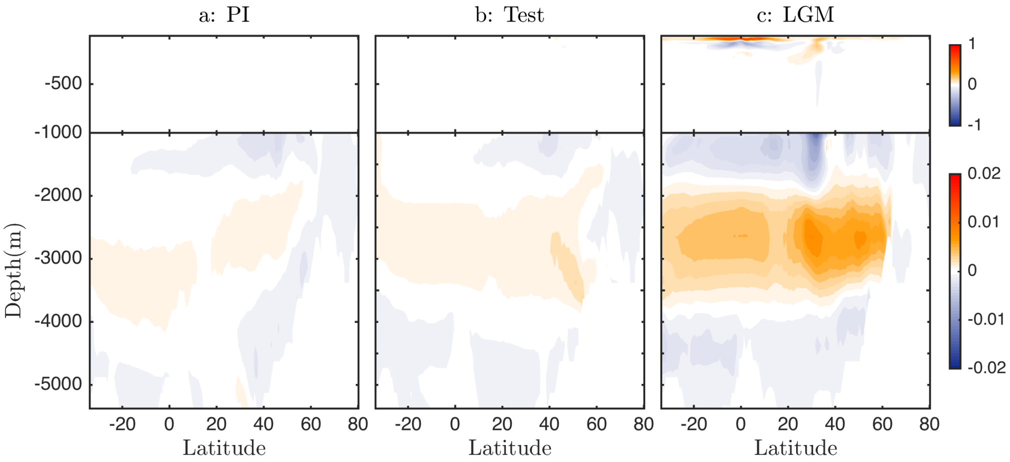

Figure A6: Change of the zonal-mean stratification in the Atlantic Ocean between the last two 30-year cycles (N^2, in units of 10^{-5} s^{-2}). Note that the magnitude of the stratification change in the deep ocean is of order 0.001×10^{-5} s^{-2}, which is 100 times smaller than in Figure A3.

stratification. In this case, Equation (A5) becomes

$$\kappa s L_y \frac{\partial}{\partial z} N^2(z) + r b(z) = r b_s(-z/s), \tag{A7}$$

where we have used $b^*(y,0) = b^*(-z/s,0) = b(z)$, i.e., the buoyancy in the basin is equal to the buoyancy at the surface of the Southern Ocean along the same isopycnal. Since $N^2 \equiv \partial b/\partial z$, Equation (A7) is a second-order ordinary differential equation for $b(z)$. In this case, the abyssal stratification is affected by the upper boundary condition for b, and so it is subject to at least slight inter-hemispheric influences as expected from Fučkar and Vallis (2007).

In Region 2, where ψ^* does not vanish, we consider the difference between the stratifications in the LGM and Test runs, which can be derived from Equation (A4) as

$$\kappa L_y L_x \frac{\partial}{\partial z}\left(N^2_{\text{LGM}}(z) - N^2_{\text{Test}}(z)\right) = \left(N^2_{\text{LGM}}(z)\psi^*_{\text{LGM}}(z) - N^2_{\text{Test}}(z)\psi^*_{\text{Test}}(z)\right) + \frac{L_x}{s}\left(B_{\text{LGM}}(-z/s) - B_{\text{Test}}(-z/s)\right), \tag{A8}$$

where the subscripts indicate the simulation name. Since both the LGM and Test simulations are subject to the same approximately fixed LGM surface forcing in the Southern Ocean, we approximate the last term in Equation (A8) to be negligibly small (see Figure 2.1 in Chapter 2), and Equation (A8) becomes

$$\begin{aligned}
\kappa L_y L_x \frac{\partial}{\partial z}\left(N^2_{\mathrm{LGM}}(z) - N^2_{\mathrm{Test}}(z)\right) =& N^2_{\mathrm{LGM}}(z)\psi^*_{\mathrm{LGM}}(z) - N^2_{\mathrm{Test}}(z)\psi^*_{\mathrm{Test}}(z)\\
=& N^2_{\mathrm{LGM}}(z)\left(\psi^*_{\mathrm{LGM}}(z) - \psi^*_{\mathrm{Test}}(z)\right) +\\
& \psi^*_{\mathrm{Test}}(z)\left(N^2_{\mathrm{LGM}}(z) - N^2_{\mathrm{Test}}(z)\right)\\
=& N^2_{\mathrm{LGM}}(z)\Delta\psi^* + \psi^*_{\mathrm{Test}}\Delta N^2\\
=& N^2_{\mathrm{LGM}}(z)\Delta\psi^*\left(1 + \frac{\psi^*_{\mathrm{Test}}\Delta N^2}{\Delta\psi^* N^2}\right).
\end{aligned} \tag{A9}$$

At the depth of isopycnal surface ρ_2 that separates the upper and lower overturning cells, defined here as z_0, $N^2_{\mathrm{LGM}} \approx N^2_{\mathrm{Test}} \gg \Delta N^2$ and $\psi^*_{\mathrm{Test}} \sim \psi^*_{\mathrm{LGM}} \sim \Delta\psi^* \sim 0$, as discussed above. Hence $\frac{\psi^*_{\mathrm{Test}}\Delta N^2}{\Delta\psi^* N^2} \ll 1$ and Equation (A9) can be approximately written near $z = z_0$ as

$$\kappa L_y L_x \frac{\partial}{\partial z}\Delta N^2(z) \approx N^2_{\mathrm{LGM}}(z)\Delta\psi^*(z), \tag{A10}$$

where $\Delta N^2 \equiv N^2_{\mathrm{LGM}} - N^2_{\mathrm{Test}}$ and $\Delta\psi^* \equiv \psi^*_{\mathrm{LGM}} - \psi^*_{\mathrm{Test}}$. Using a realistic Atlantic area of $L_x L_y = 8 \times 10^{13}\mathrm{m}^2$, diapycnal diffusivity of $\kappa = 1 \times 10^{-4}$ m^2/s, and Region 2 approximate depth range of $\delta z = 1000$m, this implies that the NADW streamfunction must differ between the LGM and Test runs by $\Delta\psi^* \approx 8\,\mathrm{Sv}$ in order to produce an order-one fractional change in the vertical change of the stratification over the depth of Region 2. Given the small change in NADW of about 2 Sv between the LGM and Test simulations, we suggest that this explains why the change in stratification across the depth range of Region 2 (approximately 2km to 3km) is similar in the LGM and Test simulations (red and green lines in Figure 2.3a).

Note that in Region 1, the influence from the surface wind-driven circulation is non-negligible, so the assumption adopted here of flat isopycnals in the basin is not applicable.

An important caveat is that this conceptual model is only used in order to achieve a qualitative understanding of the influence of the Southern Ocean surface forcing on the abyssal and mid-depth stratification. This model should not be expected to quantitatively reproduce the stratification profiles shown in Figure A4 and A5. For example, the stratification in the Atlantic is clearly different from the other basins, which is not accounted for in this conceptual model. Furthermore, the assumption of an adiabatic Southern Ocean circulation in our conceptual model is not strictly justified. This can be seen in Figure A7, which shows the residual overturning circulation streamfunction in the Southern Ocean for the three model runs, calculated in σ_2 coordinates. A diabatic component to the circulation south of 50°S is readily discernible. This enhanced diapycnal flow in the Southern Ocean is mainly associated with the deep mixed layer inside the subpolar gyre. Away from the subpolar gyre region, the residual overturning circulation streamfunction approximately follows isopycnals, i.e., the adiabatic assumption is approximately satisfied.

A.3.2 Non-constant isopycnal slope

In the analysis above, we assumed a constant isopycnal slope in the Southern Ocean for simplicity, and we concluded that the NADW streamfunction would need to differ considerably between the LGM and Test runs to produce a substantial change in the stratification of Region 2. Here we show this conclusion still holds if we relax the assumption of constant isopycnal slope in the Southern Ocean to allow the slope to vary between different isopycnals. Note that this analysis will focus on the Southern Ocean region, whereas the analysis in Section A.3.1 focused on the basin north of the Southern Ocean.

Following Nikurashin and Vallis (2011), the residual overturning circulation streamfunc-

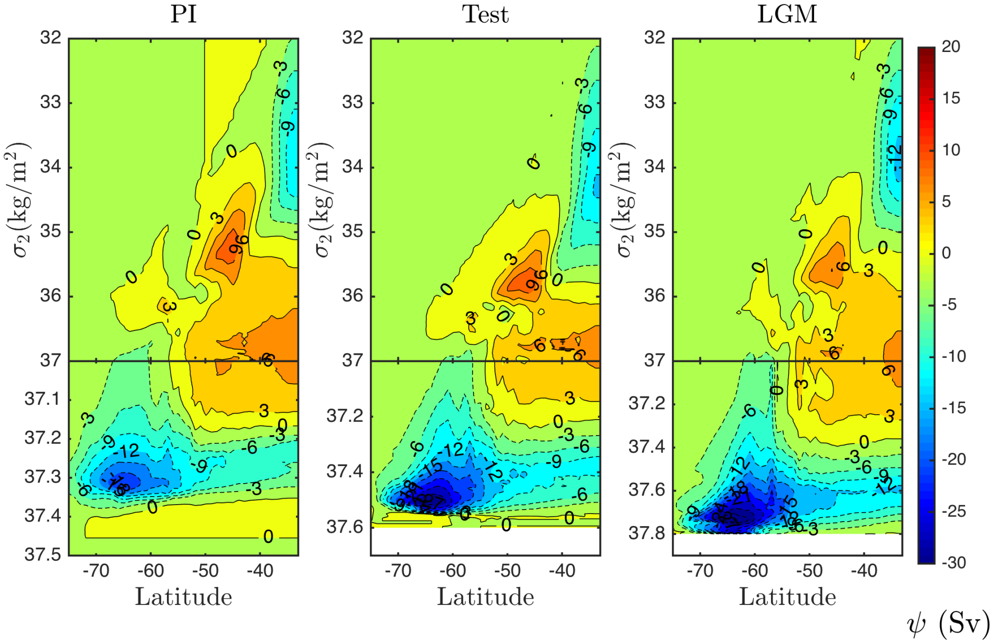

Figure A7: Residual overturning circulation streamfunction in the Southern Ocean (Sv) using σ_2 as the vertical coordinate.

tion in the Southern Ocean can be written as

$$\psi = \psi^{+} + \psi^{\#}. \tag{A11}$$

Here, ψ^{+} represents the contribution from mean flow and is given by the surface Ekman transport,

$$\psi^{+} = -\frac{\tau_0 L_x}{f_0 \rho_0}, \tag{A12}$$

and $\psi^{\#}$ is the eddy-driven overturning circulation streamfunction which can be expressed as

$$\psi^{\#} = L_x K_{\mathrm{GM}}\, s \tag{A13}$$

based on the Gent-McWilliams (GM) parameterization of mesoscale eddies. Here K_{GM} is the GM thickness diffusivity which is a function of the local stratification in our ocean-only CESM

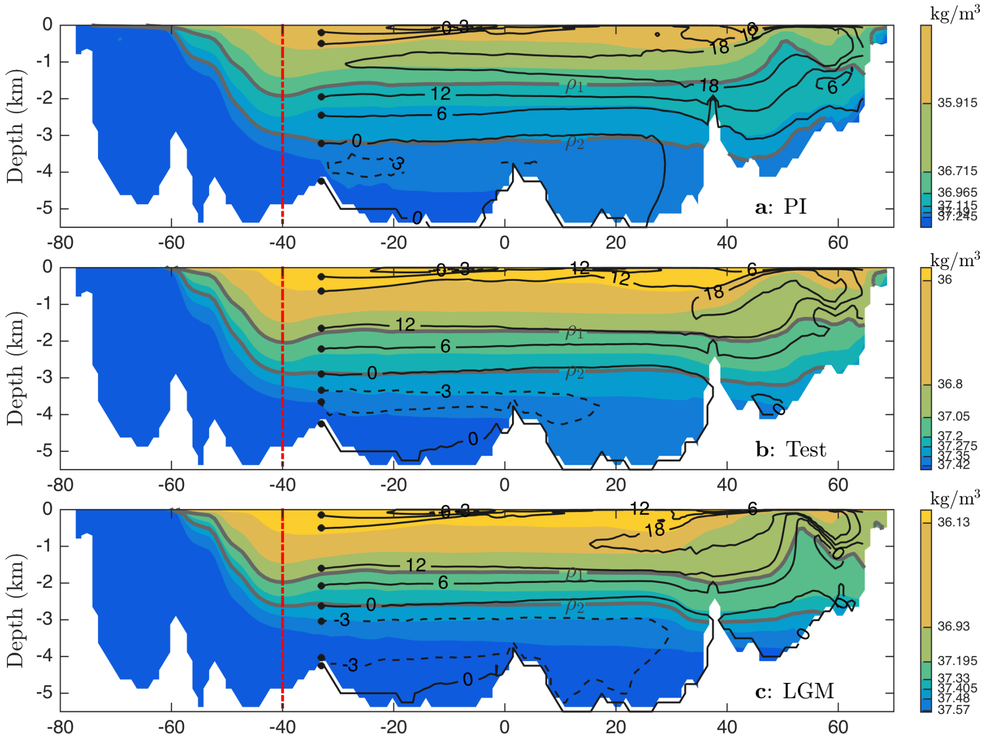

Figure A8: As in Figure 2.2b in the main text, but including the PI and LGM simulations as well as the Test simulation. (Note that panel b here is equivalent to Figure 2.2b.)

simulations. We assume for simplicity that the surface wind stress forcing (τ_0) and Coriolis parameter (f_0) are constant, which implies that ψ^+ is constant across the Southern Ocean and all Eulerian-mean vertical motions occur in the southern and northern boundary of the Southern Ocean. This simplification is also made in Nikurashin and Vallis (2011) for qualitative discussions.

In the ocean-only CESM simulations, both the GM thickness diffusivity K_{GM} and isopycnal slope s vary somewhat in the Southern Ocean (Figure A9 and A10), and they combine together to support the southward NADW transport into the Southern Ocean as in Abernathey et al. (2011), i.e., both K_{GM} and s vary to account for the vertical change of ψ at the northern boundary of the Southern Ocean. Here, for simplicity, we only allow s to vary but keep K_{GM} constant, as in previous idealized modeling studies (e.g., Wolfe and Cessi, 2011).

Furthermore, we assume the circulation in the Southern Ocean to be adiabatic, i.e., the

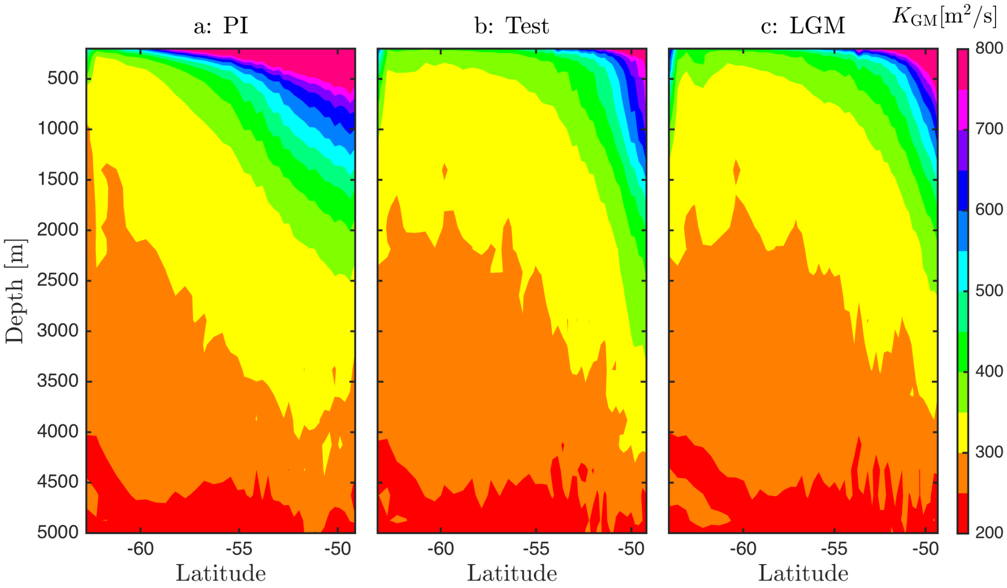

Figure A9: Gent-McWilliams (GM) thickness diffusion coefficient (K_{GM}; units of m^2/s) averaged zonally along barotropic streamlines.

residual overturning circulation streamfunction ψ is constant along each individual isopycnal surface. Hence the assumption of a constant ψ^+ implies that the eddy-driven overturning circulation streamfunction $\psi^\#$ must also be constant along each isopycnal surface.

Consider the residual overturning circulation on two isopycnals, ρ_2 and ρ_*, where ρ_2 is indicated in Figure 2.2c as the isopycnal that separates the abyssal overturning circulation from the region above, and ρ_* can be any isopycnal between ρ_1 and ρ_2. In the Southern Ocean, the southward flux of NADW (ψ_{NADW}) between ρ_2 and ρ_* has to be balanced by the vertical change in the eddy-driven overturning circulation streamfunction since the Eulerian-mean overturning circulation (ψ^+) has been assumed to be constant,

$$\psi_{\mathrm{NADW}} = \psi_* - \psi_2 = \psi_*^\# - \psi_2^\#. \tag{A14}$$

Here, ψ_* and ψ_2 are the residual overturning circulation streamfunction on isopycnal surface ρ_* and ρ_2, and $\psi_*^\#$ and $\psi_2^\#$ are the eddy-driven overturning circulation streamfunction on isopycnal

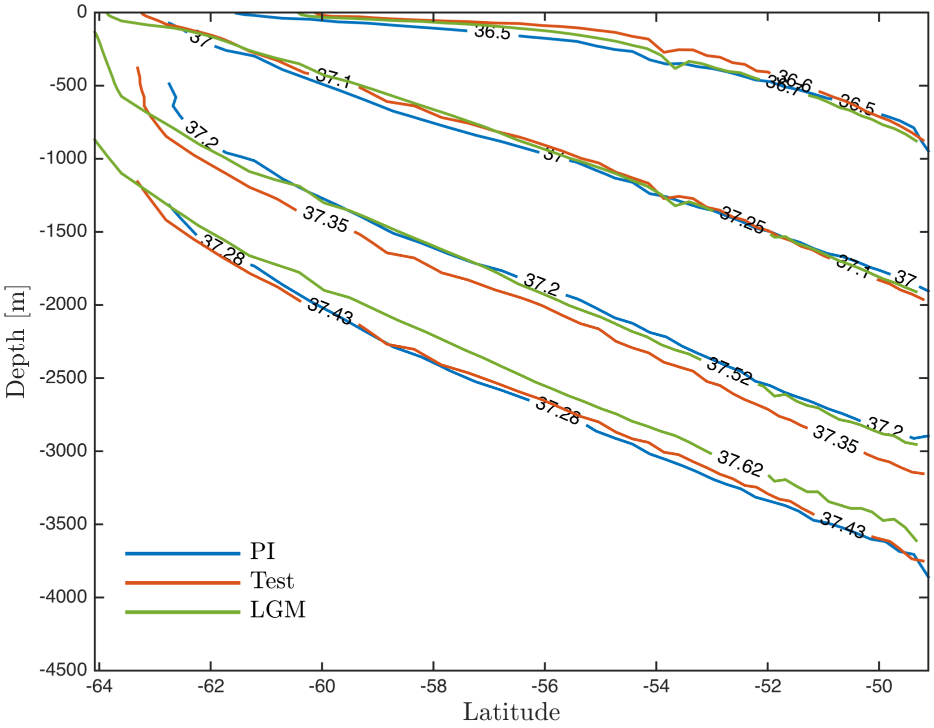

Figure A10: Isopycnal contours of σ_2 (units of kg/m^3) averaged zonally along barotropic streamlines.

surfaces ρ_* and ρ_2. Combining equation (A13) and (A14), we have

$$\psi_{\rm NADW} = L_x K_{\rm GM}(s_* - s_2), \tag{A15}$$

where s_* and s_2 are the slopes of isopycnals ρ_* and ρ_2, respectively. At the surface of the Southern Ocean, the upwelled water is transformed to lighter water by the surface buoyancy flux B (which is fixed, i.e., independent of the ocean state), which satisfies

$$\frac{B}{\partial b/\partial y} = \frac{\psi_{\rm NADW}}{L_x}. \tag{A16}$$

In Equation (A16), both B and $\partial b/\partial y$ are evaluated at the surface in the Southern Ocean where ρ_* outcrops. The buoyancy gradient $\partial b/\partial y$ can be approximated by

$$\frac{\partial b}{\partial y} \approx -\frac{(\rho_* - \rho_2)g}{\rho_0 W} = \frac{g'}{W}, \tag{A17}$$

where $g' \equiv (\rho_* - \rho_2)g/\rho_0$ and W is the distance between ρ_2 and ρ_* at the ocean surface, i.e.,

$$W = \frac{z_2}{s_2} - \frac{z_*}{s_*}. \tag{A18}$$

Based on our definition of ρ_2,

$$\psi_2 = 0 \text{ and } \mathrm{s}_2 = -\frac{\tau_0}{\rho_0 \mathrm{f}_0 \mathrm{K}_{\rm GM}} \tag{A19}$$

are specified constants.

Combining Equations (A16), (A17) and (A18), we obtain

$$\frac{B}{g'}\left(\frac{z_2}{s_2} - \frac{z_*}{s_*}\right) = \frac{\psi_{\rm NADW}}{L_x}. \tag{A20}$$

Substituting Equation (A15) into (A20) leads to

$$\frac{B}{g'}\left[\frac{z_2}{s_2} - \frac{z_*}{s_2 + \psi_{\text{NADW}}/(K_{\text{GM}}L_x)}\right] = \frac{\psi_{\text{NADW}}}{L_x}, \tag{A21}$$

from which we can obtain

$$\frac{z_*}{s_2 + \psi_{\text{NADW}}/(K_{\text{GM}}L_x)} = \frac{z_2}{s_2} - \frac{\psi_{\text{NADW}}\, g'}{BL_x}. \tag{A22}$$

Therefore, the difference in depth between ρ_* and ρ_2 is

$$z_* - z_2 = \underbrace{\frac{z_2}{s_2}\frac{\psi_{\text{NADW}}}{K_{\text{GM}}L_x}}_{\text{I}} - \underbrace{\frac{\psi_{\text{NADW}}\, g'}{BL_x}\left(s_2 + \frac{\psi_{\text{NADW}}}{K_{\text{GM}}L_x}\right)}_{\text{II}}. \tag{A23}$$

Here Term I represents the effect of the reduction in the isopycnal slope that supports a positive overturning overturning streamfunction because $s_* - s_2 = \psi_{\text{NADW}}/(L_x K_{\text{GM}})$ from equation (A15). Term II represents the contribution from the northward displacement of the outcropping latitude of ρ_* relative to ρ_2 because $(\psi_{\text{NADW}}\, g')/(BL_x) \approx W$ based on equation (A16) and (A17).

For typical values in the real ocean:

$$\psi_{\text{NADW}} = 10^7 \text{m}^3/\text{s}, \qquad s_2 = -10^{-3},$$

$$L_x = 2 \times 10^7 \text{m}, \qquad \rho_0 = 1000 \text{kg/m}^3,$$

$$K_{\text{GM}} = 1000 \text{m}^2/\text{s}, \qquad \rho_2 - \rho_* = 0.2 \text{kg/m}^3,$$

$$B = 10^{-8} \text{m}^2/\text{s}^3, \qquad z_2 = -3000 \text{m}.$$

Here the value of ρ_* is chosen close to the core of the NADW overturning circulation, where there is maximal change in the isopycnal slope.

We obtain

$$z_* - z_2 = \underbrace{1500m}_{\text{I}} + \underbrace{50m}_{\text{II}}. \tag{A24}$$

Clearly, term I dominates over term II in Equation (A23). Thus, we have

$$z_* - z_2 \approx \frac{z_2 \psi_{\text{NADW}}}{s_2 K_{\text{GM}} L_x}. \tag{A25}$$

Inserting equation (A25) into the approximate derivative $N^2 \approx g'/(z_* - z_2)$, the density stratification in Region 2 is

$$N^2 \approx \frac{\Lambda}{\psi_{\text{NADW}}}, \tag{A26}$$

with

$$\Lambda \equiv \frac{g' s_2 K_{\text{GM}} L_x}{z_2} \tag{A27}$$

being a constant. From Equation (A26), we obtain

$$\Delta N^2 \approx -\frac{\Lambda}{\psi^2_{\text{NADW:LGM}}} \Delta\psi_{\text{NADW}}. \tag{A28}$$

Here $\Delta\psi_{\text{NADW}} \equiv \psi_{\text{NADW:LGM}} - \psi_{\text{NADW:Test}}$, where $\psi_{\text{NADW:LGM}}$ and $\psi_{\text{NADW:Test}}$ are the values of ψ_{NADW} in the LGM and Test simulations. Recall that $\Delta N^2 \equiv N^2_{\text{LGM}} - N^2_{\text{Test}}$. To obtain equation (A28), we have used the assumption $\psi_{\text{NADW:LGM}} \approx \psi_{\text{NADW:Test}}$. Combining equation (A26) with (A28) leads to

$$\frac{\Delta N^2}{N^2_{\text{LGM}}} \approx -\frac{\Delta\psi_{\text{NADW}}}{\psi_{\text{NADW:LGM}}}. \tag{A29}$$

Therefore, even when the assumption of constant isopycnal slope is relaxed, an order-one change in NADW transport is still required for the Northern Hemisphere surface forcing alone to cause an order-one change in the density stratification in Region 2. Consistent with the simpler analysis in Section A.3.1, we suggest that this explains why the stratification in Region 2 was relatively insensitive to changes in Northern Hemisphere surface forcing.

Appendix B

Appendix for Chapter 3

B.1 CESM setup

The time- and zonal-mean wind stress and wind stress curl is presented in Figure B1. Consistent with our model setup, the wind stress forcing in the Test run closely follows the LGM run in the Southern Ocean until 40°S. Unlike the wind stress forcing, surface buoyancy flux in the Test run appears to differ from LGM (Figure B2). This is because more frazil ice is formed in the LGM run due to a colder global ocean temperature, which releases more brine and increases the negative buoyancy loss close to the Antarctica. The frazil ice is formed as part of the ocean model when the temperature of seawater falls below the freezing point.

In Figure B2d, we present the zonal-mean buoyancy flux from the Southern Ocean State Estimate (SOSE; Mazloff et al., 2010), which broadly resembles our PI simulation. However, the latitude where surface buoyancy forcing changes sign in SOSE is further south by 5° latitude compared to our PI simulations. Therefore, this study does not aim to reproduce the ocean circulation in the PI and LGM climate. Instead, we focus on the response of the AMOC depth to changes in the surface buoyancy forcing in the Southern Ocean.

Previous studies suggest that the simulated AMOC could be biased from the equilibrium state due to a lack of equilibration for the deep ocean circulation in climate models (e.g., Zhang et al., 2013; Marzocchi and Jansen, 2017). In order to evaluate the potential influence of model equilibrium on our results, here we use the residual-mean overturning circulation ($\tilde{\psi}$), which is reported by the model and represents the sum of the eulerian-mean overturning circulation and eddy bolus contributions, instead of the isopycnal overturning circulation (ψ) as in Chapter 3. The residual-mean overturning circulation could be a good approximate to the isopycnal overturning circulation in the basin, where the eddy activities are relatively low. We define the AMOC strength as the maximum residual-mean overturning circulation streamfunction below 500m and the AMOC depth as the depth where $\tilde{\psi}(y,z) = 0$ in the Atlantic averaged between 30°S and 0° (Figure B3). Note that the AMOC depth defined using $\tilde{\psi}$ is not qualitatively different from that using $\hat{\psi}$ (compare Figure B3 with Figure 3.1). Over the last 120 years, the trend in the annual-mean AMOC strength (thin lines in Figure B3) is -0.28 Sv/century, -0.17 Sv/century, and -0.64 Sv/century for the PI, Test, and LGM runs; and the trend in the annual-mean AMOC depth (thin lines in Figure B3) defined using $\tilde{\psi}$ is -0.45 m/year, -0.04 m/year, and -0.24 m/year for the PI, Test, and LGM runs, respectively. This implies that, if these trends persist, the AMOC depth in the Test run is going to be closer to the PI run and farther from the LGM run for a longer model simulation. Therefore, the lack of equilibrium will not affect our conclusion that the Southern Ocean surface buoyancy forcing alone can not determine the depth of the AMOC in our model.

B.2 Isopycnal slope

It is hypothesized that the isopycnal slope is constant between the PI and LGM climate in Ferrari et al. (2014). However, small changes in the isopycnal slope in response to surface forcing perturabtions are present in both observations (Böning et al., 2008) and models (e.g., Viebahn and Eden, 2010; Gent and Danabasoglu, 2011; Wolfe and Cessi, 2010) that could potentially cause discernible changes in the MOC depth. Here, we quantify the changes in the isopycnal slope between the three ocean-only simulations. Instead of calculating the isopycnal slope directly, we calculate the depth changes of isopycnals from 60°S to 30°S ($\Delta\hat{z}_1$; Figure B8):

$$\Delta\hat{z} = \hat{z}(60^{\circ}\mathrm{S}, \sigma_2) - \hat{z}(30^{\circ}\mathrm{S}, \sigma_2). \tag{B1}$$

They are mapped to depth coordinates using the mean depth of isopycnals at 50°S in Figure B8. Comparison of $\Delta\hat{z}$ between the simulations in Figure B8b reveals that a depth difference of around 50m in the MOC depth between Test and LGM simulations could be purely attributed to the small changes in the isopycnal slope (Figure 3.2d), although these changes in isopycnal slope are difficult to discern by eyes (Figure B7).

B.3 Diapycnal mixing

Following the framework of Walin (1982), we can calculate the water mass transformation due to surface buoyancy forcing as

$$\mathcal{T}(\sigma_2) = -\frac{1}{T}\frac{\partial}{\partial\sigma_2}\int_0^T \iint_{90^{\circ}\mathrm{S}<y<30^{\circ}\mathrm{S}} \mathcal{H}(\sigma_2'(x,y,0,t) - \sigma_2) F_s(x,y,t)\, dA\, dt, \tag{B2}$$

where $F_s(x,y,t)$ represents the surface buoyancy flux in the Southern Ocean. If the circulation is purely adiabatic, $\mathcal{T}(\sigma_2)$ (blue lines in Figure B9) should be the same as $\psi(30^{\circ}\mathrm{S}, \sigma_2)$ (black lines in Figure B9). The difference between the two, $\mathcal{T}(\sigma_2) - \psi(30^{\circ}\mathrm{S}, \sigma_2)$, represents the water mass transformation due to diapycnal mixing in the Southern Ocean (red lines in Figure B9). Similar to Newsom et al. (2016), we find that the water mass transformation due to diapycnal mixing is substantial in the Southern Ocean in our study. By comparing Figure B9 with Figure 3.2, it appears that most of the diapycnal mixing ($\sim$15 Sv out of 20 Sv) observed in Figure B9 occurs in the surface 1500 m in CESM.

In Figure B12, we plot the mean diapycnal diffusivity between 60°S and 30°S with respect to depth (Figure B12a) and height above the ocean bottom (Figure B12b), which is within the observed range of diapycnal diffusivity (Waterhouse et al., 2014, their Fig.7). We also calculate the mean diapycnal diffusivity close to the domain of the diapycnal and isopycnal mixing experiment in the Southern Ocean (DIMES), denoted by the two rectangulars in Figure B12b. We find a diapycnal diffusivity of $\sim 1.4\times 10^{-4}\mathrm{m}^2/\mathrm{s}$ at 1500m depth, which is consistent with Watson et al. (2013) that concludes the diapycnal diffusivity to be $O(10^{-4})\mathrm{m}^2/\mathrm{s}$ at the same depth around the same region from tracer distributions in the DIMES project. This suggests that similar effects of diapycnal mixing on the MOC depth, as discussed in Chapter 3, could be plausibly expected in the real ocean.

Unless in regions of deep convection or in the boundary layer, the diapycnal diffusivity profile is dominated by the parameterized tidally-driven mixing, which scales inversely with the density stratification (Jayne, 2009). The diapycnal diffusivity is largest between 1.5km and 3.5km depth in Figure B12a due to its weak stratification (Sun et al., 2016). This explains the largest contribution of diapycnal mixing to the MOC depth in Figure B11b. The magnitude of the diapycnal diffusivity in the Test run falls between those of the PI run and LGM run, consistent with the diapycnal mixing in Figure B11b. This suggests that the differences in diapycnal mixing can be partly attributed to the intensity of the surface buoyancy forcing in the Southern Ocean (cf. Sun et al., 2016).

Previous studies have suggested that numerical discretization of the nonlinear advection terms in tracer equation can cause substantial numerical diapycnal diffusion (e.g., Griffies et al., 2000; Hill et al., 2012). Here, we quantify how much of the diapycnal mixing could be associated with discretization errors by defining an effective diapycnal diffusivity. The effective diapycnal diffusivity (κ_{eff}) is defined as:

$$\hat{\omega}\frac{\partial \hat{\sigma}_2}{\partial z} = \frac{\partial}{\partial z}\left(\hat{\kappa}_{\mathrm{eff}}\frac{\partial \hat{\sigma}_2}{\partial z}\right), \tag{B3}$$

following the notation of Munk (1966), where the hat "ˆ" denotes quantities in depth coordinates as in Chapter 3 and $\hat{\omega}$ represents the diapycnal velocity and $\hat{\omega}(y,\hat{z}(y,\sigma_2)) = \omega(y,\sigma_2) = \frac{1}{L_x}\frac{\partial\psi(y,\sigma_2)}{\partial y}$. A small isopycnal slope has been assumed to derive (B3). For regions below the surface mixed layer and away from deep convection zones, the water column is stably stratified and the effective diapycnal diffusivity can be obtained in σ_2 coordinates as:

$$\kappa_{\text{eff}}(\sigma_2) = \frac{1}{L}\int_0^L \frac{\partial\hat{z}(y,\sigma_2)}{\partial\sigma_2}\left(\int_{\sigma_2^{\max}}^{\sigma_2}\omega(y,\sigma_2')\,d\sigma_2'\right)dy, \tag{B4}$$

where $\kappa_{\text{eff}}(\sigma_2) = \frac{1}{L}\int_0^L \hat{\kappa}_{\text{eff}}(y,\hat{z}(y,\sigma_2))dy$, L is the meridional length of the integration, ω is the diapycnal velocity in σ_2 coordinates, and $\hat{z}(y,\sigma_2)$ represents the mean depth of isopycnal, as defined in Chapter 3.

For comparison, the parameterized diapycnal diffusivity is also mapped to σ_2 coordinates as

$$\kappa(\sigma_2) = \frac{1}{T}\int_0^T \frac{1}{A}\iint \kappa_m(x,y,z,t)|_{\sigma_2'(x,y,z,t)=\sigma_2}\,dx\,dy\,dt, \tag{B5}$$

where $\kappa_m(x,y,z,t)$ is the model reported diapycnal diffusivity, and A represents the integral area on isopycnals.

We compare the diagnosed effective diapycnal diffusivity κ_{eff} with the model reported diapycnal diffusivity κ in Figure B13. It appears that the effective diapycnal diffusivity is approximately the same as the the model-reported value, implying that the numerical diapycnal mixing is not playing a significant role in CESM. Here, we have limited the calculation of κ_{eff} and κ in the deep ocean and within 30°S and 30°N. This is because a stable stratification is required in Equations (B3) and (B5) and the calculation might be not reliable in the Southern Ocean. Therefore, we cannot exclude the possibility of a larger fraction of the diapycnal mixing being due to numerical discretization errors in the Southern Ocean.

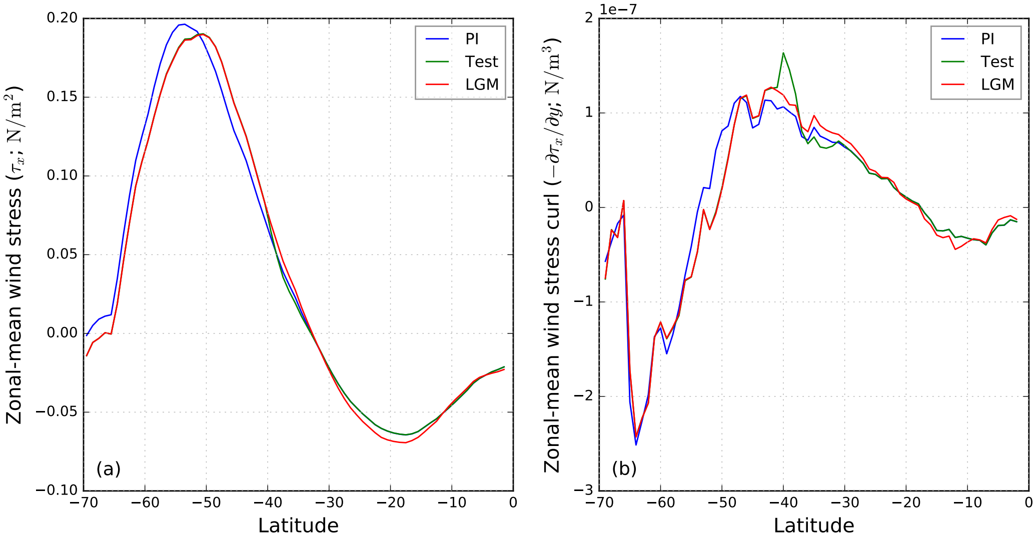

Figure B1: Zonal mean wind stress (a) and wind stress curl (b). Note that the slightly enhanced wind stress curl in the Test simulation close to 40°S is due to the feathering of the forcing fields between 40°S and 30°S.

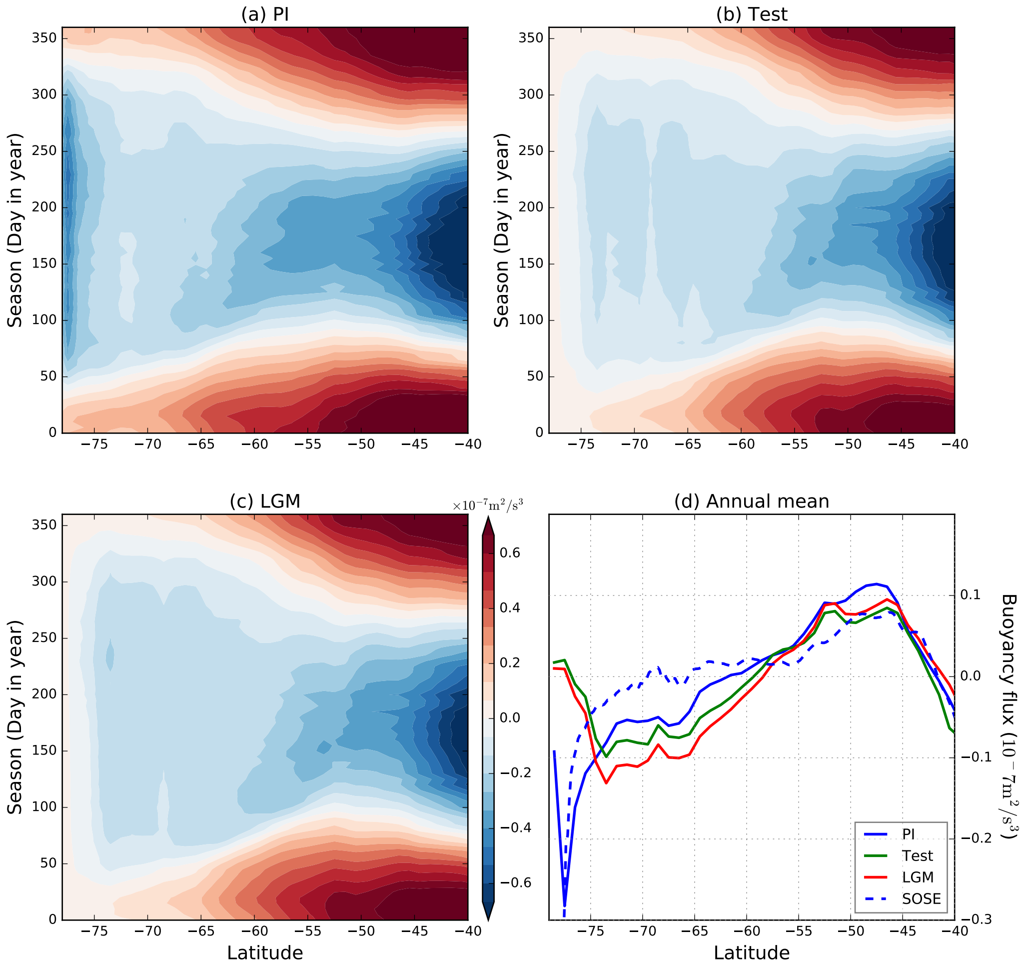

Figure B2: Long-term mean seasonally-varying zonal-mean buoyancy flux (a-c) and annual-mean buoyancy flux (d) from the three ocean-only simulations. The time- and zonal-mean buoayncy flux over years 2005-2010 from the Southern Ocean State Estimate (SOSE; Mazloff et al., 2010) is plotted in panel d as a blue dashed line for comparison.

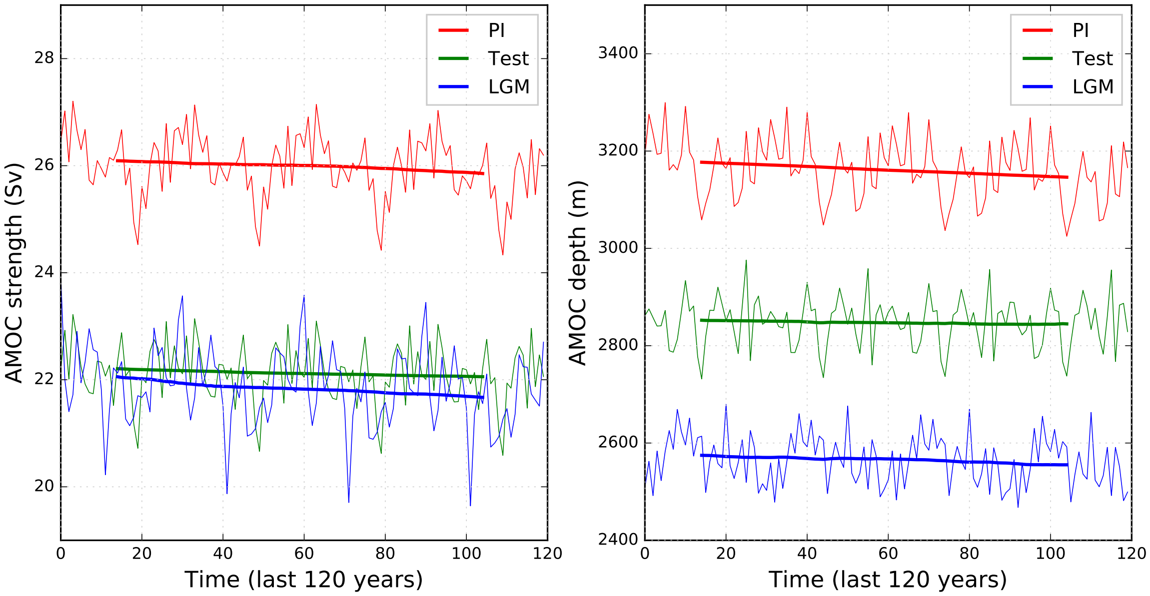

Figure B3: Annual-mean AMOC strength (left) and depth (right) over the last 120 years of the simulations. The thick lines represent 30-year running averages of the annual-mean data. The AMOC depth is averaged between 30°S and 0° in the Atlantic Ocean.

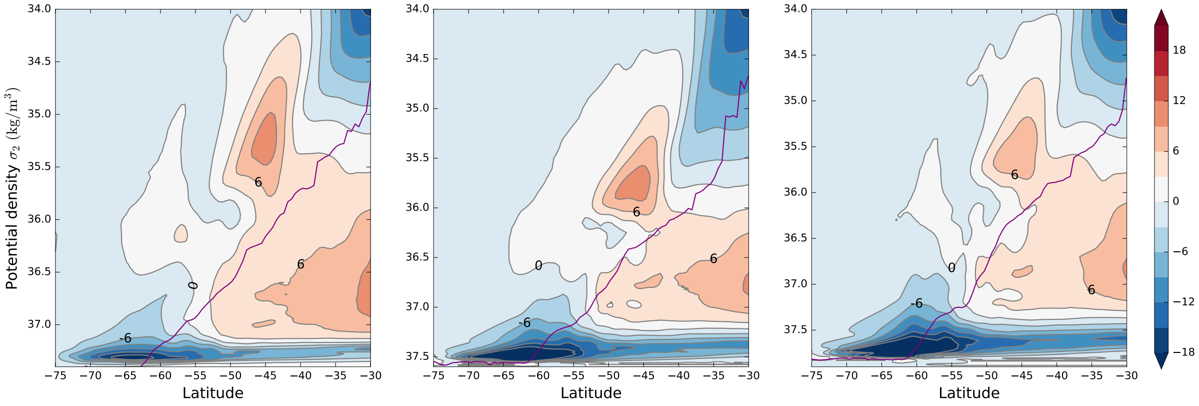

Figure B4: The MOC streamfunction on σ_2 coordinates in the Southern Ocean, with the contours and colorbar labeled in units of Sv. The purple line represents the maximum potential density that appears in the surface mixed layer at each latitude for any time and any longitude. Therefore, isopycnals below the purple line always lie below the surface mixed layer.

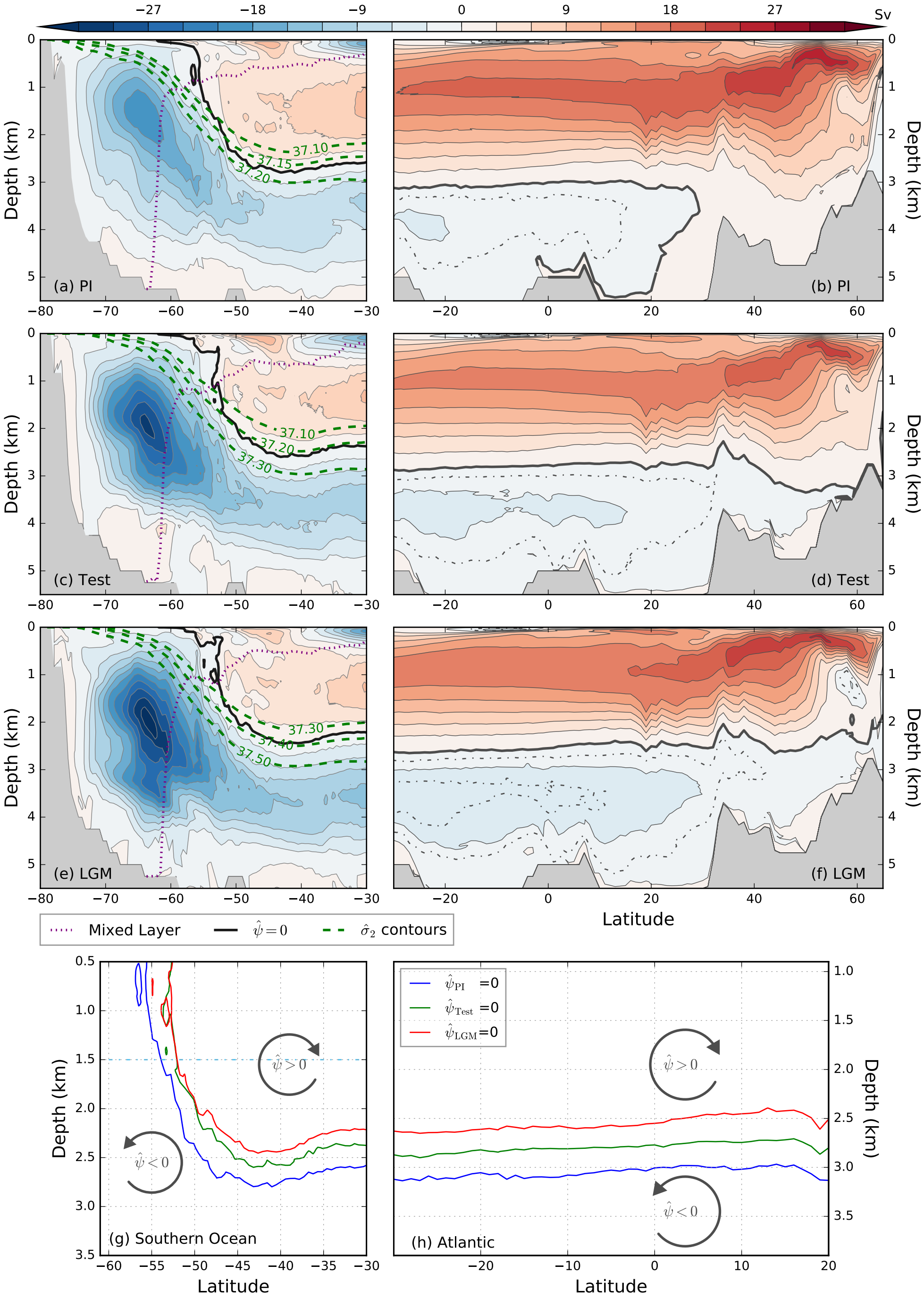

Figure B5: As in Figure 3.1, but using un-smoothed data in the Southern Ocean.

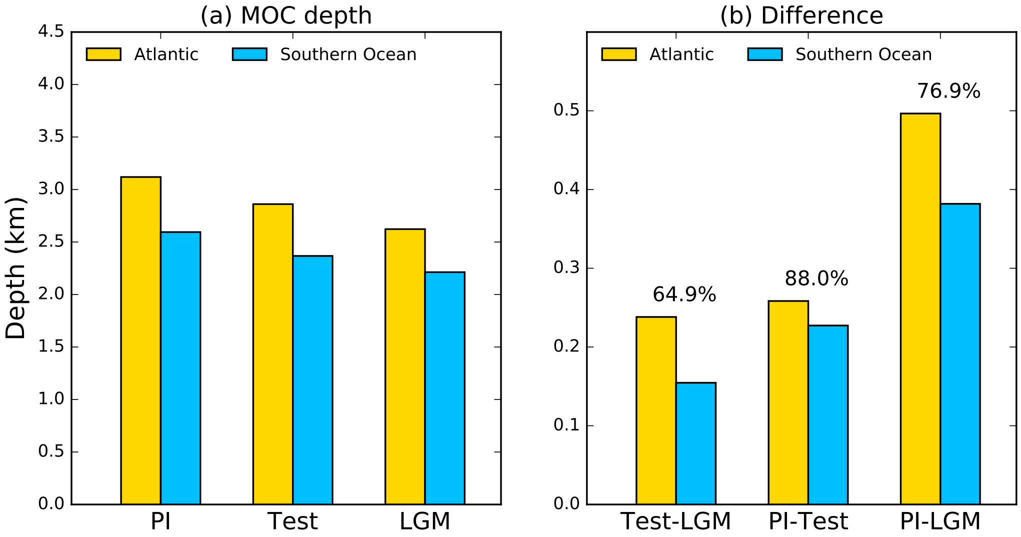

Figure B6: (a) MOC depth in Atlantic and in the Southern Ocean at 30°S and (b) comparison of the MOC depth between the three simulations. The percentage in panel (b) shows the ratio between the MOC depth differences in the Southern Ocean vs that in the Atlantic Ocean. This implies that the AMOC depth changes can be mostly attributed to the MOC changes in the Southern Ocean in our simulations. The lower percentage for "Test-LGM" and "PI-LGM" in (b) implies the importance of the North Atlantic processes in modifying the inter-basin transport of NADW between the Atlantic ocean and the Pacific ocean, which will be discussed in a later study.

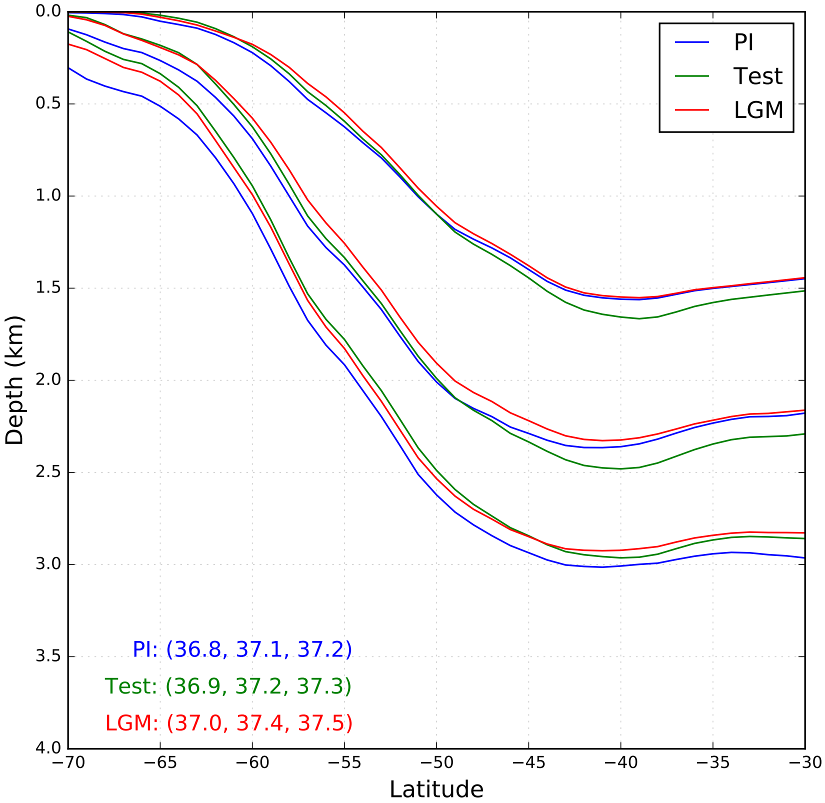

Figure B7: Contours of $\hat{\sigma}_2(y,z)$ to compare the isopycnal slopes between the three simulations. The potential densities for the three plotted isopcynals (from top to bottom) in each simulation are provided in the bottom left in units of $\mathrm{kg/m^3}$.

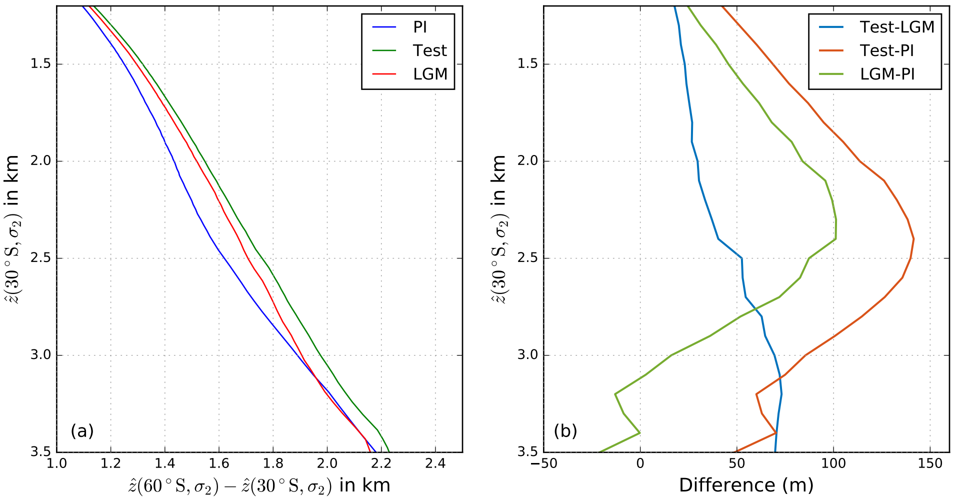

Figure B8: (a) Depth change of isopcynals $\Delta\hat{z}$ from 60°S to 30°S. (b) Difference in $\Delta\hat{z}$ between the three simulations.

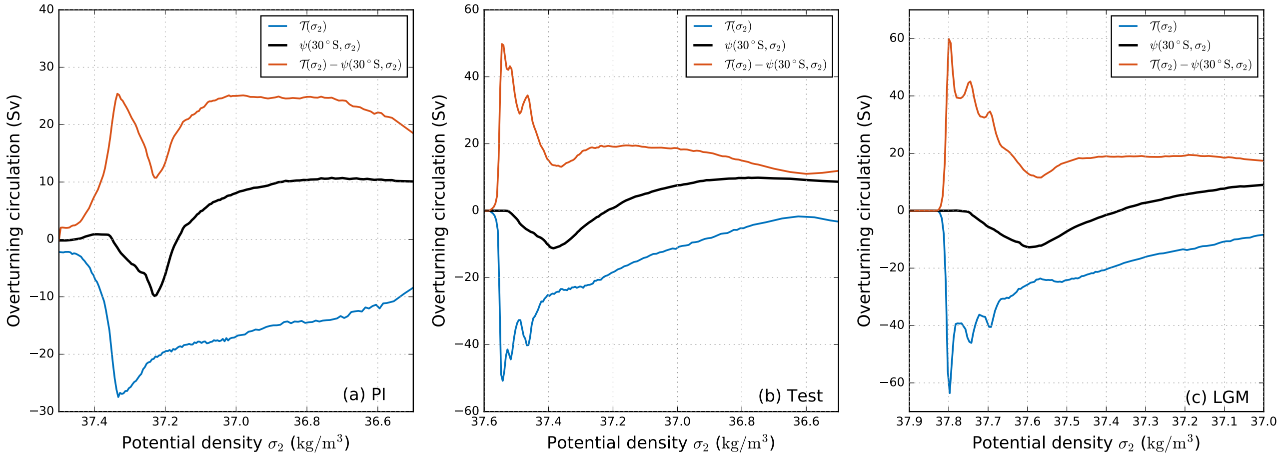

Figure B9: Water mass transformation due to surface buoyancy flux (blue lines), overturning circulation at 30°S (black lines), and the residual that is due to diapycnal transport (red lines). This is not sensitive to the reference pressure, i.e., the strong diapycnal transformation is similar if calculated using σ_0 or σ_4 coordinates.

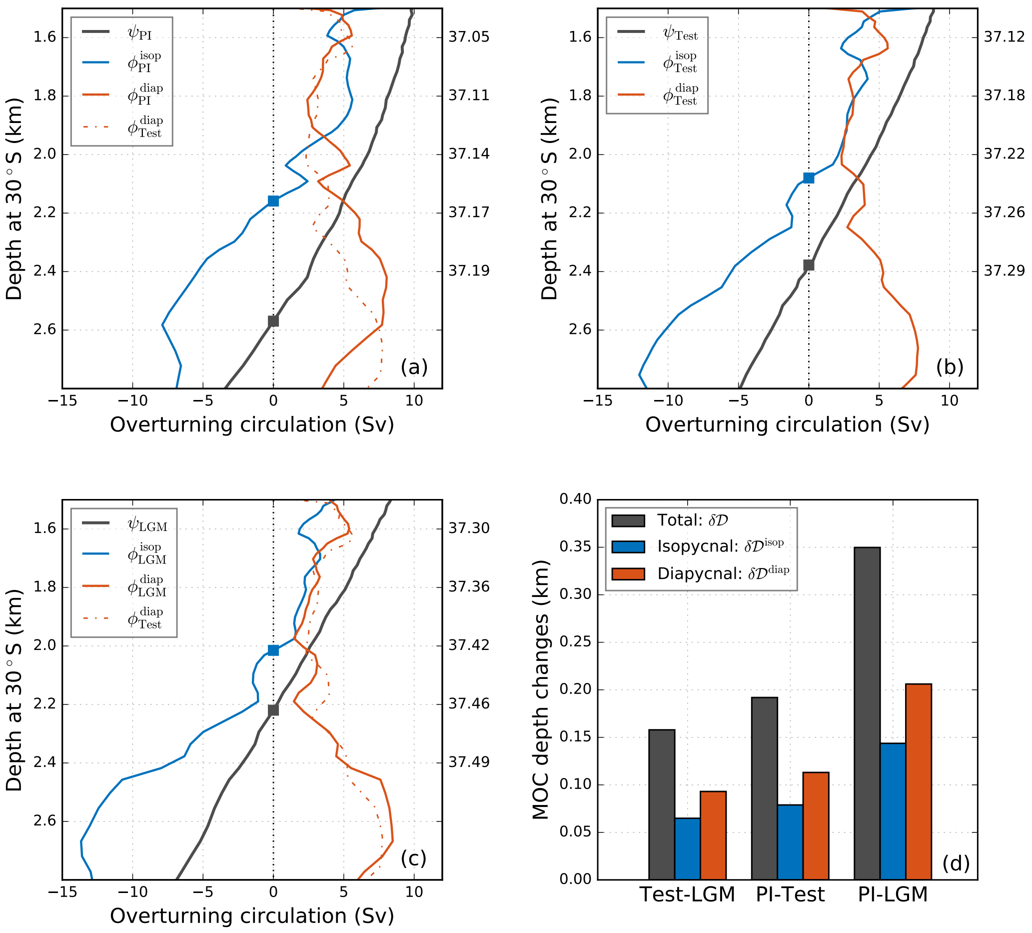

Figure B10: As in Figure 3.2 in Chapter 3, but using un-smoothed data in the Southern Ocean.

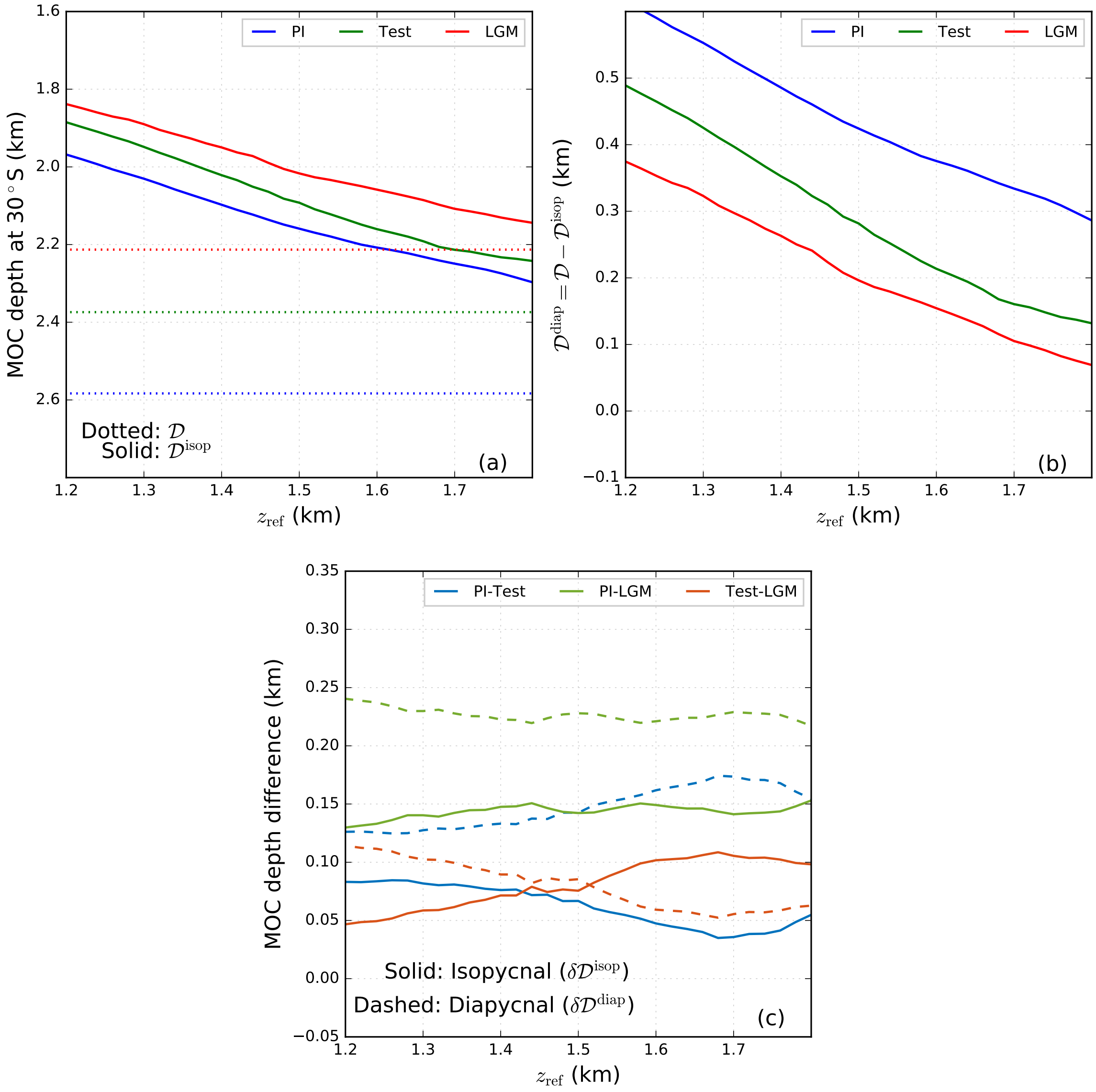

Figure B11: Dependence of $\mathcal{D}$ (a), $\mathcal{D}^{\rm isop}$ (a), $\mathcal{D}^{\rm diap}$ (b), $\delta\mathcal{D}^{\rm isop}$, and $\delta\mathcal{D}^{\rm diap}$ on the reference depth $z_{\rm ref}$ as discussed in Section 3.4. The y-axis is reversed in (a) to show that higher $\mathcal{D}$ means deeper depth. The contribution of diapycnal mixing to the MOC depth ($\mathcal{D}^{\rm diap}$) decreases with the reference depth because the integral area (represented by L_y in Figure 3.3) is smaller for larger $z_{\rm ref}$. However, the contribution of diapycnal mixing to the MOC depth difference is insensitive to the reference depth.

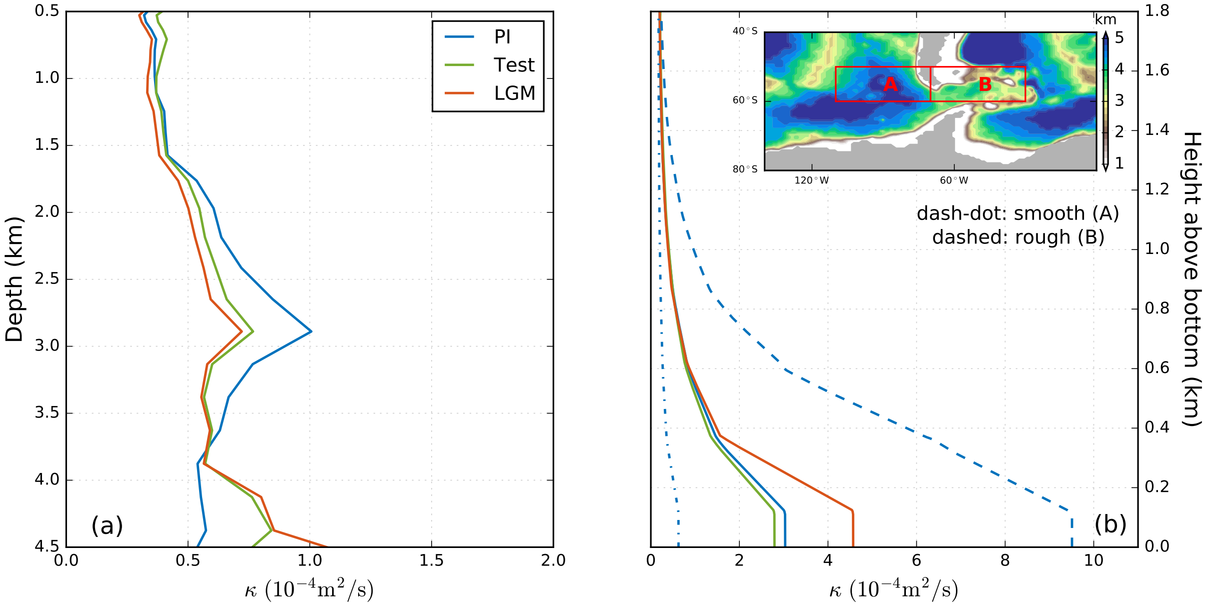

Figure B12: Diapycnal diffusivity averaged on constant depth (a) and on constant height above bottom topography (b) between 60°S and 30°S. Deep convection regions ($\kappa \approx 1\mathrm{m}^2/\mathrm{s}$) are excluded. In Panel (b), only regions deeper than 2000m are considered following Waterhouse et al. (2014). This explains why diapycnal diffusivity is the largest in the PI run in Panel (a) between 1.5km and 3.5 km depth, due to its weak stratification, but it is not seen in Panel (b). The subplot within Panel (b) shows the bathymetry (km) close to the Drake passage. To compare with observations, we calculate the mean diapycnal diffusivity profiles over smooth topography (dash-dotted lines; A) and rough topography (dashed lines; B) close to the Drake passage for the PI simulation. And we find that both diapycnal diffusivity profiles are within the observed range given by Waterhouse et al. (2014). The regions denoted by "A" and "B" correspond approximately to the domain of the DIMES project, where Mashayek et al. (2017) concludes the diapycnal mixing to be $O(10^{-4})\mathrm{m}^2/\mathrm{s}$ at 1500m depth. We averaged the diapycnal diffusivity at 1500m depth over the region denoted by "A" and "B", and we find a diapycnal diffusivity of $1.4\times10^{-4}\mathrm{m}^2/\mathrm{s}$, consistent with Watson et al. (2013).

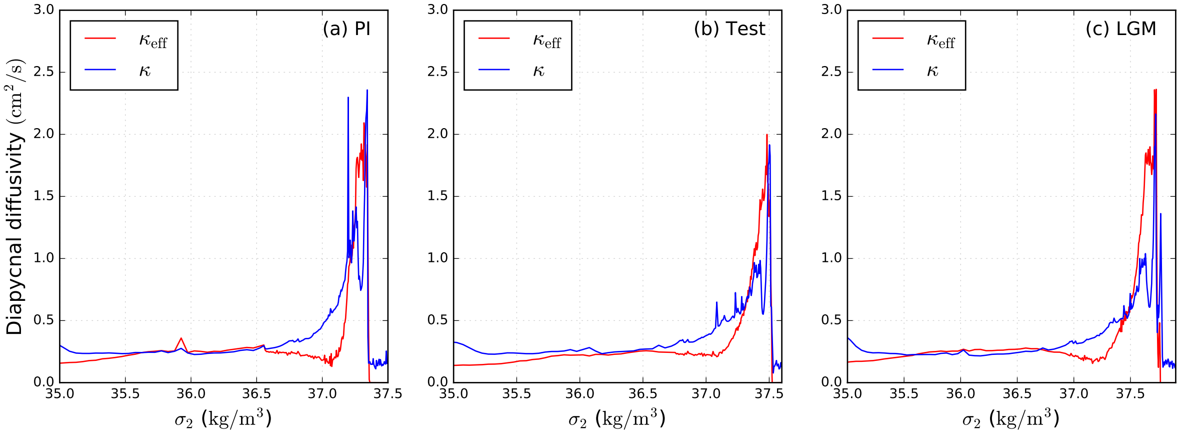

Figure B13: Effective diapycnal diffusivity (κ_{eff}, defined in Equation (B4)) and model-reported diapycnal diffusivity (κ, defined in Equation (B5)) calculated between 30°S and 30°N. The potential density range covers the depth range from intermediate depth to the ocean bottom.

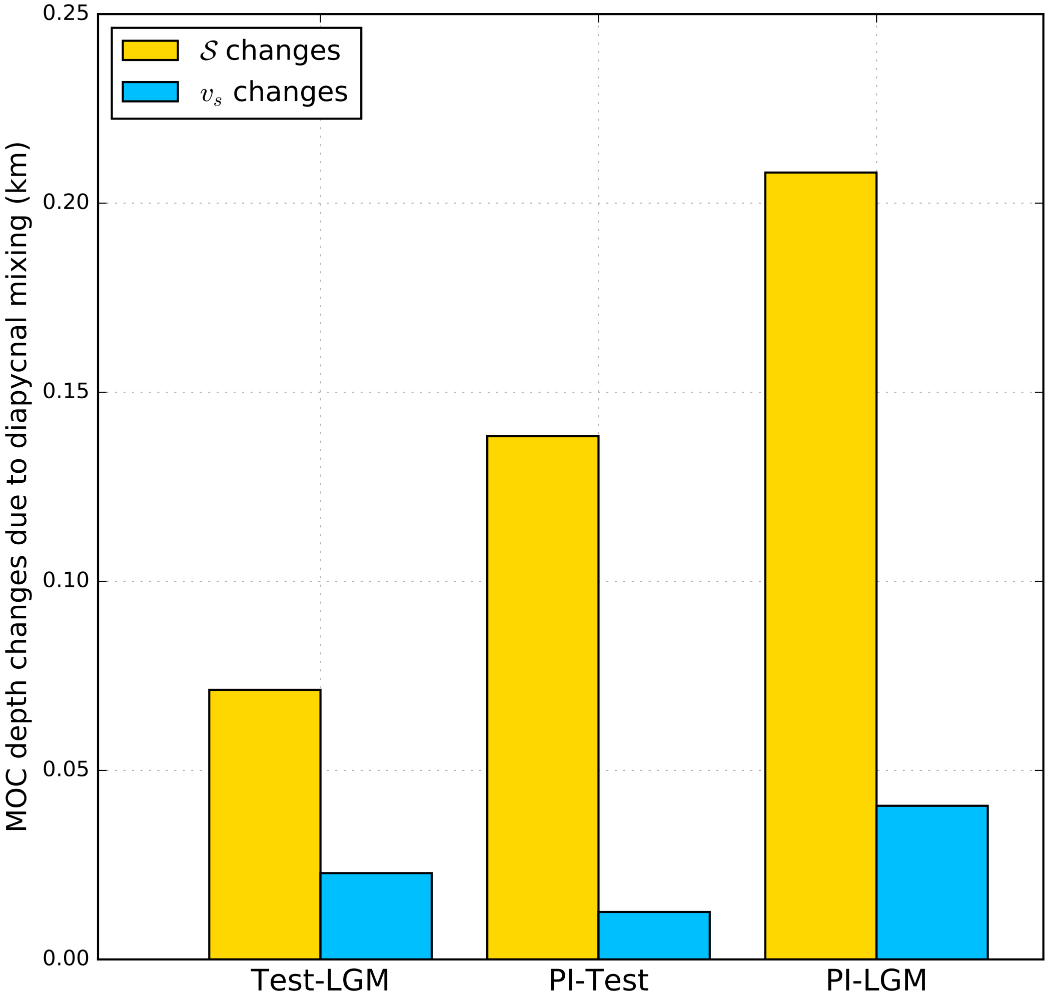

Figure B14: Contribution of diapycnal mixng to MOC depth changes due to changes in $\mathcal{S}$ and v_s according to Equation (3.9).

Appendix C

Appendix for Chapter 5

Here we discuss the impacts of varying the restoring timescales on the reproduction of the PMIP3 surface density and surface buoyancy flux in the ocean-only simulations. The equations for temperature and salinity at sea surface are

$$\frac{\partial\theta}{\partial t} = \frac{Q_{\text{net}}}{\rho_0 c_p \delta_s} + \chi_\theta = -\frac{1}{t_\theta}(\theta - \theta^*) + \frac{Q^*_{\text{net}}}{\rho_0 c_p \delta_s} + \chi_\theta, \tag{C1a}$$

$$\frac{\partial S}{\partial t} = \frac{\mathcal{S}}{\delta_S} + \chi_{\text{salt}} = -\frac{1}{t_{\text{salt}}}(S - S^*) + \frac{S_0}{\delta_s}(E^* - P^* + M^*_{\text{ice}}) + \chi_{\text{salt}}, \tag{C1b}$$

where χ represents the advection and diffusion terms in the temperature and salinity equations for the MITgcm simulations. Thus, the evolution of temperature and salinity is determined by surface buoyancy conditions and ocean processes. Similarly, the temperature and salinity at sea surface in the PMIP3 simulations can be written as

$$\frac{\partial\theta^*}{\partial t} = \frac{Q^*_{\text{net}}}{\rho_0 c_p \delta_s} + \chi^*_\theta, \tag{C2a}$$

$$\frac{\partial S^*}{\partial t} = \frac{S_0}{\delta_s}(E^* - P^* + M^*_{\text{ice}}) + \chi^*_{\text{salt}}, \tag{C2b}$$

where χ^* represents the climatological monthly-mean advection and diffusion terms in the temperature and salinity equations for the PMIP3 simulations.

Inserting Equations (C2a) and (C2b) into Equations (C1a) and (C1b) and rearranging, we can connect the evolution of temperature and salinity in the MITgcm simualtions to the PMIP3 runs as

$$\frac{\partial \theta}{\partial t} + \frac{\theta}{t_\theta} = \frac{\partial \theta^*}{\partial t} + \frac{\theta^*}{t_\theta} + \chi'_\theta, \tag{C3a}$$

$$\frac{\partial S}{\partial t} + \frac{S}{t_{\text{salt}}} = \frac{\partial S^*}{\partial t} + \frac{S^*}{t_{\text{salt}}} + \chi'_{\text{salt}}, \tag{C3b}$$

where $\chi' = \chi - \chi^*$ represents the difference in the ocean dynamics contribution to the buoyancy equations between the MITgcm and PMIP3 simulations. In the remainder of this section, we will focus on these two equations to discuss the impacts of relaxation strength on the reproduction of the PMIP3 surface properties in the MITgcm simulations.

Considering the simplified scenario in which ocean dynamics are ignored, Equations (5.4a), (5.4b), (C3a), and (C3b) together give that

$$\theta = \theta^*, S = S^*, Q_{\text{net}} = Q^*_{\text{net}}, \text{and} \mathcal{S} = \mathcal{S}^*, \tag{C4}$$

i.e., both the surface density and the surface buoyancy flux ($F = g/\rho_0\left(\alpha Q_{\text{net}}/c_p - \rho_0 \beta \mathcal{S}\right)$) in the PMIP3 simulations can be reproduced in the MITgcm runs. Here, g is the gravitational parameter, α is the thermal expansion coefficient, and β is the haline contraction coefficient.

However, with the addition of ocean dynamics, the reproduction of the surface density and the surface buoyancy flux depends on the restoring timescales t_θ and t_{salt}. In the following, we focus on the impact of restoring timescales on the simulated temperature (θ) and net surface heat flux (Q_{net}). An equivalent discussion can be applied to salinity and surface salinity flux. Therefore, a better reproduction of surface temperature is equivalent here to a better reproduction of the surface density, and a better reproduction of net surface heat flux is equivalent here to a better reproduction of the surface buoyancy flux.

We normalize the variables in the temperature equation (C3a) as

$$\theta = \theta_0\hat{\theta},\ \theta^* = \hat{\theta}^*\theta_0,\ t = t_0\hat{t},$$

$$Q_{\text{net}} = A\hat{Q}_{\text{net}},\ Q^*_{\text{net}} = A\hat{Q}^*_{\text{net}},$$

$$\chi'_\theta = \frac{\theta_0}{t_0}\hat{\chi}'_\theta,\ \chi^*_\theta = \frac{\theta_0}{t_0}\hat{\chi}^*_\theta,\ \text{and}\, \chi_\theta = \frac{\theta_0}{t_0}\hat{\chi}_\theta. \tag{C5}$$

where variables with a hat "^" are dimensionless, $A = \rho c_p \delta_s \theta_0/t_0$, $\theta_0 = 273.15$ K, $\vec{\tau}$ is the vector form of the wind stress, f is the Coriolis parameter, and $t_0 = 70$ days represents the response timescale of the top layer temperature to surface forcing (Haney, 1971a). Therefore, Equation (C3a) can be written in its dimensionless form as

$$\lambda\frac{\partial\hat{\theta}}{\partial\hat{t}} + \hat{\theta} = \lambda\frac{\partial\hat{\theta}^*}{\partial\hat{t}} + \hat{\theta}^* + \lambda\hat{\chi}'_\theta, \tag{C6}$$

where $\lambda \equiv t_\theta/t_0$ and measures the relaxation strength. Next we discuss the impacts of relaxation strength on the simulated surface temperature and net heat flux using this dimensionless temperature equation.

C.1 Strong Relaxation

For strong relaxation, $\lambda \ll 1$ and the restoring timescale is short. Taking a standard perturbation theory approach, we can write the temperature as

$$\hat{\theta} = \hat{\theta}_0 + \lambda\hat{\theta}_1 + O(\lambda^2). \tag{C7}$$

Substitution of Equation (C7) into Equation (C6) gives

$$\mathcal{O}(\lambda^0): \qquad \hat{\theta}_0 = \hat{\theta}^*, \tag{C8a}$$

$$\mathcal{O}(\lambda^1): \qquad \hat{\theta}_1 = \hat{\chi}'_\theta. \tag{C8b}$$

Therefore, the dimensionless bias in the temperature can be written as

$$\Delta\hat{\theta} \equiv \hat{\theta} - \hat{\theta}^* = \lambda\hat{\chi}'_\theta + \mathcal{O}(\lambda^2). \tag{C9}$$

Incorporating Equation (5.4a), the dimensionless bias in surface heat flux is

$$\Delta\hat{Q}_{\text{net}} \equiv \hat{Q}_{\text{net}} - \hat{Q}^*_{\text{net}} = \hat{\chi}'_\theta + \mathcal{O}(\lambda). \tag{C10}$$

Therefore, in the limit of strong relaxation, there is zero bias in the surface density (Equation (C9), since only the $\mathcal{O}(\lambda^0)$ term is included in the limit), but the surface buoyancy flux bias has a generally nonzero value that is determined by ocean dynamics (Equation (C10)).

C.2 Weak Relaxation

For weak relaxation, on the other hand, $\lambda \gg 1$ and the restoring timescale is long. Taking the same perturbation theory approach, we can write the dimensionless temperature as

$$\hat{\theta} = \hat{\theta}_0 + \eta\hat{\theta}_1 + \mathcal{O}(\eta^2), \tag{C11}$$

where $\eta \equiv 1/\lambda = t_0/t_\theta \ll 1$. Substitution of $\hat{\theta}$ into Equation (C6) leads to

$$O(\eta^0): \quad \frac{\partial \hat{\theta}_0}{\partial \hat{t}} = \frac{\partial \hat{\theta}^*}{\partial \hat{t}} + \hat{\chi}'_\theta, \tag{C12a}$$

$$O(\eta^1): \quad \frac{\partial \hat{\theta}_1}{\partial \hat{t}} + \hat{\theta}_0 = \hat{\theta}^*. \tag{C12b}$$

Combination of the above equations allows the $\hat{\theta}_1$ tendency to be written as

$$\frac{\partial \hat{\theta}_1}{\partial \hat{t}} = -\int \hat{\chi}'_\theta d\hat{t}. \tag{C13}$$

Therefore, the dimensionless bias in the temperature can be written as

$$\Delta\hat{\theta} \equiv \hat{\theta} - \hat{\theta^*} = \frac{\partial \hat{\theta}_1}{\partial \hat{t}} + O(\eta) = -\int \hat{\chi}'_\theta d\hat{t} + O(\eta). \tag{C14}$$

Using Equations (C1a), (C2a), (C11), (C12), and (C13), the dimensionless bias in surface heat flux can be written as

$$\begin{aligned}
\Delta\hat{Q}_{\text{net}} &= \hat{Q}_{\text{net}} - \hat{Q}^*_{\text{net}} \\
&= \left[\frac{\partial \hat{\theta}}{\partial \hat{t}} - \hat{\chi}_\theta\right] - \left[\frac{\partial \hat{\theta}^*}{\partial \hat{t}} - \hat{\chi}^*_\theta\right] \\
&= \frac{\partial \hat{\theta}}{\partial \hat{t}} - \frac{\partial \hat{\theta}^*}{\partial \hat{t}} - \hat{\chi}'_\theta \\
&= \eta \frac{\partial \hat{\theta}_1}{\partial \hat{t}} + O(\eta^2) \\
&= -\eta \int \hat{\chi}'_\theta d\hat{t} + O(\eta^2).
\end{aligned} \tag{C15}$$

Therefore, in the limit of weak relaxation, there is zero bias in the surface buoyancy flux (Equation (C15), since only the $O(\eta^0)$ term is included in the limit), but the surface density bias has a generally nonzero value that is determined by ocean dynamics (Equation (C14)).

This highlights a trade-off that depends on the surface relaxation timescale between reproduction of the PMIP3 surface density and reproduction of the PMIP3 surface buoyancy flux in the MITgcm simulations. In the conceptual model analyzed in this appendix, the former is better reproduced with shorter timescales (i.e., stronger relaxation), whereas the latter is better reproduced with longer timescales (i.e., weaker relaxation). Fig. 5.3 illustrates that the same qualitative behavior occurs in the MITgcm simulations presented in this study. This suggests that by varying the restoring timescales in the MITgcm simulations, we can investigate the relative importance of the surface density distribution versus the surface buoyancy flux distribution in setting the AMOC depth, as is done in Section 5.3 of Chapter 5.

Appendix D

Appendix for Chapter 7

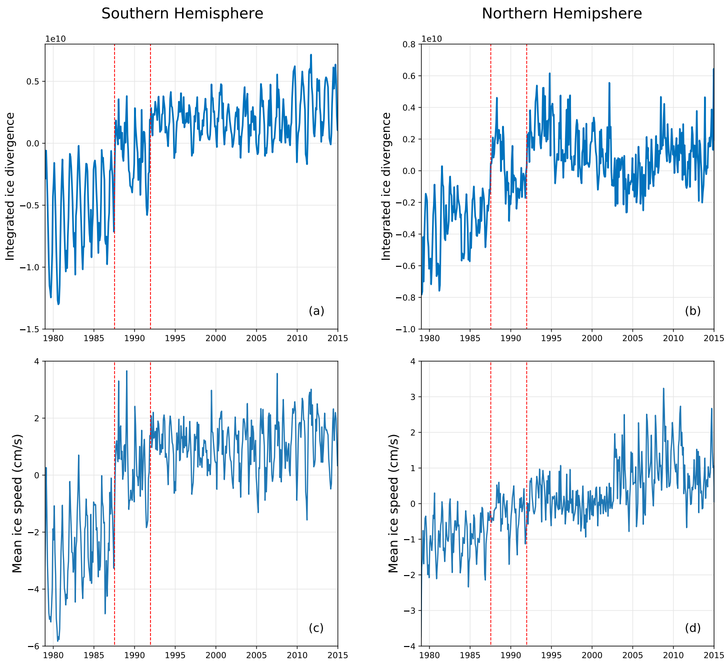

Figure D1: Area-integration of ice motion divergence (a,b) and mean ice speed (c,d) in the Antarctic (left) and the Arctic (right) The transition from the Scanning Multichannel Microwave Radiometer (SMMR) to the Special Sensor Microwave/Imager (SSM/I) on July 9, 1987 and the transition from the SSM/I flown on the Defense Meteorological Satellite Program F8 satellite to the SSM/I flown on the DMSP F11 satellite on December 3, 1991 are marked with two red dashed lines on each polot.

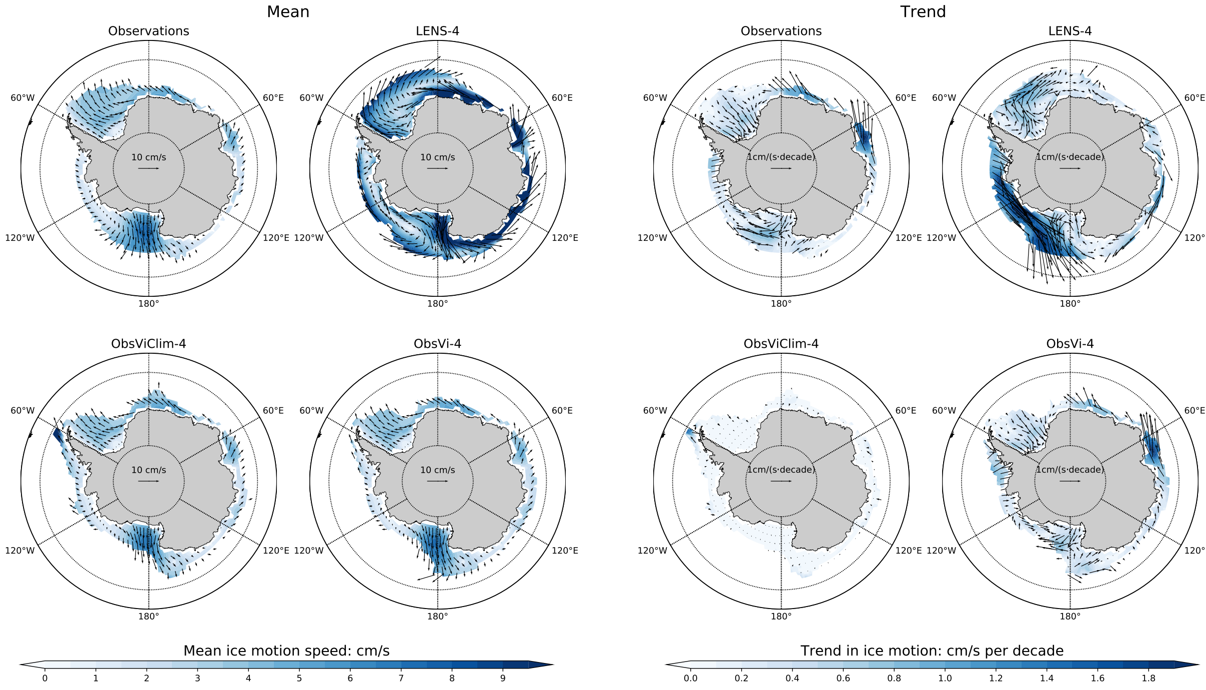

Figure D2: Same as Figure 7.1 in the main text but for “Observations”, “LENS-4”, “ObsViClim-4”, and “ObsVi-4”

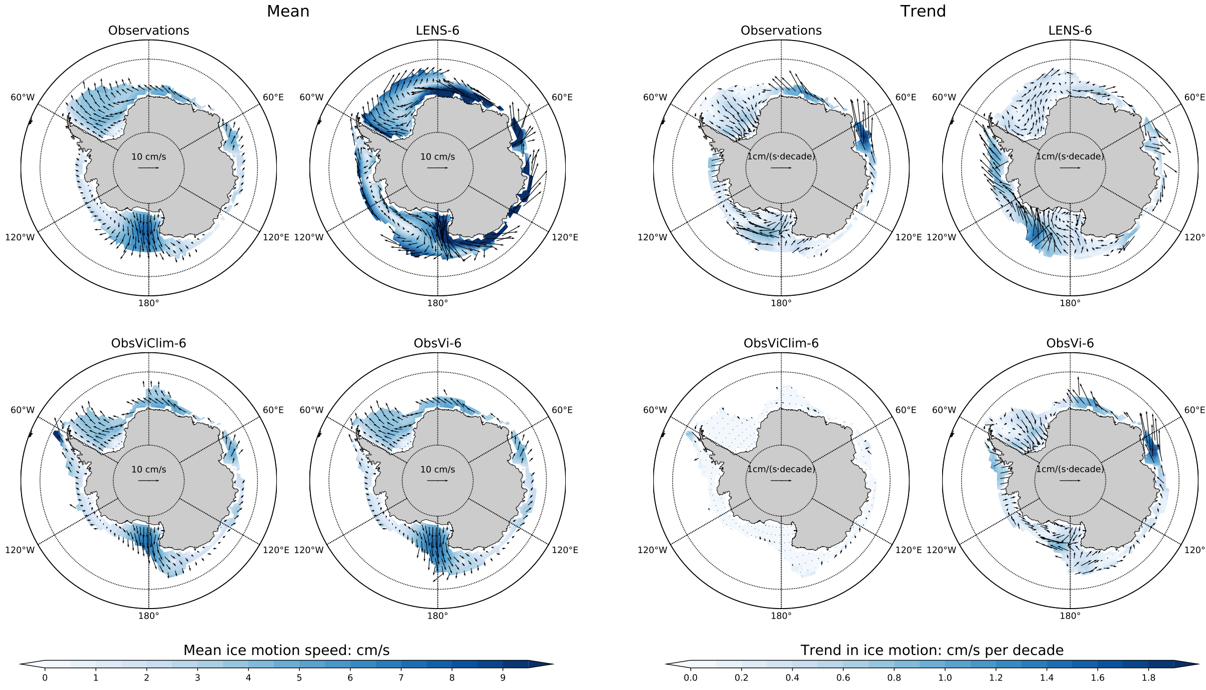

Figure D3: Same as Figure 7.1 in the main text but for “Observations”, “LENS-6”, “ObsViClim-6”, and “ObsVi-6”

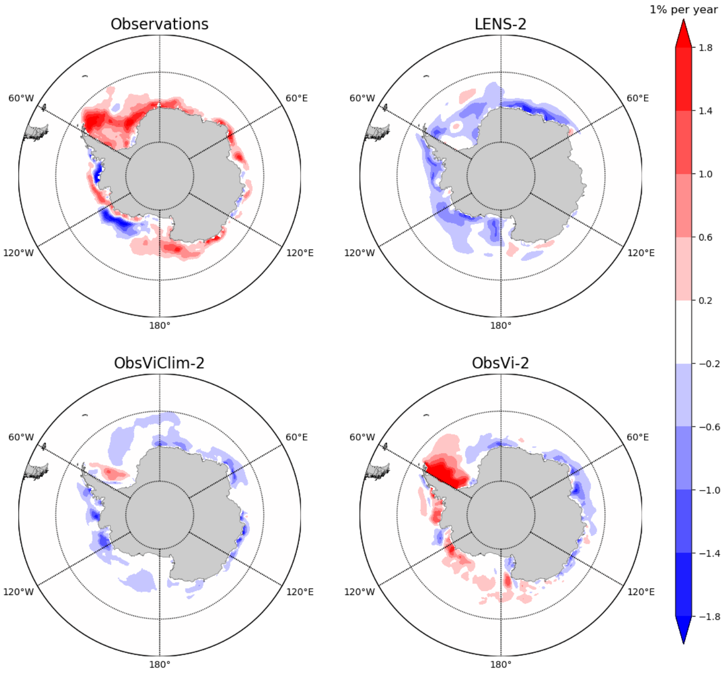

Figure D4: Linear trends of sea ice concentration in summer months (JFM) for “Observations”, “LENS-2”, “ObsViClim-2”, and “ObsVi-2”.

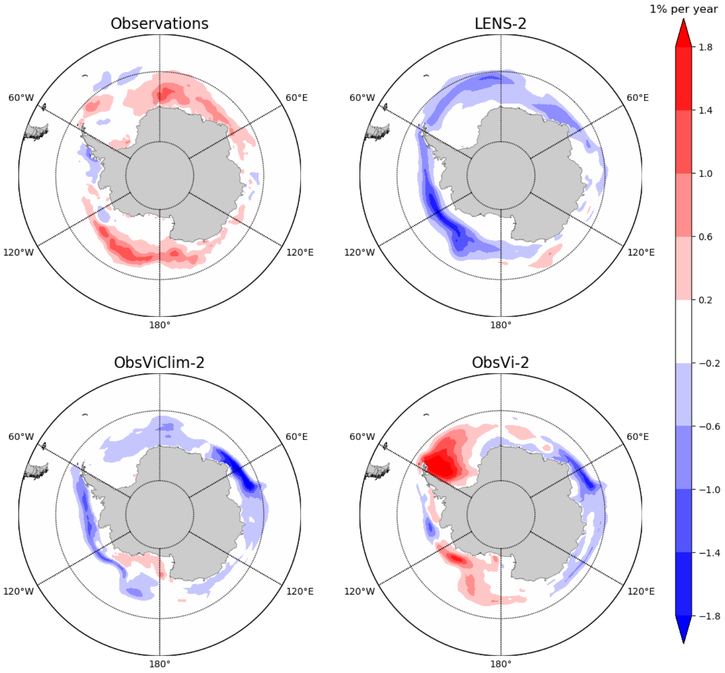

Figure D4 (cont.): Figure D4 continued but for Fall months (AMJ).

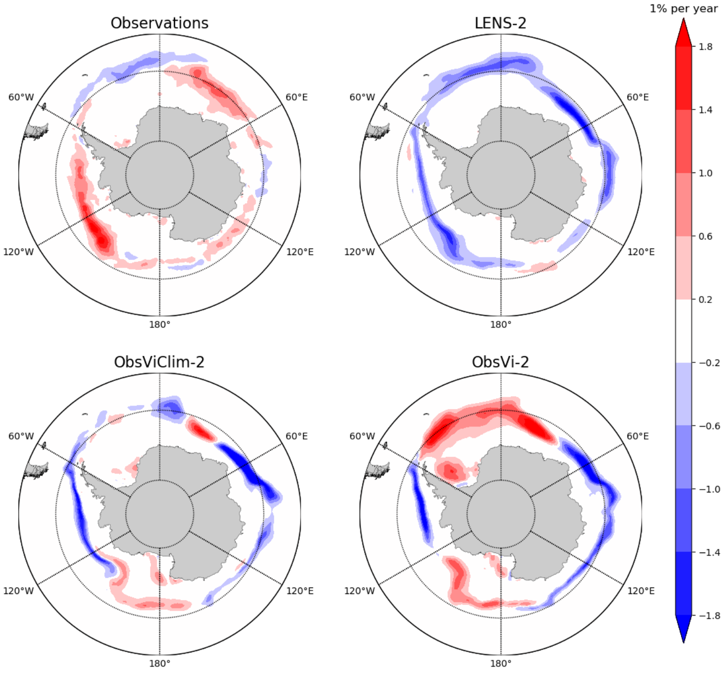

Figure D4 (cont.): Figure D4 continued but for Winter months (JAS).

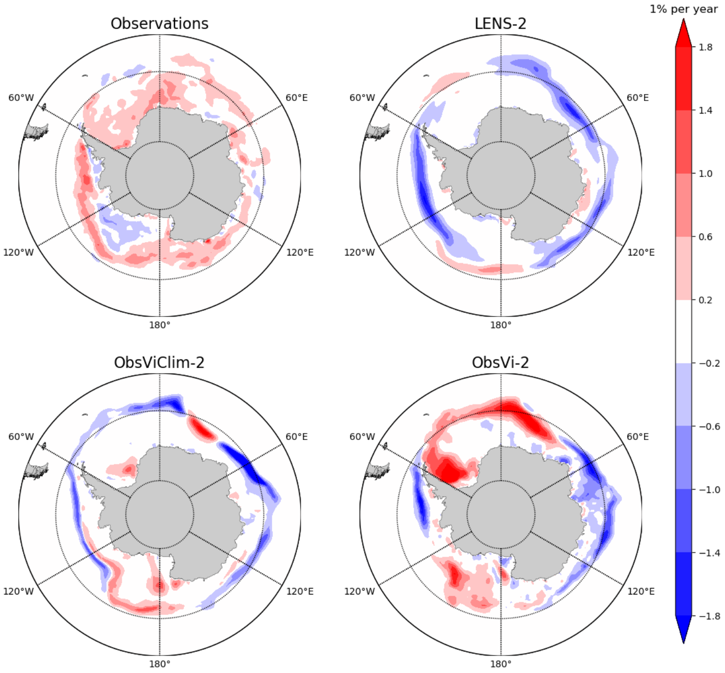

Figure D4 (cont.): Figure D4 continued but for Spring months (OND).

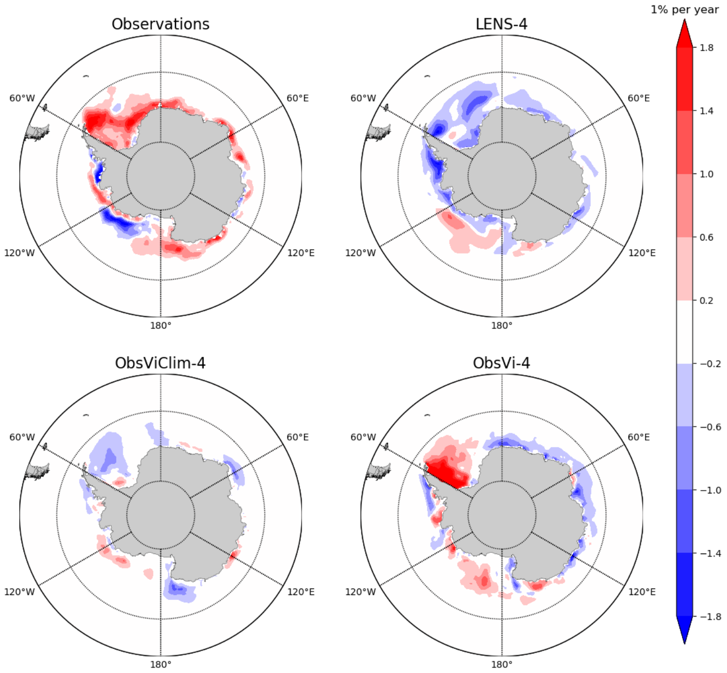

Figure D5: Same as Figure D4 but for "Observations", "LENS-4", "ObsViClim-4", and "ObsVi-4" in summer months (JFM).

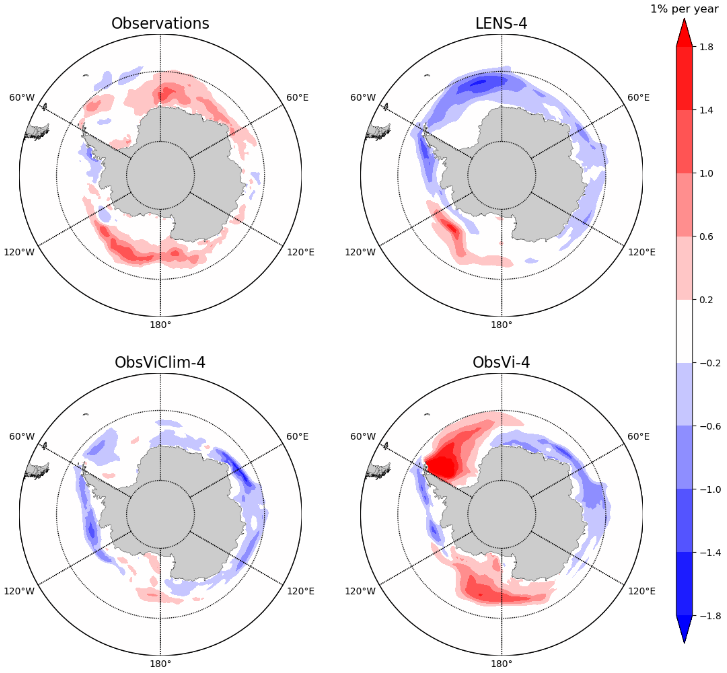

Figure D5 (cont.): Figure D5 continued but for Fall months (AMJ).

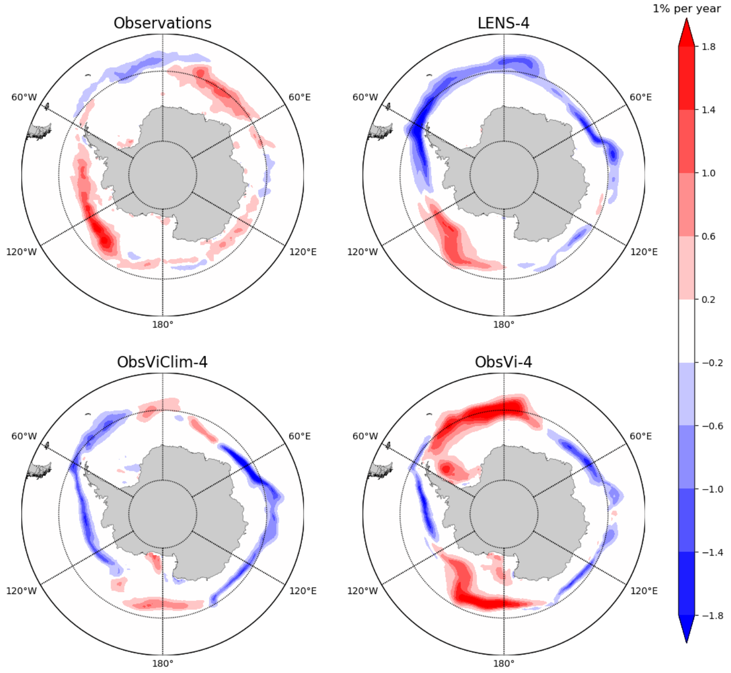

Figure D5 (cont.): Figure D5 continued but for Winter months (JAS).

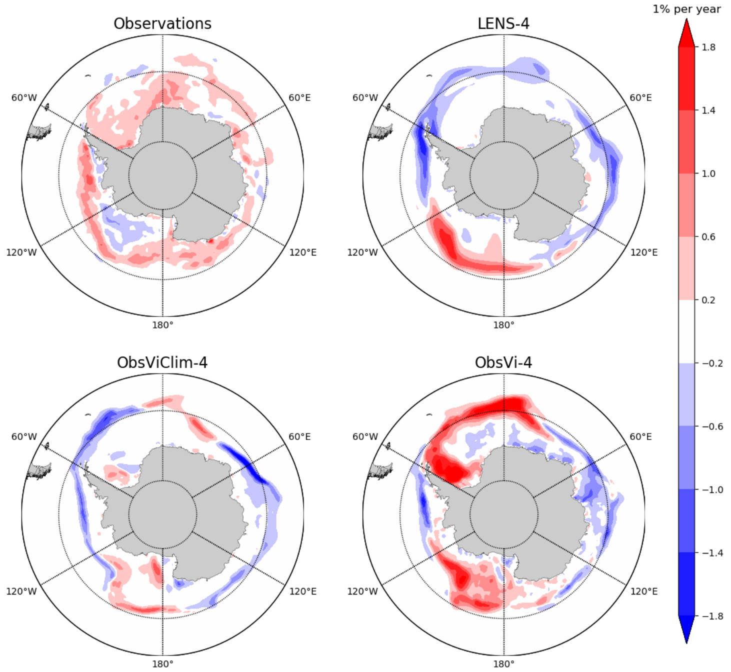

Figure D5 (cont.): Figure D5 continued but for Spring months (OND).

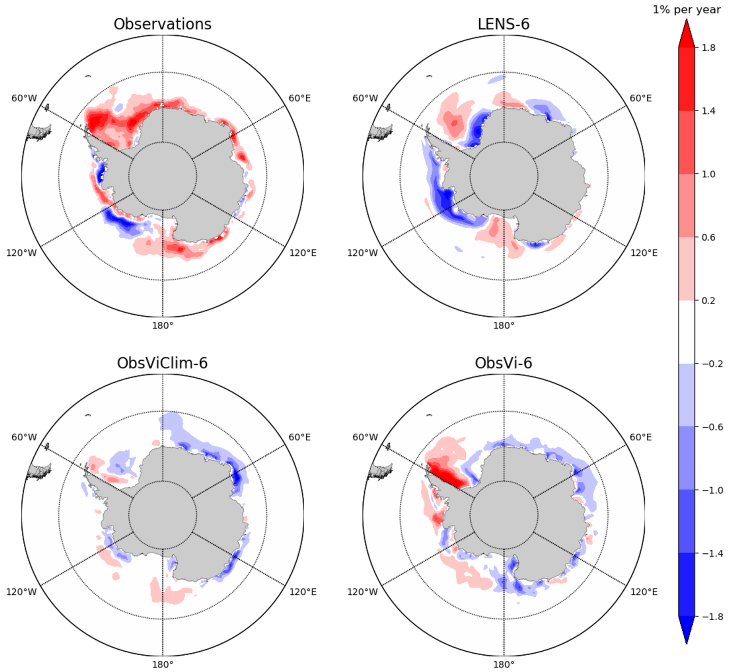

Figure D6: Same as Figure D4 but for “Observations”, “LENS-6”, “ObsViClim-6”, and “ObsVi-6” in summer months (JFM).

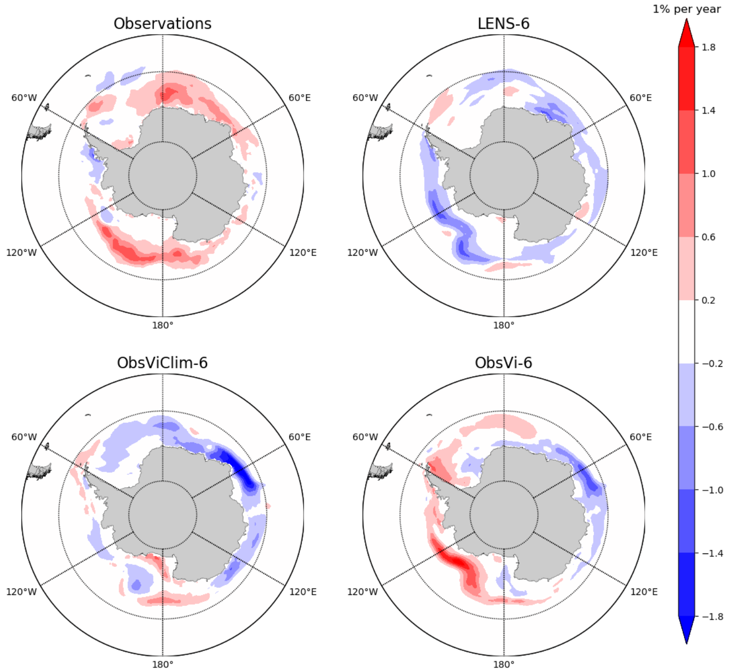

Figure D6 (cont.): Figure D6 continued but for Fall months (AMJ).

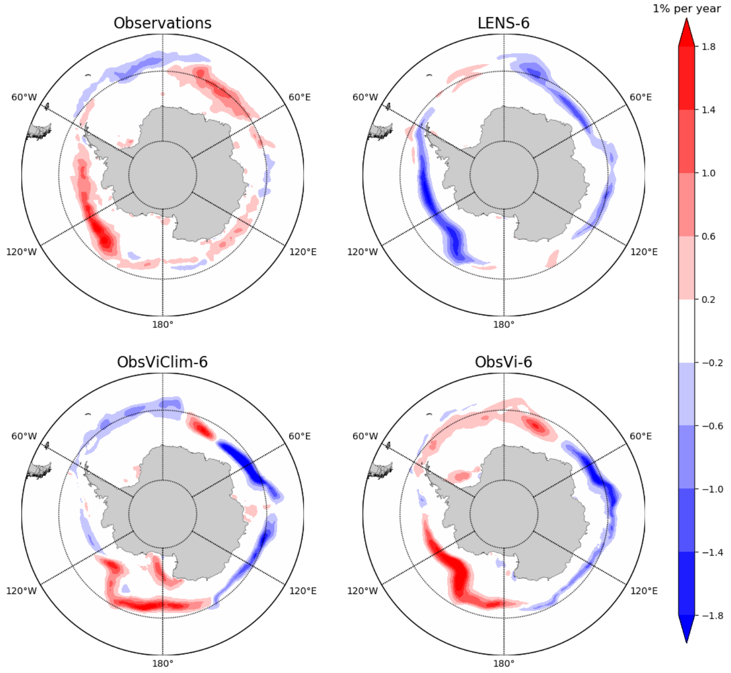

Figure D6 (cont.): Figure D6 continued but for Winter months (JAS).

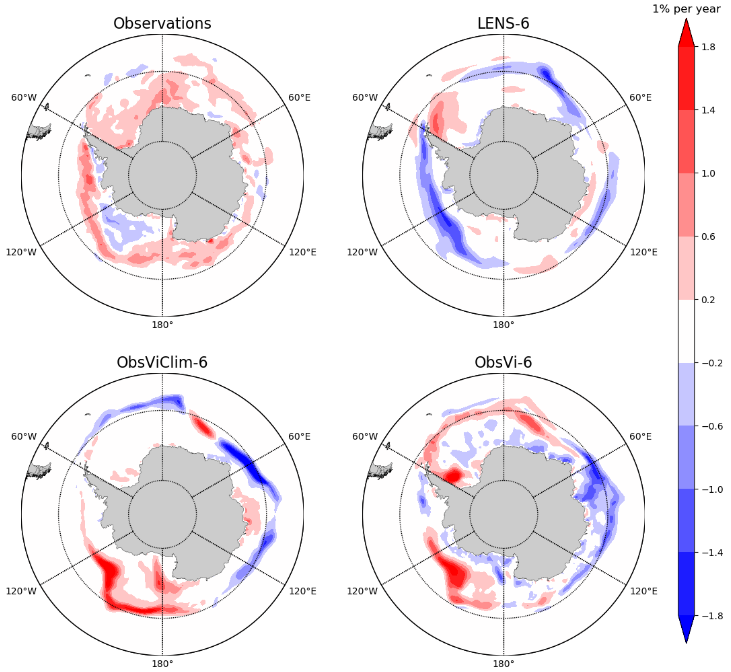

Figure D6 (cont.): Figure D6 continued but for Spring months (OND).

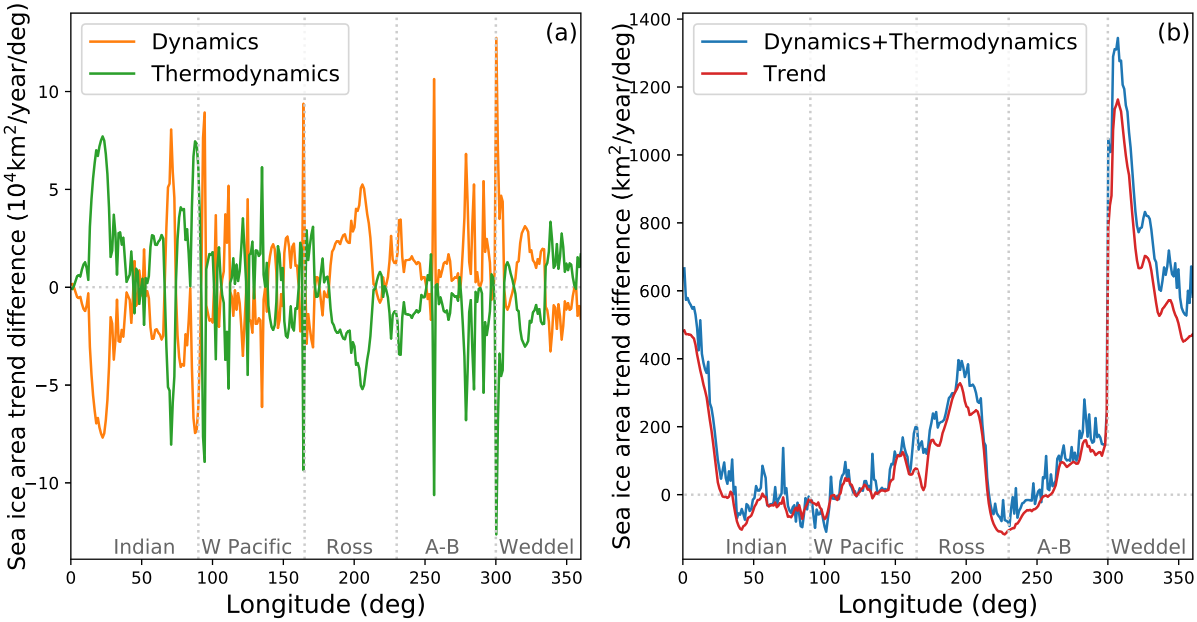

Figure D7: Same as Figure 7.4 in the main article but for “LENS-4” and “ObsVi-4”

.

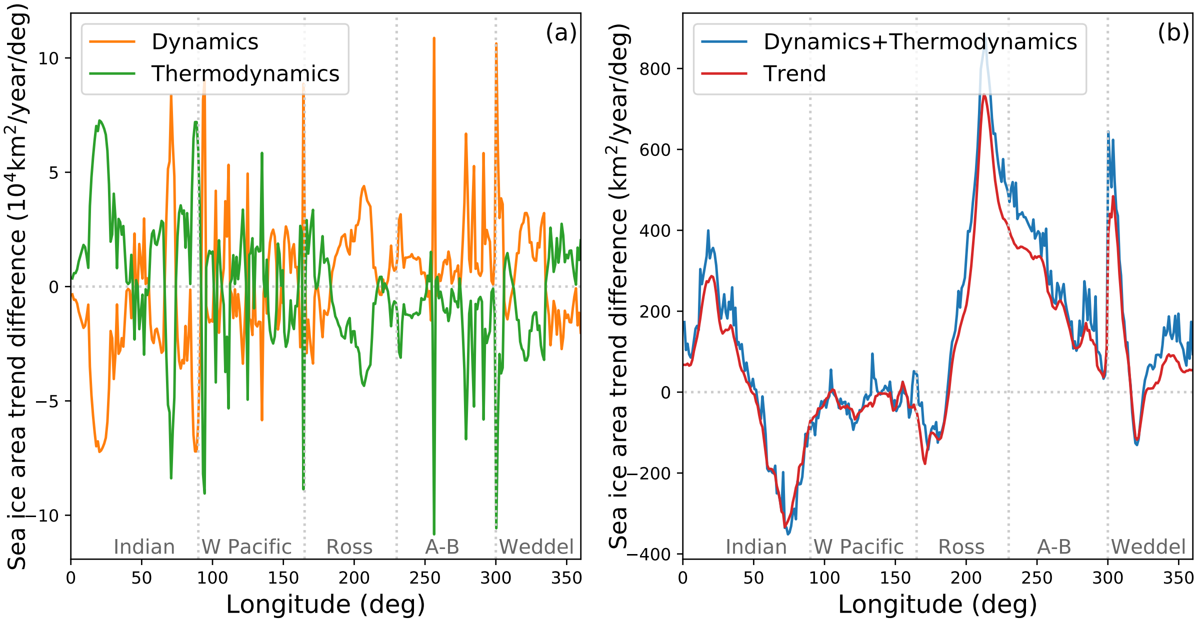

Figure D8: Same as Figure 7.4 in the main article but for “LENS-6” and “ObsVi-6”

.

Bibliography

Abernathey, R., D. Ferreira, and A. Klocker, 2013: Diagnostics of isopycnal mixing in a circumpolar channel. *Ocean Modell.*, **72**, 1–16.

Abernathey, R., J. Marshall, and D. Ferreira, 2011: The dependence of Southern Ocean meridional overturning on wind stress. *J. Phys. Oceanogr.*, **41 (12)**, 2261–2278.

Adkins, J. F., 2013: The role of deep ocean circulation in setting glacial climates. *Paleoceanogr.*, **28 (3)**, 539–561.

Allison, L. C., H. L. Johnson, and D. P. Marshall, 2011: Spin-up and adjustment of the Antarctic Circumpolar Current and global pycnocline. *J. Mar. Res.*, **69 (2-3)**, 167–189.

Anderson, R. F., S. Ali, L. I. Bradtmiller, S. H. H. Nielsen, M. Q. Fleisher, B. E. Anderson, and L. H. Burckle, 2009: Wind-driven upwelling in the Southern Ocean and the deglacial rise in atmospheric CO_2. *Science*, **323 (5920)**, 1443–1448.

Ballarotta, M., S. Drijfhout, T. Kuhlbrodt, and K. Döös, 2013: The residual circulation of the Southern Ocean: Which spatio-temporal scales are needed? *Ocean Modell.*, **64**, 46–55.

Bintanja, R., G. Van Oldenborgh, S. Drijfhout, B. Wouters, and C. Katsman, 2013: Important role for ocean warming and increased ice-shelf melt in antarctic sea-ice expansion. *Nat. Geosci.*, **6 (5)**, 376.

Bishop, S. P., P. R. Gent, F. O. Bryan, A. F. Thompson, M. C. Long, and R. Abernathey, 2016: Southern Ocean Overturning Compensation in an Eddy-Resolving Climate Simulation. *J. Phys. Oceanogr.*, **46 (5)**, 1575–1592.

Böning, C. W., A. Dispert, M. Visbeck, S. Rintoul, and F. U. Schwarzkopf, 2008: The response of the Antarctic Circumpolar Current to recent climate change. *Nat. Geosci.*, **1 (12)**, 864–869.

Bouttes, N., D. Roche, and D. Paillard, 2009: Impact of strong deep ocean stratification on the glacial carbon cycle. *Paleoceanogr.*, **24 (3)**.

Braconnot, P., S. P. Harrison, M. Kageyama, P. J. Bartlein, V. Masson-Delmotte, A. Abe-Ouchi, B. Otto-Bliesner, and Y. Zhao, 2012: Evaluation of climate models using palaeoclimatic data. *Nat. Clim. Change*, **2 (6)**, 417.

Brady, E. C., B. L. Otto-Bliesner, J. E. Kay, and N. Rosenbloom, 2013: Sensitivity to glacial forcing in the CCSM4. *J. Clim.*, **26 (6)**, 1901–1925.

Brovkin, V., A. Ganopolski, D. Archer, and S. Rahmstorf, 2007: Lowering of glacial atmospheric CO2 in response to changes in oceanic circulation and marine biogeochemistry. *Paleoceanogr.*, **22 (4)**.

Bryan, F. O., P. R. Gent, and R. Tomas, 2014: Can Southern Ocean eddy effects be parameterized in climate models? *J. Clim.*, **27 (1)**, 411–425.

Bryan, K., 1984: Accelerating the convergence to equilibrium of ocean-climate models. *J. Phys. Oceanogr.*, **14 (4)**, 666–673.

Bryan, K., and L. Lewis, 1979: A water mass model of the world ocean. *J. Geophys. Res.*, **84 (C5)**, 2503–2517.

Buckley, M. W., and J. Marshall, 2016: Observations, inferences, and mechanisms of the atlantic meridional overturning circulation: A review. *Rev. Geophys.*, **54 (1)**.

Burke, A., A. L. Stewart, J. F. Adkins, R. Ferrari, M. F. Jansen, and A. F. Thompson, 2015: The glacial mid-depth radiocarbon bulge and its implications for the overturning circulation. *Paleoceanogr.*, **30 (7)**, 1021–1039.

Cavalieri, D. J., C. L. Parkinson, P. Gloersen, and H. J. Zwally, 1996: Sea Ice Concentrations from Nimbus-7 SMMR and DMSP SSM/I-SSMIS Passive Microwave Data, Version 1. *NASA National Snow and Ice Data Center Distributed Active Archive Center, Boulder, Colorado, [accessed October 2017]*, doi:https://doi.org/10.5067/8GQ8LZQVL0VL.

Cerovecki, I., L. D. Talley, and M. R. Mazloff, 2011: A comparison of Southern Ocean air-sea buoyancy flux from an ocean state estimate with five other products. *J. Clim.*, **24 (24)**, 6283–6306.

Cessi, P., 2018: The Effect of Northern Hemisphere Winds on the Meridional Overturning Circulation and Stratification. *J. Phys. Oceanogr.*, **48 (10)**, 2495–2506.

Chapman, C., and J.-B. Sallée, 2017: Isopycnal Mixing Suppression by the Antarctic Circumpolar Current and the Southern Ocean Meridional Overturning Circulation. *J. Phys. Oceanogr.*, **47 (8)**.

Cheng, W., J. C. Chiang, and D. Zhang, 2013: Atlantic meridional overturning circulation (AMOC) in CMIP5 models: RCP and historical simulations. *J. Clim.*, **26 (18)**, 7187–7197.

Clark, P. U., and Coauthors, 2009: The Last Glacial Maximum. *Science*, **325 (5941)**, 710–714.

Danabasoglu, G., S. C. Bates, B. P. Briegleb, S. R. Jayne, M. Jochum, W. G. Large, S. Peacock, and S. G. Yeager, 2012: The CCSM4 ocean component. *J. Clim.*, **25 (5)**, 1361–1389.

Danabasoglu, G., W. G. Large, and B. P. Briegleb, 2010: Climate impacts of parameterized Nordic Sea overflows. *J. Geophys. Res.*, **115 (C11)**.

Danabasoglu, G., W. G. Large, J. J. Tribbia, P. R. Gent, B. P. Briegleb, and J. C. McWilliams, 2006: Diurnal coupling in the tropical oceans of CCSM3. *J. Clim.*, **19 (11)**, 2347–2365.

Danabasoglu, G., and J. Marshall, 2007: Effects of vertical variations of thickness diffusivity in an ocean general circulation model. *Ocean Modell.*, **18 (2)**, 122–141.

Danabasoglu, G., J. C. McWilliams, and W. G. Large, 1996: Approach to equilibrium in accelerated global oceanic models. *J. Clim.*, **9 (5)**, 1092–1110.

Dee, D. P., and Coauthors, 2011: The ERA-Interim reanalysis: Configuration and performance of the data assimilation system. *Q. J. Roy. Meteor. Soc.*, **137 (656)**, 553–597.

Downes, S. M., and A. M. Hogg, 2013: Southern ocean circulation and eddy compensation in cmip5 models. *J. Clim.*, **26 (18)**, 7198–7220.

Exarchou, E., T. Kuhlbrodt, J. M. Gregory, and R. S. Smith, 2015: Ocean heat uptake processes: a model intercomparison. *J. Clim.*, **28 (2)**, 887–908.

Ferrari, R., S. M. Griffies, A. G. Nurser, and G. K. Vallis, 2010: A boundary-value problem for the parameterized mesoscale eddy transport. *Ocean Modell.*, **32 (3)**, 143–156.

Ferrari, R., M. F. Jansen, J. F. Adkins, A. Burke, A. L. Stewart, and A. F. Thompson, 2014: Antarctic sea ice control on ocean circulation in present and glacial climates. *Proc. Natl. Acad. Sci.*, **111 (24)**, 8753–8758.

Fučkar, N. S., and G. K. Vallis, 2007: Interhemispheric influence of surface buoyancy conditions on a circumpolar current. *Geophys. Res. Lett.*, **34 (14)**.

Galbraith, E., and C. de Lavergne, 2018: Response of a comprehensive climate model to a broad range of external forcings: relevance for deep ocean ventilation and the development of late Cenozoic ice ages. *Clim. Dyn.*, 1–27.

Gebbie, G., 2014: How much did glacial North Atlantic water shoal? *Paleoceanogr.*, **29 (3)**, 190–209.

Gent, P. R., 2016: Effects of Southern Hemisphere Wind Changes on the Meridional Overturning Circulation in Ocean Models. *Annu. Rev. Mar. Sci.*, **8**, 79–84.

Gent, P. R., and G. Danabasoglu, 2011: Response to increasing Southern Hemisphere winds in CCSM4. *J. Clim.*, **24 (19)**, 4992–4998.

Gent, P. R., W. G. Large, and F. O. Bryan, 2001: What sets the mean transport through Drake Passage? *J. Geophys. Res. Oceans*, **106 (C2)**, 2693–2712.

Gent, P. R., and J. C. Mcwilliams, 1990: Isopycnal mixing in ocean circulation models. *J. Phys. Oceanogr.*, **20 (1)**, 150–155.

Gent, P. R., and Coauthors, 2011: The community climate system model version 4. *J. Clim.*, **24 (19)**, 4973–4991.

Gersonde, R., X. Crosta, A. Abelmann, and L. Armand, 2005: Sea-surface temperature and sea ice distribution of the Southern Ocean at the EPILOG Last Glacial Maximum a circum-Antarctic view based on siliceous microfossil records. *Quat. Sci. Rev.*, **24 (7)**, 869–896.

Gersonde, R., and Coauthors, 2003: Last glacial sea surface temperatures and sea-ice extent in the Southern Ocean (Atlantic-Indian sector): A multiproxy approach. *Paleoceanogr.*, **18 (3)**.

Gnanadesikan, A., 1999: A simple predictive model for the structure of the oceanic pycnocline. *Science*, **283 (5410)**, 2077–2079.

Goosse, H., and V. Zunz, 2014: Decadal trends in the antarctic sea ice extent ultimately controlled by ice–ocean feedback. *Cryosphere*, **8 (2)**, 453–470.

Green, J. A., C. L. Green, G. R. Bigg, T. Rippeth, J. D. Scourse, and K. Uehara, 2009: Tidal mixing and the meridional overturning circulation from the Last Glacial Maximum. *Geophys. Res. Lett.*, **36 (15)**.

Gregory, J., and Coauthors, 2005: A model intercomparison of changes in the Atlantic thermohaline circulation in response to increasing atmospheric CO2 concentration. *Geophys. Res. Lett.*, **32 (12)**.

Griffies, S. M., 1998: The Gent–McWilliams skew flux. *J. Phys. Oceanogr.*, **28 (5)**, 831–841.

Griffies, S. M., and R. W. Hallberg, 2000: Biharmonic friction with a Smagorinsky-like viscosity for use in large-scale eddy-permitting ocean models. *Month. Weather Rev.*, **128 (8)**, 2935–2946.

Griffies, S. M., R. C. Pacanowski, and R. W. Hallberg, 2000: Spurious diapycnal mixing associated with advection in az-coordinate ocean model. *Mon. Weather Rev.*, **128 (3)**, 538–564.

Griffies, S. M., and Coauthors, 2009: Coordinated ocean-ice reference experiments (COREs). *Ocean Modell.*, **26 (1)**, 1–46.

Haney, R. L., 1971a: Surface thermal boundary condition for ocean circulation models. *J. Phys. Oceanogr.*, **1 (4)**, 241–248.

Haney, R. L., 1971b: Surface thermal boundary condition for ocean circulation models. *J. Phys. Oceanogr.*, **1 (4)**, 241–248.

Hill, C., D. Ferreira, J.-M. Campin, J. Marshall, R. Abernathey, and N. Barrier, 2012: Controlling spurious diapycnal mixing in eddy-resolving height-coordinate ocean models–insights from virtual deliberate tracer release experiments. *Ocean Modell.*, **45**, 14–26.

Hobbs, W. R., R. Massom, S. Stammerjohn, P. Reid, G. Williams, and W. Meier, 2016: A review of recent changes in southern ocean sea ice, their drivers and forcings. *Glob. Planet. Change*, **143**, 228–250.

Hogg, A. M., 2010: An Antarctic Circumpolar Current driven by surface buoyancy forcing. *Geophys. Res. Lett.*, **37 (23)**.

Holland, P. R., and R. Kwok, 2012: Wind-driven trends in antarctic sea-ice drift. *Nat. Geosci.*, **5 (12)**, 872.

Huber, M. B., and L. Zanna, 2017: Drivers of uncertainty in simulated ocean circulation and heat uptake. *Geophys. Res. Lett.*, **44 (3)**, 1402–1413.

Hunke, E., and J. Dukowicz, 1997: An elastic–viscous–plastic model for sea ice dynamics. *J. Phys. Oceanogr.*, **27 (9)**, 1849–1867.

Ito, T., M. Woloszyn, and M. Mazloff, 2010: Anthropogenic carbon dioxide transport in the Southern Ocean driven by Ekman flow. *Nature*, **463 (7277)**, 80.

Iudicone, D., G. Madec, B. Blanke, and S. Speich, 2008: The role of Southern Ocean surface forcings and mixing in the global conveyor. *J. Phys. Oceanogr.*, **38 (7)**, 1377–1400.

Jackett, D. R., and T. J. Mcdougall, 1995: Minimal adjustment of hydrographic profiles to achieve static stability. *J. Atmos. Ocean. Technol.*, **12 (2)**, 381–389.

Jackett, D. R., and T. J. McDougall, 1997: A neutral density variable for the world's oceans. *J. Phys. Oceanogr.*, **27 (2)**, 237–263.

Jansen, M. F., 2017: Glacial ocean circulation and stratification explained by reduced atmospheric temperature. *Proc. Natl. Acad. Sci.*, **114 (1)**, 45–50.

Jansen, M. F., and L.-P. Nadeau, 2016: The Effect of Southern Ocean Surface Buoyancy Loss on the Deep Ocean Circulation and Stratification. *J. Phys. Oceanogr.*, **46 (11)**, 3455–3470, doi:10.1175/JPO-D-16-0084.1.

Jayne, S. R., 2009: The impact of abyssal mixing parameterizations in an ocean general circulation model. *J. Phys. Oceanogr.*, **39 (7)**, 1756–1775.

Jones, C. S., and P. Cessi, 2016: Interbasin Transport of the Meridional Overturning Circulation. *J. Phys. Oceanogr.*, **46 (4)**, 1157–1169.

Jones, J. M., and Coauthors, 2016: Assessing recent trends in high-latitude Southern Hemisphere surface climate. *Nat. Clim. Change*, **6 (10)**, 917.

Kamenkovich, I., Z. Garraffo, R. Pennel, and R. A. Fine, 2017: Importance of mesoscale eddies and mean circulation in ventilation of the Southern Ocean. *J. Geophys. Res. Oceans*, **122 (4)**, 2724–2741.

Karsten, R., H. Jones, and J. Marshall, 2002: The role of eddy transfer in setting the stratification and transport of a circumpolar current. *J. Phys. Oceanogr.*, **32 (1)**, 39–54.

Karsten, R. H., and J. Marshall, 2002: Constructing the residual circulation of the acc from observations. *J. Phys. Oceanogr.*, **32 (12)**, 3315–3327.

Kay, J., C. Deser, and Coauthors, 2015: The Community Earth System Model (CESM) large ensemble project: A community resource for studying climate change in the presence of internal climate variability. *Bull. Amer. Meteor. Soc.*, **96 (8)**, 1333–1349.

Killworth, P. D., 1996: Time interpolation of forcing fields in ocean models. *J. Phys. Oceanogr.*, **26 (1)**, 136–143.

Klockmann, M., U. Mikolajewicz, and J. Marotzke, 2018: Two amoc states in response to decreasing greenhouse gas concentrations in the coupled climate model mpi-esm. *J. Clim.*, **31 (19)**, 7969–7984.

Kunze, E., E. Firing, J. M. Hummon, T. K. Chereskin, and A. M. Thurnherr, 2006: Global abyssal mixing inferred from lowered ADCP shear and CTD strain profiles. *J. Phys. Oceanogr.*, **36 (8)**, 1553–1576.

Kwok, R., 2011: Observational assessment of arctic ocean sea ice motion, export, and thickness in cmip3 climate simulations. *J. Geophys. Res. Oceans*, **116 (C8)**.

Lamy, F., and Coauthors, 2015: Glacial reduction and millennial-scale variations in Drake Passage throughflow. *Proc. Natl. Acad. Sci.*, **112 (44)**, 13 496–13 501.

Large, W. G., G. Danabasoglu, S. C. Doney, and J. C. McWilliams, 1997: Sensitivity to surface forcing and boundary layer mixing in a global ocean model: Annual-mean climatology. *J. Phys. Oceanogr.*, **27 (11)**, 2418–2447.

Large, W. G., J. C. McWilliams, and S. C. Doney, 1994: Oceanic vertical mixing: A review and a model with a nonlocal boundary layer parameterization. *Rev. Geophys.*, **32 (4)**, 363–403.

Legg, S., and Coauthors, 2009: Improving oceanic overflow representation in climate models: the gravity current entrainment climate process team. *Bull. Amer. Meteor. Soc.*, **90**, 657–670.

Lozier, M., and Coauthors, 2019: A sea change in our view of overturning in the subpolar North Atlantic. *Science*, **363 (6426)**, 516–521.

Lozier, M. S., 2012: Overturning in the North Atlantic. *Annu. Rev. Mar. Sci.*, **4**, 291–315.

Lumpkin, R., and K. Speer, 2007: Global ocean meridional overturning. *J. Phys. Oceanogr.*, **37 (10)**, 2550–2562.

Lund, D., J. Adkins, and R. Ferrari, 2011: Abyssal Atlantic circulation during the Last Glacial Maximum: Constraining the ratio between transport and vertical mixing. *Paleoceanogr.*, **26 (1)**.

Mahlstein, I., P. R. Gent, and S. Solomon, 2013: Historical Antarctic mean sea ice area, sea ice trends, and winds in CMIP5 simulations. *J. Geophys. Res.*, **118 (11)**, 5105–5110.

Marshall, D. P., and L. Zanna, 2014: A conceptual model of ocean heat uptake under climate change. *J. Clim.*, **27 (22)**, 8444–8465.

Marshall, J., A. Adcroft, C. Hill, L. Perelman, and C. Heisey, 1997: A finite-volume, incompressible Navier Stokes model for studies of the ocean on parallel computers. *J. Geophys. Res. Oceans*, **102 (C3)**, 5753–5766.

Marshall, J., D. Jamous, and J. Nilsson, 1999: Reconciling thermodynamic and dynamic methods of computation of water-mass transformation rates. *Deep-Sea Res. I*, **46 (4)**, 545–572.

Marshall, J., and T. Radko, 2003: Residual-mean solutions for the Antarctic Circumpolar Current and its associated overturning circulation. *J. Phys. Oceanogr.*, **33 (11)**, 2341–2354.

Marshall, J., J. R. Scott, A. Romanou, M. Kelley, and A. Leboissetier, 2017: The dependence of the oceans MOC on mesoscale eddy diffusivities: A model study. *Ocean Modell.*, **111**, 1–8.

Marshall, J., and K. Speer, 2012: Closure of the meridional overturning circulation through Southern Ocean upwelling. *Nat. Geosci.*, **5 (3)**, 171–180.

Marsland, S. J., H. Haak, J. H. Jungclaus, M. Latif, and F. Röske, 2003: The Max-Planck-Institute global ocean/sea ice model with orthogonal curvilinear coordinates. *Ocean Modell.*, **5 (2)**, 91–127.

Marzocchi, A., and M. F. Jansen, 2017: Connecting Antarctic sea ice to deep-ocean circulation in modern and glacial climate simulations. *Geophys. Res. Lett.*, **44 (12)**, 6286–6295.

Mashayek, A., R. Ferrari, S. Merrifield, J. R. Ledwell, L. St Laurent, and A. Naveira Garabato, 2017: Topographic enhancement of vertical turbulent mixing in the Southern Ocean. *Nat. Communi.*, **8**, 14 197.

Mashayek, A., R. Ferrari, M. Nikurashin, and W. Peltier, 2015: Influence of enhanced abyssal diapycnal mixing on stratification and the ocean overturning circulation. *J. Phys. Oceanogr.*, **45 (10)**, 2580–2597.

Mazloff, M. R., R. Ferrari, and T. Schneider, 2013: The force balance of the Southern Ocean meridional overturning circulation. *J. Phys. Oceanogr.*, **43 (6)**, 1193–1208.

Mazloff, M. R., P. Heimbach, and C. Wunsch, 2010: An eddy-permitting Southern Ocean state estimate. *J. Phys. Oceanogr.*, **40 (5)**, 880–899.

McDougall, T. J., 1987: Neutral surfaces in the ocean: implications for modelling. *Geophys. Res. Lett.*, **14 (8)**, 797–800.

Meijers, A., E. Shuckburgh, N. Bruneau, J.-B. Sallee, T. Bracegirdle, and Z. Wang, 2012: Representation of the Antarctic Circumpolar Current in the CMIP5 climate models and future changes under warming scenarios. *J. Geophys. Res. Oceans*, **117 (C12)**.

Monnin, E., A. Indermühle, A. Dällenbach, J. Flückiger, B. Stauffer, T. F. Stocker, D. Raynaud, and J.-M. Barnola, 2001: Atmospheric CO2 concentrations over the last glacial termination. *Science*, **291 (5501)**, 112–114.

Morrison, A. K., and A. M. Hogg, 2013: On the relationship between southern ocean overturning and acc transport. *J. Phys. Oceanogr.*, **43 (1)**, 140–148.

Muglia, J., and A. Schmittner, 2015: Glacial Atlantic overturning increased by wind stress in climate models. *Geophys. Res. Lett.*, **42 (22)**, 9862–9868.

Munday, D., L. Allison, H. Johnson, and D. Marshall, 2011: Remote forcing of the Antarctic Circumpolar Current by diapycnal mixing. *Geophys. Res. Lett.*, **38 (8)**.

Munday, D. R., H. L. Johnson, and D. P. Marshall, 2013: Eddy saturation of equilibrated circumpolar currents. *J. Phys. Oceanogr.*, **43 (3)**, 507–532.

Munk, W., and C. Wunsch, 1998: Abyssal recipes ii: energetics of tidal and wind mixing. *Deep-Sea Res.*, **45**, 1977–2010.

Munk, W. H., 1966: Abyssal recipes. *Deep-Sea Res.*, Elsevier, Vol. 13, 707–730.

Munk, W. H., and E. Palmén, 1951: Note on the Dynamics of the Antarctic Circumpolar Current. *Tellus*, **3 (1)**, 53–55.

Nakano, H., and N. Suginohara, 2002: Effects of bottom boundary layer parameterization on reproducing deep and bottom waters in a world ocean model. *J. Phys. Oceanogr.*, **32 (4)**, 1209–1227.

Naveira Garabato, A. C., K. L. Polzin, B. A. King, K. J. Heywood, and M. Visbeck, 2004: Widespread intense turbulent mixing in the Southern Ocean. *Science*, **303 (5655)**, 210–213.

Newsom, E. R., C. M. Bitz, F. O. Bryan, R. Abernathey, and P. R. Gent, 2016: Southern Ocean deep circulation and heat uptake in a high-resolution climate model. *J. Clim.*, **29 (7)**, 2597–2619.

Newsom, E. R., and A. F. Thompson, 2018: Reassessing the role of the indo-pacific in the ocean's global overturning circulation. *Geophys. Res. Lett.*, **in press**.

Nikurashin, M., and G. Vallis, 2011: A theory of deep stratification and overturning circulation in the ocean. *J. Phys. Oceanogr.*, **41 (3)**, 485–502.

Nikurashin, M., and G. Vallis, 2012: A theory of the interhemispheric meridional overturning circulation and associated stratification. *J. Phys. Oceanogr.*, **42 (10)**, 1652–1667.

Nurser, A. G., and M.-M. Lee, 2004: Isopycnal averaging at constant height. Part I: The formulation and a case study. *J. Phys. Oceanogr.*, **34 (12)**, 2721–2739.

Oka, A., H. Hasumi, and A. Abe-Ouchi, 2012: The thermal threshold of the Atlantic meridional overturning circulation and its control by wind stress forcing during glacial climate. *Geophys. Res. Lett.*, **39 (9)**.

Otto-Bliesner, B., C. Hewitt, T. Marchitto, E. Brady, A. Abe-Ouchi, M. Crucifix, S. Murakami, and S. Weber, 2007: Last Glacial Maximum ocean thermohaline circulation: PMIP2 model intercomparisons and data constraints. *Geophys. Res. Lett.*, **34 (12)**.

Otto-Bliesner, B. L., E. C. Brady, G. Clauzet, R. Tomas, S. Levis, and Z. Kothavala, 2006: Last glacial maximum and Holocene climate in CCSM3. *J. Clim.*, **19 (11)**, 2526–2544.

Polvani, L. M., and K. L. Smith, 2013: Can natural variability explain observed Antarctic sea ice trends? New modeling evidence from CMIP5. *Geophys. Res. Lett.*, **40 (12)**, 3195–3199.

Purich, A., W. Cai, M. H. England, and T. Cowan, 2016: Evidence for link between modelled trends in antarctic sea ice and underestimated westerly wind changes. *Nat. Communi.*, **7**, 10 409.

Raphael, M., and Coauthors, 2016: The Amundsen sea low: variability, change, and impact on Antarctic climate. *Bull. Amer. Meteor. Soc.*, **97 (1)**, 111–121.

Roberts, M., and D. Marshall, 1998: Do we require adiabatic dissipation schemes in eddy-resolving ocean models? *Journal of Physical Oceanography*, **28 (10)**, 2050–2063.

Rosenblum, E., and I. Eisenman, 2017: Sea ice trends in climate models only accurate in runs with biased global warming. *J. Clim.*, **30 (16)**, 6265–6278.

Sarmiento, J. L., and N. Gruber, 2002: Sinks for anthropogenic carbon. *Phys. Today*, **August**, 30–36.

Sarmiento, J. L., and J. R. Toggweiler, 1984: A new model for the role of the oceans in determining atmospheric pCO_2. *Nature*, **308 (5960)**, 621–624.

Schmittner, A., J. Green, and S.-B. Wilmes, 2015: Glacial ocean overturning intensified by tidal mixing in a global circulation model. *Geophys. Res. Lett.*, **42 (10)**, 4014–4022.

Sigman, D. M., M. P. Hain, and G. H. Haug, 2010: The polar ocean and glacial cycles in atmospheric CO_2 concentration. *Nature*, **466 (7302)**, 47–55.

Simmonds, I., 2015: Comparing and contrasting the behaviour of arctic and antarctic sea ice over the 35 year period 1979-2013. *Ann. Glaciol.*, **56 (69)**, 18–28.

Snow, K., A. M. Hogg, B. M. Sloyan, and S. M. Downes, 2016: Sensitivity of Antarctic bottom water to changes in surface buoyancy fluxes. *J. Clim.*, **29 (1)**, 313–330.

Stewart, A. L., R. Ferrari, and A. F. Thompson, 2014: On the importance of surface forcing in conceptual models of the deep ocean. *J. Phys. Oceanogr.*, **44 (3)**, 891–899.

Stommel, H., 1961: Thermohaline convection with two stable regimes of flow. *Tellus*, **13 (2)**, 224–230.

Su, Z., 2017: Preconditioning of Antarctic maximum sea ice extent by upper ocean stratification on a seasonal timescale. *Geophys. Res. Lett.*, **44 (12)**, 6307–6315.

Sun, S., I. Eisenman, and A. L. Stewart, 2016: The influence of Southern Ocean surface buoyancy forcing on glacial-interglacial changes in the global deep ocean stratification. *Geophys. Res. Lett.*, **43 (15)**, 8124–8132.

Sun, S., I. Eisenman, and A. L. Stewart, 2018: Does Southern Ocean surface forcing shape the global ocean overturning circulation? *Geophys. Res. Lett.*, **45 (5)**, 2413–2423.

Sun, S., and J. Liu, 2017: Sensitivity of the Antarctic Circumpolar Current transport to surface buoyancy conditions in the North Atlantic. *Ocean Modell.*, **118**, 118–129.

Swart, N. C., S. T. Gille, J. C. Fyfe, and N. P. Gillett, 2018: Recent southern ocean warming and freshening driven by greenhouse gas emissions and ozone depletion. *Nat. Geosci.*, **11 (11)**, 836.

Talley, L. D., 2013: Closure of the global overturning circulation through the Indian, Pacific, and Southern Oceans: Schematics and transports. *Oceanography*, **26 (1)**, 80–97.

Tamsitt, V., L. D. Talley, M. R. Mazloff, and I. Cerovečki, 2016: Zonal variations in the Southern Ocean heat budget. *Journal of Clim*, **29 (18)**, 6563–6579.

Tamsitt, V., and Coauthors, 2017: Spiraling pathways of global deep waters to the surface of the southern ocean. *Nat. Communi.*, **8 (1)**, 172.

Taylor, K. E., R. J. Stouffer, and G. A. Meehl, 2012: An overview of cmip5 and the experiment design. *Bull. Amer. Meteor. Soc.*, **93 (4)**, 485–498.

Thompson, A. F., S. K. Hines, and J. F. Adkins, 2019: A Southern Ocean mechanism for the inter-hemispheric coupling and phasing of the bipolar seesaw. *J. Clim.*, **(2019)**.

Thompson, A. F., A. L. Stewart, and T. Bischoff, 2016: A Multibasin Residual-Mean Model for the Global Overturning Circulation. *J. Phys. Oceanogr.*, **46 (9)**, 2583–2604.

Toggweiler, J., and B. Samuels, 1995: Effect of Drake Passage on the global thermohaline circulation. *Deep-Sea Res. I*, **42 (4)**, 477–500.

Toggweiler, J. R., and J. Russell, 2008: Ocean circulation in a warming climate. *Nature*, **451 (7176)**, 286–288.

Tréguier, A.-M., M. England, S. Rintoul, G. Madec, J. Le Sommer, and J.-M. Molines, 2007: Southern Ocean overturning across streamlines in an eddying simulation of the Antarctic Circumpolar Current. *Ocean Sci.*, **4 (4)**, 653–698.

Tschudi, M., C. Fowler, J. Maslanik, J. Stewart, and W. Meier, 2016: Polar Pathfinder daily 25 km EASE-Grid Sea Ice motion vectors, version 3. *National Snow and Ice Data Center Distributed Active Archive Center, Boulder, Colorado, [accessed October, 2017]*, doi:https://doi.org/10.5067/O57VAIT2AYYY.

Turner, J., T. J. Bracegirdle, T. Phillips, G. J. Marshall, and J. S. Hosking, 2013: An initial assessment of antarctic sea ice extent in the cmip5 models. *J. Clim.*, **26 (5)**, 1473–1484.

Turner, J., J. S. Hosking, T. J. Bracegirdle, G. J. Marshall, and T. Phillips, 2015: Recent changes in Antarctic sea ice. *Philos. T. R. Soc.*, **373 (2045)**, 20140 163.

Viebahn, J., and C. Eden, 2010: Towards the impact of eddies on the response of the Southern Ocean to climate change. *Ocean Modell.*, **34 (3)**, 150–165.

Visbeck, M., J. Marshall, T. Haine, and M. Spall, 1997: Specification of eddy transfer coefficients in coarse-resolution ocean circulation models. *J. Phys. Oceanogr.*, **27 (3)**, 381–402.

Walin, G., 1982: On the relation between sea-surface heat flow and thermal circulation in the ocean. *Tellus*, **34 (2)**, 187–195.

Wang, Z., T. Kuhlbrodt, and M. P. Meredith, 2011: On the response of the Antarctic Circumpolar Current transport to climate change in coupled climate models. *J. Geophys. Res. Oceans*, **116 (C8)**.

Watanabe, M., and Coauthors, 2010: Improved climate simulation by MIROC5: mean states, variability, and climate sensitivity. *J. Clim.*, **23 (23)**, 6312–6335.

Waterhouse, A. F., and Coauthors, 2014: Global patterns of diapycnal mixing from measurements of the turbulent dissipation rate. *J. Phys. Oceanogr.*, **44 (7)**, 1854–1872.

Watson, A. J., J. R. Ledwell, M.-J. Messias, B. A. King, N. Mackay, M. P. Meredith, B. Mills, and A. C. Naveira Garabato, 2013: Rapid cross-density ocean mixing at mid-depths in the Drake Passage measured by tracer release. *Nature*, **501 (7467)**, 408.

Watson, A. J., G. K. Vallis, and M. Nikurashin, 2015: Southern Ocean buoyancy forcing of ocean ventilation and glacial atmospheric CO_2. *Nat. Geosci.*, **8 (11)**, 861–864.

Whalen, C., L. Talley, and J. MacKinnon, 2012: Spatial and temporal variability of global ocean mixing inferred from Argo profiles. *Geophys. Res. Lett.*, **39 (18)**.

Wolfe, C. L., and P. Cessi, 2010: What sets the strength of the middepth stratification and overturning circulation in eddying ocean models? *J. Phys. Oceanogr.*, **40 (7)**, 1520–1538.

Wolfe, C. L., and P. Cessi, 2011: The adiabatic pole-to-pole overturning circulation. *J. Phys. Oceanogr.*, **41 (9)**, 1795–1810.

Wolfe, C. L., and P. Cessi, 2014: Salt feedback in the adiabatic overturning circulation. *J. Phys. Oceanogr.*, **44 (4)**, 1175–1194.

Wu, L., Z. Jing, S. Riser, and M. Visbeck, 2011: Seasonal and spatial variations of Southern Ocean diapycnal mixing from Argo profiling floats. *Nat. Geosci.*, **4 (6)**, 363–366.

Yeager, S., and G. Danabasoglu, 2014: The origins of late-twentieth-century variations in the large-scale North Atlantic circulation. *J. Clim.*, **27 (9)**, 3222–3247.

Yin, J. H., 2005: A consistent poleward shift of the storm tracks in simulations of 21st century climate. *Geophys. Res. Lett.*, **32 (18)**.

Zhang, J., and R. Zhang, 2015: On the evolution of Atlantic meridional overturning circulation fingerprint and implications for decadal predictability in the North Atlantic. *Geophys. Res. Lett.*, **42 (13)**, 5419–5426.

Zhang, L., T. L. Delworth, W. Cooke, and X. Yang, 2019: Natural variability of southern ocean convection as a driver of observed climate trends. *Nat. Clim. Change*, **9 (1)**, 59.

Zhang, X., G. Lohmann, G. Knorr, and X. Xu, 2013: Different ocean states and transient characteristics in Last Glacial Maximum simulations and implications for deglaciation. *Clim. Past*, **9 (5)**, 2319.

Zhao, J., and W. Johns, 2014: Wind-driven seasonal cycle of the Atlantic meridional overturning circulation. *J. Phys. Oceanogr.*, **44 (6)**, 1541–1562.